

The University of Sheffield



Novel Flux-weakening Control of Permanent Magnet Synchronous Machines with Particular Reference to Stability Issues

Chao Wang

A thesis submitted for the degree of Doctor of Philosophy

Department of Electronic and Electrical Engineering

University of Sheffield

4 Jun 2019

ABSTRACT

For many applications, such as electric vehicles and washing machines, flux-weakening control is required for permanent magnet synchronous machine (PMSM) drives to extend the operation speed range and maximize the power capability under the voltage and current constraints. Voltage magnitude feedback flux-weakening control is widely employed due to its advantages of simple and standard control structure, robustness against parameter variation, both linear and over modulation flux-weakening operation, and automatic flux-weakening operation. However, stability problems are prone to occur in the flux-weakening region since the PMSM drive will operate on the boundary of the voltage limit. In this thesis, based on a non-salient-pole PMSM, the factors that could cause stability problems in the flux-weakening region with voltage magnitude feedback flux-weakening control are investigated and the corresponding solutions are developed.

Firstly, based on a d-axis current voltage feedback controller, an adaptive control parameter method is proposed for the PMSM machine without maximum torque per voltage (MTPV) region, which aims to ensure the stability in a wider speed range. Then, a current reference modifier (CRM) and a voltage limit reference modifier (VRM) are incorporated with the conventional voltage feedback controller in order to improve the stability in the over modulation region. As for the PMSM machine with MTPV region, an extra feedback controller is introduced with an MTPV penalty function. The MTPV penalty function is optimized in terms of its effect on the steady-state performance, the dynamic performance, and the stability in the MTPV region. Afterward, the MTPV controller is properly selected and designed. Furthermore, two flux-weakening control methods accounting for MTPV, i.e. dq-axis current based feedback flux-weakening control, and current amplitude and angle based feedback flux-weakening control, are developed and compared in terms of the stability. It shows that the two methods exhibit complimentary merits and demerits in different regions, and consequently, a hybrid feedback flux-weakening control is proposed to combine their synergies and overcome their demerits. As the feedback voltage ripples that origin from the non-ideal drive system can be amplified by a conventional speed PI controller, the oscillation may even occur if a good speed dynamics is required in the flux-weakening region. An adaptive fuzzy logic speed controller is proposed and implemented to reduce the feedback voltage ripples while maintaining good speed dynamics.

ACKNOWLEDGMENTS

First and foremost, I would like to express my sincere gratitude to my supervisor, Professor Z. Q. Zhu, for his consistent supervision, guidance, and support. His guidance on critical thinking and pursuing perfection are preciously important and invaluable.

I would like to thank my sponsoring company Midea Welling Motor Technology for giving me this opportunity to study in the most fantastic Electrical Machines and Drives (EMD) research group in the world. My particular thanks give to Dr Jintao Chen for his introduction and encouragement. Many thanks to Dr Liming Gong for his support and suggestions, and my colleagues Mr Xiaoran Zhao and Mr Tiebin Lu for their technical support and discussions.

I am very grateful to Dr Hao Hua and Dr Yue Liu for their assistance and helpful suggestions on my test machine. I also want to express thanks to my fellow colleagues in our group for their knowledgeable discussions, particularly, Dr Mohammed FH Khatab, Dr Peilin Xu, Dr Shaoshen Xue, Dr Zhongze Wu, Dr Hanlin Zhan, Dr Huayang Li, Mr Huan Qu, Mr James Dexter, Mr Bo Shuang, Mr Lei Yang, and Mr Lu Wang. Further thanks give to Dr Juntao Shi, Dr Yuan Ren for their encouragement and inspiration during my doctoral life.

My special thanks give to the EMD lab technicians, Mr Richard Garraway, Mr Lawrence Obodo, and Mr Andrew Race for their technical support.

My eternal gratitude gives to my parents and my sister for their endless support, encouragement, and love throughout my PhD study.

CONTENTS

ABSTRACT	1
ACKNOWLEDGMENTS	2
CONTENTS	3
LIST OF ABBREVIATIONS	6
LIST OF SYMBOLS	8
CHAPTER 1 GENERAL INTRODUCTION.....	11
1.1 Introduction	11
1.2 Flux-Weakening Control Strategies	14
1.1.1. Flux-Weakening Methods Based on Dual-Current Structure	15
1.1.2. Flux-Weakening Methods Based on Single-Current Control	29
1.1.3. Comparison	33
1.3 Scope and Contribution of the Thesis	35
1.1.4. Motivation	35
1.1.5. Outline	37
1.1.6. Contribution	39
CHAPTER 2 ADAPTIVE VOLTAGE FEEDBACK CONTROLLER ON PMSM..	41
2.1 Introduction	41
2.2 Machine Model and Voltage Feedback Controller.....	43
2.2.1 Machine Model	43
2.2.2 Voltage Feedback Controller	43
2.3 Analyses of Voltage Feedback Loop and Adaptive Control Parameter	46
2.3.1 Linearized Model of Voltage Loop.....	46
2.3.2 Stability Analysis and Control Parameter Design.....	48
2.4 Improvement in the Over Modulation Range.....	61
2.4.1 $M \leq 1$	61
2.4.2 $M > 1$	63
2.5 Experimental Verification	65
2.5.1 Stability with Non-adaptive λ_l and Adaptive λ_l	66
2.5.2 Performances in Over Modulation Region.....	71
2.6 Conclusion	73

CHAPTER 3	FEEDBACK TYPE FLUX-WEAKENING CONTROL ON PMSM WITH MTPV REGION	74
3.1	Introduction	74
3.2	Feedback Type Control Strategies.....	75
3.2.1	Operation Regions.....	75
3.2.2	Control Strategies.....	76
3.3	Optimized MTPV Controller.....	78
3.3.1	Penalty Function for MTPV	78
3.3.2	MTPV Controller Design.....	81
3.3.3	Over Modulation Improvement.....	84
3.4	Experimental Verification	89
3.4.1	Steady-State Performance	90
3.4.2	Dynamic Performance with Different MTPV Controllers.....	92
3.4.3	Stability in Over Modulation Region.....	97
3.5	Conclusion.....	99
CHAPTER 4	COMPARATIVE STUDY OF TWO FEEDBACK METHODS FOR FLUX-WEAKNING CONTROL OF PMSM.....	101
4.1	Introduction	101
4.2	Two Flux-Weakening Control Methods.....	102
4.2.1	Dq-axis Current Based Feedback Flux-Weakening Control (DQFFC)	102
4.2.2	Current Amplitude and Angle Based Feedback Flux-Weakening Control (CAAFFC)	104
4.3	Stability Analysis and Controller Design.....	105
4.3.1	Generalized Linearized Model of Voltage Loop.....	106
4.3.2	Stability Analysis of Voltage Loops	107
4.3.3	MTPV Controller Design.....	111
4.4	Experimental Verification	112
4.4.1	With and Without MTPV Controller in DQFFC and CAAFFC	113
4.4.2	Performance When Approaching MTPV Curve.....	116
4.4.3	Transition Between Motoring and Generating Conditions	118
4.5	Conclusion.....	118
CHAPTER 5	HYBRID FEEDBACK FLUX-WEAKENING CONTROL OF PMSM	120
5.1	Introduction	120
5.2	Issues with Existing Voltage Feedback Methods.....	121
5.3	Hybrid Feedback Flux-Weakening Control	122

5.3.1	Introduction of Hybrid Feedback Flux-Weakening Control	122
5.3.2	Design of Hybrid Voltage Feedback Controller	125
5.4	Experimental Verification	131
5.4.1	With and Without MTPV Controller in HFFC	133
5.4.2	Performance When Approaching MTPV Curve	134
5.4.3	Transition Between Motoring and Generating Conditions	137
5.5	Conclusion	137
CHAPTER 6	FUZZY LOGIC SPEED CONTROL OF PMSM AND FEEDBACK VOLTAGE RIPPLE REDUCTION IN FLUX-WEAKENING REGION	139
6.1	Introduction	139
6.2	Flux-weakening Control with Speed PI Controller	141
6.2.1	Current Vector Control System with Speed PI Controller	141
6.2.2	Voltage Ripples Analysis in Flux-weakening Region	143
6.3	Adaptive Fuzzy Logic Speed controller	150
6.3.1	PI Controller and FLC	150
6.3.2	Design of Adaptive FLC	151
6.4	Experimental Verification	155
6.4.1	Voltage Ripples in Current Control Mode and Speed Control Mode ..	156
6.4.2	Performance Comparison with PI and FLC	158
6.5	Conclusion	163
CHAPTER 7	GENERAL CONCLUSION AND FUTURE WORK.....	165
7.1	Summary of the Research Work.....	165
7.2	Conclusion.....	167
7.2.1	Tuning of Voltage Feedback Controller.....	167
7.2.2	Stability Improvement in Over Modulation Region	168
7.2.3	Optimization and Design of MTPV Controller.....	168
7.2.4	Novel Hybrid Voltage Feedback Controller	169
7.2.5	Alternative Speed Controller-FLC	170
7.3	Future Work.....	170
REFERENCES	172
APPENDIX A	EXPERIMENTAL SETUP.....	182
APPENDIX B	TUNING OF DCVFC AND CAVFC CONSIDERING MTPV	188
APPENDIX C	PUBLICATIONS.....	192

LIST OF ABBREVIATIONS

AC	Alternative current
BLAC	Brushless AC
BLDC	Brushless DC
CAAFFC	Current amplitude and angle based feedback flux-weakening control
CAVFC	Current angle based voltage feedback controller
CPSR	Constant power speed ratio
CPU	Central processing unit
CRM	Current reference modifier
CCM	Current control mode
DC	Direct current
DQFFC	Dq-axis currents based feedback flux-weakening control
DCVFC	D-axis current based voltage feedback controller
DSP	Digital signal processor
EMD	Electrical machines and drives
GUI	Graphic user interface
EMF	Electromotive force
FHFC	Feedforward based hybrid flux-weakening control
HPF	High pass filter
HVFC	Hybrid voltage feedback controller
IGBT	Insulated gate bipolar transistor
IPM	Interior permanent magnet

IPMSM	Interior permanent magnet synchronous machine
LPF	Low pass filter
MOSFET	Metal-oxide-semiconductor field-effect transistor
MTPA	Max torque per ampere
MTPV	Max torque per voltage
PI	Proportional integral
PM	Permanent magnet
PMSM	Permanent magnet synchronous machine
PWM	Pulse width modulation
RPM	Revolutions per minute
SCC	Single-current control
SCM	Speed control mode
VAC	Voltage angle control
VRM	Voltage limit reference modifier
VVM	Voltage vector modifier

LIST OF SYMBOLS

i_d, i_q	D- and q-axis currents	A
i_d^*, i_q^*	Actual d- and q-axis current commands	A
$i_{d,MTPA}^*, i_{q,MTPA}^*$	Initial d- and q-axis current commands	A
i_d^0, i_q^0	D- and q- axis currents at equilibrium point	A
$i_{dn}, i_{qn},$	Normalized dq-axis currents at equilibrium point	p.u.
i_α, i_β	α - and β -axis currents	A
i_{qf}^*, i_{sf}^*	Current outputs by MTPV controller	A
I_m	Current limit	A
I_b	Base current	A
i_{smin}^*	Minimum current required in FHFC	A
i_{dff}^*, i_{dffm}^*	Feedforward currents in FHFC	A
i_c	Characteristic current	A
k_{pd}, k_{id}	Proportional-integral gains for d-axis current regulator	
k_{pq}, k_{iq}	Proportional-integral gains for q-axis current regulator	
k_{ps}, k_{is}	Proportional-integral gains for q-axis speed regulator	
k_{pqf}, k_{iqf}	Proportional-integral gains of the MTPV controller in DQFFC	
\mathbf{I}_s	Current vector	A
J	Moment of inertia	$\text{kg}\cdot\text{m}^2$
L_s	Synchronous inductance (equal dq-axis inductance)	H
L_d, L_q	D- and q-axis inductances	A
M	Modulation coefficient	
Min	Minimum operation	

Mod	Modulo operation	
N_p	Number of pole pairs	
n^*	Speed reference	rpm
n	Speed feedback	rpm
R_s	Stator resistance	ohm
T_e	Electromagnetic torque	Nm
T_l	Load torque	Nm
V_d, V_q	D- and q-axis voltages	V
V_d^0, V_q^0	D- and q- axis voltages at equilibrium point	V
V_m	Voltage magnitude limit	V
V_b	Base voltage	V
V_{dn}, V_{qn}	Normalized dq-axis voltages at equilibrium point	p.u.
V_α, V_β	α - and β -axis voltages	V
V_{dc}	DC-link voltage	V
V_s^*	Voltage command vector (feedback voltage vector)	
V_{stmp}	Temporal voltage vector for VVM	
V_{sm}^*	Modified voltage vector	
V_{sme}^*	Temporal voltage error vector ($V_s^* - V_{stmp}$)	
V_{sr}^*	Voltage magnitude reference	
ω_{cc}	Current bandwidth	rad/s
ω_e	Electrical angular speed	rad/s
ω_b	Base speed	rad/s
ω_{en}	Normalized speed at the equilibrium point	p.u.

ω_{co}	Corner speed (minimum speed in the flux-weakening region)	rad/s
w_I, w_θ	Weight factors of DCVFC and CAVFC in HVFC	
Δ	Prefix for relevant small signal	
θ_f^*	Lead angle of current vector with respect to q axis	rad
$\lambda_I, \lambda_\theta$	Integral gains of DCVFC and CAVFC	
λ_{Is}	Integral gain of the MTPV controller in CAAFFC	
$\lambda_{Ih}, \lambda_{\theta h}$	Integral gains of HVFC	
ζ	Damping factor	

CHAPTER 1 GENERAL INTRODUCTION

1.1 Introduction

Nowadays, pursuits of advanced electrical drives with high power density and high efficiency are becoming the major goal of both academia and industry as the global environmental, economic and political concerns are increasing. Moreover, numerous emerging applications, such as electric propulsion and renewable energy, are continuously demanding high-performance electrical machines. Furthermore, the advancement of the permanent magnet (PM) materials, power electronics, and microprocessors has driven extensive researches on brushless permanent magnet synchronous machines (PMSMs), which have advantages of high efficiency, high torque and power density [ZHU07].

The conventional radial field PMSM can be categorized by two major types [SEB86] [JAH96] [GON12]:

- 1) Surface mounted permanent magnet synchronous machine (SPMSM).
- 2) Interior permanent magnet synchronous machine (i.e. IPMSM).

Fig. 1.1 illustrates the cross sections of typical rotor structures for inner rotor radial field PMSMs. For the rotor of SPMSM, as shown in Fig. 1.1(a), the PMs are mounted on the surface of the rotor. Since the rare earth PM material exhibits almost the same permeability as the air, the effective air gap is the summation of the actual air gap length and the radial thickness of the magnets. In the synchronous reference frame, the d-axis inductance is approximately the same as the q-axis inductance, i.e. $L_d=L_q$, where L_d and L_q are the d- and q-axis inductances, respectively. SPMSM is a non-salient-pole PMSM, in which the reluctance torque is negligible and the electromagnetic torque is dominated by the permanent-magnet excitation torque. For the rotor in IPMSM, the PMs are buried inside the rotor, which can be radially magnetized and circumferentially magnetized, as shown in Fig. 1.1(b) and Fig. 1.1(c), respectively. For the IPMSM, the effective air gap in d- and q-axes are not equal, and the d-axis inductance is normally smaller than the q-axis inductance due to larger effective air gap along d-axis. IPMSM is a salient-pole PMSM, in which the reluctance

torque can be utilized. Therefore, for the same torque the amount of PMs in an IPMSM can be less than that of the SPMSM.

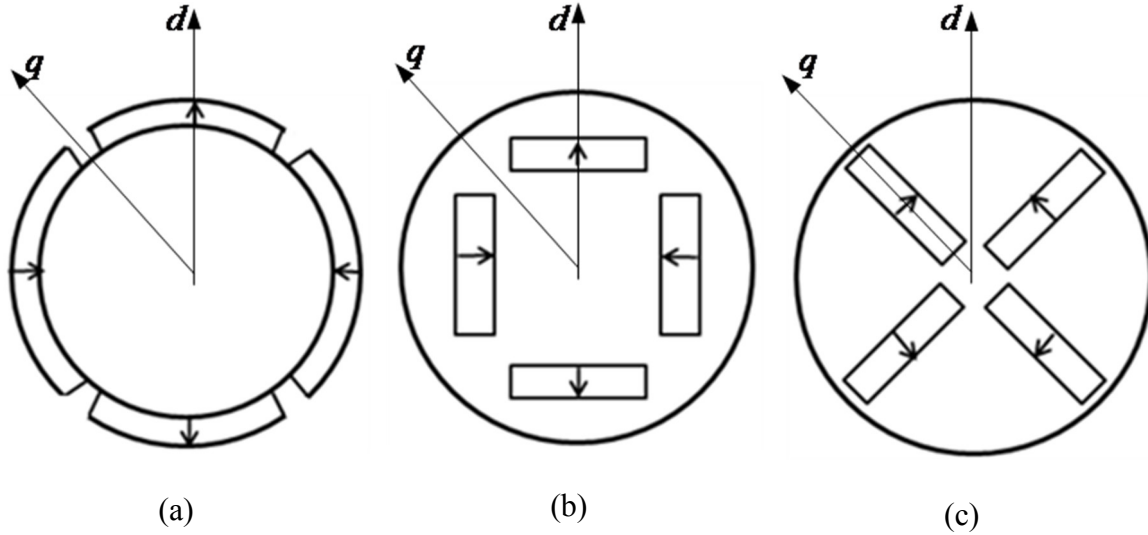


Fig. 1.1. Typical rotor structures of brushless PM synchronous machines [GON12].

The PMSMs can also be classified as either trapezoidal or sinusoidal back-electromotive force (EMF) machines [JAH84]. Ideally, in order to maximize the torque density and minimize the torque ripples, the machine with trapezoidal back-EMF is desirable to be controlled in BLDC mode. As shown in Fig. 1.2(a), the phase current waveform in BLDC mode is rectangular while the back-EMF is trapezoidal. For the machine with sinusoidal back-EMF, the machine is normally controlled in BLAC mode. As shown in Fig. 1.2(a), the phase current waveform is a pure sinusoidal as the phase back-EMF. In practice, since the back-EMF may not be ideal trapezoidal or sinusoidal, both the BLDC drive and BLAC drive could be applied for application. However, the performances, e.g. torque capability and torque ripple, could be compromised [SHI06] [ZHU06].

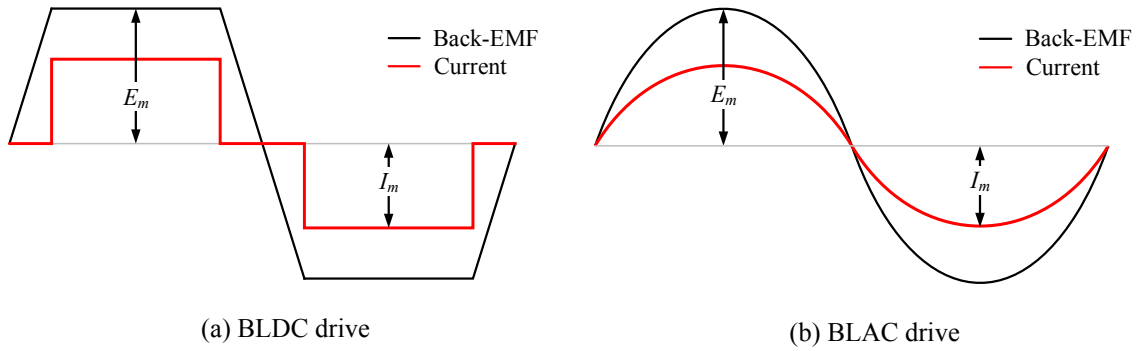


Fig. 1.2. Ideal BLDC drive and BLAC drive.
 E_m : amplitude of the phase back-EMF; I_m : amplitude of the phase current.

In BLDC mode, the phase currents only have to be commutated on and off, typically twice in one fundamental electric cycle for the two-phase, 120° conduction mode [OGA91][QIA05][TAK94]. The zero cross point of back-EMF can be set as the reference to obtain the rotor position. Therefore, the low-cost Hall sensor is normally employed. However, in BLAC mode, a sinusoidal current control is required. High-resolution position sensors, such as encoder and resolver, can be adopted. Since the phase currents are pure sinusoidal, the precise current control can be realized by the conventional current vector control (CVC) [GAB80]. In the low-speed range, the current can be easily controlled due to the low back-EMF value. However, as the speed increases, due to the increased back-EMF and limited DC-link voltage, the flux-weakening control has to be applied to extend speed range while maximizing the torque capability [JAH86] [SOO93] [MOR94].

The flux-weakening control can be realized by advancing the commutation angle. As the phase reactance increases with the increasing speed, the current waveform tends to be sinusoidal in BLDC mode when the machine speed is higher. The optimum advance commutation angle for the maximum torque is speed dependent, which is normally obtained through simulation or experimental results [ZHU06] [SHI06]. In BLAC mode, the current command in the flux-weakening region can be analytically obtained under the current and voltage constraints, and the current can be easily controlled by the synchronous PI controllers in dq-axis reference frame [LOR87]. Therefore, the optimal flux-weakening performance in BLAC mode can be predicted online or offline. Generally, the BLAC drive is more preferable for applications where high control performances are required, such as electric vehicle and

servo motor [ZHU08] [PFA84] [FUJ92]. On the other hand, the BLDC drive is normally used for low-cost applications where the control performance requirement is not very critical, such as fan and pump [CHO07] [YOU15]. In some applications where the fundamental frequency is very high and even close to the switching frequency, such as vacuum cleaner [ZHU02], the BLDC drive is more preferable. With the development of the microprocessors, the low-cost application can also employ the BLAC drive, in which the continuous rotor position can be obtained by the sensorless method [HOL98] [DEG98] [HAR00] [FOO10] or by the extrapolation method with a low-resolution Hall sensor [MOR03]. Therefore, the BLAC drive is very popular in practical applications.

For the application where only the constant torque region is required, the control strategies of the BLAC drive are straightforward. For example, based on current vector control (CVC) system, the d- and q-axis current commands can be directly obtained according to the maximum torque per ampere (MTPA) in order to improve the efficiency [JAH86]. As for the flux-weakening control, although the optimal current trajectory can be analytically obtained, more problems are prone to occur in this region due to that the system operates on the boundary of the voltage limit. In this thesis, the BLAC control based on CVC system is only considered, with particular reference to the flux-weakening control strategies.

1.2 Flux-Weakening Control Strategies

Some preliminary studies [SNE85] [JAH87] on flux-weakening control of PMSM are carried out in the middle of 1980s. The current trajectory considering the MTPA in the constant region is analysed in [JAH86], which points out that the MTPA curve is the optimal current trajectory to minimize the copper loss in the constant torque region. Later, many control strategies are developed for the flux-weakening operation. According to the current control structure, the flux-weakening methods can be mainly categorized into two types:

- 1) Flux-weakening based on dual-current structure;
- 2) Flux-weakening based on single-current structure.

1.1.1. Flux-Weakening Methods Based on Dual-Current Structure

Flux-weakening methods based on the dual-current structure can be further categorized as

- 1) Feedforward method (also known as model-based method) [MOR90] [MOR94];
- 2) Feedback method (also known as ‘robust’ method) [SON96] [KIM97];
- 3) Hybrid method [BAE03] [KWO08].

1.1.1.1. Feedforward Flux-Weakening Method

Flux-weakening methods are generally based on two supply constraints, i.e. the voltage and current constraints, which can be expressed as

$$\begin{cases} i_d^2 + i_q^2 \leq I_m^2 \\ V_d^2 + V_q^2 \leq V_m^2 \end{cases} \quad (1.1)$$

where i_d and i_q are the d- and q-axis currents, respectively; V_d and V_q are the d- and q-axis voltages, respectively; I_m and V_m are the current and voltage magnitude limits.

At steady state, V_d and V_q can be expressed as

$$\begin{cases} V_d = R_s i_d - \omega_e L_q i_q \\ V_q = R_s i_q + \omega_e (L_d i_d + \psi_m) \end{cases} \quad (1.2)$$

where R_s is the stator resistance; ψ_m is the permanent magnet flux; L_d and L_q are the d- and q-axis inductances, respectively; for the non-salient-pole PMSM, $L_d=L_q$.

In [MOR90] [MOR94], the authors give detailed analytical expressions of the current trajectory under different speed ranges with the given voltage and current constraints, the objective of which is to maximize the torque capability and minimize the copper loss. The current commands can be obtained with online calculation [MOR90] [MOR94] or off-line generated look-up table (LUT) [SHI04]. These kinds of methods are categorized as the feedforward flux-weakening method or model-based method [LIU12] [LIN12].

Based on the analytical model, the current trajectories in dq-axis current plane for the salient-pole and non-salient-pole PMSM can be illustrated in Fig. 1.3 and Fig. 1.4. Fig. 1.3(a)

and Fig. 1.3(b) show the maximum power output current trajectories (indicated by the solid red line) for the machine with finite constant power speed ratio (CPSR) and infinite CPSR, respectively. For the machine with finite CPSR, the characteristic current of the machine is higher than the current limit value, i.e. $i_c > I_m$, where i_c is the characteristic current of the machine ($i_c = \psi_m / L_d$). As the machine speed tends to infinity, the voltage limit ellipse will shrink to the center point of the voltage limit ellipse, i.e. $(-i_c, 0)$. Therefore, for the machine with infinite CPSR, it requires that $i_c \leq I_m$, under which condition the machine can theoretically achieve infinite speed. It should be noted that the actual achievable speed is also dependent on other factors, such as the mechanical stress of the rotor and the bearing, the friction torque, the sampling frequency and the switching frequency of the drive system [SUL07].

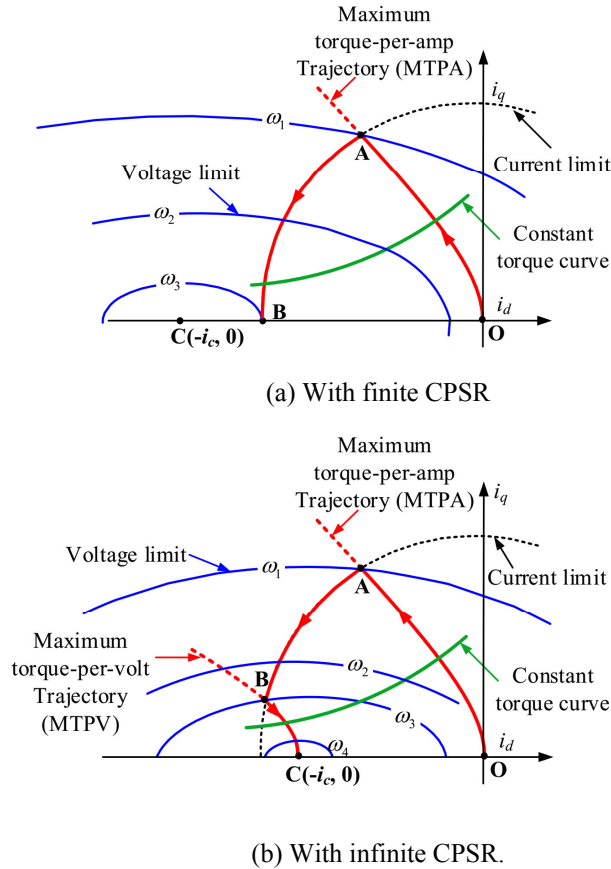
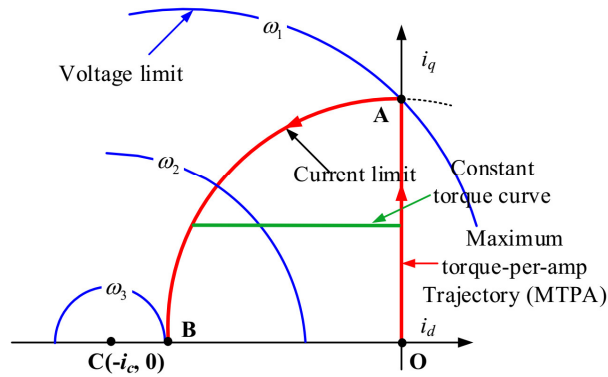
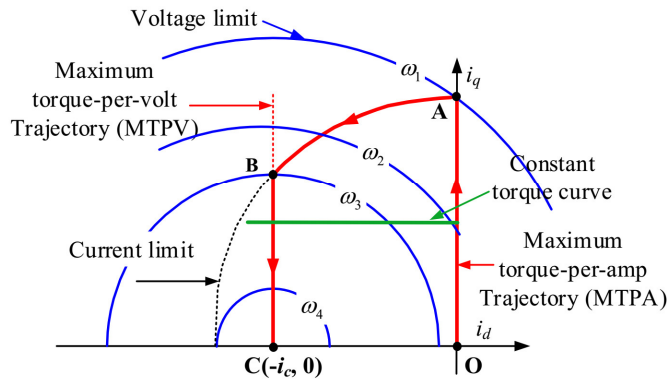


Fig. 1.3. Maximum power output current trajectory for the salient-pole PMSM ($L_d < L_q$), Finite CPSR: Curve 'OAB'; Infinite CPSR: Curve 'OABC'; Speed: $\omega_1 < \omega_2 < \omega_3 < \omega_4$.



(a) With finite CPSR.



(b) With infinite CPSR.

Fig. 1.4. Maximum power output current trajectory for the non-salient-pole PMSM ($L_d=L_q$),
 Finite CPSR: Curve ‘OAB’; Infinite CPSR: Curve ‘OABC’; Speed: $\omega_1 < \omega_2 < \omega_3 < \omega_4$.

The maximum power output current trajectories of non-salient-pole PMSM with finite CPSR and infinite CPSR are shown in Fig. 1.4(a) and Fig. 1.4(b). The conditions of the finite CPSR and infinite CPSR are the same with the salient-pole-PMSM, which are defined by the relationship between i_c and I_m . The maximum power output current trajectories of salient and non-salient-pole PMSM exhibit different profiles, which are due to their different mathematical expressions that result from the different saliency. The mathematical expressions of the maximum power output current trajectories according to Fig. 1.3 and Fig. 1.4 are listed as follows [MOR90] [MOR94].

- 1) The curve ‘OA’

On the curve ‘OA’, the machine operates in the constant torque region. According to whether the machine has saliency or not, the relationship between i_d and i_q on the curve ‘OA’ by considering MTPA curve is expressed as

$$\begin{cases} i_d = 0, & \text{when } L_d = L_q \\ i_d = \frac{-\psi_m + \sqrt{\psi_m^2 + 4(L_d - L_q)^2 i_q^2}}{2(L_d - L_q)}, & \text{when } L_d \neq L_q \end{cases} \quad (1.3)$$

2) The curve ‘AB’

On the curve ‘AB’, the machine operates on the intersection point of the current and voltage limits. The relationship between i_d and i_q on this curve by ignoring the stator resistance is expressed as

$$\begin{cases} i_d = \frac{-\psi_m + \sqrt{\left(\frac{V_m}{\omega_e}\right)^2 - (L_q i_q)^2}}{L_d} \\ i_d^2 + i_q^2 = I_m^2 \end{cases} \quad (1.4)$$

where ω_e is the electrical angular speed of the machine; for the non-salient-pole machine, L_d and L_q can be replaced by the synchronous inductance L_s .

3) The curve ‘BC’

The curve ‘BC’ is defined as maximum torque per voltage (MTPV) curve, which is only meaningful for the machine with infinite CPSR, due to that the MTPV curve intersects with the current limit circle. The relationship between i_d and i_q on this curve without considering the resistance is expressed as

$$\begin{cases} i_d = -i_c & , \text{when } L_d = L_q \\ i_d = -i_c + \frac{\rho i_c}{4(\rho - 1)} + \frac{\sqrt{\rho^2 (i_c)^2 + 8 \frac{V_m^2}{\omega_e^2 L_d^2} (\rho - 1)^2}}{4(\rho - 1)} & , \text{when } L_d \neq L_q \end{cases} \quad (1.5)$$

where ρ is the saliency ratio, i.e. $\rho = L_d / L_q$.

It should be noted that the maximum power output current trajectories do not cover the area which is enclosed by the curve ‘OABO’ and ‘OABCO’ for the machine with finite and infinite CPSR, respectively. In the area enclosed by ‘OABO’ or ‘OABCO’, the system is only constrained by the voltage limit. Therefore, the relationship between i_d and i_q can be obtained by only considering the voltage limit, and can be expressed as

$$i_d = \frac{-\psi_m + \sqrt{\left(\frac{V_m}{\omega_e}\right)^2 - (L_q i_q)^2}}{L_d} \quad (1.6)$$

(1.3), (1.4), (1.5) and (1.6) represent the relationships between the dq-axis currents at steady-state, which can be used to generate the current commands. Fig. 1.5 shows the schematic of the feedforward flux-weakening method based on online calculation [MOR94]. In Fig. 1.5, the q-axis current command is firstly obtained by a speed PI controller, and then limited by considering the maximum output power current trajectories in the flux-weakening region. The d-axis current command can be determined according to (1.3) and (1.6), and the machine speed. The d- and q-axis voltage commands are obtained by two current regulators. The conventional space vector pulse width modulation (SVPWM) method is employed as the modulation technique. It is obvious that this method highly relies on the machine parameters. The method in [ZHU03], which is based on the feedforward method, is further optimized by online adjusting the current commands with certain performance criterions under different scenarios. The initial dq-axis current commands are obtained at the maximum output power current trajectories in order to maximize the dynamic performance. The online optimization is realized by changing d-axis current with an increment variable according to its effect on the steady-state performance. Such a method can obtain better dynamic and steady-state performances. However, it requires many decision trees, and the proper criterions require much tuning work, which therefore loses its flexibility. For the small power motor, when the resistance is considered, the complexity of the optimal d- and q-axis current equations increases significantly. In order to solve this problem, a simplified current trajectory is realized in [TUR10] by using a piecewise linearization method, which is appropriate in the low-cost application. However, such simplification cannot obtain optimal

current trajectory in the flux-weakening region. The accuracy of the feedforward method can be improved with LUTs by using offline tested results or finite element results [KOC10]. However, when the environmental factor (such as temperature) is taken into account, the required LUTs would be too much, which requires much more chip storage space. What is more, the deviation of the machine parameters can even cause stability problem. The stable operation of the feedforward method requires to leave enough voltage margin to tolerate the deviation of the machine parameters and uncertainties [NAL12]. Therefore, it is rather difficult to achieve optimal flux-weakening control under varying conditions for the feedforward method.

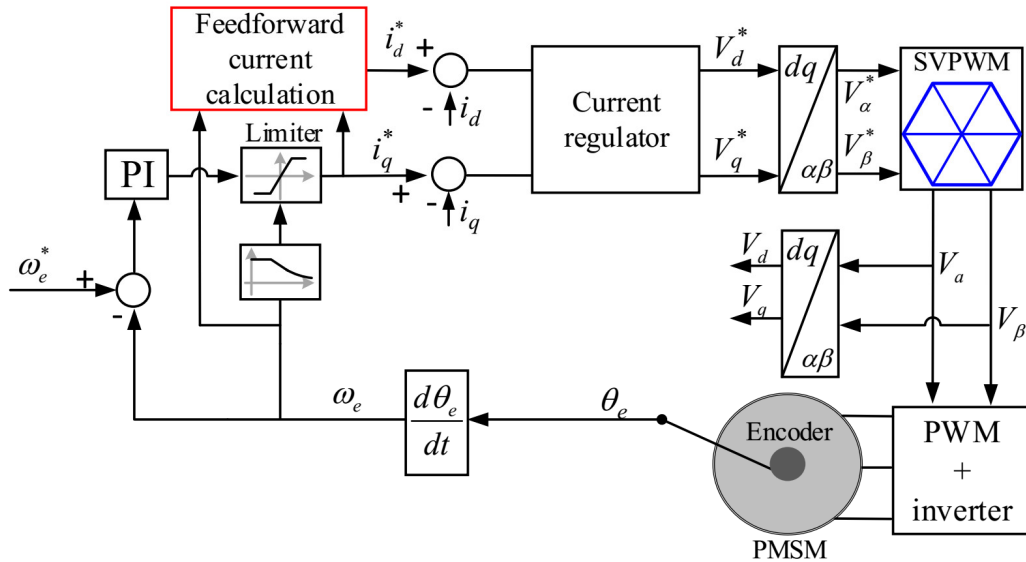


Fig. 1.5. Schematic of the feedforward flux-weakening control [MOR94].

1.1.1.2. Feedback Flux-Weakening Method

The feedback flux-weakening method utilizes a voltage feedback controller to regulate the current commands. The input of voltage feedback controller can be the voltage magnitude error [SON96] [KIM97] [BIA01] [WAI01] [BOL14] [BOZ17] [DEN19], the error between the switching period and the summation of active switching times [LIN12], voltage error before and after over modulation block [KWO06] [KWO07] [KWO08] [LIU12] [YON12]. The voltage feedback flux-weakening method for the PMSM is firstly proposed in [SON96] for an SPMSM, and then applied in IPMSM [KIM96]. Due to the close-loop structure, the

voltage feedback flux-weakening method is more robust against the parameter variation. It can automatically achieve flux-weakening control without decision trees. In addition, due to its simple and standard control structure, it is popular in many applications, such as electrical scooter [BIA01], wash machine [BOL14], aircraft electric starter-generator [BOZ19], and electrical vehicle [WAI01] [DEN19]. Fig. 1.6 shows a general schematic of the CVC system with voltage magnitude feedback flux-weakening control. Since the current references from the MTPA calculation (fed by the speed controller) can be achieved in dq-axis coordinate or polar coordinate, according to [BOL14], the flux-weakening control can be realized in two different ways. As illustrated in Fig. 1.7, the flux-weakening can be achieved by modifying the d-axis current command $i_{d,MTPA}^*$ (Fig. 1.7(a)) and the current lead angle θ_f^* (Fig. 1.7(b)) through the voltage magnitude feedback controller. These two variants of feedback magnitude controllers, namely, d-axis current based voltage feedback controller (DCVFC) and current angle based voltage feedback controller (CAVFC), are normally considered to be equivalent to achieve flux-weakening operation [BOL14]. For example, the flux-weakening method with DCVFC is utilized in [SON96] [KIM97] [BIA01] [WAI01] [BOZ17], the flux-weakening method with CAVFC is utilized in [WAI01] [DEN19] [BOL14]. However, in these references, only the linear modulation range is considered, i.e. the voltage magnitude is controlled below $V_{dc}/\sqrt{3}$, where $V_{dc}/\sqrt{3}$ represents the maximum voltage magnitude that can be achieved in the linear modulation region, as shown in Fig. 1.8(a).

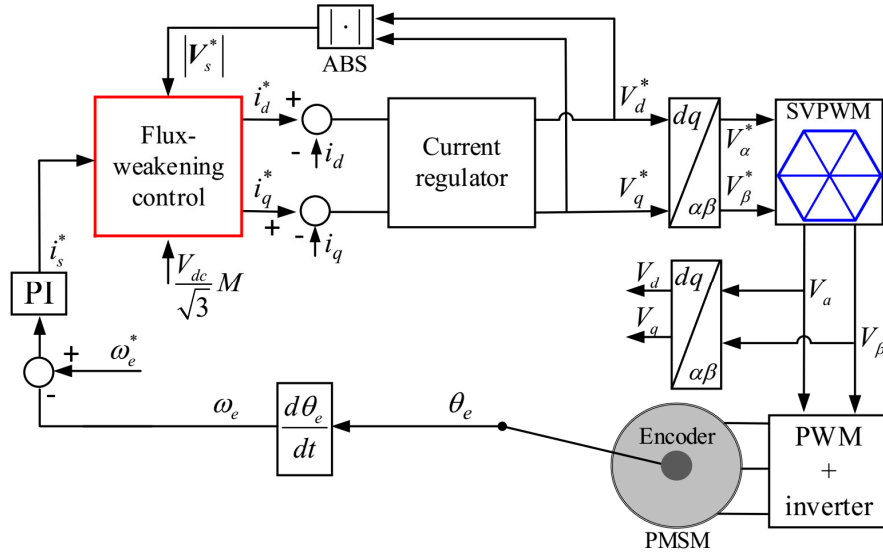
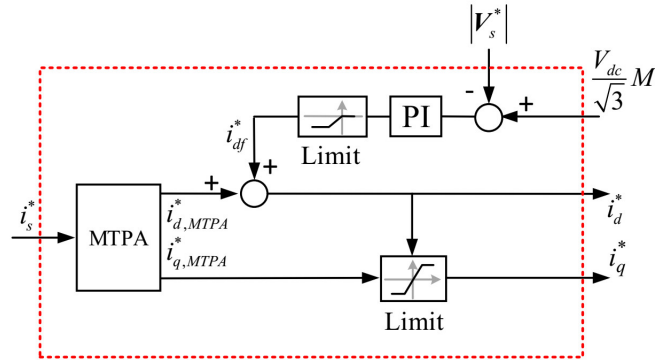
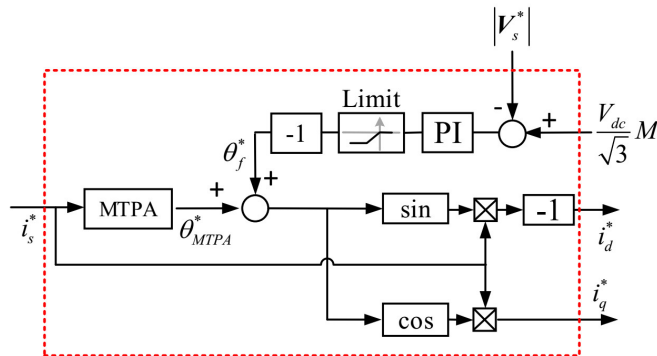


Fig. 1.6. Schematic of CVC system with voltage magnitude feedback flux-weakening.



(a) D-axis current voltage magnitude feedback control.



(b) Current angle voltage magnitude feedback control.

Fig. 1.7. Two variants of the voltage magnitude feedback control [BOL14].

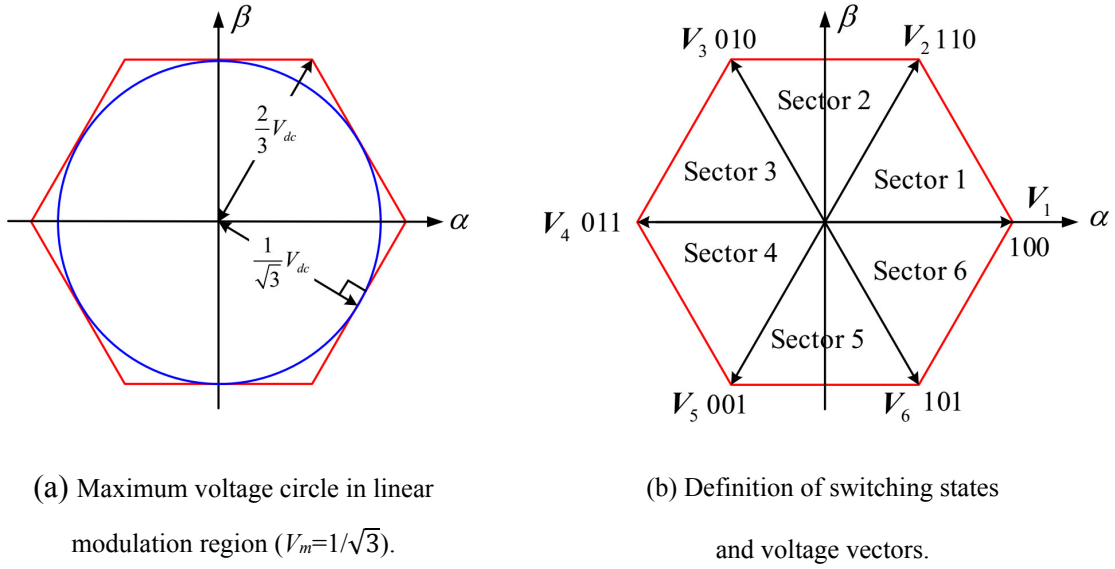


Fig. 1.8. Voltage circle and voltage vector in $\alpha\beta$ -axis voltage reference frame.

To further improve the DC-link voltage utilization, in [LIN12], the error between the switching period and the summation of active switching times for the inverter pulse width modulation (PWM) is utilized for the input of the feedback controller. Fig. 1.8(b) shows the 6 basic voltage vectors in the stationary reference ($\alpha\beta$) frame, which is defined by the switching states of the three phases, i.e. $V_1(1,0,0)$, $V_2(1,1,0)$, $V_3(0,1,0)$, $V_4(0,1,1)$, $V_5(0,0,1)$, $V_6(1,0,1)$. By taking the sector 1 as an example, as shown in Fig. 1.9, the actual vector command V_s^* can be synthesised by the two nearest basic voltage vector V_1 and V_2 , i.e.

$$V_s^* = \frac{T_1}{T_s} V_1 + \frac{T_2}{T_s} V_2 \quad (1.7)$$

where T_s is the switching period, T_1 and T_2 represent the switching times of two active basic voltage vectors. It can be seen in Fig. 1.9(a) that the condition, i.e. $T_1+T_2 < T_s$, represents that the system operates in the constant torque region, where the voltage command vector V_s^* can be fully synthesized. When $T_1+T_2 > T_s$, as shown in Fig. 1.9(b), since V_s^* outsteps the hexagon boundary, it cannot be fully synthesized, which indicates that the voltage is saturated and flux-weakening is required. In this condition, for the conventional SVPWM, which is also known as the minimum phase error over modulation (MPEOM) [YON14], the voltage command V_s^* will be truncated on the hexagon boundary with the same phase angle.

Therefore, the condition, i.e. $T_1+T_2=T_s$, which is shown in Fig. 1.9(c), can be set as the control goal to maintain that the system can operate on the hexagon boundary. The feedback flux-weakening control in [LIN12] utilizes the error between T_s and (T_1+T_2) as the input of the feedback controller, by which the over modulation flux-weakening is achieved.

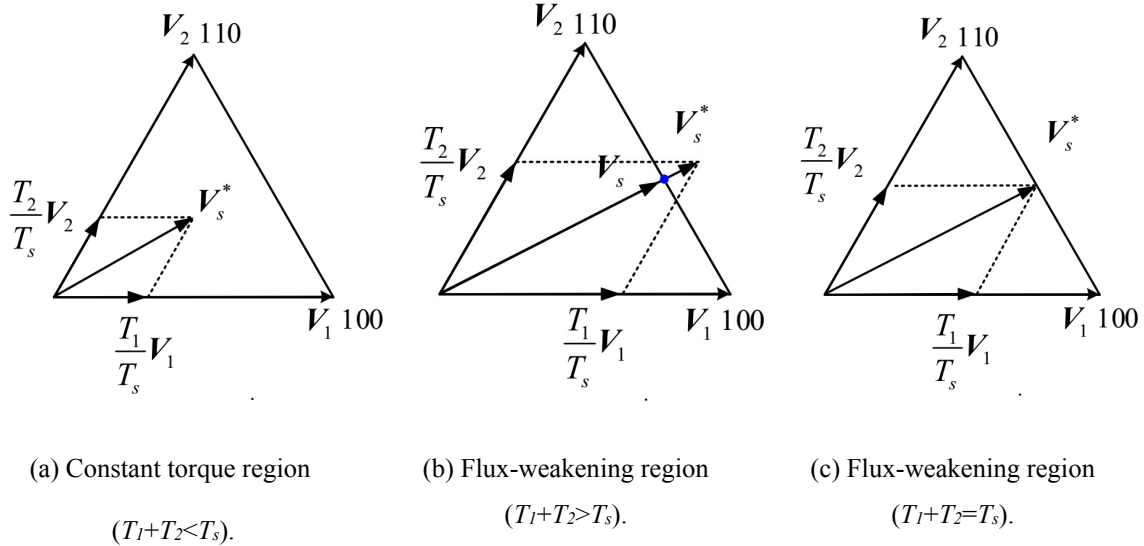


Fig. 1.9. Voltage command vector synthesis.

Alternatively, the over modulation flux-weakening control can also be achieved by utilizing the voltage error before and after the over modulation voltage [KWO07]. As shown in Fig. 1.10(a), the voltage error is firstly processed with a low pass filter (LPF) and then fed back to regulating the d-axis current command with a proportional gain. However, the dynamic performance is sacrificed due to the introduced low pass filter (LPF). In order to improve the dynamic performance, in [YON12], the q-axis voltage error processed by a high pass filter is fed back to the d-axis current command through a proportional gain, which can compensate the influence of the low pass filter, as shown in Fig. 1.10(b).

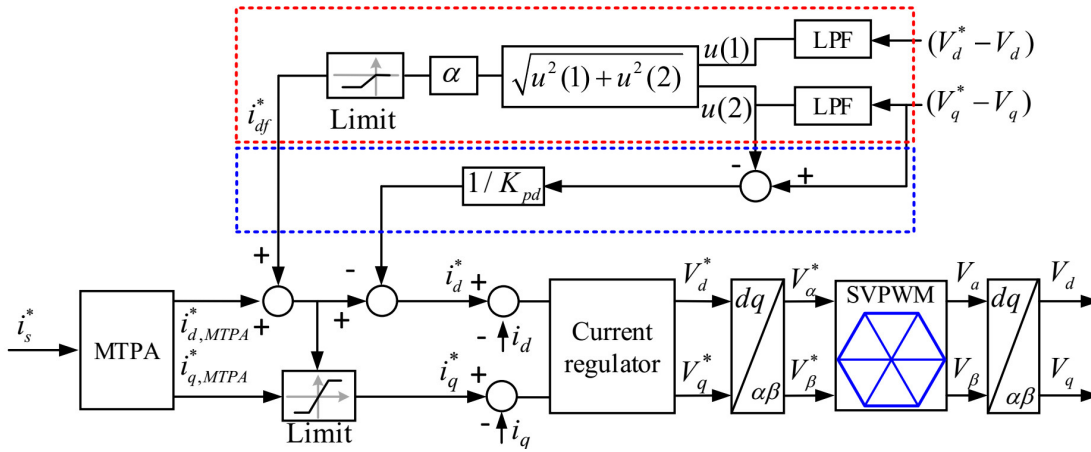
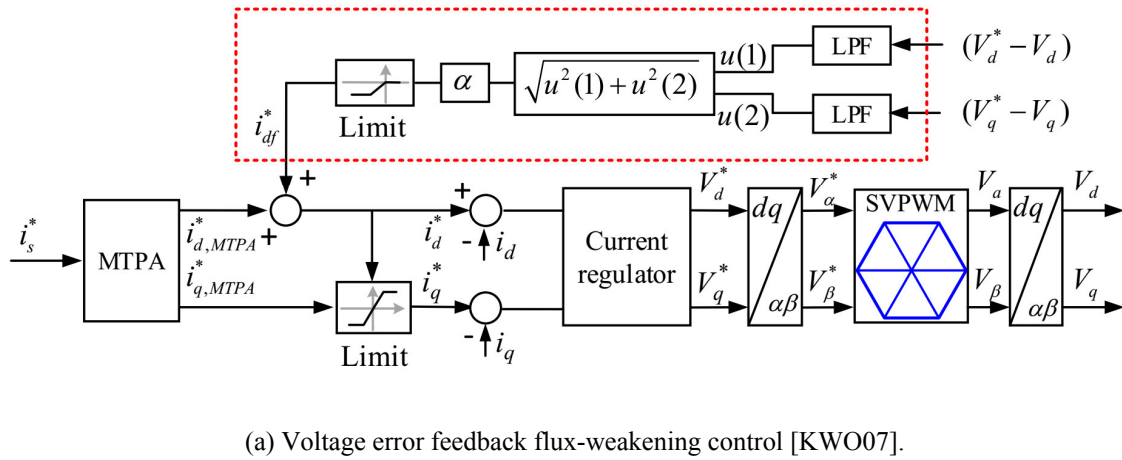


Fig. 1.10. Control diagrams of the voltage error feedback flux-weakening method.

Moreover, the DC-link voltage utilization can be further improved with different modulation techniques, such as minimum magnitude error over modulation (MMEOM) [LIU12] and so-called Bolognani's over modulation technique [YON14]. The voltage synthesis of MMEOM and Bolognani's over modulation are shown in Fig. 1.11(a) and Fig. 1.11(b). It can be seen from Fig. 1.11(a) that the voltage command vector V_s^* is limited to the hexagon boundary with the minimum magnitude. Therefore, the quasi-six-step operation [KWO06] [KWO08] can be achieved when the V_s^* tends to be infinity. In Fig. 1.11(b), with Bolognani's over modulation, the voltage command vector V_s^* which outsteps the hexagon boundary will be limited to the nearest cross point of the hexagon boundary and the voltage command circle with the radius V_s^* . Therefore, the six-operation can be achieved when $|V_s^*$

$|=2/3V_{dc}$. In [KWO06] [KWO08], a quasi-six-step flux-weakening control is achieved with the MMEOM based on voltage error feedback method. In [YON14], the six-step flux-weakening control is achieved with Bolognani's over modulation based on the voltage magnitude feedback method.

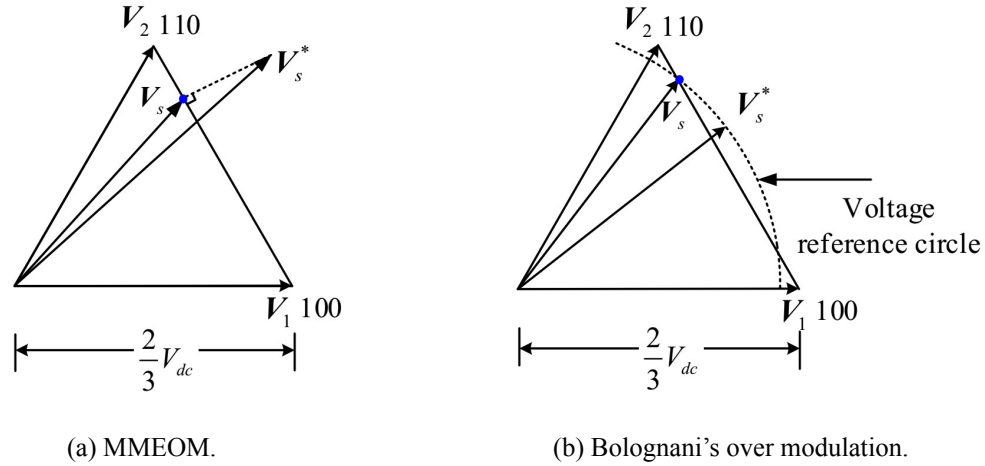


Fig. 1.11. Voltage synthesis of MMEOM and Bolognani's over modulation.

However, the above-mentioned feedback methods have not taken account of the MTPV region. When the MTPV region is considered, the MTPV control strategy should be applied to ensure that the system could operate along the MTPV curve. In [LIN12], based on the voltage error feedback method on a non-salient-pole PMSM, an extra MTPV feedback controller is introduced. The input of the MTPV feedback controller is given by an MTPV penalty function. The condition, i.e. when the penalty function equals zero, corresponds to the MTPV curve. The MTPV control is achieved by modifying the q-axis current command with the MTPV controller, which can be shown in part II of Fig. 1.12. In Fig. 1.12, the MTPV penalty function is achieved as

$$f_p = V_q - Ri_q - V_{qNL} \quad (1.8)$$

where R is the summation of the stator resistance, the resistance of the power cable and switch device; V_{qNL} is the estimated q-axis voltage error caused by the nonlinearity of the IGBT [KIM06]; f_p is the penalty function. The condition, i.e. $f_p=0$, actually corresponds to the condition $i_d+i_c=0$.

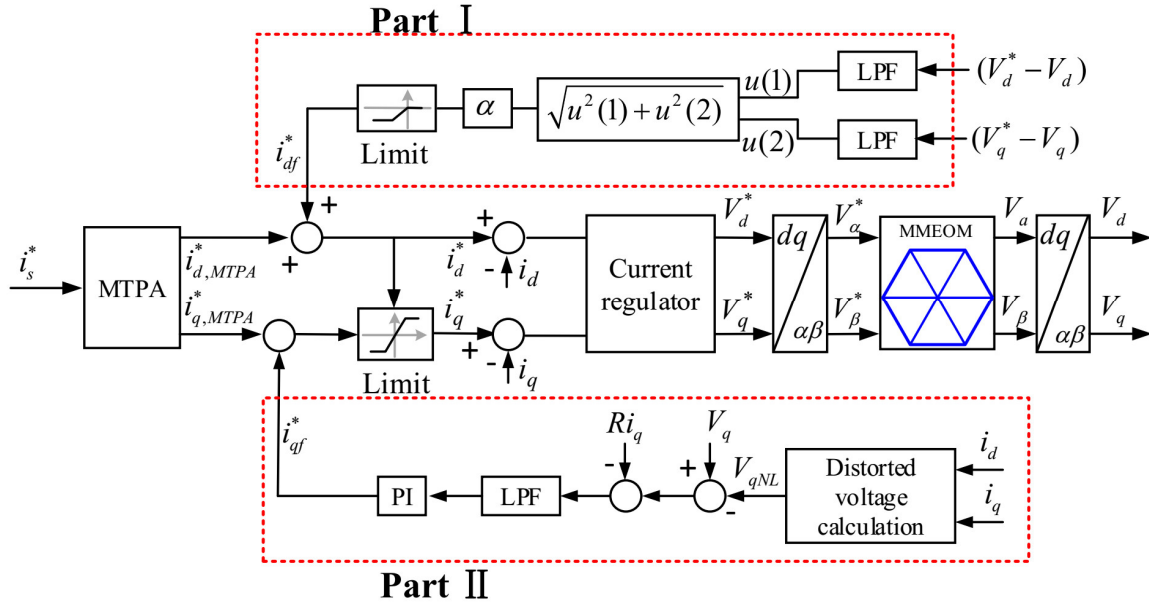


Fig. 1.12. Control diagram with consideration of MTPV control [LIN12].

1.1.1.3. Hybrid Flux-Weakening Method

As compared in [MAR99], it shows that the feedforward flux-weakening method has better dynamic performance when compared with the feedback flux-weakening method. However, the feedforward flux-weakening method suffers from the variation of the machine parameters, which exhibits poorer robustness than the feedback flux-weakening method. Therefore, in order to combine both the advantages of the feedforward and feedback flux-weakening methods, the hybrid method is proposed in [BAE03], the schematic of which is shown in Fig. 1.13.

As can be seen in Fig. 1.13, the current commands are generated with the cooperation of three parts. In Part I, the d- and q-axis current commands, i.e. i_d^* and i_q^* , are obtained by two 2-D LUTs with respect to the actual torque command T_{eref} and the flux linkage command ψ_s^* based on the analytical model. The flux linkage command ψ_s^* is directly obtained as the maximum allowable flux linkage restrained by the voltage limit, i.e. $\psi_{max}^* = V_{dc}/(\sqrt{3}|\omega_e|)$. The given torque command T_{eref}^* should be limited by a 1-D LUT, in which the maximum torque limit T_{emax}^* is obtained with respect to ψ_{max}^* , as shown in Part II. For a pure feedforward flux-weakening method, only the Part I and Part II in Fig. 1.13 are enough. However, in the

proposed hybrid method, in order to compensate the variation of the machine parameters, the flux linkage command ψ_s^* is further modified by a voltage magnitude feedback controller in a fine-tuned way, as shown in Part III of Fig. 1.13. Therefore, the hybrid method can obtain both advantages of feedforward and feedback flux-weakening methods, i.e. fast dynamics and good robustness.

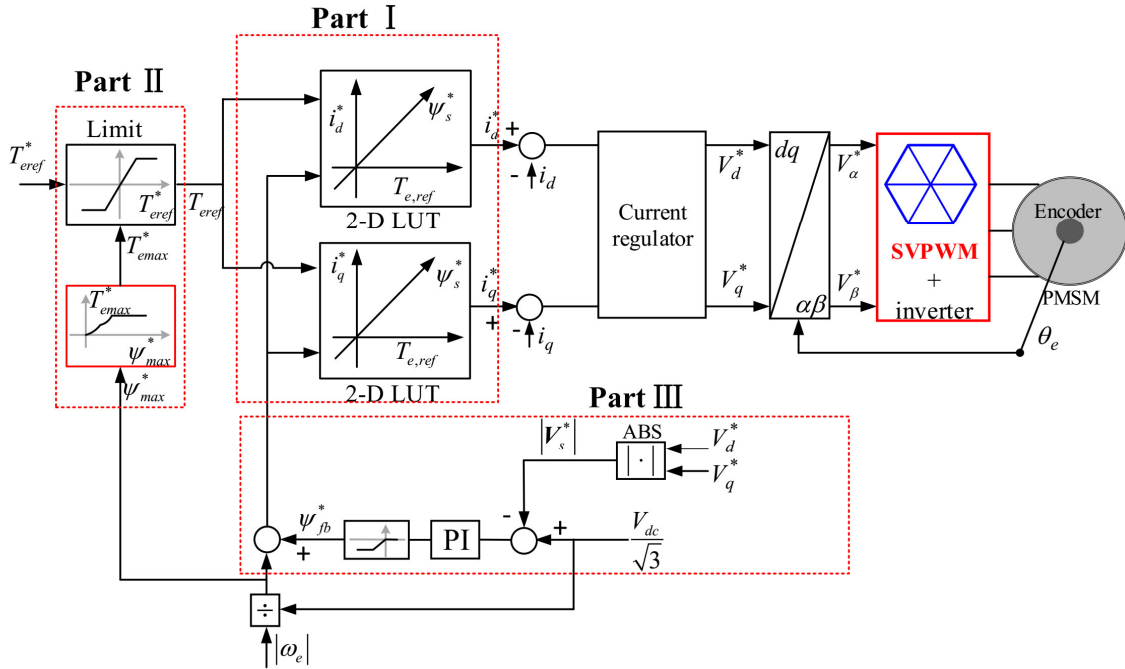


Fig. 1.13. Schematic of the hybrid flux-weakening control based voltage magnitude feedback controller [BAE03].

However, in [BAE03], only the linear modulation region is considered based on conventional SVPWM. In [KWO08], the hybrid method is based on the MMEOM, by which a quasi-six step flux-weakening control is achieved, the schematic of which is shown in Fig. 1.14. The part I has the same form as the method in [BAE03], although the LUTs are created based on the experimental results in [KWO08]. The voltage error feedback controller is utilized to regulate the base flux linkage command ψ_{base}^* that is obtained by only considering the MTPA in the constant torque region. The maximum achievable torque is embedded in the 2-D LUTs.

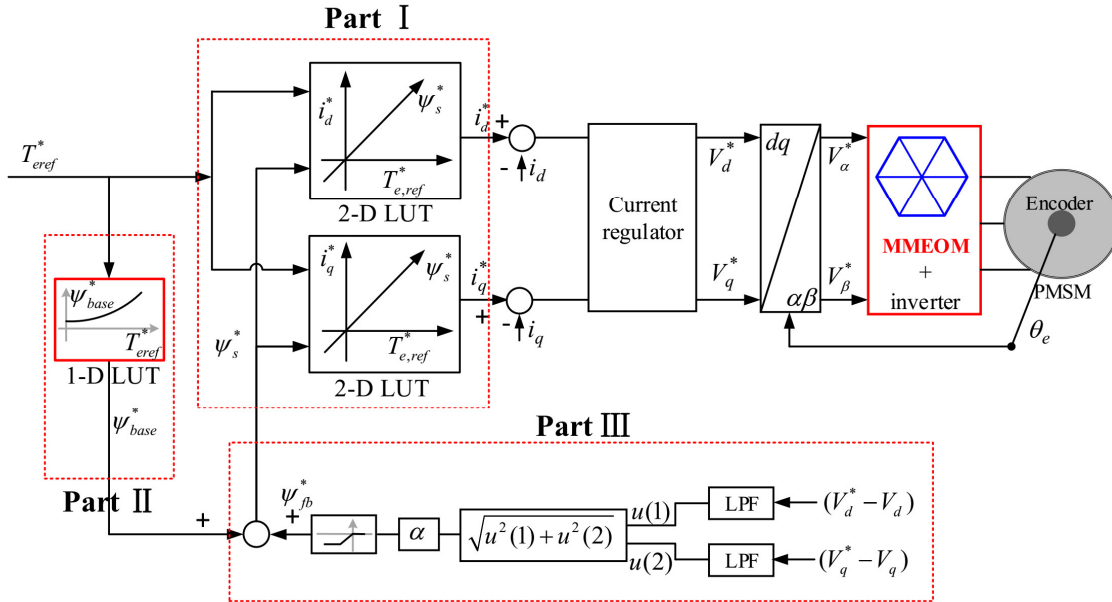


Fig. 1.14. Schematic of the hybrid flux-weakening control based on the voltage error feedback controller [KWO08].

However, since the hybrid method contains several LUTs, it will consume more resources. In addition, the control structure is not as simple as the feedforward and feedback method. As the 2-D LUTs can be built offline, the finite element and experimental results can be both utilized to assist the acquisition of the LUTs. However, it will be more time-consuming. Therefore, the hybrid method is more appropriate to apply on occasions where a high torque control performance is required especially for the machine with high nonlinearity, such as IPMSM.

1.1.2. Flux-Weakening Methods Based on Single-Current Control

In the flux-weakening region, the voltage control margin decreases. Therefore, the saturation of the current controllers often occurs. In this situation, the d- and q-axis current regulators may conflict with each other, which could cause oscillation and even instability [ZHA11]. In order to solve this conflict, the most direct way is to eliminate one of the two current regulators, which comes to single-current control (SCC).

1.1.2.1. Single-Current Control

According to the q-axis voltage equation, the q-axis current can be derived as

$$i_q = -\frac{\omega_e L_d}{R_s} i_d + \frac{V_q - \omega_e \psi_m}{R_s} \quad (1.9)$$

When the machine operates in the constant torque region, the back EMF of the machine is relatively small. Due to the sufficient voltage margin, the d- and q-axis currents can be controlled independently. However, in the flux-weakening region, due to the less voltage margin and the cross-coupling feature between the d- and q-axes, the d- and q-axis currents cannot be truly controlled independently. For example, once the voltage is saturated, V_d and V_q could be clamped at a constant value in certain period, i_q will be passively changed with i_d according to (1.9).

In [XU08] [ZHA10], the flux-weakening is achieved by using only a d-axis current controller, the control diagram of which is shown in Fig. 1.15. In Fig. 1.15, the d-axis current command is obtained as a linear relationship with the torque command T_{eref}^* by considering MTPA. The torque command T_{eref}^* comes from a speed PI controller. The q-axis current is controlled passively with a given q-axis voltage command V_q^* . In order to improve the efficiency, a recommendation is also made in choosing an optimal q-axis voltage by minimizing the copper loss, which is obtained with an offline LUT with respect to the machine speed and the load torque.

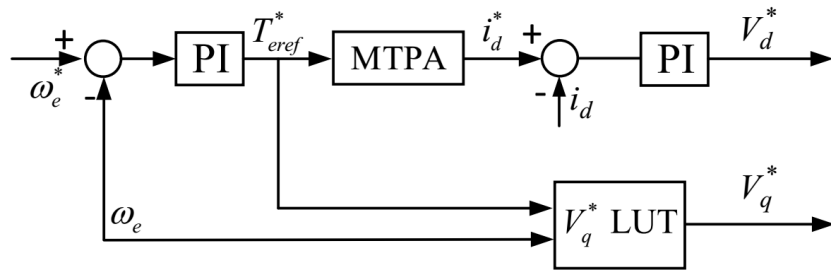


Fig. 1.15. Single-current control algorithm [XU08].

By using the SCC algorithm, there is no conflict between the two current controllers in the flux-weakening region. Therefore, the stability of the system is remarkably improved in the flux-weakening region. However, the LUT for obtaining q-axis voltage command has a nonlinear relationship with the given torque and speed, which are illustrated in [XU08] with numerical results. Therefore, SCC is still model based, rendering this method parameters

sensitive in terms of the minimum copper loss (or maximum voltage utilization). In addition, the implementation utilizes the monotonous relationship between the d-axis current and the torque by considering the MTPA. Therefore, it can only be applied to the machine with saliency. For the machine without saliency, the control strategies in the constant torque and flux-weakening should be separated, i.e. dual-current control in constant torque region and single current control in the flux-weakening region. Therefore, the proper switching algorithm between the constant and flux-weakening regions is required [CHI06]. Furthermore, due to the partial open-loop structure of the single current control, it may have larger current ripple.

1.1.2.2. Voltage Angle Control

The voltage angle control (VAC) [LEI10] [STO12] [MYI13] aims firstly to solve the same problem as SCC, i.e. the conflict between d- and q-axes. Therefore, it also utilizes the single current structure, but only in the flux-weakening region. In the flux-weakening region, the d- and q-axis currents can be expressed as the function of the controlled voltage angle, i.e.

$$\begin{cases} i_d = \frac{V_m \sin(\theta_v^*) - \omega_e \psi_m}{\omega_e L_d} \\ i_q = -\frac{V_m \cos(\theta_v^*)}{\omega_e L_q} \end{cases} \quad (1.10)$$

where θ_v^* is defined by the angle between the voltage vector and the d-axis. (1.10) clearly shows that the voltage angle θ_v^* influences the currents i_d and i_q . In the VAC, the voltage angle can be controlled based on d-axis or q-axis current controller, and the available DC-link voltage defines the voltage vector magnitude. Therefore, in the flux-weakening region, the given voltage is the voltage magnitude rather than the q-axis voltage command, rendering this method parameters insensitive.

The schematic of the control system with the VAC is shown in Fig. 1.16. It can be seen in Fig. 1.16 that the voltage commands V_d^* and V_q^* come from two blocks, which are specifically designed for the constant torque region and flux-weakening region. In the

constant torque region, the conventional dual-current structure is still maintained. In the flux-weakening region, the system switches to the VAC.

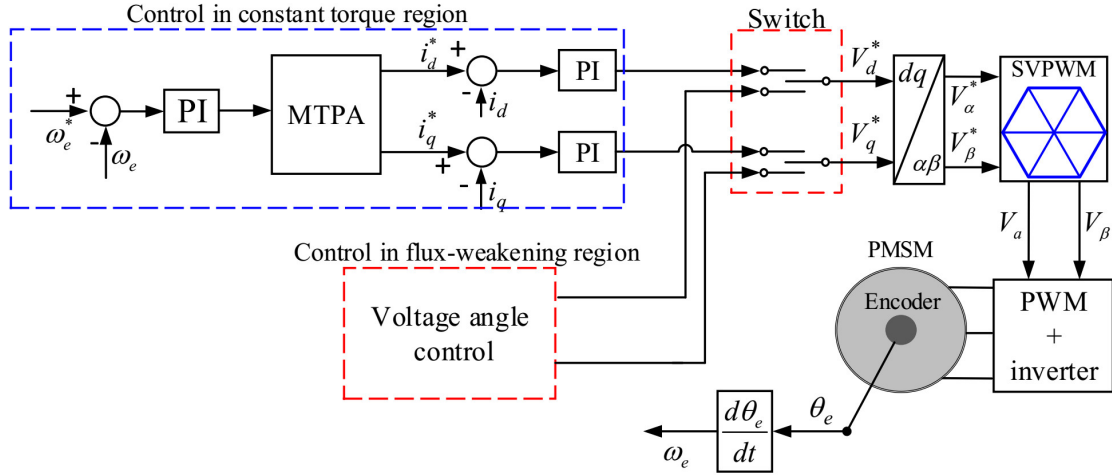
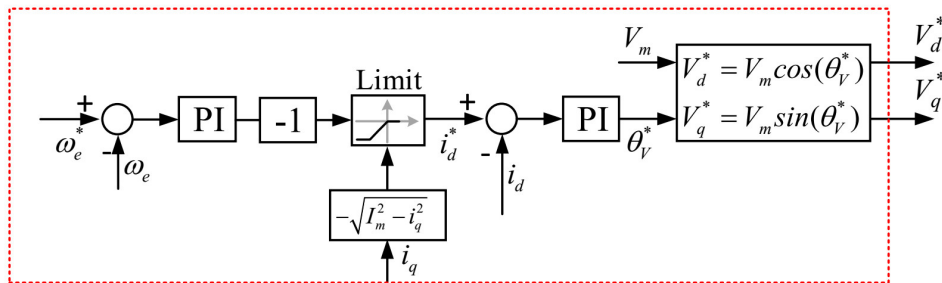
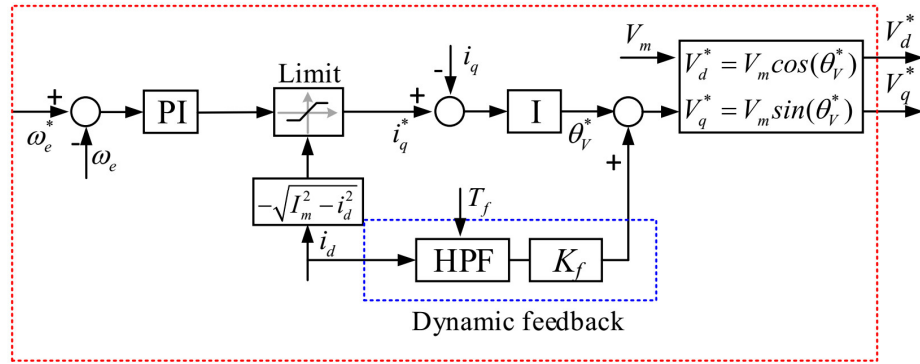


Fig. 1.16 Schematic of the control system with the voltage angle control (VAC) in the flux-weakening region.

The block diagram of the VAC in [LEI10] and [STO12] are shown in Fig. 1.17(a) and Fig. 1.17 (b), respectively. In Fig. 1.17(a), the voltage angle is regulated by a d-axis current controller (PI type), while the d-axis current command comes from a speed PI controller multiplied with a negative gain. In contrast, in Fig. 1.17(b), the voltage angle is regulated by a q-axis current controller (integral type), while the q-axis current command comes from a speed PI controller. In addition, an extra dynamic feedback block is introduced to assist the regulation of the voltage angle, which is verified to be effective to improve the stability and the current dynamics. The dynamic feedback is composed of a high pass filter (HPF) that is multiplied with a gain K_f .



(a) VAC based on d-axis current control [LEI10].



(b) VAC based on q-axis current control [STO12].

Fig. 1.17. Block diagrams of the voltage angle control (VAC).

It should be noted that the controller in Fig. 1.17(a) and Fig. 1.17(b) are specifically designed for the motoring condition with the machine running in the positive rotation direction. Therefore, in practice, when the generating condition and reverse rotation are considered, cautions must be taken when tuning the controller gains and its signs. For example, when the machine tries to operate in the reverse rotation, for the method in Fig. 1.17(a), the output of the speed PI controller should be multiplied with a positive gain rather than a negative gain; for the method in Fig. 1.17(b), it is analysed in [STO12] that K_f should be negative to maintain stability. In addition, the switching criterions between the constant torque and the flux-weakening regions are essential to achieve a smooth transition performance, which requires trial and error [STO12] [MY113].

1.1.3. Comparison

According to the flux-weakening methods reviewed above, the relationship between different flux-weakening methods is illustrated in Fig. 1.8, and a rough comparison of the different flux-weakening methods are summarized in Table 1.1 in terms of dynamic performance, transition performance, parameter insensitivity, simplicity, and stability.

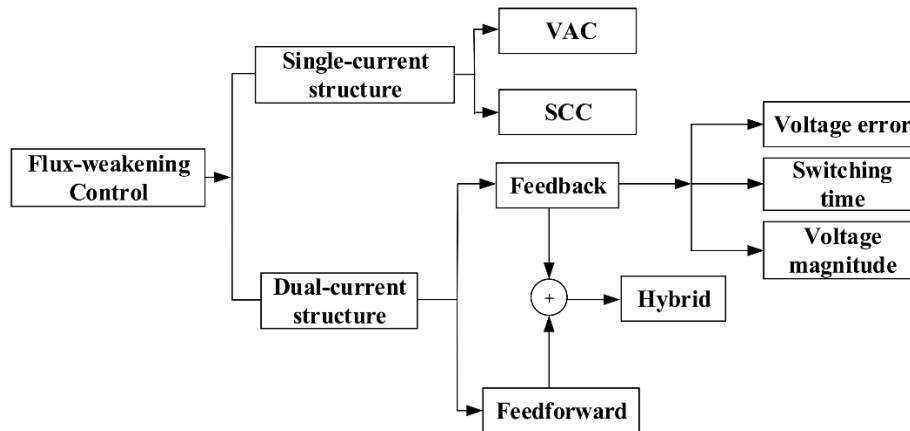


Fig. 1.18. Relationship between different flux-weakening methods.

It can be seen in In Table 1.1 that

- The methods, i.e. feedforward method and hybrid method, have better dynamic performance than other methods due to that the current commands are obtained in feedforward path. As for SCC, the q-axis current is passively controlled. Therefore, this method has the poorest dynamic performance.
- The methods based on dual-current structure, i.e. feedforward method, feedback method, and hybrid method, have better transition performance due to the consistency of the control structure under various operation conditions, e.g. constant torque and flux-weakening operations, motoring and generating operations, positive rotation and reverse rotation directions.
- The methods in which the current trajectory relies on the machine model, i.e. feedforward method and SCC, are sensitive to the machine parameters.
- The methods in which only a feedback controller is required, i.e. feedback methods, have the simplest control structure.
- The method based on the single current control structure while no extra control parameters are introduced, i.e. SCC, has the best stability characteristic.

Table 1.1 Comparison of different methods

Comparison points		Dynamic performance	Transition performance*	Parameter insensitivity	Simplicity	Stability
Methods						
Dual-current structure	Feedforward					
	Feedback					
	Hybrid					
Single-current structure	SCC					
	VAC					
: Good : Middle : Poor						

* Transition performance: Performance when transiting between different operation regions, i.e. constant torque region, flux-weakening region.

1.3 Scope and Contribution of the Thesis

1.1.4. Motivation

From the above review, the trends of the flux-weakening methods can be highlighted as follows:

(a) The feedforward method is the most direct way to achieve flux-weakening. However, the main drawback of this method is parameter sensitivity. The application of this kind of method should leave enough voltage margin to maintain stability

(b) Although the hybrid method can obtain the advantages of both feedback and feedforward methods, i.e. fast dynamics and robustness against parameter variation, it has a more complicated structure. In addition, as the LUTs can consider the nonlinearity of the machine, it is more preferable for the machine with high nonlinearities, e.g. IPMSM, especially when a high torque control performance is required.

(c) Although the single current control structure can solve the conflict between the d- and q-axis current controllers, the method is normally designed for some specific operation condition, which lacks flexibility. In addition, the control parameter is required to be properly tuned in VAC. The transition performance between different operation regions is not as good as the method based on dual-current structure.

(d) The feedback flux-weakening methods are very popular in practical applications due to their advantages, i.e. robustness against parameter variation, simple and standard control structure, automatic flux-weakening operation.

(e) The feedback flux-weakening control based on switching time [LIN12] or voltage error [KWO07] [YON12] requires that the system operates in the over modulation region, they cannot achieve linear flux-weakening operation. In addition, as the system in linear modulation region has better current dynamics and fewer harmonics, the linear modulation region is still preferred for the applications where the DC-link voltage is not a great concern.

(f) For the voltage magnitude feedback method [SON96] [KIM97], the voltage magnitude reference can be directly specified. Therefore, it can achieve both linear and over modulation flux-weakening operation, which is beneficial to the general purpose application. Currently, the voltage magnitude feedback method is regarded as a standard flux-weakening method and appears in many application manuals of microprocessors [STM16] [TI18].

The researches in this thesis are based on the voltage magnitude feedback method on the non-salient-pole PMSM. The motivations mainly origin from an important issue, i.e. the stability issue, in the flux-weakening region that the author encountered in both laboratories and industries. The investigations of the stability issues in the flux-weakening can provide a good guidance when developing the programs and troubleshooting the problems in a practical system. Generally, the tuning of the voltage feedback controller is considered as a disadvantage for the feedback flux-weakening method when compared with the feedforward method. In [STM16] [TI18], the control parameters of the voltage feedback controller are open to the users with a graphical user interface (GUI) in order to facilitate the trial and error tuning in practical application. However, as will be analysed in this thesis, the control parameter is not the only reason that could lead to the stability problem. The investigation in this thesis will show that the stability issues in the flux-weakening region are also related to other factors, such as

- 1) Different speed operation ranges, including motoring and generating;
- 2) Linear or over modulation region;

- 3) The machine with and without MTPV region;
- 4) The control structure of the voltage magnitude feedback method;
- 5) The influence of the feedback voltage ripples origin from the non-ideal drive system.

1.1.5. Outline

The structure of this thesis is illustrated in Fig. 1.19.

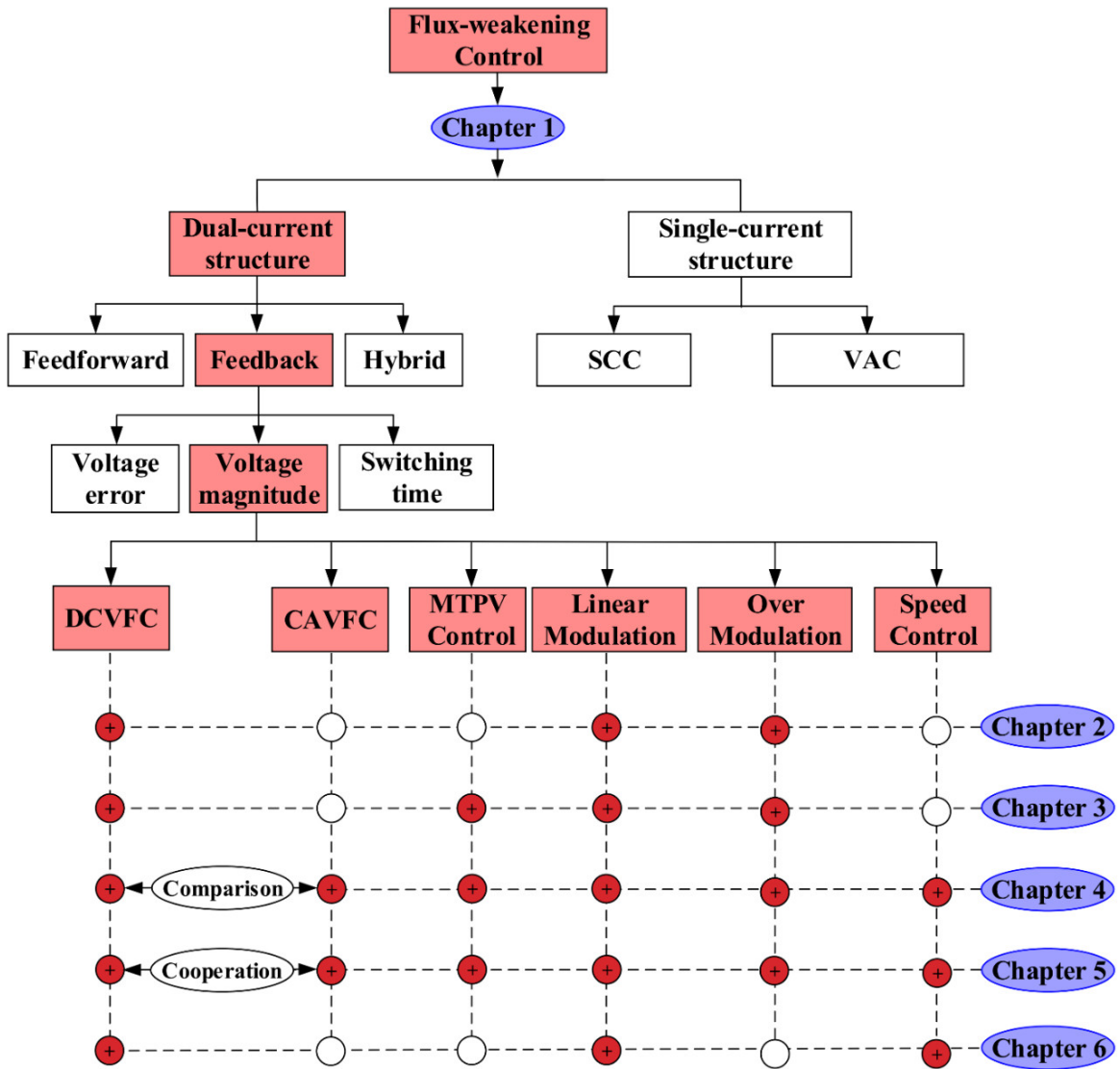


Fig. 1.19. Outline of the research.

This thesis is organized as follows:

In chapter 2, the voltage loop with DCVFC is analysed based on the linearized model on a PMSM with $i_c \leq I_m$, i.e. the machine without MTPV region. An adaptive control parameter method is given, which can ensure a much wider operation speed range in the flux-weakening region. Furthermore, a current reference modifier (CRM) and a voltage limit reference modifier (VRM) are proposed to improve the current dynamics and stability in the over modulation region.

In chapter 3, the linearized model based on the DCVFC is analysed on a PMSM with $i_c > I_m$, i.e. the machine with MTPV region. The feedback MTPV control strategy is optimized by considering the steady-state performance, dynamic performance, and stability. The design guidance of the MTPV controller is given. The over modulation stability in the MTPV region is improved with the voltage vector modifier (VVM).

In chapter 4, by considering the MTPV control, based on DCVFC and CAVFC, two feedback flux-weakening methods, i.e. dq-axis currents based feedback flux-weakening control (DQFFC) and current amplitude and angle based feedback flux-weakening control (CAAFFC), are comparatively studied in terms of the stability. The analysis and experimental results show that the oscillation or instability could occur for the DQFFC and CAVFC at different flux-weakening regions, which are mainly due to the different operation modes (defined by the small signal behaviour) that result from the different control structures.

In chapter 5, based on the comparisons in chapter 4, a hybrid voltage feedback controller (HVFC) is proposed by regulating both the d-axis current and current angle simultaneously. The HVFC is composed of the DCVFC part and the CAVFC part but with different weight factors. The weight factors are further optimized by considering both advantages of the DCVFC and the CAVFC. With the HVFC, the stability in different flux-weakening regions can be remarkably improved.

In chapter 6, it further investigates the influence of the resultant feedback voltage ripple that originates from the non-ideal drive system based on the control system with DCVFC. It indicates that the oscillation may even occur in certain flux-weakening region with excessive

feedback voltage ripples, which posing difficulty to increase the speed bandwidth for a conventional speed PI controller. Furthermore, an adaptive fuzzy logic speed controller is proposed, which can reduce feedback voltage ripples while maintaining a good speed dynamics. Therefore, the system can achieve both good dynamic and steady-state performance in the flux-weakening region.

In chapter 7, the conclusions are drawn and some future work is discussed.

1.1.6. Contribution

The major contributions in this thesis include:

1) An adaptive control parameter method is developed. The symbolic forms of the control parameter of the DCVFC, CAVFC, and HVFC are given, which can ensure a wider stable operation range (including both motoring and generating conditions) and ease the parameterization for the practical system.

2) The stability is improved in the over modulation region. CRM and VRM are developed for the machine without the MTPV region. The VVM is demonstrated to be more effective to maintain the stability in the MTPV and over modulation regions

3) The feedback MTPV controller is optimized. The stability in the MTPV region is improved by using MTPV penalty function in current command form rather than the voltage command form. A PI type MTPV controller is selected and designed for the system with DCVFC, while a pure integral MTPV controller is selected and designed for the system with CAVFC or HVFC.

4) A HFFC is proposed based on HVFC. The stability characteristics of the DQFFC and the CAQFFC are compared when the machine operates under different operation regions. It indicates that oscillation and instability could occur for the DQFFC and the CAQFFC, respectively, which is the intrinsic nature of the DQFFC and the CAQFFC due to different control structures. A HFFC is proposed based on a HVFC by utilizing the both advantages of the DQFFC and CAQFFC under different regions, by which the stability of the system is remarkably improved in both linear and over modulation regions.

5) An adaptive fuzzy logic speed controller is proposed to reduce the feedback voltage ripples without sacrificing the speed dynamics, by which both the steady-state and dynamic performance in the flux-weakening can be improved.

CHAPTER 2 ADAPTIVE VOLTAGE FEEDBACK CONTROLLER ON PMSM

This chapter proposes an adaptive control parameter method of the conventional d-axis current based voltage magnitude feedback controller (DCVFC) for the non-salient-pole PMSM without the MTPV region. A simple symbolic form of the control parameter is given based on the linearized model analysis, which can ensure a wide and stable flux-weakening operation range. Furthermore, the system performance in the over modulation and flux-weakening regions are improved with the current and voltage limit reference modifiers.

2.1 Introduction

It is known [REF05] [REF06] that the optimal flux weakening can be achieved when the current limit I_m equals to characteristic current i_c which is defined as

$$i_c = \psi_m / L_s \quad (2.1)$$

where ψ_m is the permanent magnet flux-linkage; L_s is the synchronous inductance. In the thesis, the notion, i.e. characteristic current ratio i_{cn} is introduced and defined as

$$i_{cn} = i_c / I_m \quad (2.2)$$

Therefore, the optimal flux weakening which has infinite constant power speed ratio (CPSR) occurs at the condition $i_{cn}=1$. When $i_{cn}>1$, the machine has a finite CPSR. The infinite CPSR can also be achieved when $i_{cn}<1$, however, requiring the machine operating in the maximum torque per voltage (MTPV) region [MOR90] [LIU12].

Due to the current and voltage constraints, the system in the flux-weakening region operates on the boundaries of the current or voltage limit circle. More stability problems are prone to occur in this region. In [SHI04], even for the feedforward methods, the oscillation occurs in the deep flux-weakening region, which is caused by quantization error on a fixpoint processor and can be solved by using a float processor or look-up tables (LUTs). For the voltage feedback controller, the non-linear behaviour of the voltage loop complicates the

tuning process [BOL14] [BOZ16]. In [MAR99], the control parameter of the voltage feedback controller is designed at only one specific point (d -axis voltage equals q -axis voltage, i.e., $|V_d|=|V_q|$), which cannot represent the whole flux-weakening region. In [BIA01], the authors claim that the proportional part in the voltage feedback controller greatly reduces the stability of the voltage loop and a pure integral controller is preferable. In [GUO09] [BOZ14], the analyses based on the linearized model of the voltage feedback controller confirm that a pure integral controller is more preferable to ensure the stability over a wider flux-weakening operation range. In [WAL04] [BOL14], the authors provide an adaptive control parameter of the voltage feedback controller based on the linearized model on a given machine. However, few details are provided for the stability in the deep flux-weakening region, and the generating condition is not considered. In [BOZ16], the control parameter of the voltage feedback controller is obtained within the stable boundary that is derived from Routh criteria on a given machine. However, the above methods are only considered in the linear modulation region.

In this chapter, based on the machine with $i_{cn} \geq 1$, i.e. the condition without MTPV control, a simple symbolic form of the adaptive control parameter of DCVFC is obtained by incorporating the generating condition, which ensures a wider stable operation region and eases the parameterization in the practical system. The system stability is also compared under different characteristic current ratios. As for the over modulation region, firstly, a current reference modifier (CRM) in [YON12] is combined with the conventional voltage feedback controller, which can improve the current dynamic performance. Secondly, a voltage limit reference modifier (VRM) is proposed to solve the conflict between the CRM and the conventional voltage feedback controller, by which the steady-state performance in the over modulation region can also be improved. Finally, the experiments are implemented to verify the effectiveness of the proposed method.

2.2 Machine Model and Voltage Feedback Controller

2.2.1 Machine Model

The mathematical model of non-salient-pole PMSM in the synchronous reference frame is given as follows [SUL11]

$$\begin{cases} V_d = R_s i_d + L_s \frac{di_d}{dt} - \omega_e L_s i_q \\ V_q = R_s i_q + L_s \frac{di_q}{dt} + \omega_e (L_s i_d + \psi_m) \\ \frac{J}{N_p} \frac{d\omega_e}{dt} = K_T i_q - T_L \\ K_T = 1.5P\psi_m \end{cases} \quad (2.3)$$

where V , i are the stator voltage, and current, respectively; the variables with subscript ‘ d ’ or ‘ q ’ indicate the corresponding components in d - or q -axis; R_s is the stator resistance; L_s is the synchronous inductance; ω_e is the electrical angular frequency; ψ_m is the permanent magnet flux linkage; T_L is the load torque; J is the moment of inertia; N_p is the number of pole pairs.

2.2.2 Voltage Feedback Controller

There are two supply constraints, i.e. current and voltage constraints, which can be written as

$$\begin{cases} |\mathbf{I}_s|^2 = i_d^2 + i_q^2 \leq I_m^2 \\ |\mathbf{V}_s|^2 = V_d^2 + V_q^2 \leq V_m^2 \end{cases} \quad (2.4)$$

where \mathbf{I}_s is the current vector, i.e. $(i_d + ji_q)$ in d - and q -axis frame or $(i_\alpha + ji_\beta)$ in α - and β -axis frame; \mathbf{V}_s is the voltage vector, i.e. $(V_d + jV_q)$ in d - and q -axis frame or $(V_\alpha + jV_\beta)$ in α - and β -axis frame; I_m is the current limit, which is mainly restricted by the thermal limit of machine and inverter; V_m is the voltage limit which is mainly restricted by the DC-link voltage V_{dc} .

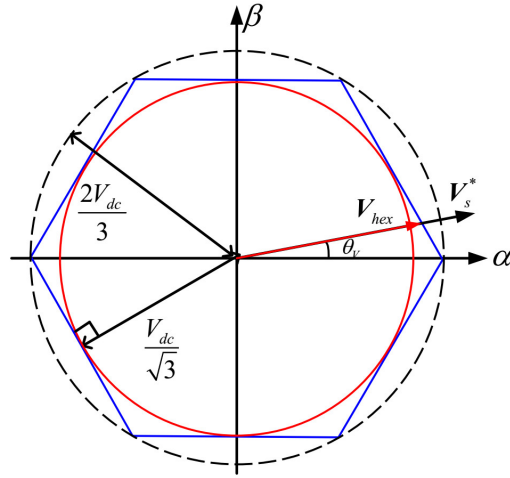


Fig. 2.1. Hexagon boundary in the stationary reference frame.

For the conventional SVPWM [BRO88] [LIN12], as shown in Fig. 2.1, when the voltage vector command V_s^* outsteps to the hexagon boundary limit, it will be truncated to V_{hex} , which is on the hexagon boundary and has the same phase as V_s^* . Since $V_{dc}/\sqrt{3}$ is the maximum voltage magnitude in the linear modulation range, the voltage magnitude reference $|V_{sr}^*|$ can be set as $MV_{dc}/\sqrt{3}$, where M is the coefficient that can be used to adjust the voltage magnitude reference. When $M \leq 1$, the system operates in the linear modulation region at steady state. When $M = 2/\sqrt{3}$, the actual voltage magnitude can be extended to the hexagon boundary, under which condition the fundamental component of the voltage magnitude of is $0.6057V_{dc}$ [HOL92].

The schematic of CVC with d-axis current voltage feedback controller (DCVFC) is shown in Fig. 2.2. In the constant torque region, the torque control is realized by controlling d - and q -axis current commands $i_{d,MTPA}^*$ and $i_{q,MTPA}^*$, which are obtained by considering maximum torque per ampere (MTPA). Since there is no reluctance torque for the non-salient-pole PMSM, $i_{d,MTPA}^* = 0$ and $i_{q,MTPA}^*$ can be given directly according to torque demand T_e^* , which has a linear relationship with $i_{q,MTPA}^*$, i.e. $T_e^* = K_T i_{q,MTPA}^*$.

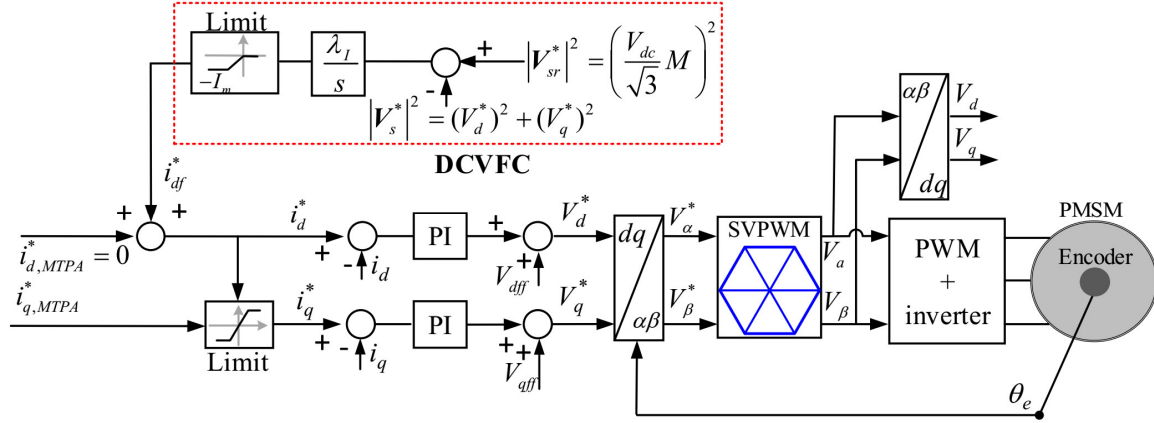


Fig. 2.2. Schematic of CVC with the voltage feedback controller.

The structure of DCVFC is employed with a pure integral regulator as that in [BIA01] [HAR01] [WAL04] [BOZ16]. Therefore, the voltage feedback controller can be expressed as

$$i_{df}^* = \lambda_I \int (|V_{sr}^*|^2 - |V_s^*|^2) dt \quad (2.5)$$

where λ_I is the gain of the integral controller, i_{df}^* is the d-axis weakening current; V_s^* is the voltage command vector, i.e. $(V_d^* + jV_q^*)$ in d- and q-axis frame; V_d^* and V_q^* are the d- and q-axis voltage commands from the conventional synchronous PI controller with feedforward decoupling compensation [MOR94]. V_d^* and V_q^* can be expressed as

$$\begin{cases} V_d^* = k_{pd}(i_d^* - i_d) + k_{id} \int (i_d^* - i_d) dt + V_{dff} \\ V_q^* = k_{pq}(i_q^* - i_q) + k_{iq} \int (i_q^* - i_q) dt + V_{qff} \end{cases} \quad (2.6)$$

where V_{dff}^* and V_{qff}^* are the decoupling terms, i.e.

$$\begin{cases} V_{dff}^* = -\omega_e L_s i_q \\ V_{qff}^* = \omega_e L_s i_d + \omega_e \psi_m \end{cases} \quad (2.7)$$

k_{pd} and k_{id} are the proportional and integral gains of the d-axis current controller, respectively. k_{pq} and k_{iq} are the proportional and integral gains of the q-axis current controller, respectively.

The parameters of the current controller can be chosen according to the pole-zero cancellation method [KWO06], which can be obtained that

$$k_{pd} = k_{pq} = \omega_{cc} L_s, k_{id} = k_{iq} = \omega_{cc} R_s \quad (2.8)$$

with which the current loop can be equalized to a first order low pass filter (LPF) with the bandwidth ω_{cc} .

2.3 Analyses of Voltage Feedback Loop and Adaptive Control

Parameter

2.3.1 Linearized Model of Voltage Loop

In the flux-weakening region, the voltage loop exhibits nonlinear behaviour that is related to the operation points [BOL14]. The small signal analysis can be employed to analyse the local stability of the voltage loop on the equilibrium point. The equivalent diagram of the linearized voltage loop can be shown in Fig. 2.3.

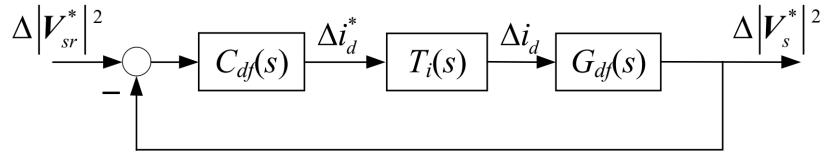


Fig. 2.3. Block diagram of the linearized model of voltage Loop.

In Fig. 2.3, the variable with the prefix ‘ Δ ’ indicates the corresponding small signal. $C_{df}(s)$ and $T_i(s)$ are the transfer functions of the integrator and the equivalent current loop, respectively, which can be expressed as

$$C_{df}(s) = \frac{\lambda_I}{s} \quad (2.9)$$

$$T_i(s) = \frac{\omega_{cc}}{s + \omega_{cc}} \quad (2.10)$$

$G_{df}(s)$ is the control plant which can be expressed as the transfer function from Δi_d to $\Delta |V_s^*|^2$. On the equilibrium point, the voltage command vector V_s^* can be approximated as the actual voltage vector V_s . Therefore,

$$\begin{aligned}
G_{df}(s) &= \frac{\Delta |V_s^*|^2}{\Delta i_d} \\
&\approx \frac{\Delta |V_s|^2}{\Delta i_d} = 2V_d^0 \frac{\Delta V_d}{\Delta i_d} + 2V_q^0 \frac{\Delta V_q}{\Delta i_d}
\end{aligned} \tag{2.11}$$

where the variables with superscript ‘0’ denote their steady-state value on the equilibrium point.

On assumption that the system’ mechanical time constant is much higher than the electrical time constant, the variation of the machine speed is ignored from the perspective of the small signal analysis. Therefore, on assumption that $\Delta \dot{i}_q = k \Delta i_d$, $G_{df}(s)$ can be derived as

$$G_{df}(s) = bs + a \tag{2.12}$$

where the coefficient a and b are

$$\begin{cases} a = 2\omega_e^0 (V_q^0 L_s - V_d^0 k L_s) + 2R_s (V_d^0 + V_q^0 k) \\ b = 2(V_d^0 L_s + V_q^0 L_s k) \end{cases} \tag{2.13}$$

The coefficient k is determined by the small signal behaviour of the current command, which can be obtained as the slope of the current trajectory at the equilibrium point. To be more specific, the coefficient k can be obtained according to the different operation modes, i.e. mode A and mode B. As shown in Fig. 2.4, in mode A, the machine is regulated along the current limit circle. In mode B, the machine is regulated along the constant torque curve. Therefore, when the machine operates in mode A, k can be derived as

$$k = \text{sign}(i_q) \left. \frac{d\sqrt{I_m^2 - i_d^2}}{di_d} \right|_{i_d=i_d^0} = -\frac{i_d^0}{i_q^0} \tag{2.14}$$

In mode B, i_q^* is a constant, and the coefficient k is zero.

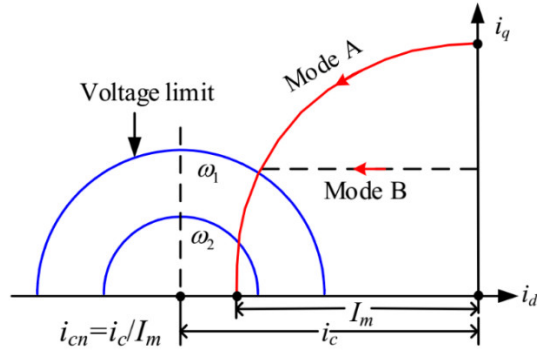


Fig. 2.4. Operation mode under different flux-weakening operation regions.

Therefore, under the different operation mode, the coefficient a and b can be obtained by substituting k into (2.13). With obtained a and b , the close-loop transfer function of the voltage loop can be expressed as

$$\Phi_I(s) = \frac{\omega_{cc} \lambda_I (bs + a)}{s^2 + \omega_{cc} (1 + b\lambda_I)s + \omega_{cc} \lambda_I a} \quad (2.15)$$

or

$$\Phi_I(s) = \frac{\omega_{cc} (b_{\lambda I} s + a_{\lambda I})}{s^2 + \omega_{cc} (1 + b_{\lambda I})s + \omega_{cc} a_{\lambda I}} \quad (2.16)$$

where $b_{\lambda I} = \lambda_I b$, $a_{\lambda I} = \lambda_I a$.

2.3.2 Stability Analysis and Control Parameter Design

2.3.2.1 Analysis of the Voltage Loop

According to the Routh stability criterion [FRA94], the stable condition of the voltage loop requires that

$$\begin{cases} \lambda_I a > 0 \\ 1 + \lambda_I b > 0 \end{cases} \quad \text{or} \quad \begin{cases} a_{\lambda I} > 0 \\ 1 + b_{\lambda I} > 0 \end{cases} \quad (2.17)$$

Since the voltage feedback controller aims to generate a negative d-axis current command, the control parameter λ_I is normally set as a positive value. According to (2.17), when $a \leq 0$, λ_I should be negative to maintain $a_{\lambda I} > 0$. However, it is impractical to change the

sign of the control parameter λ_I according to the sign of a . Because the coefficient a highly relies on the operation points and is sensitive to the system parameters. In addition, a is a dynamic term which suffers from noises. As a result, the condition $a \leq 0$ implies the intrinsic instability of the system in the flux-weakening region. Therefore, it is necessary to investigate the condition, i.e. when $a \leq 0$ in the flux-weakening region first.

At the equilibrium point, V_d^0 and V_q^0 can be written as

$$\begin{cases} V_d^0 = R_s i_d^0 - \omega_e^0 L_s i_q^0 \\ V_q^0 = R_s i_q^0 + \omega_e^0 (L_s i_d^0 + \psi_m) \\ \quad = R_s i_q^0 + \omega_e^0 L_s (i_d^0 + i_c) \end{cases} \quad (2.18)$$

1) *Mode A*

In mode A, by combing (2.13), (2.14), and (2.18), a can be derived as

$$a|_{ModeA} = 2\omega_e^0 \psi_m (\omega_e^0 L_s - R_s i_d^0 / i_q^0) \quad (2.19)$$

where $a|_{modeA}$ denoted the value of a in mode A.

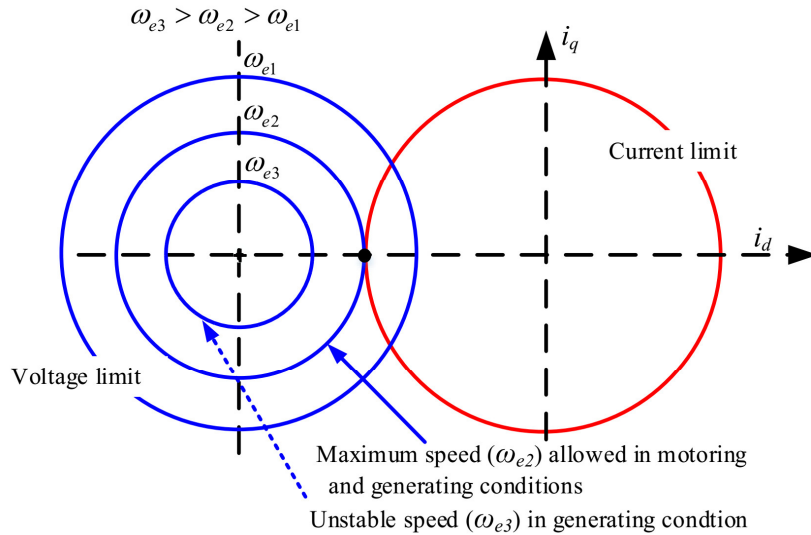
Since $i_d^0 < 0$ in the flux-weakening region, equation (2.19) implies that $a|_{ModeA} < 0$ only occurs when the system operates under generating condition ($\omega_e^0 i_q^0 < 0$) and $|i_q^0 / i_d^0| < |R_s / \omega_e^0 L_s|$. It should be noted that $a|_{ModeA} = 0$ actually corresponds to the condition, i.e.

$$\frac{\partial |I_s^0|^2}{\partial i_d^0} \frac{\partial |V_s^0|^2}{\partial i_q^0} - \frac{\partial |I_s^0|^2}{\partial i_q^0} \frac{\partial |V_s^0|^2}{\partial i_d^0} = 0 \quad (2.20)$$

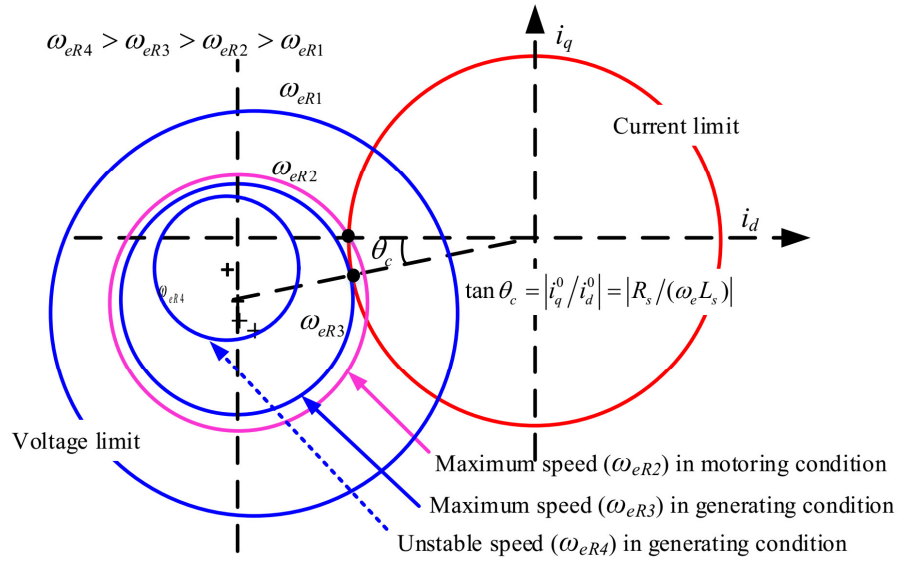
In consequence, the critical stability condnion, i.e. $a|_{ModeA} = 0$, corresponds to the operation point, i.e. where the voltage limit circle is tangent to the current limit circle. Fig. 2.5(a) and (b) illustrated the voltage and current limit circles without and with considering resistance, respectively, when the machine speed is positive. The machine running at the operation points on the up-half plane represent the motoring condition, while the machine running at the operation points on the low-half plane represent the generation condition. As shown in

Fig. 2.5(a), the voltage limit circle without considering the resistance is symmetrical against d axis. The maximum speeds in motoring and generating conditions are actually the same, i.e. ω_{e2} in Fig. 2.5(a), which occurs when the voltage limit circle is tangent to the current limit circle. In practice, the machine speed in the generating condition is not allowed to exceed the maximum speed ω_{e2} . For example, when the machine speed is ω_{e3} , which is higher than ω_{e2} , there will be no intersection point between the voltage and current limit circles, and the system will inevitably lose control.

On the other hand, when the resistance is considered, the voltage limit circle becomes asymmetric against the d -axis. The maximum speed in the generating condition (ω_{eR3} shown in Fig. 2.5(b)) is higher than the maximum speed in the motoring mode (ω_{eR2} shown in Fig. 2.5(b)) and occurs when $|i_q^0/i_d^0| = |R_s/\omega_e^0 L_s|$. Similarly, in practice, the speed in the generating condition is not allowed to exceed the maximum speed ω_{eR3} .



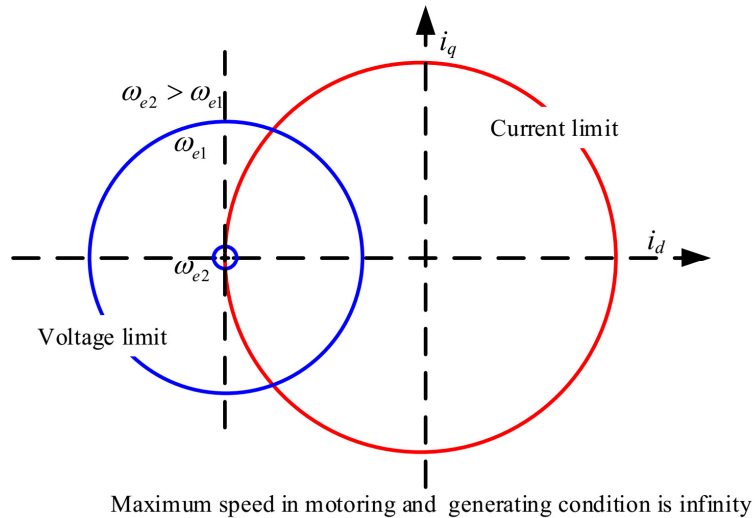
(a) Without considering resistance.



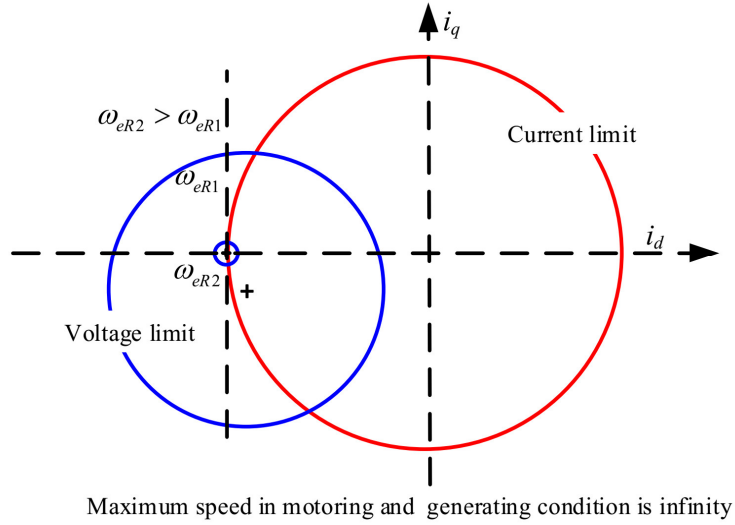
(b) With considering resistance.

Fig. 2.5. Voltage and current limit circles when $i_{cn} > 1$.

However, for the machine with infinite CPSR and $i_{cn}=1$, as shown in Fig. 2.6, the maximum speed could be infinity no matter the resistance is considered or not due to that the center point of the voltage limit circle tends to be $(-I_m, 0)$. Therefore, in theory, in terms of the voltage and current constraints, there will be no speed limit for the machine with infinite CPSR in the generating condition.



(a) Without considering resistance.



(b) With considering resistance.

Fig. 2.6. Voltage and current limit circles when $i_{cn}=1$.

2) Mode B

In mode B, a can be derived as

$$a|_{ModeB} = 2\omega_e^0 V_q^0 L_d + 2R_s V_d^0 \quad (2.21)$$

where $a|_{modeB}$ denotes the value of a in mode B.

It should be noted that the $a|_{ModeB} = 0$ actually defines the MTPV curve, i.e.

$$a|_{ModeB} = \frac{\partial |V_s^0|^2}{\partial i_d^0} \frac{\partial T_e^0}{\partial i_q^0} - \frac{\partial |V_s^0|^2}{\partial i_q^0} \frac{\partial T_e^0}{\partial i_d^0} = 0 \quad (2.22)$$

For the machine without MTPV region, the system operates on the right side of the MTPV curve. Therefore, $a|_{ModeB} > 0$ valid for the system without MTPV region. The system with MTPV control will be further discussed in chapter 3. For the machine with $i_{cn} \geq 1$, the control parameter can be tuned based on the assumption that the system operates only below the maximum allowable speed condition, i.e. $a > 0$.

2.3.2.2 Adaptive Control Parameter

2.3.2.2.1 In Mode A

From the foregoing analyses, when designing the control parameter λ_I , it can be assumed that $a > 0$. By ignoring the extreme condition, i.e. the system operates close to the maximum allowable speed in the generating condition, the resistance can be ignored when designing the control parameter of the voltage loop. Therefore, according to (2.15) and (2.18), the characteristic equation of the voltage loop can be written as

$$q(s) = s^2 + \omega_{cc} \left(1 + 2\lambda_I L_s (V_d^0 + kV_q^0) \right) s + 2\lambda_I \omega_{cc} \omega_e^0 L_s (V_q^0 - V_d^0 k) \quad (2.23)$$

By substituting (2.14) and (2.18) into (2.23), the characteristic equation in mode A can be further derived as

$$q(s) = s^2 + \omega_{cc} \left(1 - \frac{\omega_{ml}}{\omega_b} \sigma_I \right) s + \omega_{cc} \omega_{ml} \quad (2.24)$$

where ω_b , ω_{ml} and σ_I are

$$\omega_b = \frac{V_m}{L_s I_m} \quad (2.25)$$

$$\omega_{ml} = 2\lambda_I \omega_e^0 L_s \omega_e^0 L_s i_c \quad (2.26)$$

$$\sigma_I = (1/i_{cn} + i_{dn}) / (\omega_{en} i_{qn}) \quad (2.27)$$

where i_{dn} and i_{qn} are i_d^0 and i_q^0 normalized by I_m respectively; ω_{en} is ω_e^0 normalized by ω_b ; σ_I is an introduced normalized value and can be seen as a non-dimensional coefficient which varies with the operation points.

Since the Routh stability criterion requires that $1 - \omega_{ml} / (\omega_b \sigma_I) > 0$, the system could lose stable at the operation point where σ_I becomes higher. As the voltage loop can be seen as a typical second-order system, the control parameter can be designed according to the damping factor ζ , which can be calculated as

$$\xi = \sqrt{\frac{\omega_{cc}}{4\omega_{ml}} \left(1 - \frac{\omega_{ml}}{\omega_b} \sigma_l\right)} \quad (2.28)$$

In addition, the voltage and current limits can be written in the normalized form as

$$\begin{cases} i_{dn}^2 + i_{qn}^2 = 1 \\ (i_{dn} + i_{cn})^2 + i_{qn}^2 = \frac{1}{\omega_{en}^2} \end{cases} \quad (2.29)$$

With the normalized torque, i.e. $T_{en} = i_{cn} i_{qn}$, by taking several i_{cn} as examples, the flux-weakening capabilities represented by torque-speed curve are shown in Fig. 2.7. As can be seen in Fig. 2.7, the flux-weakening capability decreases significantly as i_{cn} goes higher from 1 to 2.

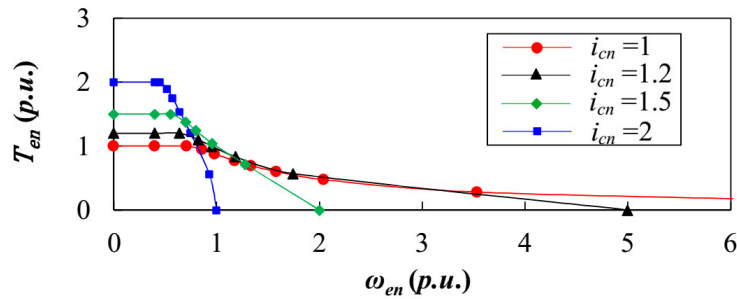
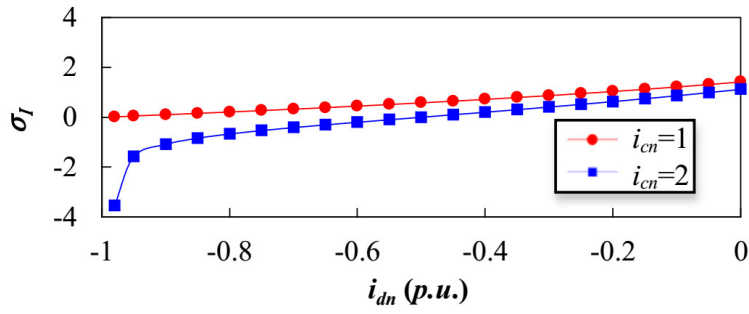
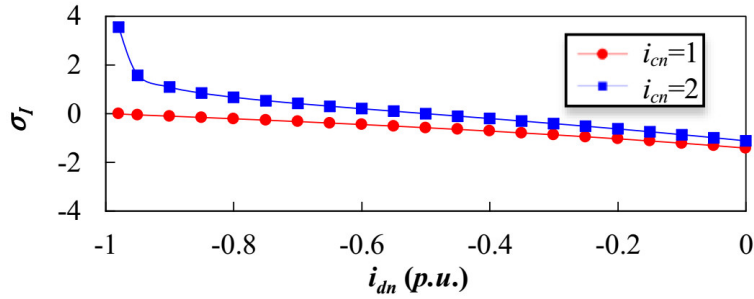


Fig. 2.7. Normalized torque-speed curve under different i_{cn} .

For a reasonable flux-weakening capability, only the machine with i_{cn} not greater than 2 are considered. By taking two cases as examples, i.e. $i_{cn}=1$ and $i_{cn}=2$, Fig. 2.8 shows the numerical results of σ_l in mode A (from $i_{dn}=-0.99$ to 0) including both motoring and generating conditions. It can be seen that the variation trend of σ_l in motoring and generating conditions are opposite, which implies that the system tuned well in motoring condition may not necessarily perform well in the generating condition.



(a) Motoring condition.



(b) Generating condition.

Fig. 2.8. Variation of σ_I in the flux-weakening region.

Assuming that ζ is selected at critical damping condition ($\zeta=1$) at the operation point where $\sigma_I = \sigma_{Is}$, ω_{ml} can be solved as

$$\begin{aligned} \omega_{ml} &= \frac{\omega_{cc}}{\sigma_{Is} \frac{\omega_{cc}}{\omega_b} + 2 + \sqrt{(\sigma_{Is} \frac{\omega_{cc}}{\omega_b} + 2)^2 - (\frac{\omega_{cc}}{\omega_b})^2 \sigma_{Is}^2}} \\ &\geq \frac{\omega_{cc}}{4} \frac{1}{\frac{\sigma_{Is}}{2} \frac{\omega_{cc}}{\omega_b} + 1} \end{aligned} \quad (2.30)$$

where σ_{Is} can be selected according to the variation of σ_I .

For a conservative design, ω_{ml} can be set as its lower limit, i.e.

$$\omega_{ml} = \frac{\omega_{cc}}{4} \frac{1}{\frac{\sigma_{Is}}{2} \frac{\omega_{cc}}{\omega_b} + 1} \quad (2.31)$$

Therefore, with (2.26) and (2.29), the symbolic form of the control parameter λ_I in mode A can be derived as

$$\lambda_I|_{modeA} = \frac{\omega_m}{2|\omega_e^0|L_sV_m}, \omega_m = \omega_{mIA} \quad (2.32)$$

where $\lambda_I|_{modeA}$ denotes λ_I tuned in mode A; ω_{mIA} is expressed as

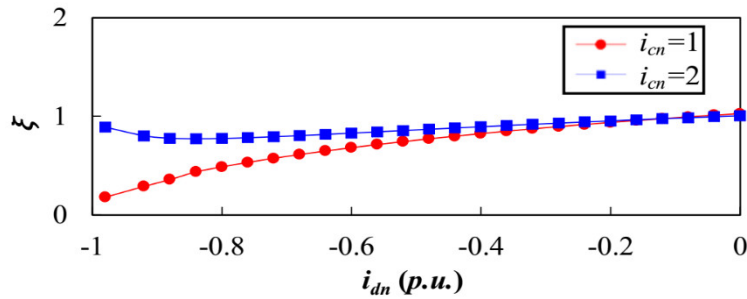
$$\omega_{mIA} = \omega_{mI}\beta, \beta = \frac{V_m}{|\omega_e^0|L_s i_c} = \frac{1}{|\omega_{en}|i_{cn}} \quad (2.33)$$

For practical implementation, $|\omega_e^0|$ in (2.32) should have a lower limit, which can be set at the absolute value of the minimum speed in the flux-weakening region, i.e. so-called corner speed ω_{co} .

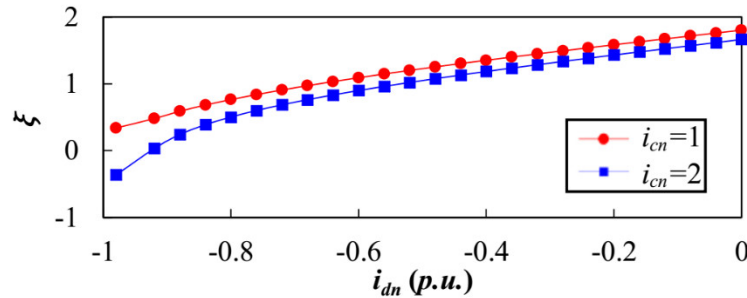
According to (2.28), the damping factor is inversely proportional to σ_I , ideally, σ_{Is} can be set as the maximum σ_I in the whole flux-weakening region to avoid the underdamped condition. However, for the machine with finite CPSR, i.e. $i_{cn} > 1$, as can be referred from (2.27), when the system operates in the generating condition ($\omega_{en}i_{qn} < 0$) and when i_{qn} approaches zero (i_{dn} approaches to -1) in mode A, σ_I tends to be positive infinity. Obviously, σ_{Is} cannot be set at positive infinity. Otherwise, λ_I will be zero. Moreover, as mentioned above, the operation point, i.e. $i_{dn} = -1$ and $i_{qn} = 0$, corresponds to the maximum allowable speed in the flux-weakening region when the resistance is ignored, the machine will inevitably lose control in the generation condition if the machine speed exceeds the maximum allowable speed. Therefore, from the perspective of designing control parameter λ_I , the extreme condition, i.e. i_{dn} close to -1 in generation condition can be reasonably ignored. In practice, the proper σ_{Is} can be selected according to the variation of σ_I in mode A. By comparing the variation of σ_I in both motoring and generating conditions in Fig. 2.8(a) and Fig. 2.8(b), a typical value of σ_{Is} can be set at the maximum value in the motoring condition, i.e. when $i_{dn} = 0$. When $i_{dn} = 0$, σ_{Is} can be derived as $\sqrt{i_{cn}^2 + 1} / i_{cn}$ by referring (2.27) and (2.29).

In order to see the effectiveness of the proposed tuning method, Fig. 2.9 and Fig. 2.10 illustrate the damping factor variation in the mode A with non-adaptive λ_I and adaptive λ_I based on the parameters in Table 2.1 (shown in the experimental verification section of this

chapter). The non-adaptive λ_l in Fig. 2.9 is only a comparison case, which is tuned on the corner speed and obtained by replacing $|\omega_e^0|$ in (2.32) with the corner speed ω_{co} . For example, if $i_{cn}=1$, the operation point at the corner speed ω_{co} actually corresponds to the condition $|V_d^0|=|V_q^0|$, which is the design point selected in [MAR99]. As can be seen in Fig. 2.9 (a), in motoring condition, when the system is applied with a non-adaptive λ_l , the damping factor ζ shows a decreasing trend when i_{dn} approaches to -1 for the case $i_{cn}=1$. However, in the generating condition, as shown in Fig. 2.9 (b), ζ shows a decreasing trend when i_{dn} approaches to -1 for the case $i_{cn}=2$. The decrease of damping factor could lead to an underdamped voltage loop or even instability. In Fig. 2.10, when the adaptive λ_l is employed, the voltage loops in both motoring and generating conditions for the cases, i.e. $i_{cn}=1$ and $i_{cn}=2$, are all well damped.



(a) Motoring condition.



(b) Generating condition.

Fig. 2.9. Damping factor variation in mode A with non-adaptive λ_l .

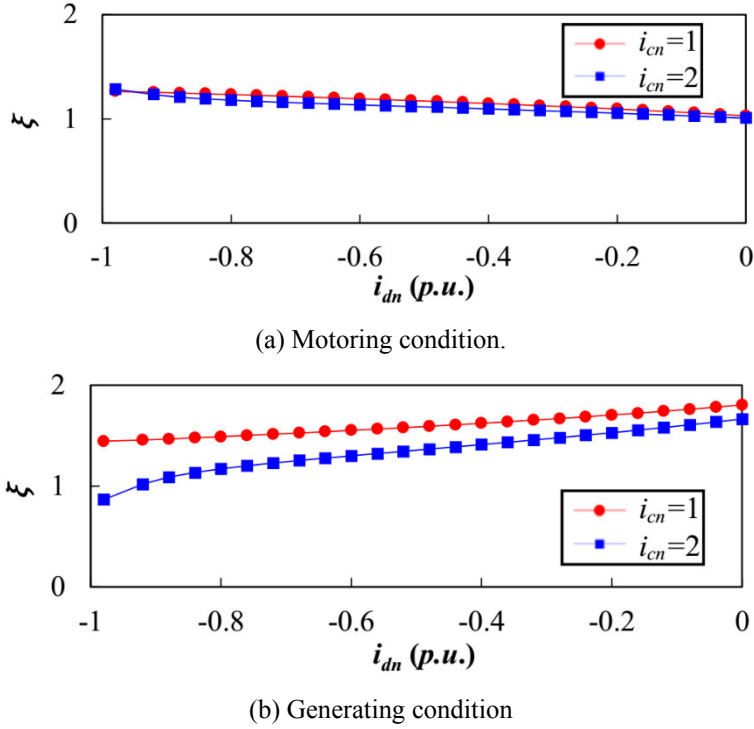


Fig. 2.10. Damping factor variation in mode A with adaptive λ_l .

As shown in Fig. 2.10, with the adaptive λ_l , in mode A, most of the values of damping factor lie between 1 and 2 except some operation points in the generating condition when $i_{cn}=2$. By approximating that $\zeta=5/4$ and $\omega_{ml} = \omega_{cc}/4$, $q(s)$ can be approximated as $(s+\omega_{cc})(s+\omega_{cc}/4)$. Thus, the bandwidth of the voltage loop can be approximated to $\omega_{cc}/4$. However, since ζ could be higher than $5/4$, and ω_{ml} is smaller than $\omega_{cc}/4$, the actual bandwidth of the voltage loop is smaller than $\omega_{cc}/4$. In practice, the bandwidth of the voltage loop can be adjusted by setting σ_{Is} .

2.3.2.2.2 In Mode B

In mode B, $k=0$. The characteristic equation of the voltage loop can be expressed as

$$q(s) = s^2 + \omega_{cc} (1 + 2\lambda_l L_s V_d^0) s + 2\lambda_l \omega_{cc} \omega_e^0 L_s V_q^0 \quad (2.34)$$

The upper limit of λ_l is constrained by the Routh stable criterion, i.e. $1 + 2\lambda_l L_s V_d^0 > 0$.

The worst condition happens when V_d^0 is minimum, i.e. $V_d^0 = -V_m$, which defines the

minimum stable range for the control parameter λ_I . By considering the worst condition, i.e. $V_d^0 = -V_m$, λ_I can be set by assuming that $1 + 2\lambda_I L_s V_m \geq 0.5$, which lead to

$$\lambda_I|_{modeB} = \frac{\omega_m}{2|\omega_e^0|L_s V_m}, \omega_m < \omega_{mB} \quad (2.35)$$

where $\omega_{mB} = 0.5|\omega_e^0|$.

Therefore, by considering mode A and mode B, the symbolic form of the control parameter can be finally obtained as

$$\lambda_I = \frac{\omega_m}{2|\omega_e^0|L_s V_m}, \omega_m = \min\{\omega_{ImA}, \omega_{ImB}\} \quad (2.36)$$

It can be proved as follows that the voltage loop is also damped well in mode B with λ_I in (2.36).

Proof:

In mode B, since the damping factor can be calculated as

$$\xi = \sqrt{\omega_{cc}/(8\lambda_I V_q^0 \omega_e^0 L_s)}(1 + 2V_d^0 L_s \lambda_I) \quad (2.37)$$

By substituting (2.36) into (2.37), ξ can be derived as

$$\xi = \frac{1}{2\sqrt{\frac{\omega_m}{\omega_{cc}}}} k_\xi, k_\xi = \frac{1 + V_{dn} \frac{\omega_m}{|\omega_e^0|}}{\sqrt{|V_{qn}|}} \quad (2.38)$$

where V_{dn} and V_{qn} are V_d^0 and V_q^0 normalized by V_m , respectively.

Since $\frac{\omega_m}{|\omega_e^0|} \leq 0.5$, it can be derived that

$$k_\xi \geq \frac{1 - 0.5|V_{dn}|}{\sqrt{|V_{qn}|}} \quad (2.39)$$

With the constraint $V_{qn}^2 + V_{dn}^2 = 1$, it can be derived that the minimum of $\frac{1-0.5|V_{dn}|}{\sqrt{|V_{qn}|}}$ can be

obtained at $|V_{qn}| = \sqrt{2\sqrt{3}-3} \approx 0.68$. Therefore, $k_\xi \geq 0.77$. In addition, $\frac{\omega_m}{\omega_{cc}} \leq \frac{\omega_{ml}\beta}{\omega_{cc}} < \frac{\beta}{4}$.

According to (2.33), it can be derived that the maximum β can be obtained at the corner speed when $i_{dn}=0$, $|i_{qn}|=1$. Therefore it can be derived as

$$\frac{\omega_m}{\omega_{cc}} < \frac{\beta}{4} \leq \frac{\sqrt{i_{cn}^2 + 1}}{4i_{cn}} \quad (2.40)$$

According to (2.38), it can be obtained that

$$\xi \geq 0.77 \frac{i_{cn}}{\sqrt{i_{cn}^2 + 1}} \quad (2.41)$$

Since only $i_{cn} \geq 1$ is considered, $\xi > 0.54$. Therefore, it verifies that the system is also damped well in mode B.

In practice, a slight difference of V_m for calculating λ_I will not cause problem because of the conservative design. V_m in (2.33) can be replaced by the reference $|V_{sr}^*|$ in both linear and over modulation regions. With λ_I in (2.36), $q(s)$ in mode B can be approximated as $(s + \omega_{cc})(s + |V_q^0|/V_m \omega_m)$, under which condition the bandwidth of the voltage loop can be approximated to $|V_q^0|/V_m \omega_m$. Therefore, in mode B, the bandwidth of the voltage loop will become smaller in lower $|V_q^0|$ area. Since $|V_q^0|=0$ corresponding the MTPV condition, the system has to change to the MTPV control to maintain the stability on the MTPV curve. However, the system with MTPV control happens on the machine with $i_{cn} < 1$, which is out of the scope of this chapter and will be discussed in chapters 3, 4 and 5.

2.4 Improvement in the Over Modulation Range

2.4.1 $M \leq 1$

When $M \leq 1$, the system operates mainly in the linear modulation region. Therefore, the over modulation region is only used in the transient state. For example, under a step q-axis current command, the voltage command vector V_s^* could jump into the over modulation region, as shown in Fig. 2.11. Since the voltage loop analysis based on the linearized model can only reflect the small signal behaviour within the neighbourhood of the equilibrium points, it cannot guarantee large signal dynamics when the system jumps into over modulation region. Due to the less voltage margin, the current dynamic performance is degraded, which consequently deteriorates the voltage loop performance. Since the flux-weakening controller aims to deter the voltage saturation by controlling the current command, the current dynamics is very essential in the over modulation region.

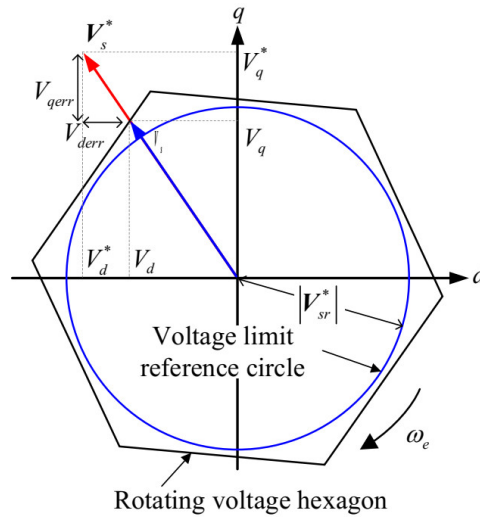


Fig. 2.11. Voltage vector synthesis when the system jumps into over modulation region.

As shown in Fig. 2.11, when the voltage command vector V_s^* oversteps the voltage hexagon boundary, by considering the voltage differences between the voltage command and the real voltage fed to the inverter in d- and q-axes, i.e. $V_{derr} = V_d^* - V_d$ and $V_{qerr} = V_q^* - V_q$, it can be derived that [KWO12]

$$\begin{cases} i_d = \frac{\omega_{cc}}{s + \omega_{cc}} i_{de}^*, (i_{de}^* = i_d^* - \frac{V_{derr}}{k_{pd}} \frac{s}{s + R_s/L_s}) \\ i_q = \frac{\omega_{cc}}{s + \omega_{cc}} i_{qe}^*, (i_{qe}^* = i_q^* - \frac{V_{qerr}}{k_{qd}} \frac{s}{s + R_s/L_s}) \end{cases} \quad (2.42)$$

According to (2.42), it can be seen that d- and q-axis current references can be equivalent to i_{de}^* and i_{qe}^* , respectively. When the system jumps into the over modulation region, since i_d^* is still regulated by the voltage feedback controller and the DC values of V_{derr} and V_{qerr} will diminish at steady state, the system will finally reach a new equilibrium point. However, due to the existence of V_{derr} and V_{qerr} , i.e. less voltage margin, the current dynamic performance will be degraded. On the other hand, the voltage feedback controller is relatively slow to generate the required d-axis current instantly when the system jumps into the over modulation region, which therefore could lead to more serious voltage saturation problem.

In order to improve the current dynamics and alleviate the voltage saturation, the current reference modifier (CRM) which is firstly applied in [KWO12] for the voltage error feedback control will be adopted here for the voltage magnitude feedback control. As shown in Fig. 2.12, the q-axis voltage error V_{qerr} multiplied with a coefficient is fed back to the d-axis current reference, and the d-axis current reference is modified as

$$i_{dm}^* = i_d^* + i_{da}^*, (i_{da}^* = -\frac{V_{qerr}}{k_{pd}} \text{sign}(\omega_e)) \quad (2.43)$$

Since $V_{qerr} \approx V_q^* - (\omega_e L_s i_d + \omega_e \psi_m)$, the basic idea by using a current reference modifier is to secure the q-axis voltage margin by reducing the d-axis current reference. In addition, the CRM actually acts as an anti-windup controller in the over modulation region, which tries to move the voltage magnitude back to the hexagon boundary. Therefore, the voltage saturation problem will be alleviated and the system dynamic performance can be improved.

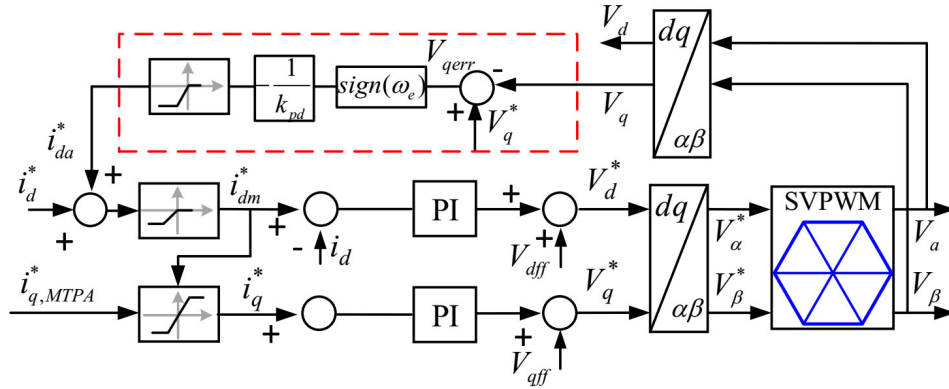


Fig. 2.12. Current reference modifier (CRM).

2.4.2 $M > 1$

Since when $M \leq 1$, the voltage limit reference is within the inscribed circle of the hexagon boundary, V_{qerr} only appears when the system jumps into the over modulation region at transient state. However, when $M > 1$, as the voltage limit reference locates at the outside of the inscribed circle of the hexagon boundary, V_{qerr} always exists. As shown in Fig. 2.13(a), when the voltage command V_s^* locates at the shadowed area between the voltage limit reference circle and the hexagon boundary, the voltage feedback controller tries to move V_s^* back to the voltage limit reference circle. However, the CRM tries to move V_s^* back to hexagon boundary. Therefore, a conflict occurs between the voltage feedback controller and CRM. As a result, the system performance is degraded at steady state.

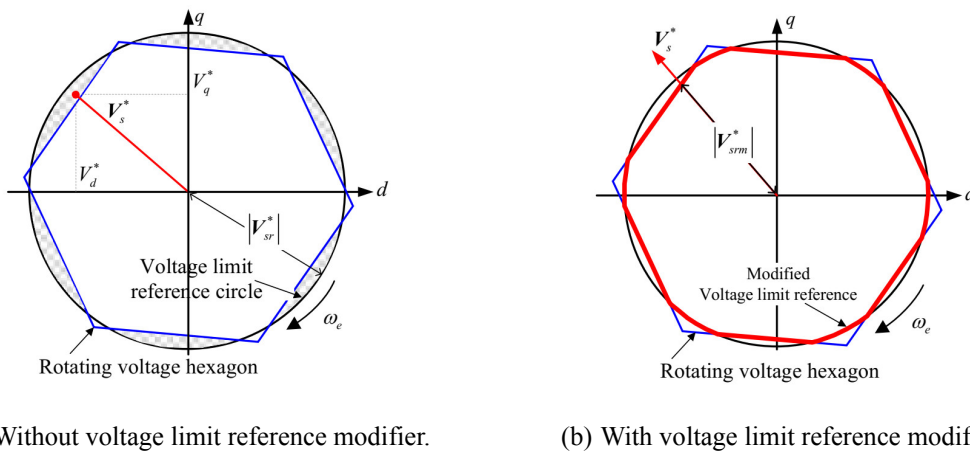


Fig. 2.13. Voltage limit reference circle in d-q reference frame.

In order to overcome the conflict between the voltage feedback controller and the CRM. The voltage limit reference modifier (VRM) is introduced. As shown in Fig. 2.13(b), compared with original voltage limit reference circle, the red thick line indicates the modified voltage limit reference which is defined as that: when the original voltage limit reference is outside the hexagon boundary, the voltage limit reference is modified to the hexagon boundary, otherwise no modification is required. Therefore, the magnitude of the modified voltage limit reference, i.e. $|V_{srm}^*|$ can be obtained as

$$|V_{srm}^*| = \min\left(\frac{V_{dc}}{\sqrt{3}}M, |V_{hex}|\right) \quad (2.44)$$

where V_{hex} is the vector with the same phase as the voltage command V_s^* , and with the magnitude on the hexagon boundary. From the geometric relations of the voltage vector in the stationary (α - β) reference frame shown in Fig. 2.1, $|V_{hex}|$ can be obtained as

$$|V_{hex}| = \frac{V_{dc}}{\sin(\text{mod}(\theta_V, \frac{\pi}{3}) + \frac{\pi}{3})\sqrt{3}} \quad (2.45)$$

where θ_V is the voltage command angle in the stationary reference frame.

With the VRM, the conflict between the CRM and the voltage feedback controller is eliminated automatically. Consequently, both the steady-state and dynamic performance can be improved in the over modulation region. The overall control diagram with added VRM and CRM can be shown in Fig. 2.14.

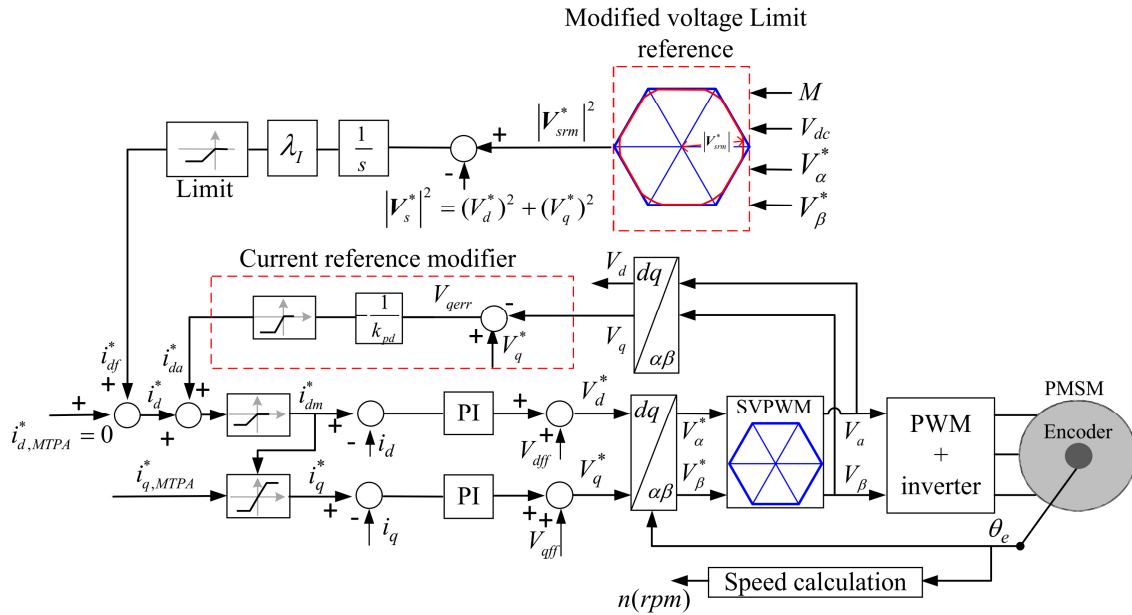


Fig. 2.14. Schematic of flux-weakening control with added CRM and VRM.

2.5 Experimental Verification

The experiments based on dSPACE (DS1006) platform are implemented on a non-salient-pole PMSM. The experimental setup is detailed in Appendix A, in which the test rig-I is used as the load torque machine, i.e. a wound field type DC machine with the rated speed at 1500 rpm. The combined inertia of the transmission system is $0.012 \text{ kg}\cdot\text{m}^2$. The power switches of the inverter are IRFH7440 MOSFET. The PWM switching frequency is 10 kHz. The machine parameters are listed in Table 2.1. It should be noted that the different characteristic current ratios are realized by setting different current limits of the machine rather than using different machines.

Table 2.1 Machine and drive parameters

Parameters	Value
Phase resistance (R_s)	0.25 Ω
Synchronous inductance (L_s)	1.7 mH
PM-flux linkage(ψ_m)	10 mWb
Number of pole pairs (N_p)	10
DC link voltage (V_{dc})	14 V
Current limit (I_m) when $i_{cn}=1$	5.9 A
Current limit (I_m) when $i_{cn}=2$	2.9 A
Current bandwidth (ω_{cc})	1200 rad/s

2.5.1 Stability with Non-adaptive λ_I and Adaptive λ_I

The stability of the system with adaptive λ_I is compared with a non-adaptive λ_I in mode A, and then verified in mode B in the linear modulation region ($M=0.9$).

2.5.1.1 In Mode A

In mode A, the motoring condition is realized by setting q -axis current command $i_{q,MTPA}^*$ at its maximum value, i.e., I_m . Therefore, in the flux-weakening region, the machine is forced to operate along the current limit circle. The generating condition is realized by reversing the current command to $-I_m$ when the machine is operating at motoring condition. A power resistance (4 Ω , 14A) is connected to the DC bus to absorb the feedback energy in the generating condition. In the experiments, the condition, i.e. $i_{cn}=1$ and 2, are selected to verify the analysis.

When $i_{cn}=1$, the dynamic performance of the machine in mode A with non-adaptive λ_I and adaptive λ are shown in Fig. 2.15(a) and Fig. 2.15(b), respectively. As shown in Fig. 2.15(a), when the control parameter λ_I is kept at a constant in the flux-weakening region, the machine operates well at the early stage of the flux-weakening region. However, as the machine speed increases, the system oscillates in the motoring condition. This phenomenon can also be verified through the decrease of the calculated damping factor in the deep flux

weakening region. Therefore, the flux-weakening operation range is significantly restricted. When the machine switches to the generating condition, the oscillation disappears at this point which is due to the relative higher damping factor in the generating condition as can also be referred to the Fig. 2.9(b). Another reason is due to that the d -axis current in the generating condition at the switching point is slightly higher than that in the motoring condition. This is caused by the increase of the DC-link voltage, which then makes the system back to the operation point without oscillation. When the system is applied with the adaptive λ_I , as shown in Fig. 2.15(b), the system is damped well in the whole flux-weakening region. Therefore, a wider stable speed range can be achieved.

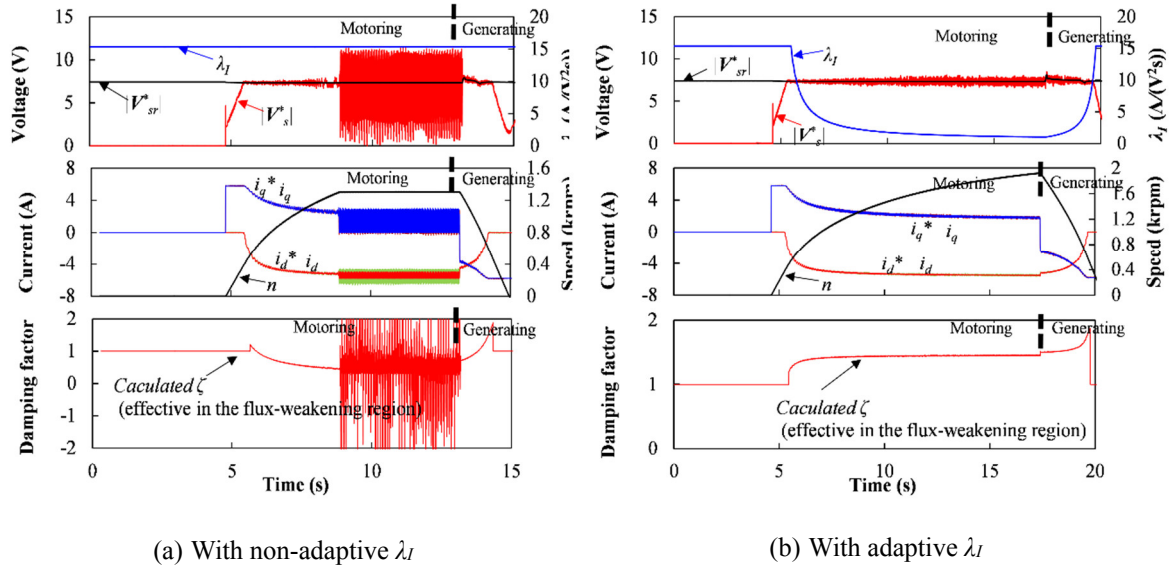


Fig. 2.15. Dynamic performance in flux weakening region (mode A) when $i_{cn}=1$.

When $i_{cn}=2$, the dynamic performance of the machine in the mode A with non-adaptive λ_I and adaptive λ_I are shown in Fig. 2.16(a) and (b), respectively. It can be seen from Fig. 2.16(a) that the system operates well in the motoring condition even with a non-adaptive λ_I . However, when the machine switches into generating condition, the calculated damping factor could even become negative. Therefore, the system oscillates. By applying the adaptive λ_I , as shown in Fig. 2.16(b), the system is damped well in the whole flux-weakening region.

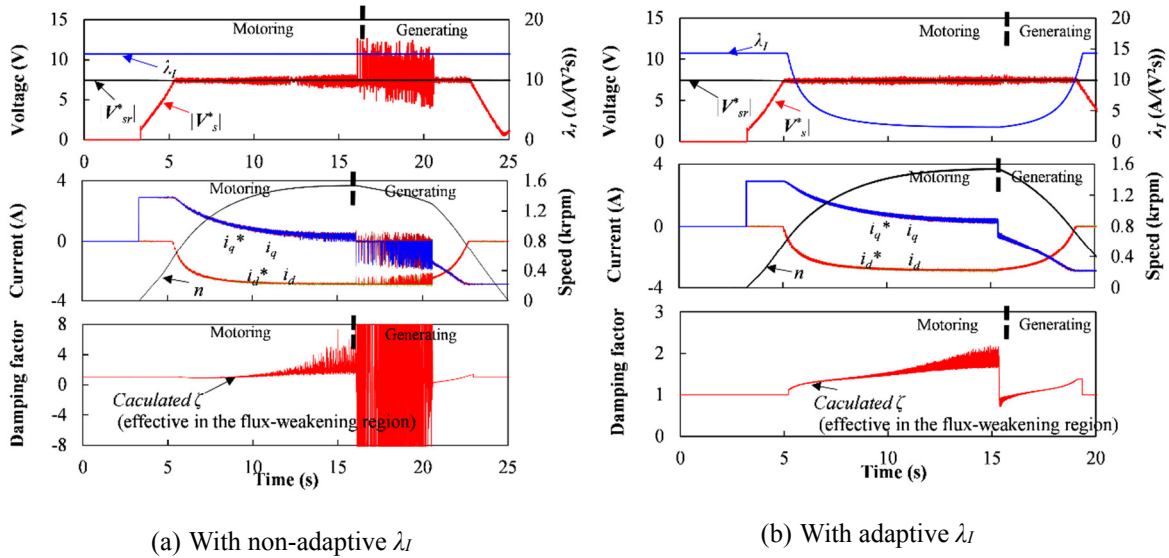
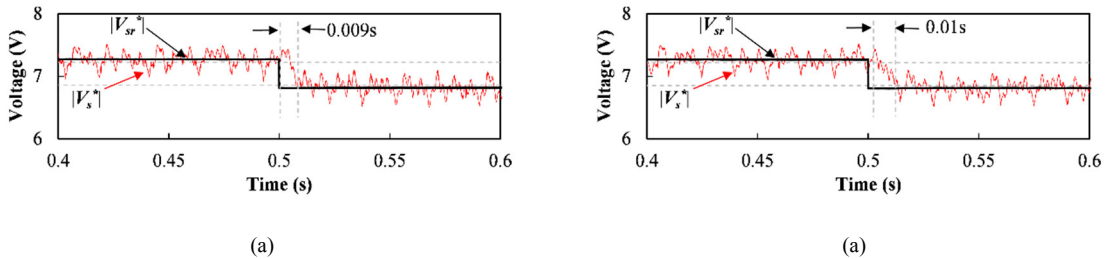
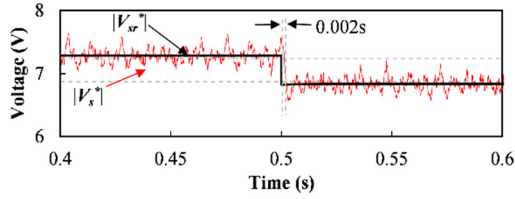


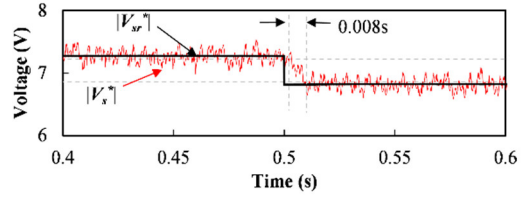
Fig. 2.16. Dynamic performance in flux weakening region (mode A) when $i_{cn}=2$.

Furthermore, when $i_{cn}=1$, on the different operation points in mode A, the large signal response to a stepwise reduction of the voltage magnitude reference under the non-adaptive λ_l and adaptive λ_l are shown in Fig. 2.17 and Fig. 2.18, respectively. In Fig. 2.18, it can be seen that the voltage loop shows nonlinear behaviour at different operation points when using a non-adaptive λ_l . The voltage loop dynamics increases with the increasing speed until the voltage loop oscillates at 1150 rpm. Nevertheless, the nonlinear behaviour of voltage loop at different operation points can be alleviated by adopting the adaptive λ_l , as shown in Fig. 2.18. By approximating that the voltage loop has first order dynamic response, as a rule of thumb, the bandwidth of the voltage can be evaluated by $\ln(9)/t_r$, where t_r is the rise time. For example, as shown in Fig. 2.18(a), when $t_r=0.01$ s, the bandwidth of the voltage loop is 220 rad/s. Due to the visual error caused by the ripples in the voltage magnitude, the actual bandwidth of the voltage loop should be around 220 rad/s.

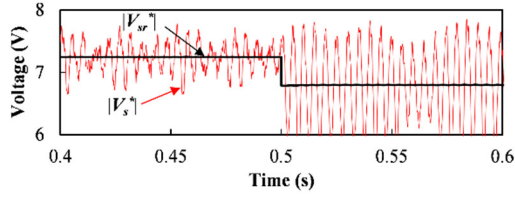




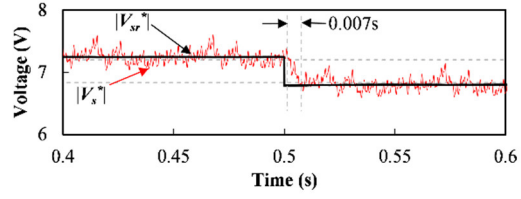
(b)



(b)



(c)



(c)

Fig. 2.17. Large signal response of voltage magnitude in mode A when $i_{cn}=1$ with non-adaptive λ_L .

- (a) $i_d=-1$ A, $i_q=5.8$ A, $n=400$ rpm.
- (b) $i_d=-5$ A, $i_q=3.1$ A, $n=830$ rpm.
- (c) $i_d=-5.5$ A, $i_q=2.1$ A, $n=1150$ rpm.

Fig. 2.18. Large signal response of voltage magnitude in mode A when $i_{cn}=1$ with adaptive λ_L .

- (a) $i_d=-1$ A, $i_q=5.8$ A, $n=400$ rpm.
- (b) $i_d=-5$ A, $i_q=3.1$ A, $n=830$ rpm.
- (c) $i_d=-5.5$ A, $i_q=2.1$ A, $n=1150$ rpm.

2.5.1.2 In Mode B

The operation mode B is realized by setting a smaller $i_{q,MTPA}^*$ than the current limit I_m , by which the machine can operate inside the current limit circle. Fig. 2.19 shows the current trajectories when $i_{q,MTPA}^*$ is set at 3 A and 2 A when $i_{cn}=1$ and 2, respectively. The machine starts from the constant torque region and then accelerates to modes B and A subsequently. Afterward, by changing the sign of $i_{q,MTPA}^*$, the machine operates in the generating condition. It can be seen that the currents are stably controlled in the mode B, which confirms the effectiveness of the adaptive control parameter used in the mode B.

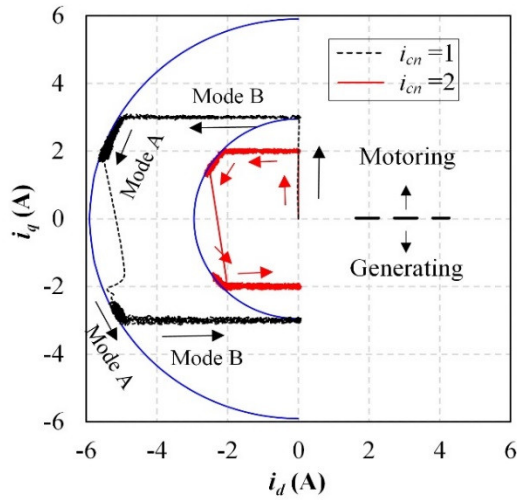
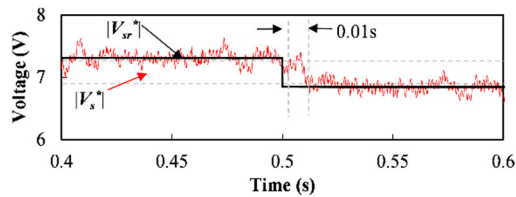
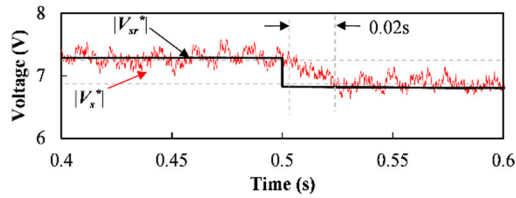


Fig. 2.19. Current trajectories in modes A and B.

Fig. 2.20 shows the large signal response to a stepwise reduction of the voltage magnitude reference with the adaptive λ_l on two different operation points. In Fig. 2.20(a), the voltage loop in mode B in higher q-axis voltage point shows almost the same dynamics as mode A. In Fig. 2.20(b), the voltage loop dynamics becomes slower in lower q-axis voltage point, which is consistent with the small signal analysis.



(a)



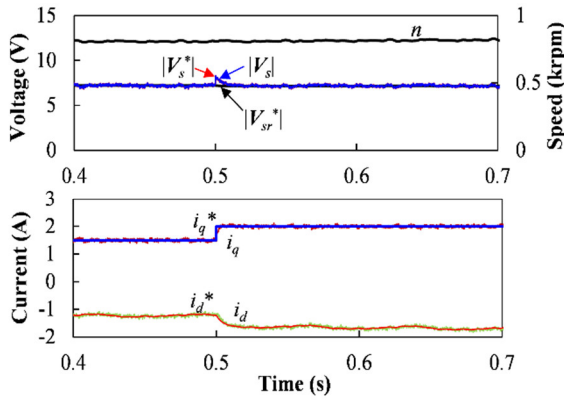
(b)

Fig. 2.20. Large signal response of voltage magnitude in mode B when $i_{cn}=1$ with adaptive λ_l . (a) $i_d=-1$ A, $i_q=3$ A, $V_q=6$ V, $n=600$ rpm. (b) $i_d=-3.5$ A, $i_q=3$ A, $V_q=3.8$ V, $n=800$ rpm.

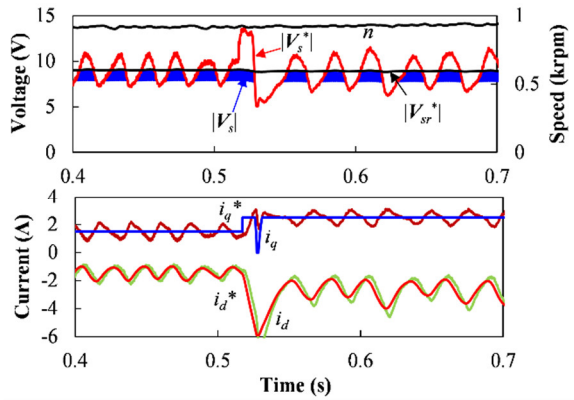
2.5.2 Performances in Over Modulation Region

Based on the system with the adaptive λ_L , the current dynamic performance in the linear and over modulation regions is further compared by taking $i_{cn}=1$ as example. Fig. 2.21(a) shows the current and voltage dynamic performance in the flux-weakening region for the conventional voltage feedback controller with $M=0.9$ when the q-axis current reference changes from 1.5A to 2A. It can be seen that the voltage command magnitude $|V_s^*|$ is the same as $|V_s|$, which means the voltage command is fully realized by the inverter. Therefore, the current has a good dynamic performance. However, when $M=1$ and the q-axis current reference changes from 1.5A to 2.5A, as shown in Fig. 2.21(b), the system jumps into the over modulation region, $|V_s|$ is much lower than $|V_s^*|$ which implies the insufficient voltage margin. Therefore, the current and voltage dynamic performances are deteriorated. Fig. 2.21(c) shows the alleviated voltage saturation and improved current dynamic performance when the CRM is applied.

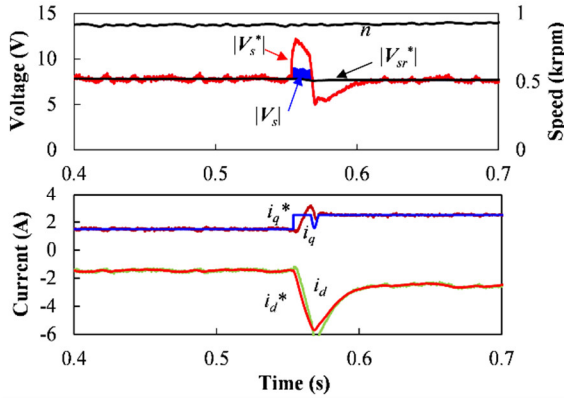
Fig. 2.22 shows the current and voltage dynamic performance in the flux-weakening region when the q-axis current reference changes from 1.5A to 2.5A at the condition $M=1.15$. As shown in Fig. 2.22(a), the current and voltage even show oscillation at steady state for the conventional voltage feedback controller, not to mention the dynamic performance. Fig. 2.22(b) shows that the current and voltage are stably controlled by adding the CRM. In addition, good current and voltage dynamic performance can still be obtained even when $M=1.15$. Fig. 2.22(c) shows the current and voltage dynamic performance when both the CRM and VRM are applied. It can be seen that the modified term i_{da}^* is only dominant at the dynamic stage. Therefore, both the dynamic and steady-state performance can be improved in the over modulation region with the CRM and VRM.



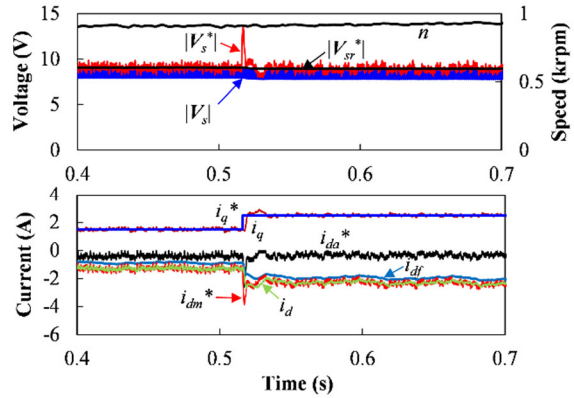
(a) With only conventional voltage feedback controller, ($M=0.9$)



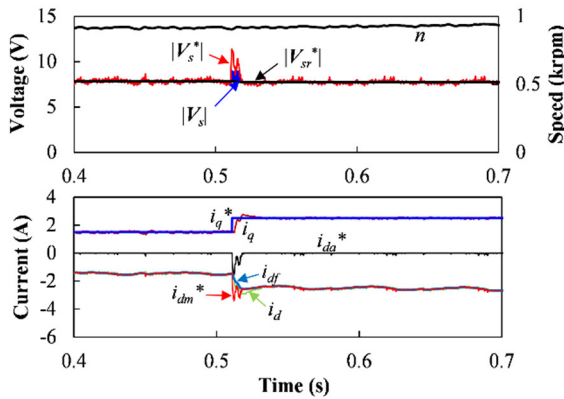
(a) With only conventional voltage feedback controller, ($M=1.15$).



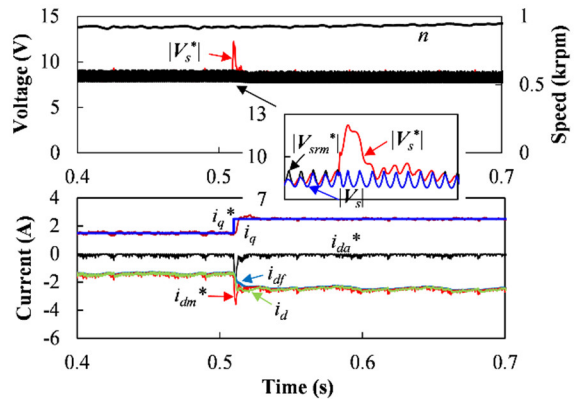
(b) With only conventional voltage feedback controller ($M=1$).



(b) With added CRM, ($M=1.15$).



(c) With added CRM, ($M=1$).



(c) With added CRM and VRM, ($M=1.15$).

Fig. 2.21. Current and voltage dynamic performance, ($M \leq 1$).

Fig. 2.22. Current and voltage dynamic performance, ($M > 1$).

2.6 Conclusion

This chapter has proposed an adaptive control parameter tuning method for the conventional voltage feedback controller in the flux-weakening region for the non-salient-pole PMSM without MTPV region. The analysis and experimental results have indicated the proposed adaptive control parameter can effectively maintain the system stability in a wider speed range, including both motoring and generating conditions, when compared with a constant control parameter used in the flux-weakening region. In addition, VRM combined with the CRM is proposed to improve the over modulation flux-weakening performance, which has been verified through experimental results.

CHAPTER 3 FEEDBACK TYPE FLUX-WEAKENING CONTROL ON PMSM WITH MTPV REGION

For the machine with MTPV region, an extra MTPV control strategy is required. Based on the conventional voltage magnitude feedback controller, by also considering the MTPV region, this chapter aims to optimize a feedback type flux-weakening control strategy with considering steady-state performance, dynamic performance and stability in both linear and over modulation regions.

3.1 Introduction

For the machine having high inductance [REF05] [REF06] [KWO07] [LIU12] or even under the overload condition, the characteristic current of the machine ($i_c = \psi_m / L_s$) could be lower than the current limit I_m . Under such condition, the MTPV control is required to maximize the torque capability and achieve an infinite constant power speed ratio (CPSR) [SOO94] [MOR94]. In [KWO07] [KWO08] [LIU12], the demagnetizing d-axis current command is generated by utilizing the voltage error between the input and output of the over modulation block, the MPTV control on a non-salient-pole PMSM is achieved by forcing the MTPV penalty function to zero with an extra voltage feedback loop. However, the voltage error feedback control can not achieve flux-weakening operation in linear modulation region. For some applications where the DC-link voltage is not a great concern, the linear modulation region is still preferred due to fewer harmonics and more voltage margin. Therefore, the control strategy which can cover both linear and over modulation flux-weakening controls is beneficial to the general purpose application. In order to achieve flux weakening in both linear and over modulation regions, the conventional voltage magnitude feedback controller can be employed [YON14]. However, the MTPV region is not considered in [YON14].

In this chapter, a feedback MTPV control is proposed based on the conventional voltage magnitude feedback controller. In addition, the MTPV controller is optimized in terms of

steady-state performance, dynamic performance and stability. Firstly, the MTPV penalty function is optimized by considering the influence of the resistance, which is important for the small power motor. Then, a current command feedback MTPV controller, rather than the voltage command feedback MTPV controller in [KWO07] [LIU12], is employed to ensure the stability while maintaining good dynamics. Furthermore, by considering the stability issue in the MTPV region, the MTPV loop is analysed and a proportional-integral (PI) type MTPV controller is used and designed, which is rarely discussed in other references. Moreover, the stability in the over modulation region is improved with a simple voltage modifier (VVM) by also considering the MTPV region. Finally, the analyses are verified through experimental results.

3.2 Feedback Type Control Strategies

3.2.1 Operation Regions

At steady state, the transient voltage on inductance can be ignored. In addition, by also considering the resistance of the power switch device, and power cable, the voltage constraint described in the d- and q-axis current plane can be derived as

$$\left(i_d + \frac{\omega_e^2 L_s \psi_m}{Z_s^2}\right)^2 + \left(i_q + \frac{\omega_e R \psi_m}{Z_s^2}\right)^2 = \frac{V_m^2}{Z_s^2} \quad (3.1)$$

where $Z_s = \sqrt{R^2 + (\omega_e L_s)^2}$; R is total resistance by also considering the power switch device, and power cable [LIU12].

From (3.1), it can be seen that the voltage constraint is a circle whose center point is $(\omega_e^2 L_s \psi_m / Z_s^2, \omega_e R \psi_m / Z_s^2)$ and radius is V_m / Z_s . As the speed increases, the voltage limit circle shrinks. If the resistance is ignored or the machine speed is infinity, the center of the voltage limit circle is $(-i_c, 0)$, i.e. ψ_m / L_s . For the machine with MTPV region, as shown in Fig. 3.1, the entire speed range can be divided into three regions:

1) Region I

In the region I, as shown in Fig. 3.1, the machine operates on the curve ‘OA’, aiming to achieve max torque per ampere (MTPA). Since the machine operates inside the current and voltage limit circle, i.e. $|I_s| < I_m$ and $|V_s| < V_m$, no flux-weakening control is required in this region.

2) Region II

The region II includes the curve ‘AB’ and the area within the closed curve ‘OABCO’. On the curve ‘AB’, the machine operates on the intersection point of the voltage and current limit circle, i.e. $|V_s| = V_m$ and $|I_s| = I_m$. In the area ‘OABCO’, the machine operates on the voltage limit circle and inside the current limit circle, i.e. $|V_s| = V_m$ and $|I_s| < I_m$. In region II, the flux-weakening control is required to satisfy the voltage and current constraints.

3) Region III

In region III, the machine operates on the MTPV curve ‘BC’ that inside the current limit circle, i.e. $|I_s| < I_m$ and $|V_s| = V_m$. In this region, the MTPV control strategy can be applied to maximize the torque capability and extend the operation speed range.

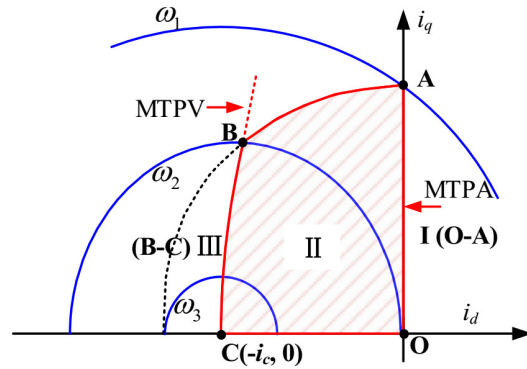


Fig. 3.1. Operation regions considering MTPV.

3.2.2 Control Strategies

Fig. 3.2 shows the schematic of the feedback type flux-weakening control based on current vector control (CVC) system. In the region I, as with chapter 2, d- and q-axis current commands, i.e. $i_{d,MTPA}^*$ and $i_{q,MTPA}^*$ are obtained according to MTPA, i.e. $i_{d,MTPA}^* = 0$ and $i_{q,MTPA}^*$ can be given directly as it is proportional to the torque demand.

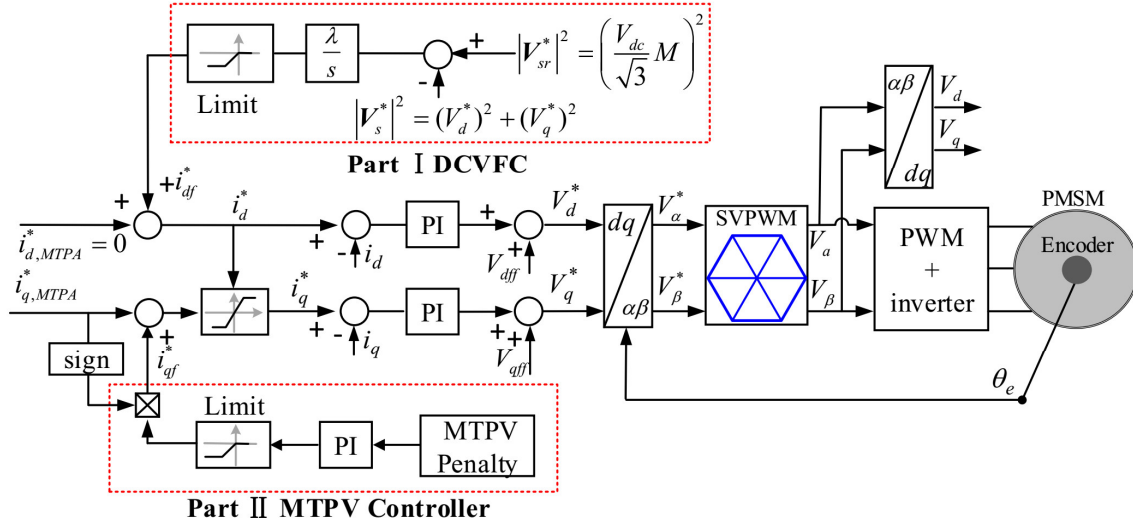


Fig. 3.2. Schematic of the feedback type flux-weakening control based on CVC system.

In region II, the d-axis current voltage magnitude feedback controller (DCVFC) with a pure integrator is employed, as shown in the part I of Fig. 3.2.

In the region III, the MTPV control strategy is achieved by introducing an extra feedback loop which forces the MTPV penalty function to zero by regulating the q-axis current command [KWO07] [LIU12]. According to the definition of MTPV, i.e. maximum torque per voltage, the MTPV curve can be obtained at the tangent point of the voltage limit circle and constant torque curve. Therefore, the penalty function for the MTPV operation, i.e. P can be defined as

$$P = \frac{1}{2} \left(\frac{\partial |V_s|^2}{\partial i_d} \frac{\partial T_e}{\partial i_q} - \frac{\partial T_e}{\partial i_d} \frac{\partial |V_s|^2}{\partial i_q} \right) \quad (3.2)$$

where the condition $P=0$ represents the MTPV curve.

The MTPV controller is denoted in Part II of Fig. 3.2. With the MTPV controller, the q-axis current command is further modified by the output of a PI controller. The modified term, i.e. i_{qf}^* can be expressed

$$i_{qf}^* = \text{sign}(i_{q,MTPA}^*) \min\left(0, \frac{k_{pqf}s + k_{iqf}}{s} P\right) \quad (3.3)$$

where k_{pqf} and k_{iqf} are the proportional and integer gains of the PI controller.

Therefore, the q-axis current command can be obtained as

$$i_q^* = \text{sign}(i_{q,MTPA}^*) \min(\sqrt{I_m^2 - (i_d^*)^2}, |i_{q,MTPA}^* + i_{qf}^*|) \quad (3.4)$$

3.3 Optimized MTPV Controller

3.3.1 Penalty Function for MTPV

At steady state, by referring (3.2), P can be derived in voltage and current form as

$$P = \begin{cases} P_v = \omega_e V_q L_s + R V_d \\ P_c = (i_d + i_c \frac{(\omega_e L_s)^2}{Z_s^2}) Z_s^2 \end{cases} \quad (3.5)$$

where P_v and P_c represent the voltage and current form of the penalty function, respectively.

According to (3.5), if the resistance is ignored, MTPV curve can be simplified as $\omega_e V_q = 0$ [KWO07] or $i_d = -i_c$ [LIU12]. However, as shown in Fig. 3.3, for the small power motor especially when the power cable is required, the ignorance of the resistance could cause a notable deviation of the current trajectory from the actual one, i.e. $P=0$.

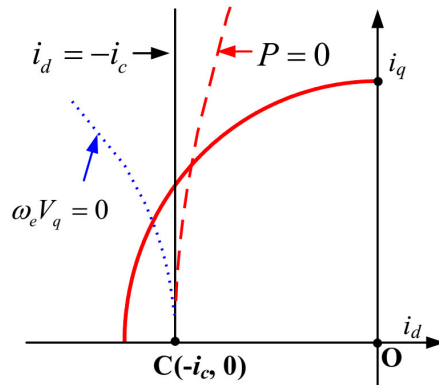


Fig. 3.3. The current trajectory under different conditions.

Therefore, in terms of the optimal current trajectory, the penalty function with consideration of the resistance is preferred. The penalty function in voltage form, i.e. P_v in

(3.5), can be constructed by the voltage command V_d and V_q [KWO07] [LIU12]. However, if the system operates in the over modulation region, there are voltage ripples in V_d and V_q that caused by the over modulation block. In addition, the voltage command is not a pure steady-state variable, and it contains the dynamic component that is caused by the output of the current PI controller. By way of example, in the linear modulation region, since $V_q=V_q^*$, as shown in Fig. 3.2, the output of the q-axis current PI controller, i.e. V_q^* , will be fed back to the q-axis current command through an MTPV PI controller. Therefore, the ripples in the q-axis current can be magnified by the current PI controller and MTPV PI controller. As the PI controller can not reject high-frequency ripples, the magnified q-axis current could lead to oscillation and even instability. In [LIU12], a precede first order low pass filter (LPF) is added to the MTPV controller to solve this problem, and the penalty function is revised to P_{vLpf} , i.e.

$$P_{vLpf} = P_v \frac{\omega_c}{s + \omega_c} \quad (3.6)$$

where ω_c is the cut off frequency of the LPF. However, the introduced LPF will limit the dynamics of the MTPV loop. Thereofre, in order to improve the dynamic performance, the penalty function without LPF is preferred.

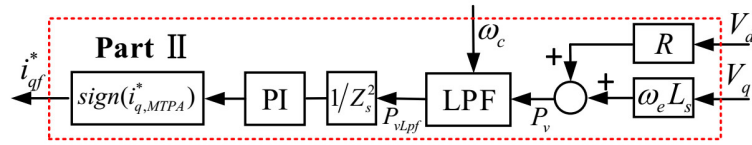
Alternatively, the penalty function can also be achieved in the current form, i.e. P_c in (3.5). Since the MTPV controller aims to plan the current command trajectory in the region III, i_d in P_c can be replaced by the d-axis current command i_d^* . In addition, as $P_c=0$ represent the MTPV curve, the term Z_s^2 in (3.5) can be canceled out. Therefore, the penalty function in the current form can be revised as

$$P_c = i_d^* + i_c \frac{(\omega_e L_s)^2}{Z_s^2} \quad (3.7)$$

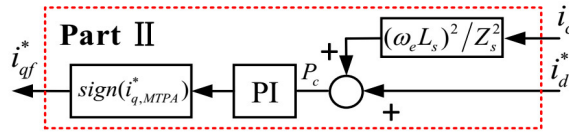
At the equilibrium point, the variation of the machine speed can be ignored due to the larger mechanical time constant when compared with the electrical time constant. Therefore, (3.7) implies that the variation of P_c mainly origins from the variation of i_d^* , i.e., $\Delta P_c = \Delta i_d^*$, where the prefix ‘ Δ ’ denote the corresponding small signals. From the small signal point of

view, in ΔP_c , only Δi_d^* is the information required for the MTPV control. According to (3.3), the d-axis current command output by DCVFC will be directly transformed to the q-axis current command by the MTPV controller. Therefore, no extra filter is required, and better dynamics can be expected than that by using the voltage command feedback MTPV controller.

For ease of comparison in the experimental section, the penalty function P_{vLpf} is divided by Z_s^2 to keep the same dimension as P_c in (3.7). The block diagram of the MTPV controller by using voltage command feedback and current command feedback are shown in Fig. 3.4(a) and (b), respectively.



(a) Voltage command feedback controller.



(b) Current command feedback controller.

Fig. 3.4. Block diagram of the MTPV controllers.

Since the optimal current trajectory for the MTPV requires accurate parameters, in practice, this could be done by online parameter estimation [LIU11] [LIU14]. As the parameter estimation is out the scope of this thesis, it will not be discussed further. It should be noted that accurate parameters are only required to improve steady-state performance. Therefore, the parameters used for the estimating P_c can be updated much slower than the dynamics of the MTPV loop. It means that the MTPV control and parameter estimation will not interfere with each other if the penalty term P_c is employed. In other words, the improvement of the dynamic performance and the steady-state performance can be done separately.

Therefore, P_c is finally used as the penalty function for the MTPV control owing to its better dynamic performance.

3.3.2 MTPV Controller Design

As with chapter 2, the flux-weakening controller can be designed based on the linearized model. For the machine with MTPV region, according to the small signal behaviours of the current, the operation mode in the flux-weakening region can be distinguished by mode A, mode B, and mode C, as shown in Fig. 3.5. In mode A, the machine operates on the current limit circle; in mode B; the machine operates along the constant torque curve; in mode C, the machine operates on the MTPV curve.

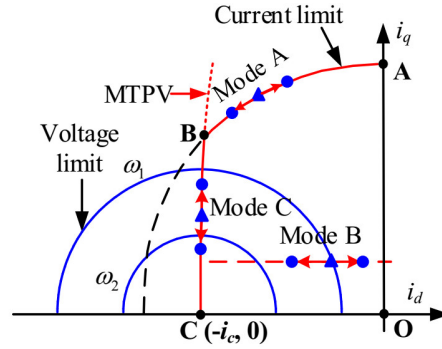


Fig. 3.5. The operation modes with considering MTPV control.

In region II, the MTPV controller is not activated, only the DCVFC is required. In region III, since the DCVFC and MTPV controller are both involved in control, DCVFC is still an important part for the MTPV control. As the voltage loop with DCVFC has been analysed in chapter 2, for convenience, according to (2.15), the close-loop transfer function from $\Delta |V_{sr}^*|^2$ to $\Delta |V_s^*|^2$ is directly given here as

$$\Phi_I(s) = \frac{\Delta |V_s^*|^2}{\Delta |V_{sr}^*|^2} = \frac{\omega_{cc} \lambda_I (bs + a)}{s^2 + \omega_{cc} (1 + b\lambda_I) s + \omega_{cc} \lambda_I a} \quad (3.8)$$

The selection of λ_I for the machine with MTPV region can follow the same approach as the chapter 2. The details of the selection of λ_I for the machine with MTPV region can be

referred to Appendix B. When the machine operates in the region III, the operation mode B that activated by the DCVFC cooperates with the mode C that activated by the MTPV controller. For the DCVFC, the voltage loop can be analysed in mode B. Since in mode B, $k=0$, the coefficient a and b can be derived as

$$\begin{cases} a|_{modeB} = 2(\omega_e^0 V_q^0 L_s + R V_d^0) \\ b|_{modeB} = 2V_d^0 L_d \end{cases} \quad (3.9)$$

At the equilibrium point, it can be seen that $a|_{modeB}=2P_v$. Therefore, $a|_{modeB}=0$ also defines the MTPV curve.

In the region III, since $a|_{modeB}=0$, it means that the voltage loop with only a DCVFC cannot maintain stable in this region. Therefore, it is necessary to investigate the MTPV loop as the MTPV controller will be activated in region III. The equivalent linearized model of MTPV loop can be seen in Fig. 3.6. In Fig. 3.6, $C_{qf}(s)$ and $G_{qf}(s)$ are the transfer functions of the PI controller and the control plant of the MTPV loop, respectively; δ is the assumed reference of MTPV loop, which is an infinitesimal value.

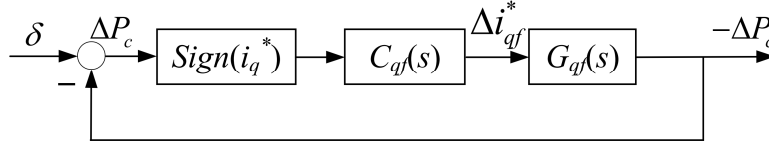


Fig. 3.6. Block diagram of the linearized model of MTPV Loop.

$C_{qf}(s)$ and $G_{qf}(s)$ can be obtained as

$$C_{qf}(s) = \frac{k_{pqf}s + k_{iqf}}{s} \quad (3.10)$$

$$G_{qf}(s) = -\frac{\Delta P_c}{\Delta i_q^*} \quad (3.11)$$

According to (3.7), $\Delta P_c = \Delta i_d^*$, $G_{qf}(s)$ can be rewritten as

$$G_{qf}(s) = -\frac{\Delta i_d^*}{\Delta i_q^*} \quad (3.12)$$

Since Δi_d^* origins from DCVFC, $G_{qf}(s)$ can be reconstructed as

$$G_{gf}(s) = -\frac{\Delta i_d^*}{\Delta |V_s^*|^2} \frac{\Delta |V_s^*|^2}{\Delta i_q^*} \quad (3.13)$$

In region III, the transfer function from $\Delta |V_s^*|^2$ to Δi_d^* can be obtained according to the linearized model of the voltage loop with DCVFC, as shown in Fig.2.3. When $a|_{modeB} = 0$, it can be derived as

$$\frac{\Delta i_d^*}{\Delta |V_s^*|^2} = -\frac{\lambda_I}{s} \frac{(s + \omega_{cc})}{(s + \omega_{cc}(1 + b|_{modeB} \lambda_I))} \quad (3.14)$$

According to Appendix B, in region III, $b|_{modeB} \lambda \approx 0$ and $\frac{\Delta i_d^*}{\Delta |V_s^*|^2} \approx -\frac{\lambda_I}{s}$. In addition,

$\frac{\Delta |V_s^*|^2}{\Delta i_q^*}$ can be derived as

$$\frac{\Delta |V_s^*|^2}{\Delta i_q^*} = 2V_d^0 \frac{\Delta V_d^*}{\Delta i_q^*} + 2V_q^0 \frac{\Delta V_q^*}{\Delta i_q^*} \quad (3.15)$$

Moreover, since V_q^0 is close to zero, and $V_d^0 \approx -V_m \text{sign}(\omega_e^0 i_q^*)$ due to that $i_d \approx -i_c$ in region

III, $\frac{\Delta |V_s^*|^2}{\Delta i_q^*}$ can be approximated as

$$\begin{aligned} \frac{\Delta |V_s^*|^2}{\Delta i_q^*} &\approx -2V_m \frac{\Delta V_d^*}{\Delta i_q^*} \text{sign}(\omega_e^0 i_q^*) \\ &\approx -2V_m \frac{\Delta V_d}{\Delta i_q} \frac{\Delta i_q}{\Delta i_q^*} \text{sign}(\omega_e^0 i_q^*) = -2 \text{sign}(i_q^*) V_m \left| \omega_e^0 \right| L_s T_i(s) \end{aligned} \quad (3.16)$$

In consequence, the control plant of the MTPV loop can be derived as

$$G_{gf} = K_{gf} \frac{1}{s} T_i(s) \text{sign}(i_q^*) \quad (3.17)$$

where $K_{qf} = 2V_m |\omega_e^0| L_s \lambda_f$.

(3.17) explains that a pure integral controller is not applicable for the MTPV controller, as the system could oscillate due to the resultant origin pole of the close-loop transfer function. Therefore, a PI controller can be adopted, which can ensure the stability in region III. The open-loop transfer function of the MTPV loop with PI controller, i.e. $G_{oqf}(s)$ can be derived as

$$G_{oqf} = K_{qf} \frac{k_{pqf}s + k_{iqf}}{s} \frac{1}{s} T_i(s) \quad (3.18)$$

It is reasonable to make a further simplification of (3.18) by approximating $T_i(s)$ as a unity gain if the MTPV loop is tuned with the bandwidth much lower than the current bandwidth. Therefore, the close-loop function of the MTPV loop can be obtained as

$$\frac{-P_c}{\delta} = \frac{(k_{pqf}K_{qf}s + K_{qf}k_{iqf})}{s^2 + k_{pqf}K_{qf}s + K_{qf}k_{iqf}} \quad (3.19)$$

As a second-order system [FRA94], the control parameters can be tuned as

$$k_{pqf} = \frac{2\xi\omega_{Nqf}}{K_{qf}} = \frac{2\omega_{Nqf}}{K_{qf}}, k_{iqf} = \frac{\omega_{Nqf}^2}{K_{qf}} \quad (3.20)$$

where ω_{Nqf} is the selected natural frequency, ξ is selected damping factor which is set at 1 in the experiments.

3.3.3 Over Modulation Improvement

Fig. 3.7 shows the voltage synthesis in the linear and over modulation region. It can be seen in Fig. 3.7(a) that the voltage command vector V_s^* in the linear modulation region can be fully realized. In the over modulation region, as shown in Fig. 3.7(b), only the voltage command vector inside the hexagon boundary can be fully realized. Fig. 3.8 shows the spectral distribution of the α -axis voltage normalized by V_{dc} under two conditions, i.e. $M=0.9$ and $M=1.1$. The fundamental component in Fig. 3.8 can be seen as the index of the DC link voltage utilization. It can be seen that the system in the over modulation region has better

voltage utilization than the linear modulation region. However, the voltage margin decreases and larger harmonics appear. Therefore, the voltage saturation problem is more serious in the over modulation region, which degrades the current dynamics and could lead to instability [LER08]. In fact, the flux-weakening controller aims to deter the voltage saturation problem by generating the proper d-axis current command (by DCVFC) and q-axis current command (by MTPV controller). Therefore, the current dynamics is very essential for the stability in the flux-weakening region.

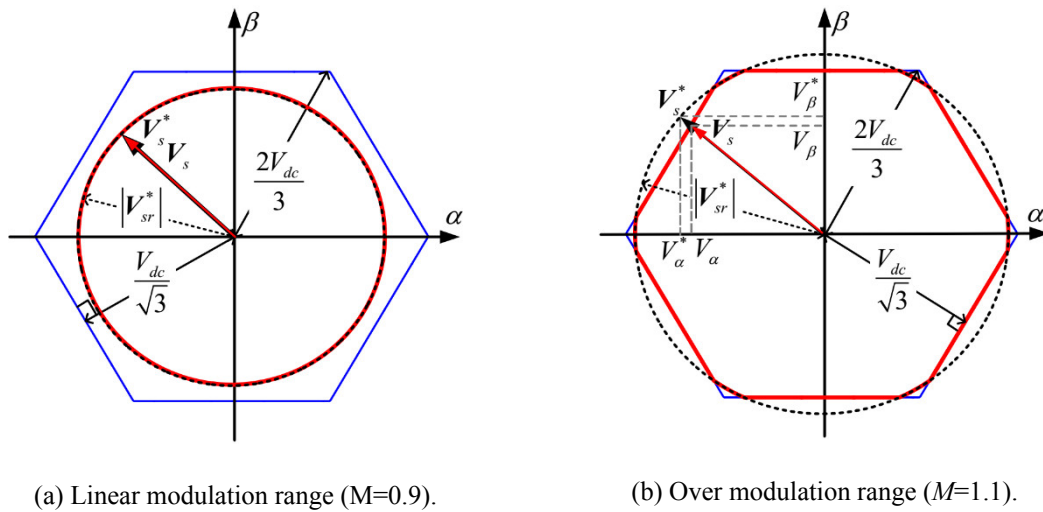


Fig. 3.7. Voltage synthesis with MPEOM.

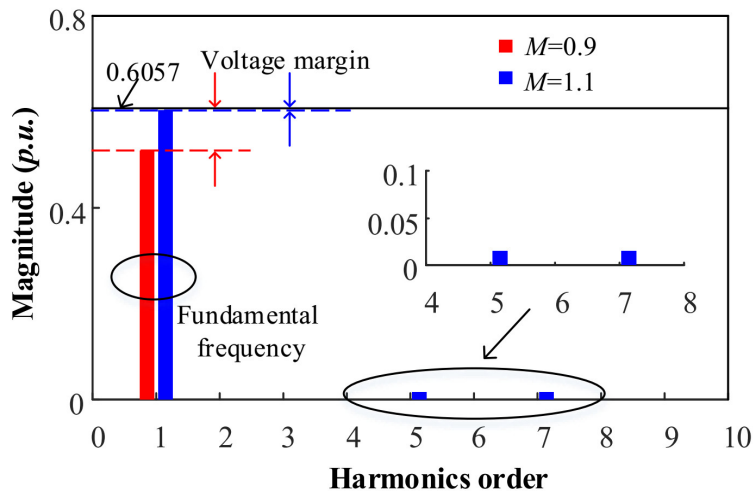


Fig. 3.8. Voltage spectra with SVPWM when $M=0.9$ and $M=1.1$.

Chapter 2 has proposed a current reference modifier (CRM) to improve the current dynamics in the over-modulation region, the effectiveness of which has been verified for the

machine without region III, i.e. without MTPV control. With the CRM in (2.43), the d-axis voltage command can be expressed as

$$\begin{aligned} V_d^* &= \frac{k_{pd}s + k_{id}}{s} (i_{da}^* + i_d^* - i_d) \\ &= \frac{k_{pd}s + k_{id}}{s} (i_d^* - i_d) + V_{derr}^* \end{aligned} \quad (3.21)$$

where V_{derr}^* can be seen as the modified term of d-axis voltage command after the CRM is employed, which is

$$V_{derr}^* = \frac{k_{pd}s + k_{id}}{s} i_{da}^* = \frac{k_{pd}s + k_{id}}{s} \frac{V_q^* - V_q}{k_{pd}} \quad (3.22)$$

It can be assumed that the proportional part in (3.22) is dominant in the transient state, as $k_{pd} \gg k_{id}T_s$, where T_s is the control period of the current loop. Therefore, V_{derr}^* can be approximated as

$$V_{derr}^* \approx V_q^* - V_q = V_{qerr} \quad (3.23)$$

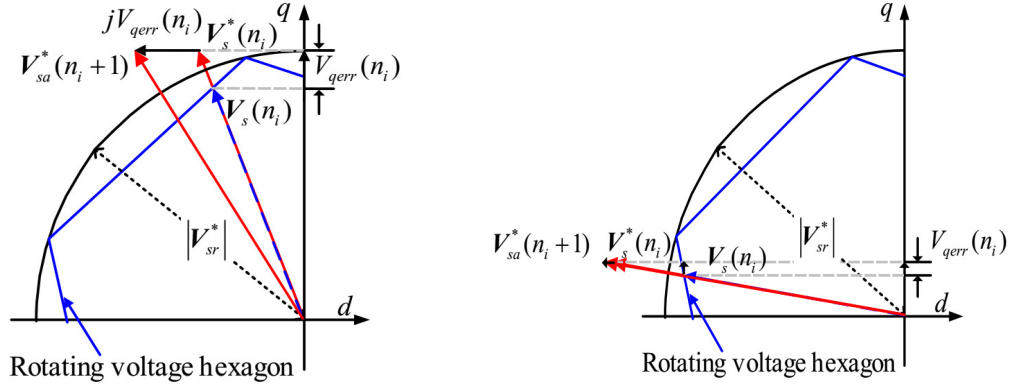
The adjusted voltage command vector considering the effect of CRM can be expressed in the discrete form as

$$\mathbf{V}_{sa}^*(n_i + 1) = \mathbf{V}_s^*(n_i) + jV_{qerr}(n_i) \quad (3.24)$$

where ' n_i ' in the bracket indicates the step number of the control cycle; $\mathbf{V}_s^*(n_i)$ is the voltage command in the n_i step; $\mathbf{V}_{sa}^*(n_i + 1)$ is the adjusted voltage vector command with CRM in the $(n_i + 1)$ step.

Fig. 3.9 illustrates the effect of the CRM on the voltage command vector in dq-axis voltage plane at different q-axis voltage region. It can be seen from Fig. 3.9(a) and Fig. 3.9(b) that $V_{qerr}(n_i)$ is quite big in the high q-axis voltage region and becomes smaller in the low q-axis voltage region. Therefore, the CRM shows its effectiveness in the high q-axis voltage region. However, it could lose its effect when the q-axis voltage approaches to zero. Since

when the system operates in region III, the q-axis voltage is close to zero, the system performance in over modulation region cannot be improved with CRM.



(a) High q-axis voltage region.

(b) Low q-axis voltage region.

Fig. 3.9. Effect of the CRM to voltage command vector in dq-axis voltage plane.

A voltage vector modifier (VVM) is firstly adopted in [YON14] to improve the current dynamics in the over modulation region for the machine without region III. As compared with CRM, it will be shown that the VVM is also suitable for the over modulation operation in region III. The working principle of the VVM is shown in Fig. 3.10. In Fig. 3.10, the voltage command vector V_s^* output from the current regulator is limited by the hexagon boundary and will be truncated to the voltage vector V_{stmp} , which is regarded as the temporal voltage vector. Then, the modified voltage vector V_{sm}^* is obtained by adding a rotated 90° temporal voltage error vector to the original voltage vector. The modified voltage vector V_{sm}^* is obtained as

$$V_{sm}^* = V_s^* + jV_{sme}^* \text{sign}(\omega_e) \quad (3.25)$$

where $V_{sme}^* = V_s^* - V_{stmp}$ is the temporal voltage vector. Unlike the CRM, V_{sme}^* is a voltage vector error, but not just q-axis voltage error. Therefore, the VVM also shows its effectiveness in low q-axis voltage region, as shown in Fig. 3.10(b).

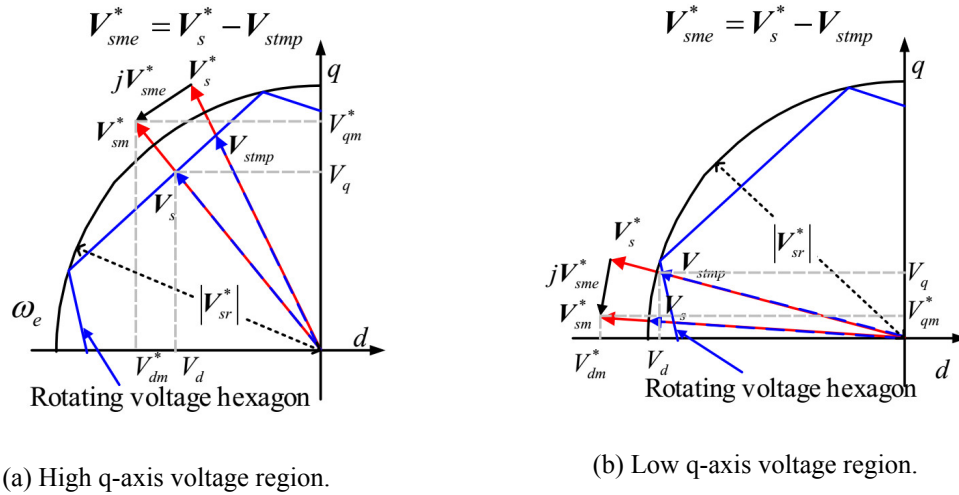


Fig. 3.10. Voltage vector modifier (VVM).

Fig. 3.11 shows the block diagram of the VVM which is implemented in the scalar form. With the VVM, the voltage command from the current regulator, i.e. V_d^* and V_q^* are modified to V_{dm}^* and V_{qm}^* , which will be processed again by modulation block, i.e. SVPWM, and then fed to the inverter.

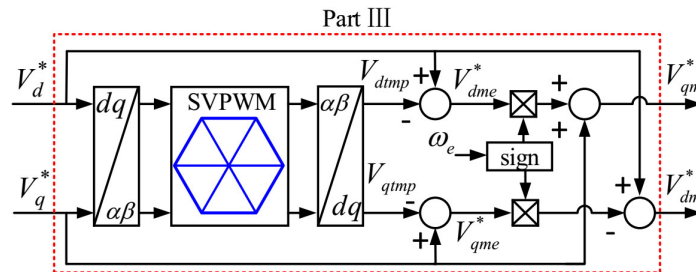


Fig. 3.11. The block diagram of VVM.

The schematic of feedback type flux-weakening control with VVM can be seen in Fig. 3.12. Since the temporal voltage error vector V_{sme}^* only exists in the over modulation region, the VVM will not influence the steady-state performance in the linear modulation region.

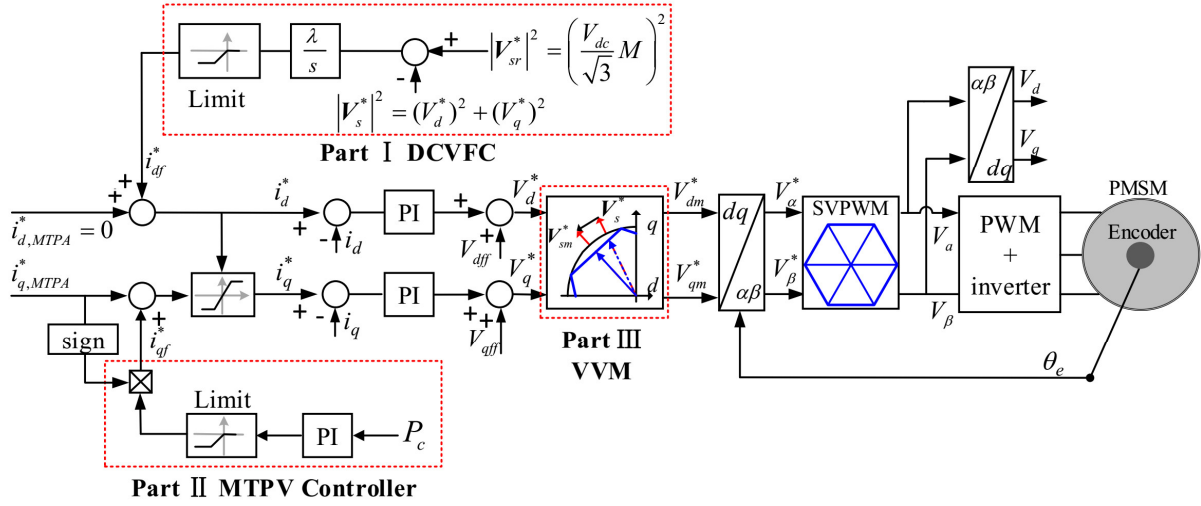


Fig. 3.12. Schematic of feedback type flux-weakening control system with VVM.

3.4 Experimental Verification

The experiments based on the dSPACE platform are implemented on a non-salient-pole PMSM. The power switches of the inverter are IRFH7440 MOSFET. The drain-to-source resistance of the MOSFET is less than $2.4\text{m}\Omega$, which can be ignored when compared with the machine resistance. The PWM switching frequency is 10 kHz. In the experiments, two test rigs are utilized, the load torque of which are provided by two wound field type DC-machines. The test rig-I has a big inertia ($0.012\text{kg}\cdot\text{m}^2$) and is coupled with a torque transducer which is used to measure the steady-state performance. The test rig-II has a smaller inertial ($0.001\text{kg}\cdot\text{m}^2$) which is used to verify the dynamic performance. The machine and driving parameters are listed in Table 3.1. It should be noted that the MTPV region of the machine is achieved by setting the current limit at 7.35 A, under which condition $i_{cn}=0.8$.

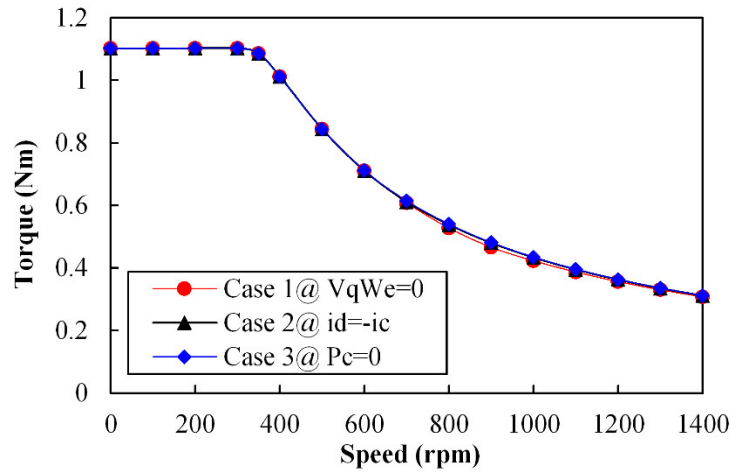
Table 3.1 Machine and drive parameters

Parameters	Value
Phase resistance (R_s)	0.25 Ω
Synchronous inductance (L_s)	1.7 mH
PM-flux linkage(ψ_m)	10 mWb
Number of pole pairs	10
DC link voltage (V_{dc})	14 V
Current limit (I_m) when $i_{cn}=1$	7.35A
Current bandwidth (ω_{cc})	1200 rad/s
Cable resistance	0.1 Ω

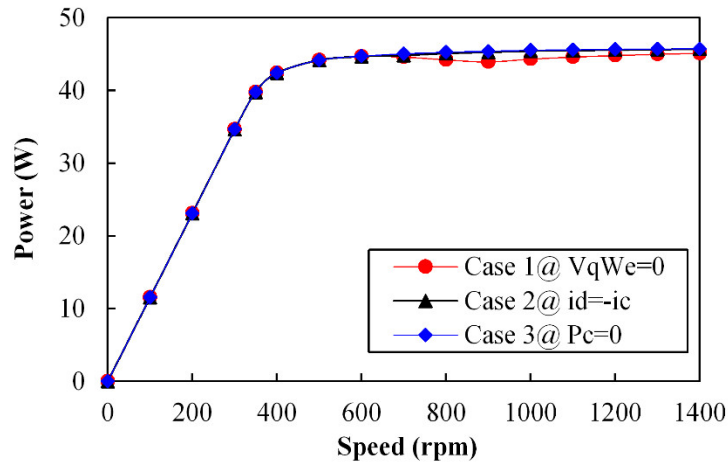
In the following experiments, the steady-state performance is firstly measured on the test rig I in order to illustrate the advantages when the resistance is considered in the MTPV region. Afterward, the dynamic performance by using the current command feedback MTPV controller is demonstrated and compared with the one by using the voltage command feedback MTPV controller. Furthermore, the system stabilities in the over modulation region with and without VVM are compared.

3.4.1 Steady-State Performance

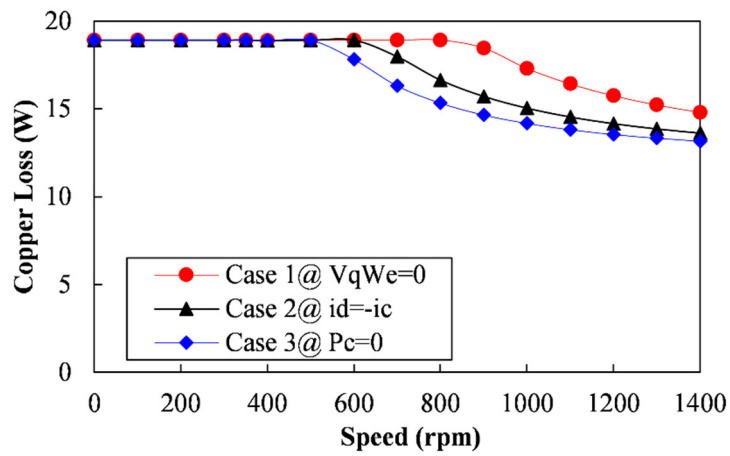
Fig. 3.13 shows the steady-state performance when $M=0.9$ under different MTPV penalty functions, i.e. $V_q\omega_e=0$ (case 1) $i_d=-i_c$ (case 2) and $P_c=0$ (case 3). Case 1 and case 2 represent the conditions without considering resistance when the penalty function is realized in voltage and current forms, respectively. The case 3 is the condition when the resistance is considered. The resistance used in P_c is the total resistance which is 0.35 Ω .



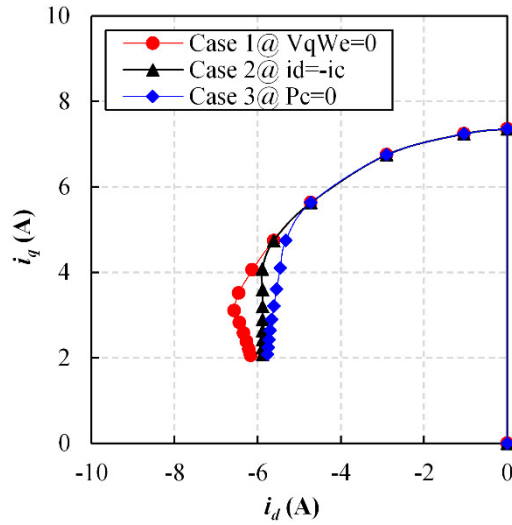
(a) Torque-speed curve.



(b) Power-speed curve.



(c) Copper loss speed curve



(d) Current trajectories.

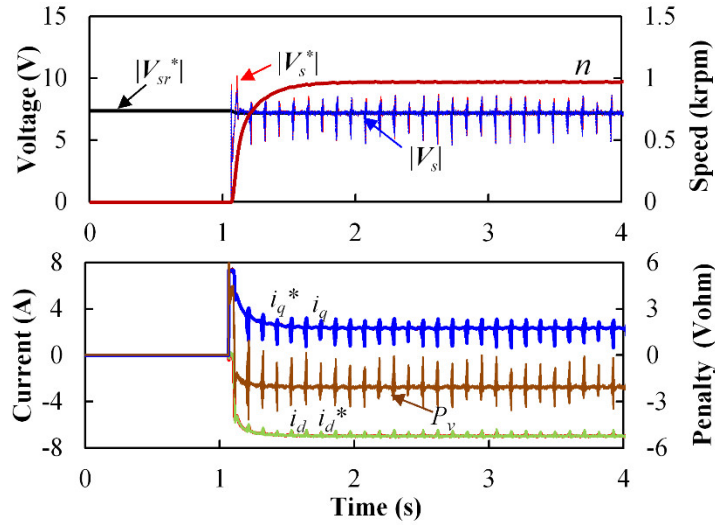
Fig. 3.13. Steady-state performance under different cases.

Fig. 3.13(a) and Fig. 3.13(b) show the torque-speed curve and power-speed curve, respectively, under the three cases. Although the differences between the three cases about torque and output power are minor, it can still be observed that the case 3 shows slightly higher torque and output power than other two cases when the machine speed is approximately higher than 650 rpm, while the case 1 shows the least torque and output power. However, it is apparent in Fig. 3.13(c) that the case 3 shows the least copper loss when comparing to the case 1 and case 2. The copper loss at 900rpm in case 3 can be reduced by about 25% than that in case 1. As observed in Fig. 3.13(d), the condition with consideration of the resistance (case 3) shows the minimum current magnitude especially around the region when the system transfers from mode A to mode C, which results in the least copper loss. In addition, it can be seen that the case 3 enters into the MTPV region earliest. If the MTPV curve can be tracked well at the dynamic stage, the dynamic performance can also be improved.

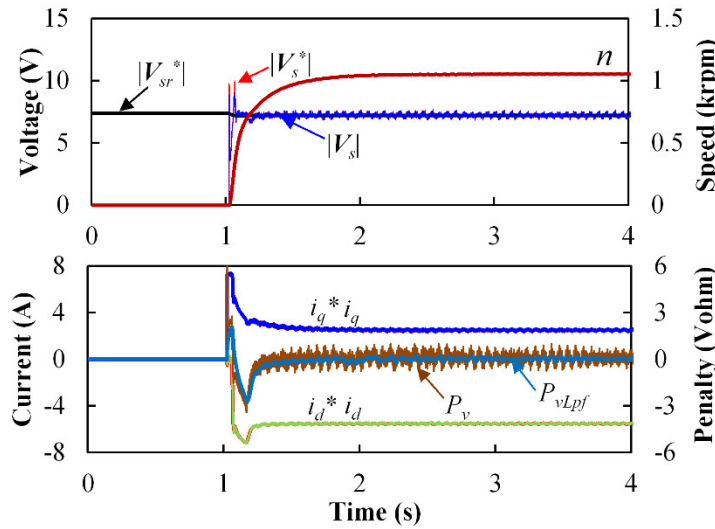
3.4.2 Dynamic Performance with Different MTPV Controllers

The dynamic performance with voltage and current command feedback MTPV controllers are compared by applying a step current command ($i_{q,MTPA}^*=7.35\text{A}$) when $M=0.9$. Fig. 3.14 shows the dynamic performance by using the voltage command feedback MTPV

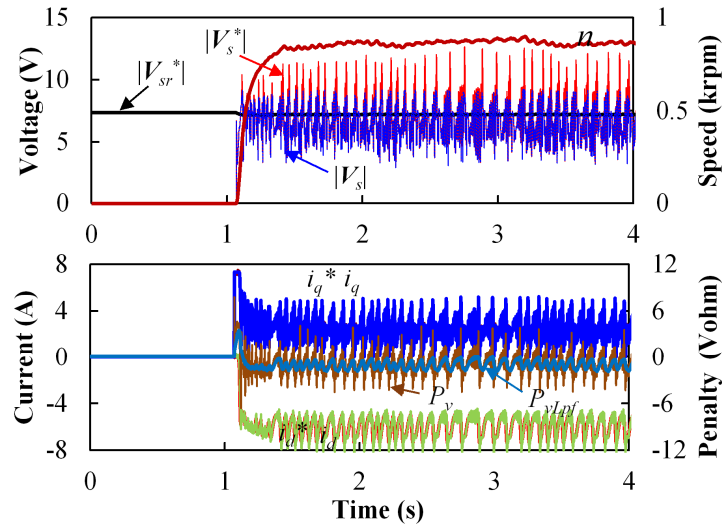
controller under different control parameters. In Fig. 3.14(a), the system oscillates when there is no low pass filter applied. By properly tuning the parameters of the PI controller and low pass filter, i.e. $\omega_{Nqf}=50$ rad/s and $\omega_c=600$ rad/s, the system can operate stably, as shown in Fig. 3.14(b). However, the current and P_{vLpf} waveforms shows an apparent overshoot. By increasing ω_{Nqf} to 100, as shown in Fig. 3.14(c), the system oscillates again.



(a) Without low pass filter and $\omega_{Nqf}=50$ rad/s.



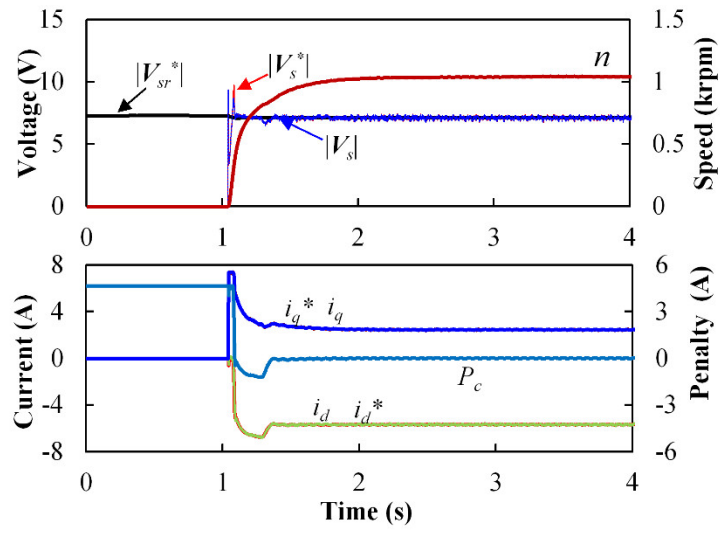
(b) With low pass filter $\omega_c=600$ rad/s and $\omega_{Nqf}=50$ rad/s.



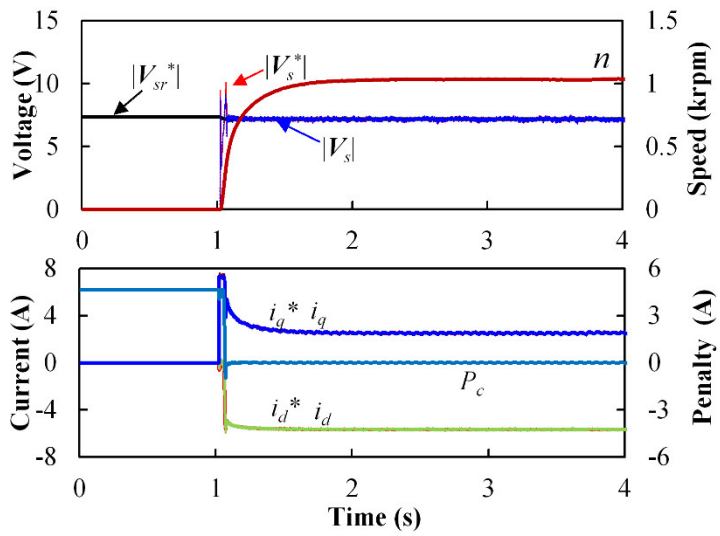
(c) With low pass filter $\omega_c=600$ rad/s and $\omega_{Nqf}=100$ rad/s.

Fig. 3.14. Dynamic performance with voltage command feedback MTPV controller.

Fig. 3.15 shows the dynamic performance by using the current command feedback MTPV controller under different parameters of the PI controller. It can be seen that the system can operate stably when ω_{Nqf} are 50 rad/s and 200 rad/s, as shown in Fig. 3.15(a) and Fig. 3.15(b), respectively. Fig. 3.16 illustrates the current trajectories when $\omega_{Nqf}=50$ rad/s and 200 rad/s. When $\omega_{Nqf}=50$, as shown in Fig. 3.16(a), although the current shows overshoot when approaching MTPV curve, this overshoot is much less when ω_{Nqf} is increased to 200 rad/s. As a result, better speed dynamics can be obtained, which can be seen in Fig. 3.17.



(a) $\omega_{Nqf}=50$ rad/s.



(b) $\omega_{Nqf}=200$ rad/s.

Fig. 3.15. Dynamic performance with current command feedback MTPV controller.

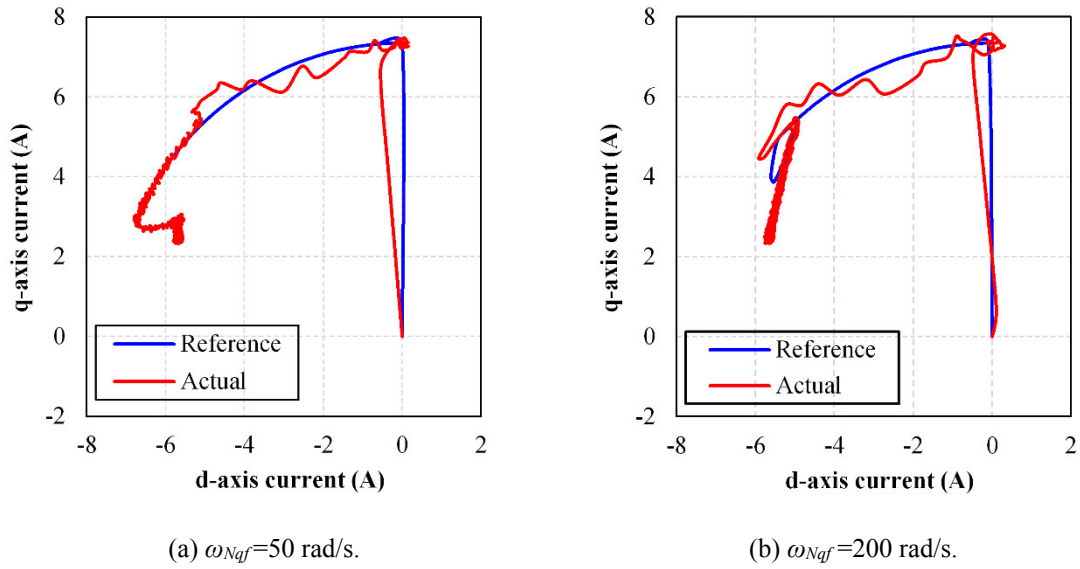


Fig. 3.16. Dynamic current trajectories with current command feedback MTPV controller.

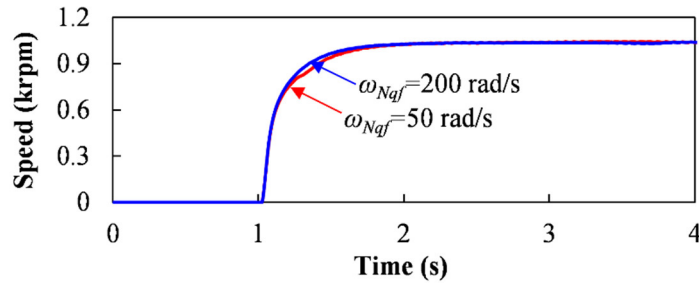


Fig. 3.17. Speed dynamics of current command feedback MTPV controller under different control parameters.

From the foregoing analysis, the pure integral MTPV controller can hardly maintain the stability in the MTPV region. In order to demonstrate this phenomenon, by using the current command feedback controller, Fig. 3.18 shows one of the oscillation cases when the integral gain is tuned by disabling the proportional controller while $\omega_{Nqf}=50$ rad/s.

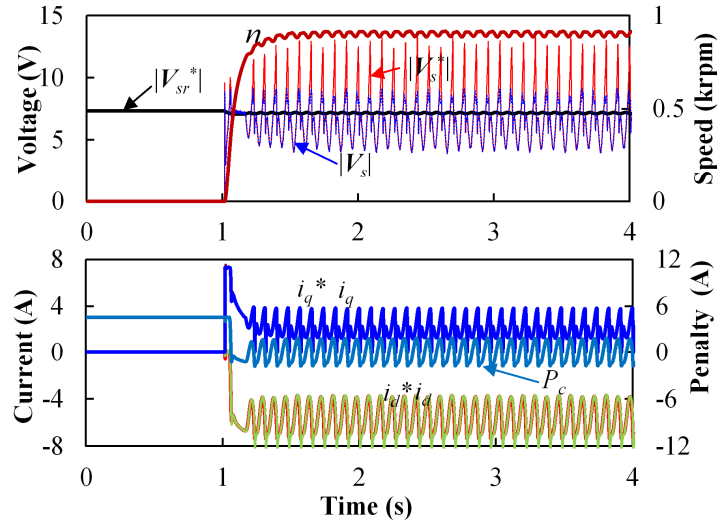
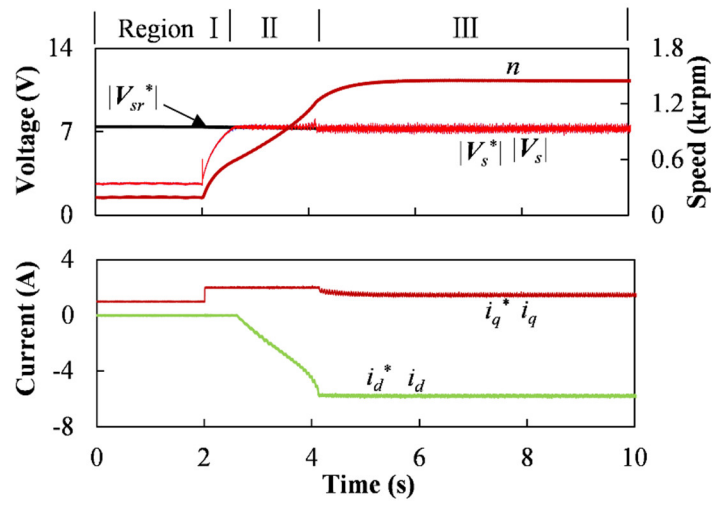


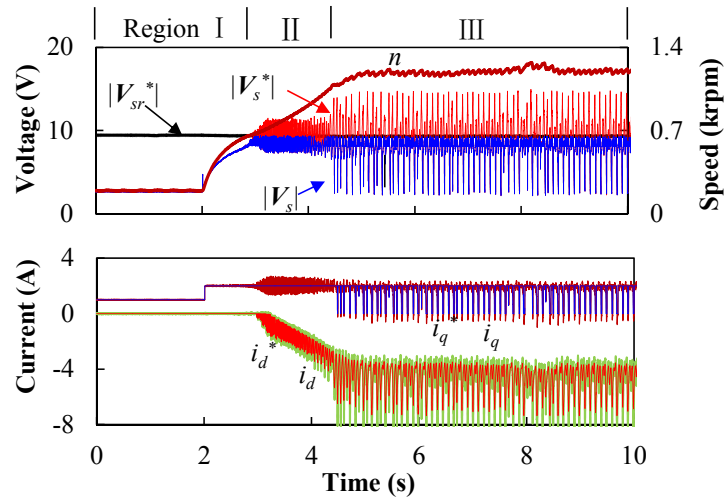
Fig. 3.18. Dynamic performance with current command feedback MTPV controller (integral controller).

3.4.3 Stability in Over Modulation Region

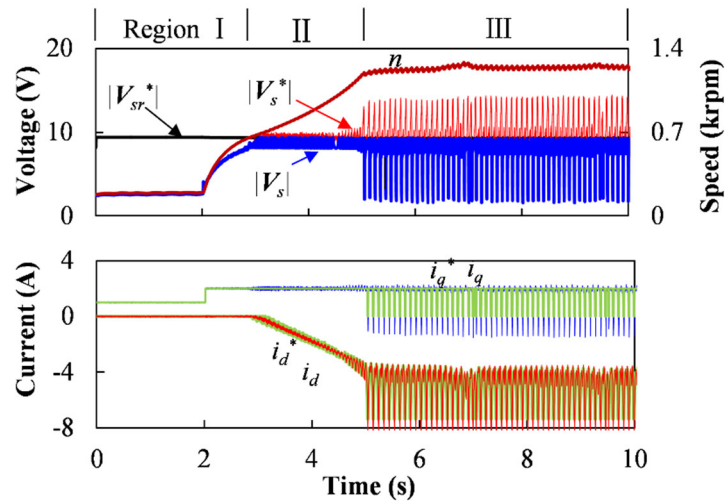
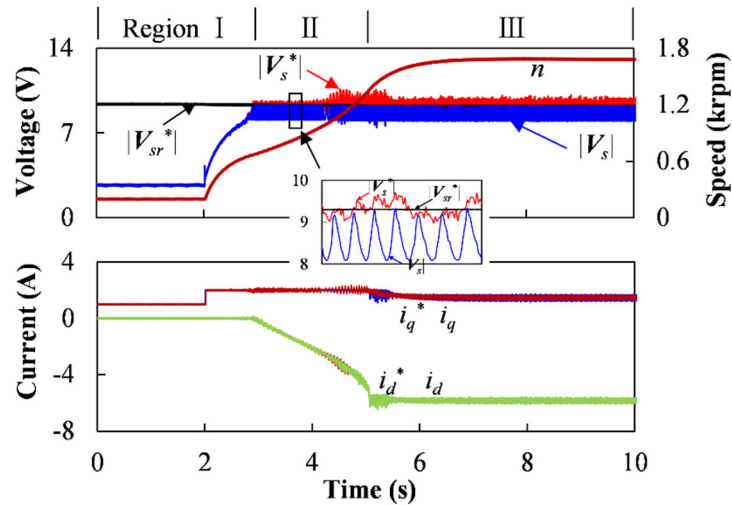
By using the current command MTPV controller, the system stability are compared under four conditions, i.e. with only DCVFC ($M=0.9$), with only DCVFC ($M=1.15$), with added CRM ($M=1.15$), and with added VVM ($M=1.15$). As shown in Fig. 3.19, by changing q-axis current command from 1A to 2A at 2 seconds, the machine accelerates from region I to region II, and then region III. Fig. 3.19(a) shows the system performance in the linear modulation region ($M=0.9$) with only a DCVFC, it can be seen that the system performs well from region I to region III. Fig. 3.19(b) shows the system performance in the over modulation region ($M=1.15$) with only a DCVFC, it can be seen that both current and voltage oscillate in the flux-weakening regions (region II and region III). However, as shown in Fig. 3.19(c), with added CRM and $M=1.15$, the system performs well in region II, but it oscillates when it operates in region III. With the VVM and $M=1.15$, as shown in Fig. 3.19(d), the system stability in over modulation region is remarkably improved under different flux-weakening regions. Consequently, the machine can achieve higher speed at steady-state when compared with that in the linear modulation condition. It should be noted that the ripples of $|V_s|$ in Fig. 3.19(d) is due to the hexagon boundary limit of the over modulation block.



(a) With only conventional DCVFC, $M=0.9$.



(b) With only conventional DCVFC, $M=1.15$.

(c) With added CRM and VRM, $M=1.15$.(d) With added VVM, $M=1.15$.Fig. 3.19. System performance in the over modulation region ($M=1.15$).

3.5 Conclusion

In this chapter, a feedback type flux-weakening control on a non-salient-pole PMSM including MTPV region has been analysed and optimized. The resistance influence has been considered in order to improve the steady-state performance in the flux-weakening region, especially for a small power motor. Two kinds of MTPV feedback controllers, i.e. voltage

command feedback controller and current command feedback controller, have been compared. The design guidance of a PI MTPV controller has been given by considering the stability issue in the MTPV region. A VVM has been utilized to improve the stability in the over modulation and different flux-weakening regions. The analyses and the experimental results have verified that:

- 1) The steady-state performance in the MTPV region can be improved by considering the resistance especially for the small power motor;
- 2) The current command feedback MTPV controller can achieve better dynamics than the voltage command feedback controller;
- 3) A PI MTPV controller is preferred as the pure integral MTPV controller can hardly maintain the stability in the MTPV region;
- 4) The stability in the over modulation region and flux-weakening regions (region II and region III) can be improved with VVM.

CHAPTER 4 COMPARATIVE STUDY OF TWO FEEDBACK METHODS FOR FLUX- WEAKNING CONTROL OF PMSM

In this chapter, two different feedback type flux-weakening methods, i.e. dq-axis currents based feedback flux-weakening control (DQFFC), current amplitude and angle based feedback flux-weakening control (CAAFFC), are comparatively studied in terms of the system stability, based on a non-salient-pole PMSM. Meanwhile, the design guidance of the MTPV controller in CAAFFC is given due to its difference with that in DQFFC. The analyses indicate that two flux-weakening methods could oscillate and even become unstable in different flux-weakening regions, which is the intrinsic stability characteristics.

4.1 Introduction

Conventionally, two variants of the voltage feedback controller, i.e. d-axis current based voltage magnitude feedback controller (DCVFC) [KIM97] [BIA01] [HAR01] [YON14] [BOZ17] and current angle based voltage magnitude feedback controller (CAVFC) [WAI01] [DEN19] [QIA16] [BOL14], are normally considered to be equivalent to achieve flux-weakening operation. However, the differences between DCVFC and CAVFC from the stability point of view are seldom investigated, especially when the maximum torque per voltage (MTPV) control is considered. By further considering the MTPV control, in this chapter, two feedback-type flux-weakening methods, namely, dq-axis currents based feedback flux-weakening control (DQFFC), current amplitude and angle based feedback flux-weakening control (CAAFFC), are introduced and comparatively studied in terms of the system stability in the speed control mode. In chapter 3, DQFFC has been optimized with a current feedback MTPV controller and a voltage vector modifier (VVM), which aims to improve the dynamic performance and stability in over modulation region. In this chapter, the current feedback MTPV controller and VVM will be used as the basis in both DQFFC and CAAFFC. The linearized models of the voltage loop in DQFFC and CAAFFC are generalized first, based on which the stability of the two methods are compared. Furthermore,

the MTPV controller in CAAFFC is designed in order to facilitate the practical parameterization, which also shows the difference with that in DQFFC. Finally, the experiments are implemented to verify the analyses.

4.2 Two Flux-Weakening Control Methods

Fig. 4.1 shows the general schematic of the current vector control (CVC) system with flux-weakening control. The two flux-weakening methods are included in the flux-weakening block shown Fig. 4.1, which aims to generate the proper d- and q-axis current commands. The voltage vector modifier (VVM) is adopted to improve the current dynamics in the over modulation region.

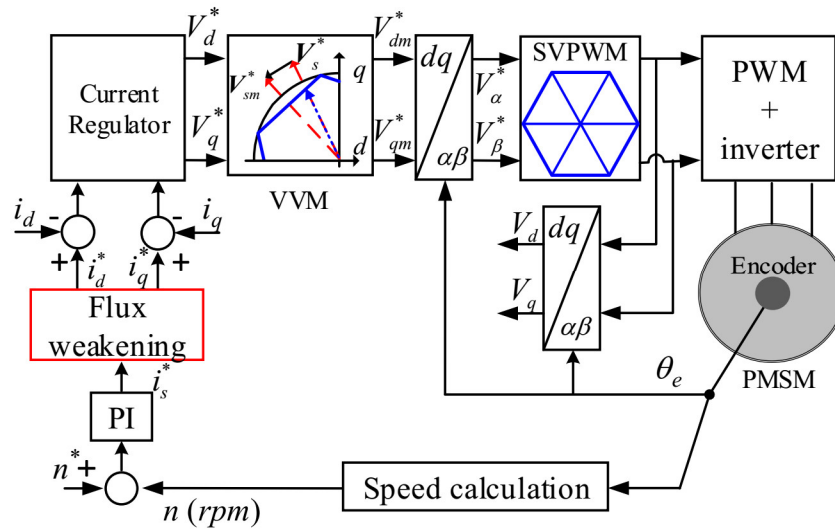


Fig. 4.1 General schematic of current vector control(CVC) system with flux weakening.

4.2.1 Dq-axis Current Based Feedback Flux-Weakening Control (DQFFC)

For the DQFFC, as shown in Fig. 4.2, the initial d- and q-axis current commands, i.e. $i_{d,MTPA}^*$ and $i_{q,MTPA}^*$, are obtained by considering MTPA in region I, i.e. $i_{d,MTPV}^*=0$, $i_{q,MTPA}^*=i_s^*$, where i_s^* is the output of the speed PI controller.

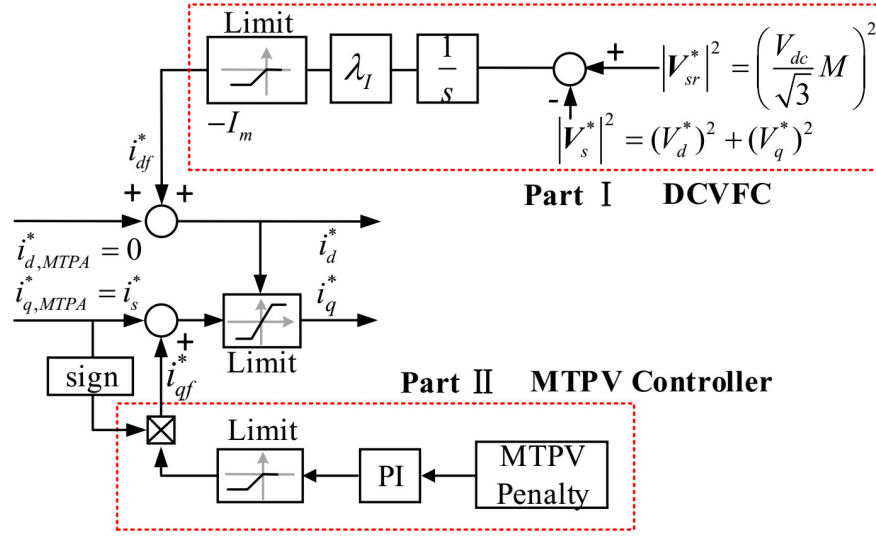


Fig. 4.2 Block diagram of DQFFC.

In the flux-weakening region, the initial d- and q-axis current commands are further modified by DCVFC and MTPV controller, respectively. Since DQFFC has been addressed in chapter 3, for convenience, the expressions of DCVFC in Part I and MTPV controller in Part II are directly given as follows.

DCVFC in DQFFC:

$$\frac{di_d^*}{dt} = \lambda_l (|V_{sr}^*|^2 - |V_s^*|^2) \quad (4.1)$$

MTPV controller in DQFFC:

$$i_{qf}^* = \text{sign}(i_{q,MTPA}^*) \min \left\{ 0, \frac{k_{pqf}s + k_{iqf}}{s} P_c \right\} \quad (4.2)$$

Therefore, the q-axis current command is finally obtained as

$$i_q^* = \text{sign}(i_{q,MTPA}^*) \min \left\{ 0, \frac{k_{pqf}s + k_{iqf}}{s} P_c \right\} \quad (4.3)$$

4.2.2 Current Amplitude and Angle Based Feedback Flux-Weakening Control (CAAFFC)

For the CAAFFC, as shown in Fig. 4.3, considering the MTPA in region I, the initial lead angle of the current vector with respect to q-axis is zero, the current amplitude i_s^* is obtained from the speed controller. In the flux-weakening region, the initial current lead angle and amplitude are modified by CAVFC and MTPV controller, respectively.

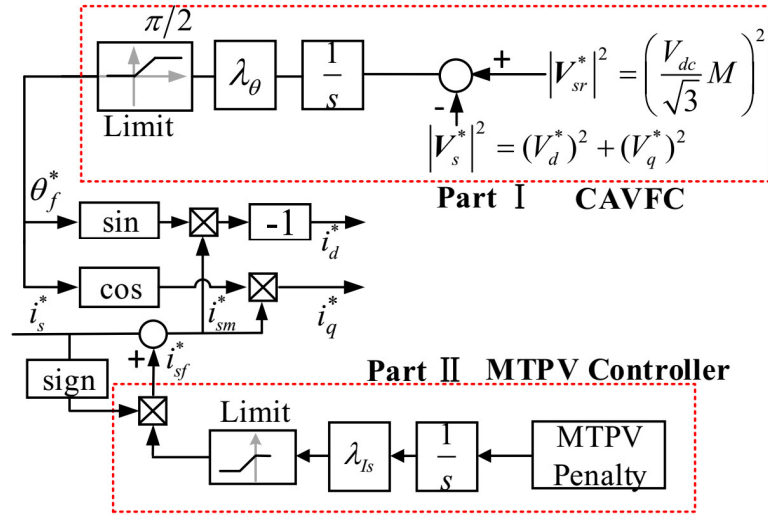


Fig. 4.3 Block diagram of CAAFFC.

According to the part I of Fig. 4.3, CAVFC can be expressed as

$$\frac{d\theta_f^*}{dt} = -\lambda_{\theta} (|V_{sr}^*|^2 - |V_s^*|^2) \quad (4.4)$$

where λ_{θ} is the integral gain of CAVFC; θ_f^* is the lead angle of the current vector with respect to q-axis.

As shown the part II in Fig. 4.3, the MTPV controller for the CAAFFC can be expressed as

$$i_{sf}^* = \text{sign}(i_s^*) \min \left\{ 0, \frac{\lambda_{Is}}{s} P_c \right\} \quad (4.5)$$

where λ_{Is} is the integral gain of the MTPV controller; i_{sf}^* is the output of the MTPV controller.

Therefore, the current amplitude can be finally obtained as

$$i_{sm}^* = \text{sign}(i_s^*) \min\{0, |i_s^* + i_{sf}^*|\} \quad (4.6)$$

where i_{sm}^* is the modified current amplitude.

It should be noted that the MTPV controller in DQFFC is a PI controller while the MTPV controller in CAAFFC is a pure integral controller. The difference between the two MTPV controllers will be further addressed in the following section.

4.3 Stability Analysis and Controller Design

For easy comparison, the operation modes in DQFFC and CAAFFC are illustrated in Fig. 4.4(a) and Fig. 4.4(b), respectively. When the method CAAFFC is considered, the mode A is defined in a more general way. In mode A, the machine is regulated along the current circle with a specific radius, but not just along the current limit circle. The definition of the mode B and mode C are consistent with that in chapter 3. In mode D, the machine is regulated along the normal direction of the current circle. Therefore, as shown in Fig. 4.4(a), for the DQFFC, the operation modes include mode A, mode B and mode C. As shown in Fig. 4.4(b), for CAAFFC, the operation modes include only mode A and mode D.

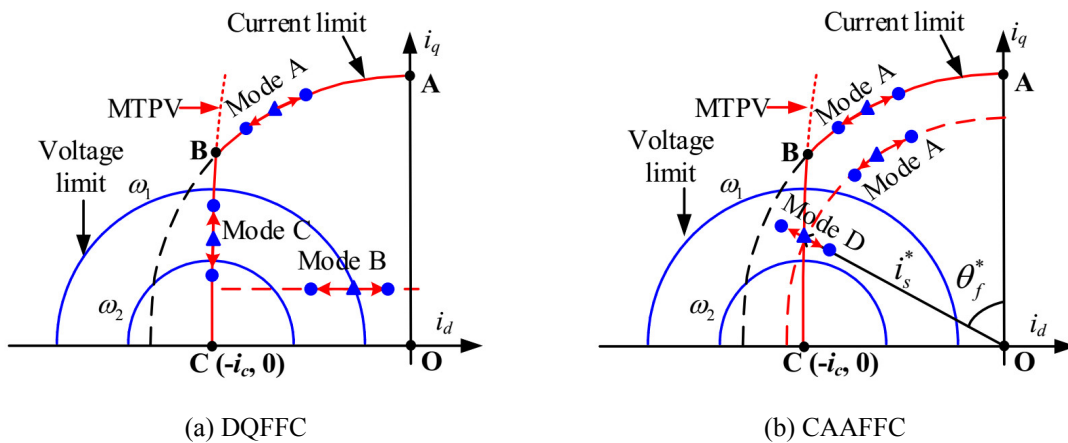


Fig. 4.4. Operation modes in the flux-weakening region.

In region II, no MTPV controller is required, only the voltage feedback controllers, i.e. DCVFC and CAVFC are activated. Therefore, the voltage loop can be analysed firstly under

mode A and mode B without considering MTPV controller. Subsequently, the MTPV loops of the two methods are analysed in region III.

4.3.1 Generalized Linearized Model of Voltage Loop

In order to generalize the analysis of the voltage loop with DCVFC and CAVFC, the expression of CAVFC can be transformed into the equivalent form as DCVFC by using the following relationship

$$\frac{d\theta_f^*}{dt} = -\frac{1}{|i_q^0|} \frac{di_d^*}{dt} \quad (4.7)$$

By substituting (4.7) into (4.4), the expression of CAVFC can be derived as

$$\frac{di_d^*}{dt} = \lambda_\theta |i_q^0| (|V_{sr}^*|^2 - |V_s^*|^2) \quad (4.8)$$

Therefore, the equivalent block diagram of the linearized voltage loop with CAVFC has the same structure as the DCVFC. The generalized linearized model of the voltage with DCVFC and CAVFC can both be depicted in Fig. 4.5.

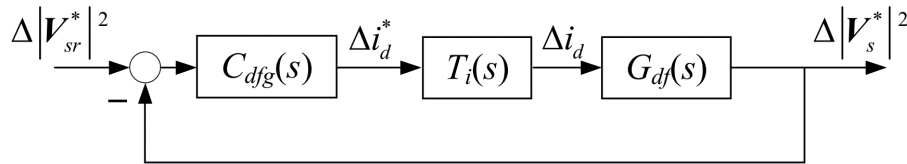


Fig. 4.5. Generalized linearized model of voltage loop.

In Fig. 4.5, $C_{dfg}(s)$ is the transfer function of the generalized voltage feedback controller, which can be expressed as

$$C_{dfg}(s) = \frac{\lambda}{s} \quad (4.9)$$

where λ is

$$\begin{cases} \lambda = \lambda_1, & DCVFC \\ \lambda = \lambda_\theta |i_q^0|, & CAVFC \end{cases} \quad (4.10)$$

$T_i(s)$ and $G_{df}(s)$ are the transfer function of the equivalent current loop, and the control plant, respectively, which can be seen in (2.9) and (2.10). According to (2.10), (2.12), and (4.9), the close-loop transfer function of the voltage loop with DCVFC and CAVFC, i.e. $\Phi_I(s)$ and $\Phi_\theta(s)$ can be expressed as

$$\begin{cases} \Phi_I(s) = \frac{\omega_{cc}\lambda_I(b_I s + a_I)}{s^2 + \omega_{cc}(1 + b_I\lambda_I)s + \omega_{cc}\lambda_I a_I}, & DCVFC \\ \Phi_\theta(s) = \frac{\omega_{cc}\lambda_\theta(b_\theta s + a_\theta)}{s^2 + \omega_{cc}(1 + \lambda_\theta b_\theta)s + \omega_{cc}\lambda_\theta a_\theta}, & CAVFC \end{cases} \quad (4.11)$$

where $b_I = b$, $a_I = a$; $b_\theta = b|i_q^0|$, $a_\theta = |i_q^0|a$.

4.3.2 Stability Analysis of Voltage Loops

According to (4.11), by referring to the Routh stability criterion, the stability of the voltage loop with DCVFC and CAVFC requires that

$$\begin{cases} 1 + b_I\lambda_I > 0 \text{ and } \lambda_I a_I > 0, DCVFC \\ 1 + \lambda_\theta b_\theta > 0 \text{ and } \lambda_\theta a_\theta > 0, CAVFC \end{cases} \quad (4.12)$$

Since the negative d-axis current is required for the flux-weakening control, the control parameters λ_I and λ_θ are normally set at positive values. In addition, the conditions $1 + b_I\lambda_I > 0$ and $1 + b_\theta\lambda_\theta > 0$ can be satisfied with the properly tuned control parameter (Appendix B). Therefore, the condition $a_I \leq 0$ and $a_\theta \leq 0$, i.e. $a \leq 0$ defines the intrinsic unstable area of the voltage loop.

Based on the machine parameters in Table 4.1 (shown in the experimental verification section of this chapter), when $\omega_e^0 > 0$, the map of the coefficients a in dq-axis current plane of mode A and mode B can be illustrated in Fig. 4.6, which are denoted as $a|_{modeA}$ and $a|_{modeB}$, respectively. It can be seen that both the mode A and mode B have unstable area, i.e. where $a \leq 0$.

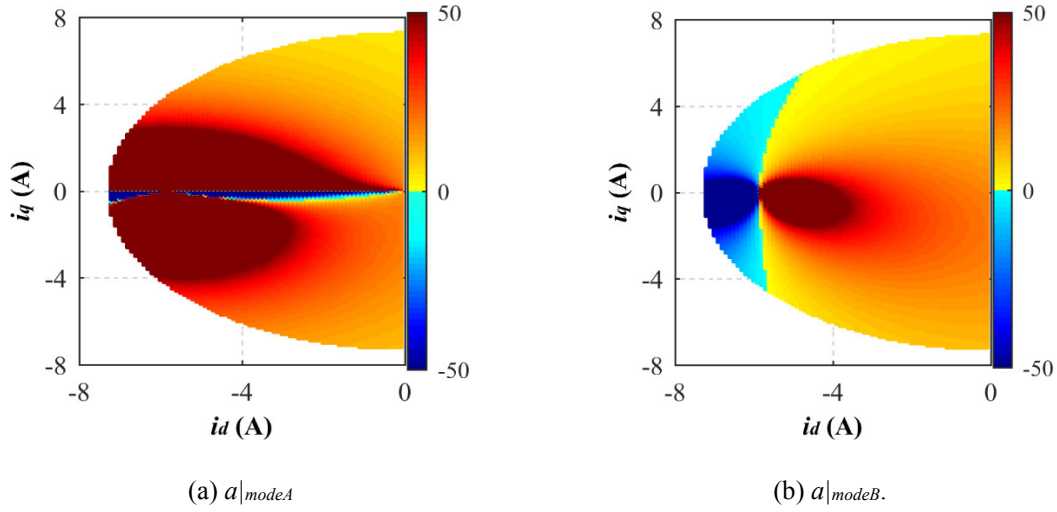


Fig. 4.6. Map of coefficient a under different operation modes.

In mode A and mode B, the coefficient a has been derived in (2.19) and (2.20) for the machine without MTPV region in chapter 2. For the machine with MTPV region, the coefficient a in mode A and mode B keep the same formulars as (2.19) and (2.20), which are given as

$$a|_{ModeA} = 2\omega_e^0 \psi_m (\omega_e^0 L_s - R_s i_d^0 / i_q^0) \quad (4.13)$$

$$\begin{aligned} a|_{ModeB} &= 2\omega_e^0 V_q^0 L_d + 2R_s V_d^0 \\ &= 2Z_s^2 P_c \end{aligned} \quad (4.14)$$

Since $i_d^0 < 0$ in the flux-weakening region, (4.13) implies that $a|_{ModeA} \leq 0$ only occurs when $\omega_e^0 i_q^0 < 0$ and $|i_q^0 / i_d^0| \leq |R_s / (\omega_e^0 L_s)|$. Therefore, in the mode A, the instability happens at light load in generating condition, which is located at the lower half part of the current plane, as shown in Fig. 4.6(a). According to operation mode definition of the two flux-weakening methods, this unstable condition can occur in CAAFFC.

In addition, it can be seen in (4.14) that $a|_{ModeB} = 0$ also defines the MTPV curve. As show in Fig. 4.6(b), in the mode B, only the right part of the MPTV curve, i.e. where $a|_{ModeB} > 0$, can allow a stable voltage control. Since when $a|_{ModeB} = 0$, the MTPV controller will be activated, the system will transfer to the mode C (region III), the stability of the DQFFC can be maintained by the proper designed MTPV controller which has been

addressed in chapter 3. However, there still exists a region where $a|_{modeB}$ is positive but very close to zero, which is close to and on the right side of the MTPV curve. This area implies the weak voltage regulation capability of the voltage loop in DQFFC. The system in this area is in a fragile state and could easily oscillate especially in the over modulation region due to the reduced voltage margin and the increased harmonics. Although the VVM can boost the current dynamics in the over modulation region, it cannot improve the voltage regulation capability reflected by the coefficient a , which is operation point relevant. This phenomenon will be further demonstrated in the experimental part. On the contrary, CAAFFC shows advantage when the system approaches to MTPV curve due to the large coefficient a in the mode A, which indicates that the voltage loop in CAAFFC is stable in the region III even without MTPV control.

The different stability characteristics can also be easily explained in Fig. 4.7. As shown in Fig. 4.7, two areas that are labelled as ‘A1’ and ‘A2’, represent two special operation conditions, where the area ‘A1’ is close to the MTPV curve and the area ‘A2’ is close to the light load in generating condition. Due to the different operation modes in DQFFC and CAAFFC, the current regulation directions in ‘A1’ of CAAFFC (shown in Fig. 4.7(a)) and ‘A2’ of DQFFC (shown in Fig. 4.7(b)) tend to be perpendicular to the voltage limit circle. However, the current regulation directions in ‘A2’ of CAAFFC (shown in Fig. 4.7(a)) and ‘A1’ of DQFFC (shown in Fig. 4.7(b)) tend to be tangent to the voltage limit circle. Since when the current limit circle is tangent to the voltage limit circle, the voltage feedback controller tries to move the operation point to the outside of the voltage limit circle in both regulation directions, implying that the voltage feedback controller loses its voltage regulation capability. Therefore, due to the different operation mode in the current limit circle, the weak stability in DQFFC and CAAFFC occurs at different operation regions.

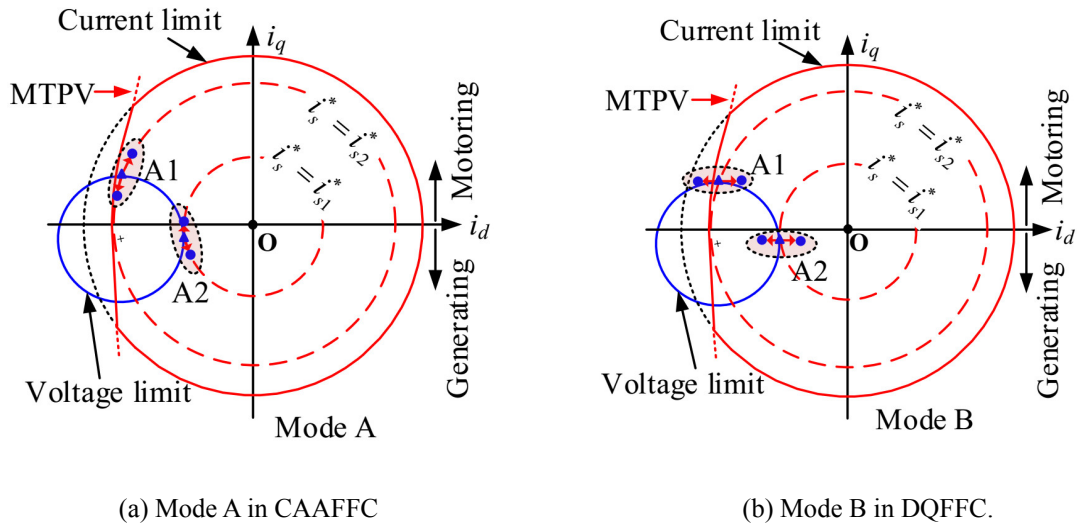


Fig. 4.7. Voltage regulation illustration in different operation modes ($\omega_e^l > 0$).

Besides, since two flux-weakening methods are regulated in two different coordinate systems, CAAFFC has poor transition performance between motoring and generating condition. As shown in Fig. 4.8(a), for the CAAFFC, when the system tries to transfer from the motoring condition to generating condition, e.g. from point F_1 to F_4 , as the speed controller can only regulate the current amplitude, the current command trajectory has to shrink to the original point first. Therefore, it will pass a region, e.g. the point F_2 in Fig. 4.8(a), which is outside of the voltage limit circle. The point F_2 is unstable due to that the CAVFC tries to regulate it to the point F_3 , which is still outside of the voltage limit circle. Therefore, the transition between the motoring and generating conditions requires to pass an unstable area, which deteriorates the system performance especially at light load condition. On the contrary, for DQFFC, as shown in Fig. 4.8(b), the system can smoothly transfer from F_1 to F_4 due to that the transition points F_2 and F_3 are all stable.

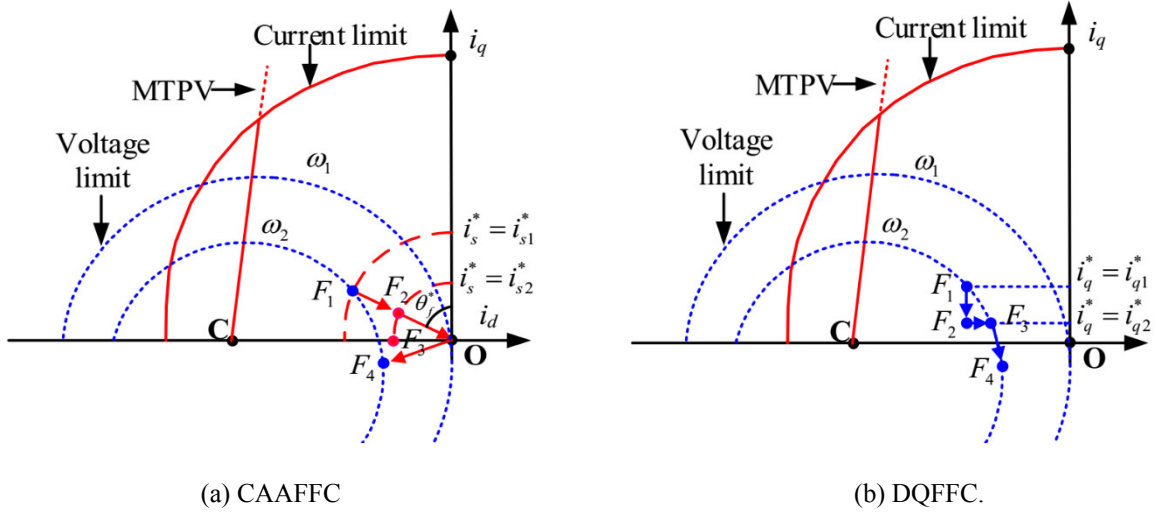


Fig. 4.8. Transition from motoring to generating condition.

4.3.3 MTPV Controller Design

In the region III, the system is regulated by both the MTPV controller and the voltage feedback controller, the operation mode B or A activated by DCVFC and CAVFC cooperates with the mode C or mode D activated by the MTPV controllers in DQFFC and CAAFFC, respectively. The MTPV controller design in DQFFC can be referred to the chapter 3, which has been indicated that a PI controller rather than a pure integral controller can be adopted to maintain stability in region III. As for CAAFFC, the linearized model of the MTPV loop can be shown in Fig. 4.9.

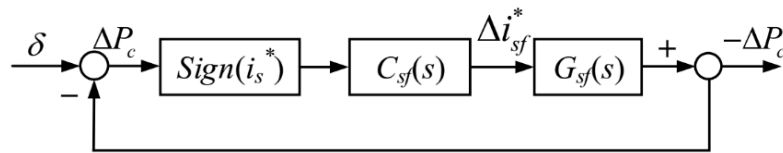


Fig. 4.9. Linearized model of the MTPV Loop in CAAFFC.

In Fig. 4.9, $C_{sf}(s)$ is the transfer function of the MTPV controller in CAAFFC, i.e. a pure integral regulator; $G_{sf}(s)$ is the transfer function of the control plant of the MTPV loop in CAAFFC; δ is the assumed reference, which is an infinitesimal value. $C_{sf}(s)$ and $G_{sf}(s)$ can be expressed as

$$C_{sf}(s) = -\frac{\lambda_{Is}}{s}, \quad G_{sf}(s) = -\frac{\Delta P_c}{\Delta i_{sf}^*} = -\frac{\Delta i_d^*}{\Delta i_{sf}^*} \quad (4.15)$$

It is reasonable to assume that the speed loop is much slower than the MTPV loop. Therefore, at the equilibrium point, Δi_{sf}^* can be approximated as Δi_{sm}^* , and $G_{sf}(s)$ can be further expressed as

$$G_{sf}(s) = -\frac{\Delta i_d^*}{\Delta i_{sm}^*} \quad (4.16)$$

According to the foregoing analysis, the voltage loop in CAAFFC is stable in region III, and Δi_{sm}^* can induce Δi_d^* directly, $G_{sf}(s)$ can be derived as

$$G_{sf}(s) = -\frac{\Delta i_d^*}{\Delta i_{sm}^*} = -\frac{i_d^0}{i_{sm}^0} = \text{sign}(i_{sm}^0) \frac{|i_d^0|}{|i_{sm}^0|} = \text{sign}(i_s^*) \frac{|i_d^0|}{|i_{sm}^0|} \quad (4.17)$$

It can be seen that the control plant is only a proportional gain. Therefore, a pure integral controller is enough. In addition, in the region III, $|i_d^0| \approx i_c$ and $|i_d^0|/|i_{sm}^0| < 1$. For a conservative design, the controller can be tuned when $G_{sf}(s) = \text{sign}(i_s^*)$. Therefore, the close-loop transfer function of the MTPV loop in CAAFFC can be derived as

$$\frac{-P_c}{\delta} \Big|_{CAAFFC} = \frac{\lambda_{Is}}{s + \lambda_{Is}} \quad (4.18)$$

where λ_{Is} can be approximated as the bandwidth of the MTPV loop.

4.4 Experimental Verification

The experiments based on dSPACE (DS1006) platform are implemented on a non-salient-pole PMSM with MTPV region, which is the same as the chapter 3, i.e. $i_{cn}=0.8$. The test rig-II is used as the load torque machine, i.e. a would field excited DC machine with a rated power of 150 W and a rated speed at 4000 rpm. The combined inertia of the transmission system is 0.001 kg·m². The power switches of the inverter are IRFH7440 MOSFET. The PWM switching frequency is 10 kHz. The machine and drive parameters are listed in Table 4.1.

Table 4.1 Machine and drive parameters

Parameters	Value
Machine stator resistance (R_s)	0.25 Ω
Resistance of power cable	0.1 Ω
Synchronous inductance (L_s)	1.7 mH
PM-flux linkage(ψ_m)	10 mWb
Number of pole pairs (N_p)	10
DC link voltage (V_{dc})	14 V
Current limit (I_m)	7.35A
Current bandwidth (ω_{cc})	1200 rad/s
Control parameter ω_{Nqf}	200 rad/s
Control parameter λ_{Is}	200 rad/s

In the experiments, the stability of the voltage loop in DQFFC and CAAFFC when the systems approach and pass through the MTPV curve are firstly demonstrated by enabling and disabling the MTPV controller. Subsequently, with the enabled MTPV controller, the performance when the systems approach the MTPV curve are compared between the two flux-weakening methods in both linear and over modulation regions. Finally, the transition performance of the two flux-weakening methods between motoring and generating conditions are demonstrated.

4.4.1 With and Without MTPV Controller in DQFFC and CAAFFC

When $M=0.9$, for a given speed command $n^*=1500$ rpm with the speed ramp at 750 rpm/s, Fig. 4.10 shows the system performance with and without MTPV controller in DQFFC. In Fig. 4.10(a), without MPTV controller, it can be seen that the system cannot stabilize on the MTPV curve ($P_c=0$). In addition, the voltage $|V_s^*|$ shows a short untracked period after P_c passes through zero. Fig. 4.10(b) shows that the system is stable on the MTPV curve ($P_c=0$) with the PI MPTV controller, and the machine can achieve a higher speed than the system without MTPV controller. In contrast, Fig. 4.11(a) shows the signals waveform in CAAFFC without MTPV controller. It can be seen that the voltage is well tracked even after P_c passes through zero without MTPV controller in CAAFFC. Fig. 4.11(b) shows that the system can

stabilize on the MTPV curve when an integral MTPV controller is applied, and thus the machine can achieve a higher speed.

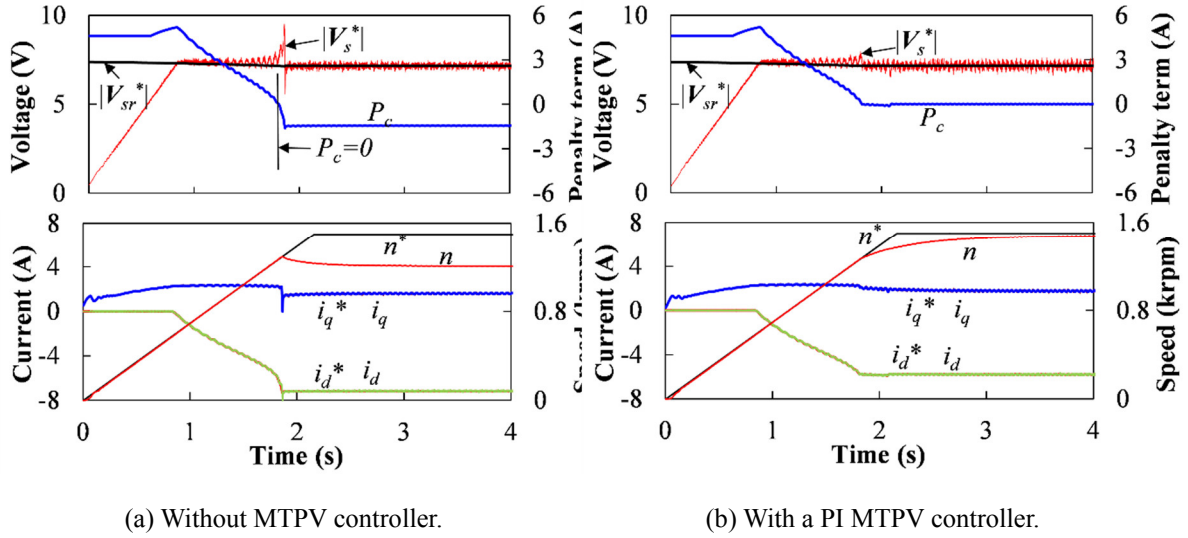


Fig. 4.10. System performance of the DQFFC.

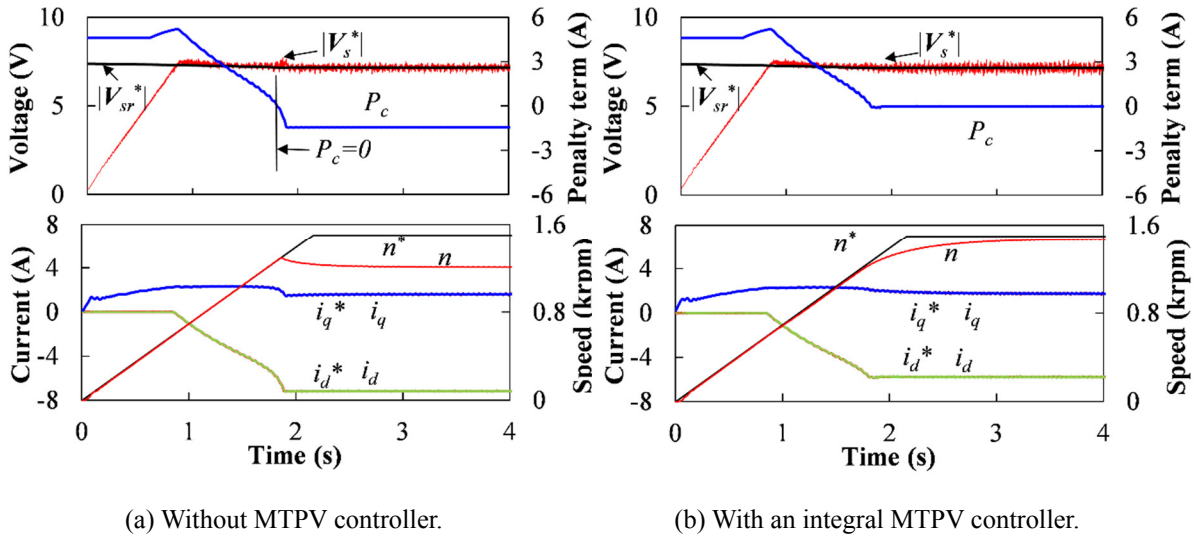


Fig. 4.11. System performance of the CAAFFC.

Meanwhile, the current trajectories with and without MTPV controller in DQFFC and CAAFFC are shown in Fig. 4.12 and Fig. 4.13, respectively. For the DQFFC without MTPV controller, it can be seen from Fig. 4.12(a) that the current cannot be tracked well after the system passes through the MTPV curve, and the system is finally stabilized on the current limit. Fig. 4.12(b) shows the well tracked current trajectory after the applied MTPV controller,

and the system is finally stabilized on the MTPV curve. For the CAAFFC without MTPV controller, it can be seen from Fig. 4.13(a) that the current can be tracked well even after the system passes through the MTPV curve, and the system is also stabilized on the current limit. In Fig. 4.13(b), it indicates that the MTPV loop is still required to force the system to operate on the MTPV curve for CAAFFC.

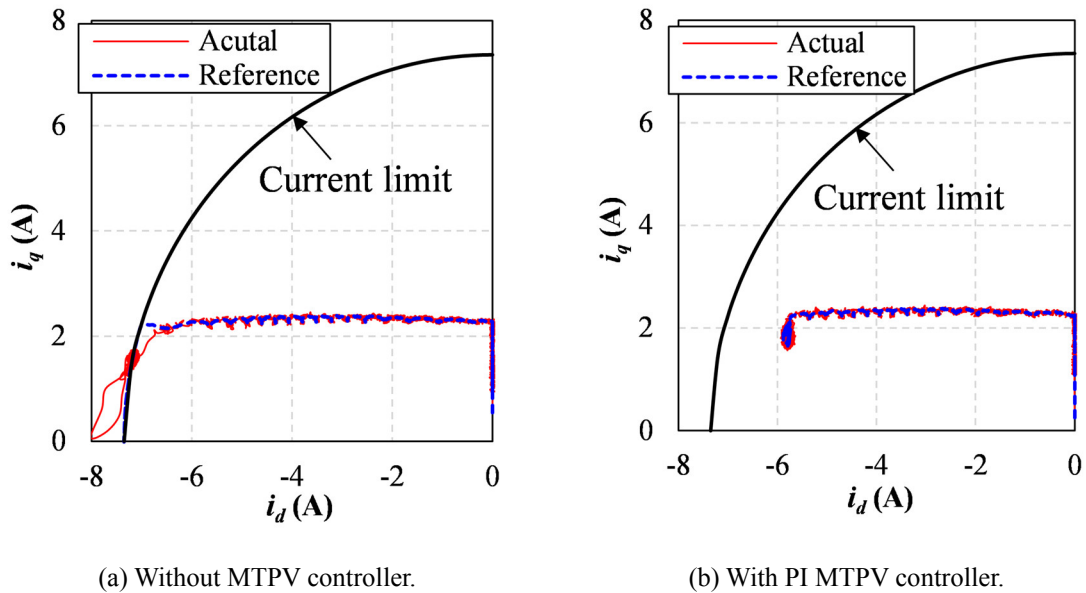


Fig. 4.12. Current trajectory of the system with DQFFC.

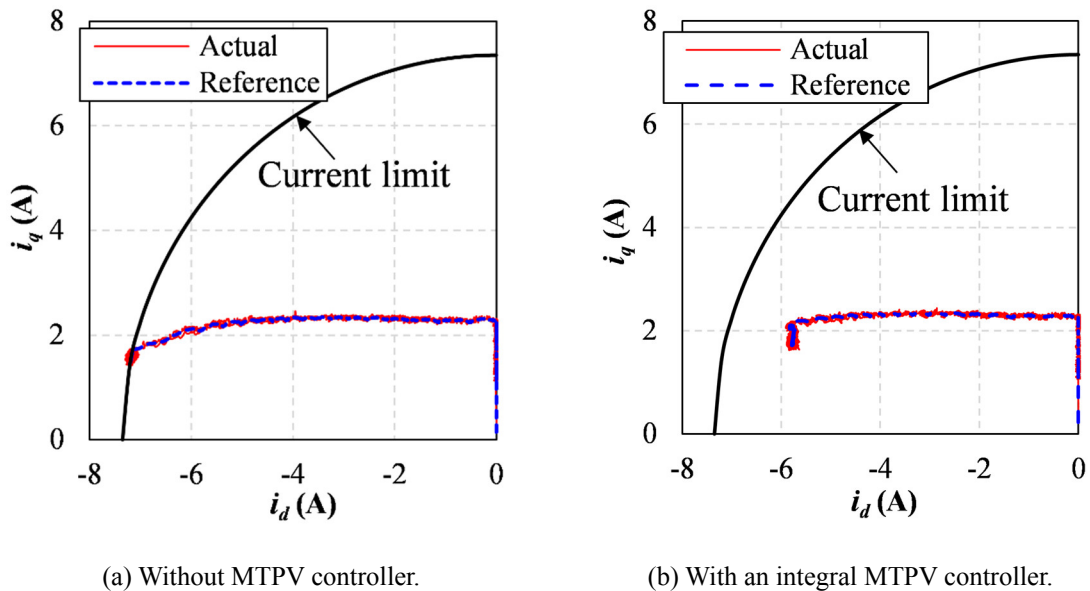


Fig. 4.13. Current trajectory of the system with CAAFFC.

4.4.2 Performance When Approaching MTPV Curve

With the applied MTPV controller, the system performance of when approaching MTPV curve is observed by changing the speed command from 0 rpm to 600 rpm, 700rpm, 800rpm, 900rpm, and 1000 rpm every 2 seconds. Fig. 4.14 shows the system performance of the two flux-weakening methods in the linear modulation region and $M=0.9$. As shown in Fig. 4.14, although a short voltage pulse appears when approaching the MTPV curve for DQFFC, overall, the systems perform well for the two flux-weakening methods.

Fig. 4.15 shows the system performance without VVM in the over modulation region and $M=1.15$. It can be seen from Fig. 4.15(a) that the system with DQFFC oscillates seriously in the flux-weakening region. In Fig. 4.15 (b), the CAAFFC in the flux-weakening region is not as serious as DQFFC. However, the ripples in both current and voltage are much higher than those in the linear modulation region.

Fig. 4.16 shows the system performance with VVM when $M=1.15$. It can be seen from Fig. 4.16(a) that the oscillation in DQFFC disappears on the MTPV curve and when the system is not close to MTPV curve. However, the oscillation still appears when the system gets closer to the MTPV curve. In Fig. 4.16(b), no oscillation occurs when the VVM is employed for CAAFFC. It should be noted that the voltage ripple in $|V_s|$ is caused by the over modulation block. The frequency of the ripple in $|V_s|$ is six times of the fundamental frequency.

Therefore, when approaching to the MTPV curve, the CAAFFC shows better stability than the DQFFC especially in the over modulation region.

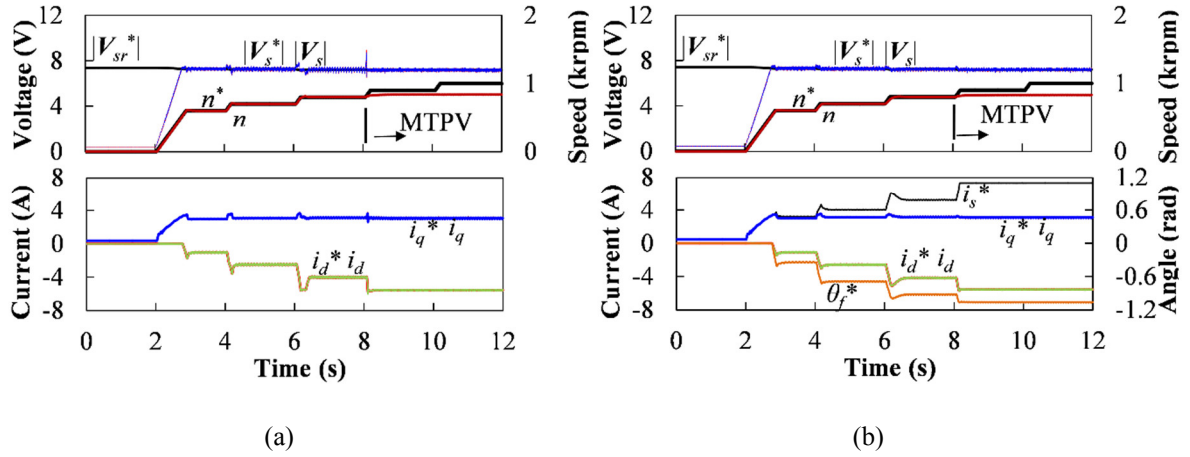


Fig. 4.14. System performance when approaching MTPV curve without VVM ($M=0.9$).

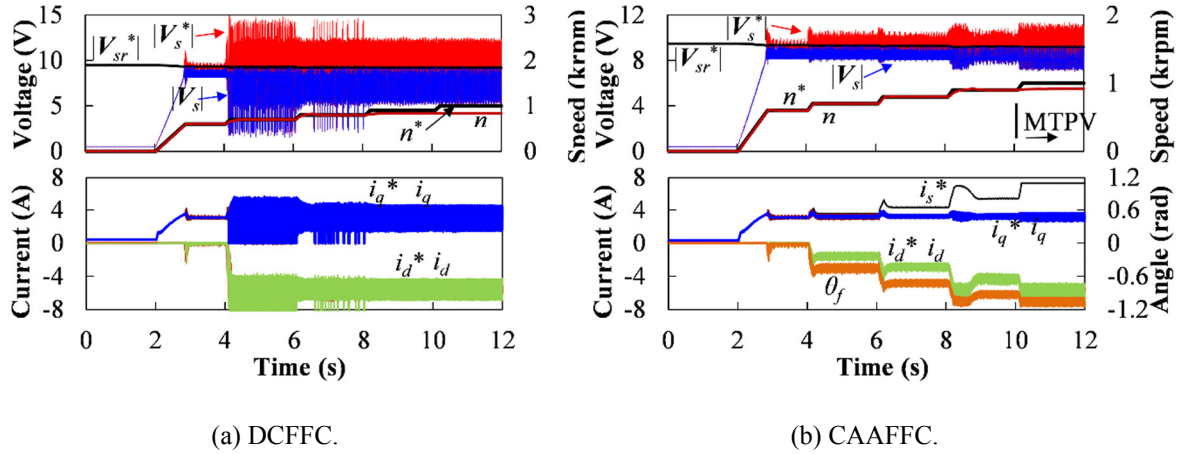


Fig. 4.15. System performance when approaching MTPV curve without VVM. ($M=1.15$).

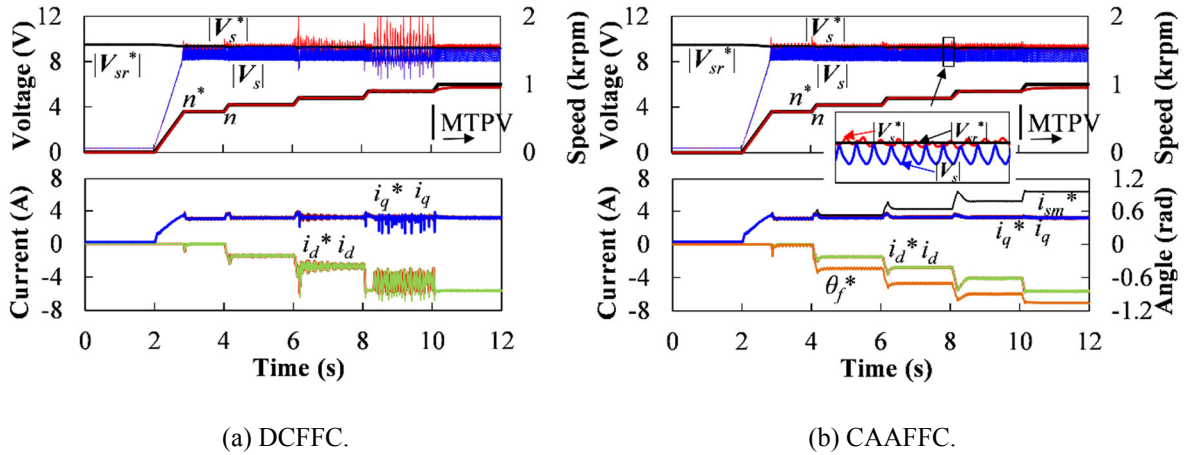


Fig. 4.16. System performance when approaching MTPV curve with VVM. ($M=1.15$).

4.4.3 Transition Between Motoring and Generating Conditions

Fig. 4.17 shows the transition performance of the two flux-weakening methods with the speed command $n^*=1200$ rpm and when $M=0.9$. The load torque is regulated manually by changing the excitation current of the DC machine. It can be seen from Fig. 4.17(a) that the system with DQFFC can stably and smoothly transfer between motoring and generating conditions. However, as shown in Fig. 4.17(b), the system with CAAFFC cannot stably transfer between motoring and generating conditions. In addition, the current oscillates and the voltage loop loses control when the system tries to operate at the light load and generating condition in CAAFFC, which confirms the foregoing analyses.

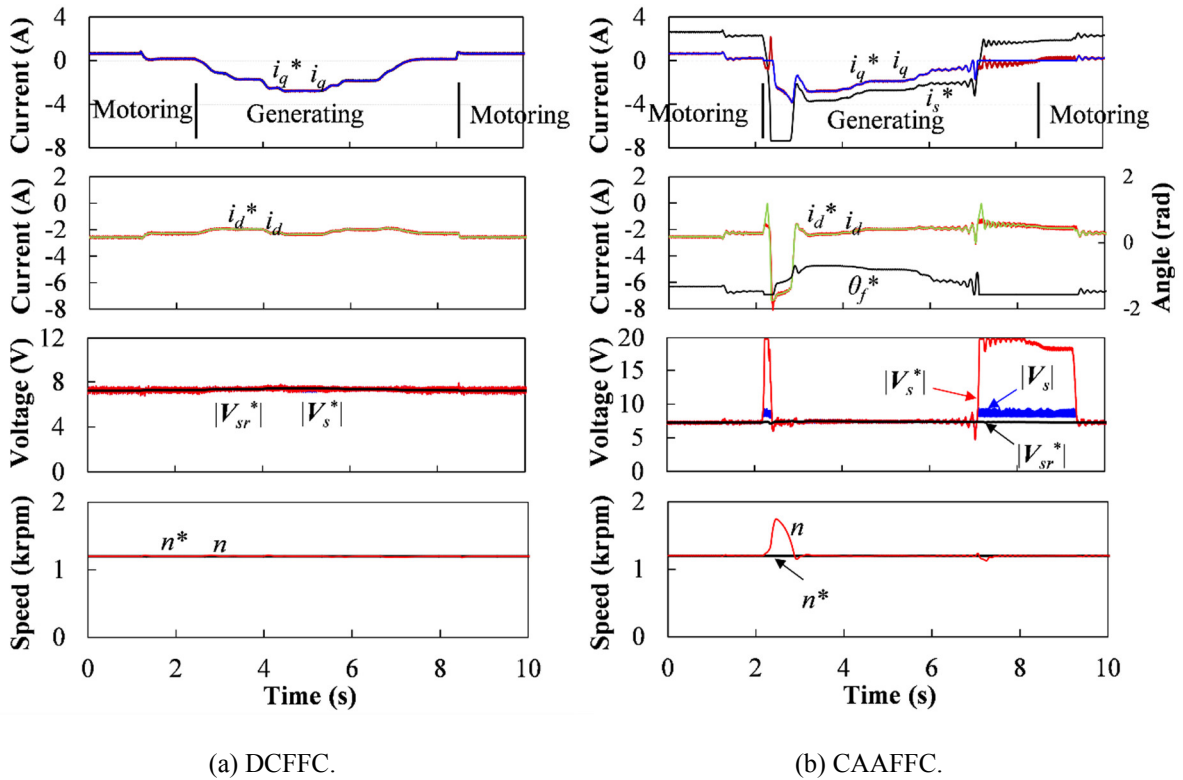


Fig. 4.17. Transition performance between motoring and generating conditions.

4.5 Conclusion

Based on the conventional two voltage magnitude feedback controllers, i.e. DCVFC and CAVFC, by further considering the MTPV control, this chapter has comparatively studied the stability of the two flux-weakening methods, i.e. DQFFC and CAAFFC. Due to the

different small signal behaviour in DCFFC and CAAFFC, they exhibit different stability characteristics, which have been analysed based on the voltage loop analysis.

The analyses and experimental results have verified that

1) The DCFFC has weak voltage regulation capability when the system approaches the MTPV curve, which could lead to oscillation in the over modulation region. However, this oscillation in the over modulation region can be alleviated in CAAFFC, and are eliminated in CAAFFC with the VVM.

2) The CAAFFC could lead to instability at light load in generating condition. However, this instability will not occur in DCFFC.

3) The DCFFC can achieve a smooth and stable transition between motoring and generating conditions while the system with CAAFFC cannot.

CHAPTER 5 HYBRID FEEDBACK FLUX-WEAKENING CONTROL OF PMSM

As the stability problem in dq-axis current based feedback flux-weakening control (DQFFC) and current amplitude and angle based feedback flux-weakening control (CAVFFC) are operation mode relevant, a proper way to solve the stability problem is to optimize the operation mode. In this chapter, a hybrid feedback flux-weakening control (HFFC) method is proposed. It is based on a novel hybrid voltage feedback controller (HVFC) which contains both d-axis current voltage feedback controller (DCVFC) and current angle voltage feedback controller (CAVFC). The operation mode is optimized by designing the weight factors of the DCVFC and CAVFC parts in HVFC. The effectiveness of the proposed HFFC in different flux-weakening regions are verified through experimental results.

5.1 Introduction

In the flux-weakening region, since the system operates close to the voltage limit boundary, the system is easy to be saturated. Therefore, the voltage feedback controller can be regarded as a kind of anti-windup controller to deter the voltage saturation problem. Therefore, the voltage regulation capability of the voltage loop reflects the effectiveness of the anti-windup control. However, due to the nonlinear behaviour of the voltage loop [BOL14], the voltage regulation capability varies with the operation points, rendering the system perform differently at different regions. In the chapter 4, the analysis of the voltage loop based on the linearized model has shown that the oscillation or instability could occur in dq-axis current based feedback flux-weakening control (DQFFC) and current amplitude and angle based feedback flux-weakening control (CAAFFC) which are based on the d-axis current voltage magnitude feedback controller (DCVFC) and current angle voltage magnitude feedback controller (CAVFC), respectively. In this chapter, the voltage feedback control structure is still preserved due to its advantages of simplicity and robustness against the parameter variation. Meanwhile, the feedback control structure is optimized, aiming to improve the system stability at different flux-weakening regions, including the over

modulation region. Unlike directly regulating only d-axis current command or only current angle command in DCVFC or CAVFC, a hybrid voltage feedback controller (HVFC) is introduced by regulating d-axis current command and current angle command simultaneously, which can utilize the complementary advantages of the DCVFC and CAVFC at different flux-weakening regions. Therefore, the major concern is to optimize the weight factors of the DCVFC part and CAVFC part in HVFC, which will be detailed in this chapter. By further considering a feedback type MTPV control, the flux-weakening method with HVFC, namely, hybrid feedback flux-weakening control (HFFC) is proposed. Finally, the effectiveness and advantages of the proposed method at various conditions are verified through the experimental results.

5.2 Issues with Existing Voltage Feedback Methods

The two flux-weakening methods, i.e. DQFFC and CAAFFC are based on the rectangular coordinate system and polar coordinate system, respectively, which result in different operation modes, and therefore different linearized models and different transfer functions. The coefficients of the close-loop transfer functions, which are operation mode relevant, define the intrinsic stability characteristics of the flux-weakening methods. The analyses and experimental results in the previous chapter have indicated that

1) Both the voltage loops in DQFFC and CAAFFC have an unstable area when the system operates inside the current limit circle;

2) With the properly designed MTPV controller, the stability of DQFFC in region III is maintained. However, the region close to the MTPV curve has a weak voltage loop regulation capability, leading to oscillation in the over modulation even with the VVM;

3) The instability of CAAFFC occurs at light load in generating condition;

4) The oscillation or instability only occurs in region II where only DCVFC or CAVFC is activated.

In order to solve the stability issues in the DQFFC and CAFFC, a hybrid feedback flux-weakening control is proposed, as will be detailed in the following section.

5.3 Hybrid Feedback Flux-Weakening Control

5.3.1 Introduction of Hybrid Feedback Flux-Weakening Control

The voltage loops with both DCVFC and CAVFC have an unstable area where $a \leq 0$, which is located at different regions due to different operation modes. The different operation modes are originally induced by the different control objects, i.e. d-axis current command and current angle command, respectively. Therefore, in order to obtain a more uniform distribution of a and avoid the area where $a \leq 0$, it is possible to combine DCVFC and CAVFC together by regulating both the d-axis current command and current angle command simultaneously, which naturally comes to the proposed HVFC. By further considering the feedback-type MTPV control, the flux-weakening method with HVFC, namely, hybrid feedback flux-weakening control (HFVC) is proposed with the block diagram shown in Fig. 5.1. In Fig. 5.1, the HVFC is composed of two voltage feedback controllers, i.e. DCVFC and CAVFC, which are connected in parallel and share the same input, i.e. the voltage magnitude error. The output of the DCVFC part and the CAVFC part in HVFC are denoted as i_{dfh}^* and θ_{fh}^* , respectively. Two weight factors, i.e. w_I and w_θ are introduced to represent the ratio of the contribution of the DCVFC part and the CAVFC part, respectively.

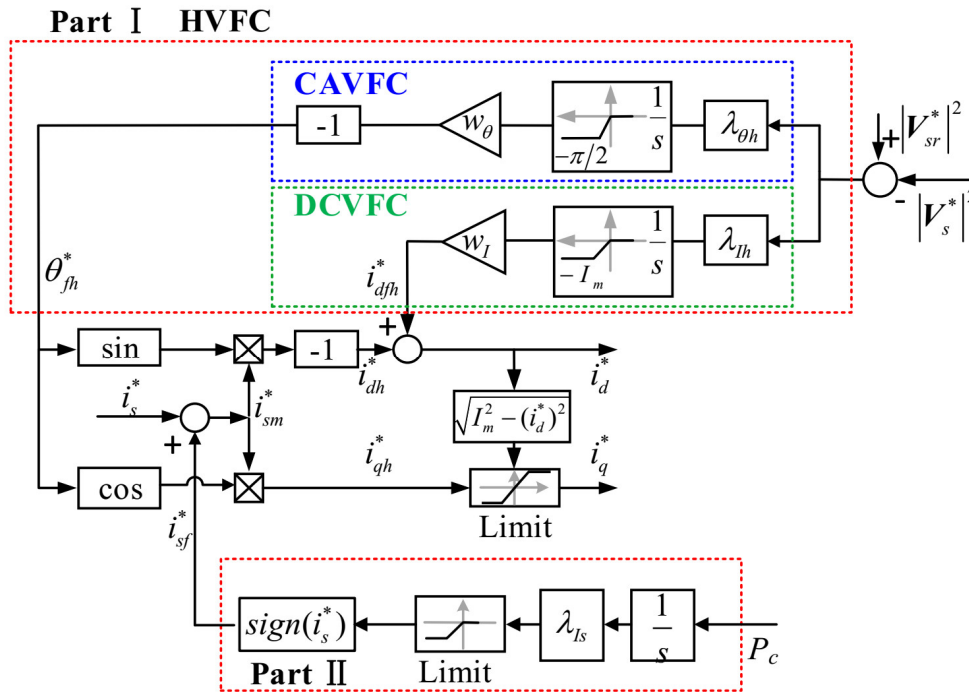


Fig. 5.1. The block diagram of HFFC.

Fig. 5.2 shows the evolution process of the operation modes in the proposed HFFC. Fig. 5.2(a) and Fig. 5.2(b) show the operation modes that are activated by the DCVFC and CAVFC, respectively. As the HVFC is to utilize both advantages of DCVFC and CAVFC at the different regions, the operation mode of HVFC can be optimized so that the operation mode at light load condition is dominated by the mode B while the operation mode close to MTPV curve (region III) is dominated by the mode A. Fig. 5.2(c) illustrates the operation modes activated by the desired HVFC. With the MTPV control, the operation modes in HFFC is shown in Fig. 5.2(d). It can be seen that the operation mode of HFFC in region III is similar to that in CAAFFC. Therefore, the MTPV controller in HFFC can be designed to be the same as the one in CAAFFC. In consequence, how to select the proper weight factors and control parameters are the key issues and will be detailed as follows.

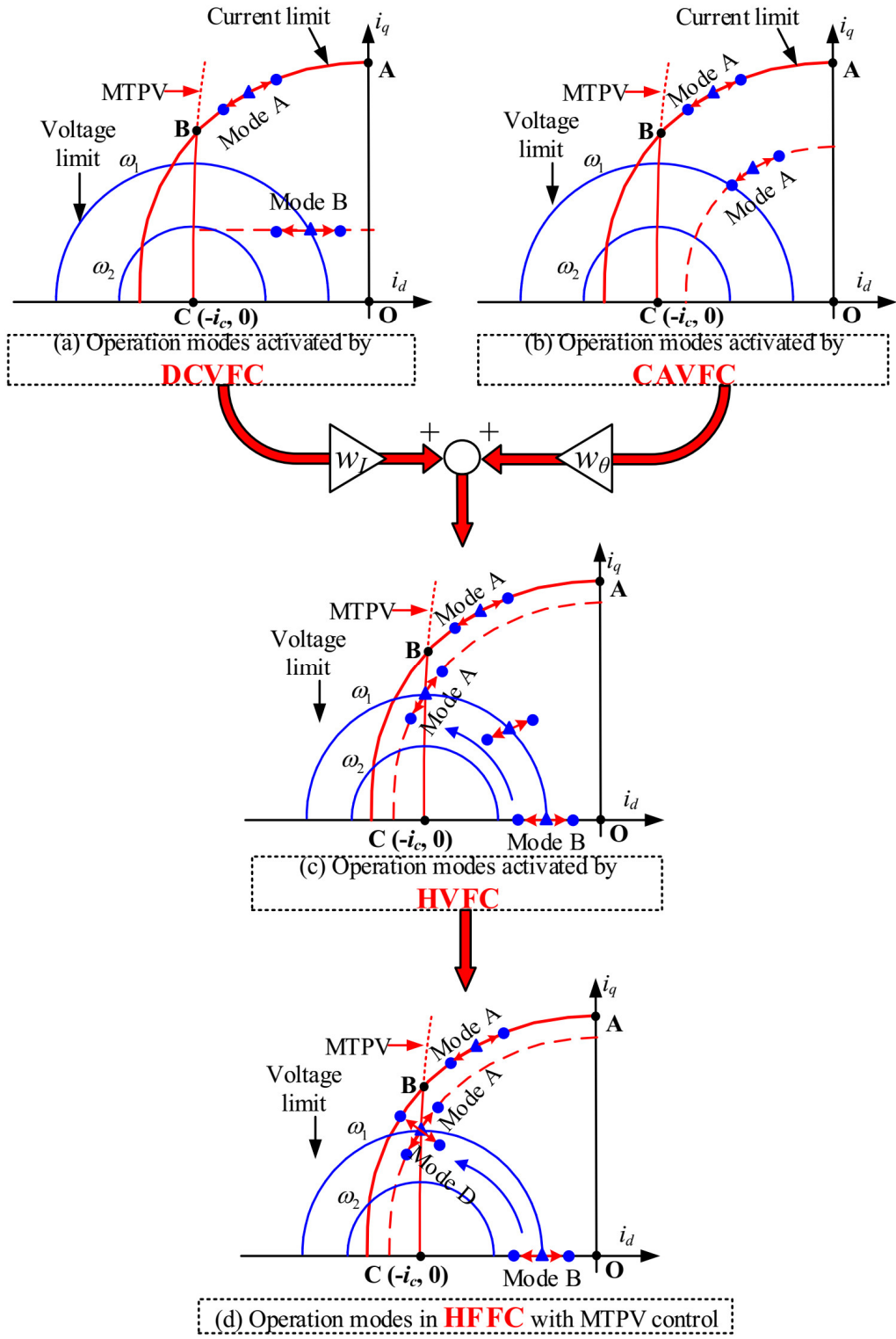


Fig. 5.2. The evolution process of the operation modes in the proposed HFEC.

5.3.2 Design of Hybrid Voltage Feedback Controller

5.3.2.1 Linearized Model of HVFC

Since DCVFC and CAVFC can both contribute to the actual d -axis current command, the linearized model of the voltage loop with HVFC can be seen as the combination of the linearized model of the voltage loop with DCVFC and CAVFC, which can be shown in Fig. 5.3.

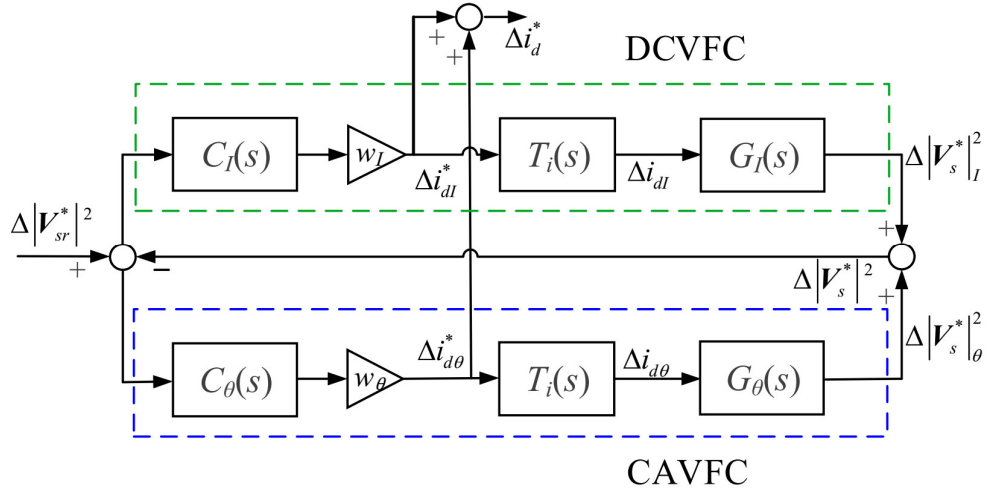


Fig. 5.3. Linearized model of the voltage loop with HVFC.

In Fig. 5.3, $C_I(s)$ and $C_\theta(s)$ are the DCVFC part and the CAVFC part in HVFC, respectively; $T_i(s)$ is the transfer function of the equivalent current loop; $G_I(s)$ and $G_\theta(s)$ are the transfer functions of the control plants corresponding to the DCVFC part and the CAVFC part, respectively. Therefore, $C_I(s)$ and $C_\theta(s)$ can be expressed as

$$\begin{cases} C_I(s) = \frac{\lambda_{Ih}}{s} \\ C_\theta(s) = \frac{\lambda_{\theta h}}{s} |i_q^0| \end{cases} \quad (5.1)$$

where λ_{Ih} and $\lambda_{\theta h}$ are the control parameters of the DCVFC part and the CAVFC part in HVFC, respectively.

$G_I(s)$ and $G_\theta(s)$ can be expressed as

$$\begin{cases} G_I(s) = \frac{\Delta |V_s^*|_I^2}{\Delta i_{dI}} \\ G_\theta(s) = \frac{\Delta |V_s^*|_\theta^2}{\Delta i_{d\theta}} \end{cases} \quad (5.2)$$

where Δi_{dI} and $\Delta i_{d\theta}$ are the small signals of d-axis current contributed by the DCVFC part and the CAVFC part, respectively; $\Delta |V_s^*|_I^2$ and $\Delta |V_s^*|_\theta^2$ are the small signals of the square value of the voltage magnitude that is induced by Δi_{dI} and $\Delta i_{d\theta}$, respectively.

According to the operation mode definition, $G_I(s)$ and $G_\theta(s)$ can be expressed

$$\begin{cases} \begin{cases} G_I(s) = G_{df}(s)|_{ModeA} \\ G_\theta(s) = G_{df}(s)|_{ModeA} \end{cases}, \text{On the current limit circlce} \\ \begin{cases} G_I(s) = G_{df}(s)|_{ModeB} \\ G_\theta(s) = G_{df}(s)|_{ModeA} \end{cases}, \text{In the current limit circlce} \end{cases} \quad (5.3)$$

where $G_{df}(s) = bs + a$; in mode A, b and a are denoted as $b|_{modeA}$ and $a|_{modeA}$, respectively; in mode B, b and a are denoted as $b|_{modeB}$ and $a|_{modeB}$, respectively.

Therefore, the open-loop transfer function of the voltage loop can be derived as

$$G_{oHVFC}(s) = T_i(s)(C_I(s)w_I G_I(s) + C_\theta(s)w_\theta G_\theta(s)) \quad (5.4)$$

The close-loop transfer function with HVFC, i.e. $\Phi_h(s)$ can be derived as

$$\Phi_h(s) = \frac{\omega_c b_{\lambda h} s + \omega_c a_{\lambda h}}{s^2 + \omega_{cc}(1 + b_{\lambda h})s + \omega_{cc} a_{\lambda h}} \quad (5.5)$$

where the coefficients $a_{\lambda h}$ and $b_{\lambda h}$ are

$$\begin{cases} a_{\lambda h} = a_{\lambda Ih} w_I + a_{\lambda \theta h} w_\theta \\ b_{\lambda h} = b_{\lambda Ih} w_I + b_{\lambda \theta h} w_\theta \end{cases} \quad (5.6)$$

where $a_{\lambda Ih}$, $a_{\lambda \theta h}$, $b_{\lambda Ih}$ and $b_{\lambda \theta h}$ are

$$\begin{cases} a_{\lambda Ih} = \lambda_{Ih} a_I \\ a_{\lambda \theta h} = \lambda_{\theta h} a_\theta \\ b_{\lambda Ih} = \lambda_{Ih} b_I \\ b_{\lambda \theta h} = \lambda_{\theta h} b_\theta \end{cases} \quad (5.7)$$

where $b_I = b$, $a_I = a$; $b_\theta = b|i_q^0|$, $a_\theta = a|i_q^0|$.

Since the instability occurs when a_I or a_θ is zero or negative for the voltage loop with only DCVFC or CAVFC, to avoid the instability conditions, the design objective of HVFC is to make sure that $a_{\lambda h}$ is positive with the proper combinations of a_I and a_θ . In addition, as the coefficients a_I and a_θ are only sensitive to the resistance when they are close to zero, the resistance influence can be neglected when designing HVFC. By ignoring the resistance, $a_{\lambda Ih}$, $a_{\lambda \theta h}$, $b_{\lambda Ih}$ and $b_{\lambda \theta h}$ can be derived and listed in Table 5.1, in which σ_I and σ_θ are

$$\begin{cases} \sigma_I = (1/i_{cn} + i_{dn})/(\omega_{en} i_{qn}) \\ \sigma_\theta = (1/i_{cn} + i_{dn})/\text{sign}(\omega_{en} i_{qn}) \end{cases} \quad (5.8)$$

Table 5.1 Values of coefficients $a_{\lambda Ih}$, $a_{\lambda \theta h}$, $b_{\lambda Ih}$ and $b_{\lambda \theta h}$

	On the current limit circle	In the current limit circle
$a_{\lambda Ih}$	$a_{\lambda Ih} _{ModeA} = \lambda_{Ih} 2\omega_e^0 L_s i_c \omega_e^0 L_s$	$a_{\lambda Ih} _{ModeB} = \lambda_{Ih} 2 \omega_e^0 L_s V_m V_{qn} $
$b_{\lambda Ih}$	$b_{\lambda Ih} _{ModeA} = -\lambda_{Ih} 2\omega_e^0 L_s i_c \omega_e^0 L_s \sigma_I / \omega_b$	$b_{\lambda Ih} _{ModeB} = \lambda_{Ih} 2V_m V_{dn} L_s$
$a_{\lambda \theta h}$	$a_{\lambda \theta h} _{ModeA} = \lambda_{\theta h} i_c 2 \omega_e^0 L_s V_m V_{dn} $	
$b_{\lambda \theta h}$	$b_{\lambda \theta h} _{ModeA} = -\lambda_{\theta h} 2 \omega_e^0 L_s i_c V_m \sigma_\theta / \omega_b$	

5.3.2.2 Control Parameter Selection

As can be seen in (5.6) and (5.7), there are four variables that need to be designed, i.e. λ_{Ih} , $\lambda_{\theta h}$, w_I and w_θ . It is reasonable to assume that λ_{Ih} and $\lambda_{\theta h}$ have the same form as λ_I and λ_θ that are tuned in the DCVFC and CAVFC, respectively. Therefore, λ_{Ih} and $\lambda_{\theta h}$ can be expressed as

$$\lambda_{lh} = \frac{\omega_{mh}}{2V_m L_s |\omega_e^0|} g_{lh}, \lambda_{\theta h} = \frac{\omega_{mh}}{2V_m L_s |\omega_e^0|} g_{\theta h} \quad (5.9)$$

where ω_{mh} , g_{lh} and $g_{\theta h}$ are the parameters that need to be tuned.

Accordingly, by substituting (5.9) into Table 5.1, $a_{\lambda lh}$, $a_{\lambda \theta h}$, $b_{\lambda lh}$ and $b_{\lambda \theta h}$ can be derived and listed in Table 5.2, in which

$$\beta = 1/(\omega_{en} |i_{cn}|) \quad (5.10)$$

Table 5.2 The value of the coefficient $a_{\lambda lh}$, $a_{\lambda \theta h}$, $b_{\lambda lh}$ and $b_{\lambda \theta h}$ with the obtained λ_{lh} and $\lambda_{\theta h}$

	On the current limit circle	In the current limit circle
$a_{\lambda lh}$	$a_{\lambda lh} _{ModeA} = g_{lh} \omega_{mh} \frac{1}{\beta}$	$a_{\lambda lh} _{ModeB} = g_{lh} \omega_{mh} V_{qn} $
$b_{\lambda lh}$	$b_{\lambda lh} _{ModeA} = -g_{lh} \sigma_I \frac{\omega_{mh}}{\omega_b} \frac{1}{\beta}$	$b_{\lambda lh} _{ModeB} = -g_{lh} i_{qn} \text{sign}(\omega_{en}) \frac{\omega_{mh}}{\omega_b}$
$a_{\lambda \theta h}$	$a_{\lambda \theta h} _{ModeA} = g_{\theta h} i_c \omega_{mh} V_{dn} $	
$b_{\lambda \theta h}$	$b_{\lambda \theta h} _{ModeA} = -g_{\theta h} i_c \sigma_\theta \frac{\omega_{mh}}{\omega_b}$	

As the instability or oscillation occurs in the current limit circle, the parameters of the HVFC can be designed according to the operation regions, i.e. in the current limit circle or on the current limit circle.

1) In the current limit circle

According to (5.6) and Table 5.2, in the current limit circle, $a_{\lambda h}$ and $b_{\lambda h}$ can be expressed as

$$\begin{cases} a_{\lambda h}|_{In} = g_{lh} \omega_{mh} |V_{qn}| w_I + g_{\theta h} i_c \omega_{mh} |V_{dn}| w_\theta \\ b_{\lambda h}|_{In} = -g_{lh} i_{qn} \text{sign}(\omega_{en}) \frac{\omega_{mh}}{\omega_b} w_I - g_{\theta h} i_c \sigma_\theta \frac{\omega_{mh}}{\omega_b} w_\theta \end{cases} \quad (5.11)$$

where $a_{\lambda h}|_{In}$ and $b_{\lambda h}|_{In}$ denote the value of $a_{\lambda h}$ and $b_{\lambda h}$ in the current limit circle, respectively.

In order to avoid $a_{\lambda l}|_{In} \leq 0$ and obtain a more uniform distribution of $a_{\lambda l}|_{In}$, the parameters g_{lh} , $g_{\theta h}$, w_l and w_θ can be set as

$$w_l = |V_{qn}|, w_\theta = |V_{dn}|, g_{lh} = g_{\theta h} i_c = 1 \quad (5.12)$$

Accordingly, $a_{\lambda l}|_{In}$ and $b_{\lambda h}|_{In}$ can be simplified as

$$\begin{cases} a_{\lambda h}|_{In} = \omega_{mh} \\ b_{\lambda h}|_{In} = -\sigma_h \omega_{mh} / \omega_b \end{cases} \quad (5.13)$$

where $\sigma_h = (|i_{cn} + i_{dn}| + 1/i_{cn} + i_{dn})V_{dn} < i_{cn} + 1/i_{cn}$.

Therefore, the damping factor of the voltage loop with HVFC, i.e. ζ can be derived as

$$\zeta = \frac{\omega_{cc} (1 - \sigma_h \omega_{mh} / \omega_b)}{2\sqrt{\omega_{cc} \omega_{mh}}} \quad (5.14)$$

It can be seen from (5.14) that ζ is inversely proportional to σ_h . Therefore, the system can be designed on the operation point where σ_h is maximum in the flux-weakening region. By setting $\zeta=1$ at the operation point where $\sigma_h = \sigma_{hmax}$, ω_{mh} in the current limit circle can be approximated as

$$\omega_{mh}|_{In} = \frac{\omega_{cc}}{4} \left/ \left(1 + \frac{\omega_{cc}}{\omega_b} \frac{\sigma_{hmax}}{2} \right) \right. \quad (5.15)$$

where σ_{hmax} can be set as $(i_{cn} + 1/i_{cn})$.

Since $a_{\lambda l}|_{In}$ is a constant in the current limit circle which is irrelevant with the operation points, the proposed HVFC can avoid the instability or the oscillation when the system operates in the current limit circle.

2) On the current limit circle

According to (5.6) and Table 5.2, when the system operates on the current limit circle, $a_{\lambda h}$ and $b_{\lambda h}$ can be expressed as

$$\begin{cases} a_{\lambda h}|_{On} = g_{lh} \omega_{mh} \frac{1}{\beta} w_I + g_{\theta h} i_c \omega_{mh} |V_{dn}| w_\theta \\ b_{\lambda h}|_{On} = -g_{lh} \sigma_I \frac{\omega_{mh}}{\omega_b} \frac{1}{\beta} w_I - g_{\theta h} i_c \sigma_\theta \frac{\omega_{mh}}{\omega_b} w_\theta \end{cases} \quad (5.16)$$

where $a_{\lambda l}|_{On}$ and $b_{\lambda l}|_{On}$ denote the values of $a_{\lambda h}$ and $b_{\lambda h}$ on the current limit circle.

By substituting (5.12) in (5.16) and, $a_{\lambda l}|_{On}$ and $b_{\lambda l}|_{On}$ can be derived as

$$\begin{cases} a_{\lambda h}|_{On} = \omega_{mh} \left(\frac{1}{\beta} |V_{qn}| + |V_{dn}|^2 \right) \\ b_{\lambda h}|_{On} = -(\sigma_I \frac{1}{\beta} |V_{qn}| + \sigma_\theta |V_{dn}|) \frac{\omega_{mh}}{\omega_b} \end{cases} \quad (5.17)$$

By assuming that

$$\eta = \left(\frac{1}{\beta} |V_{qn}| + |V_{dn}|^2 \right) \quad (5.18)$$

$a_{\lambda l}|_{On}$ and $b_{\lambda l}|_{On}$ can be further simplified as

$$\begin{cases} a_{\lambda h}|_{On} = \eta \omega_{mh} \\ b_{\lambda h}|_{On} = -\sigma_I \frac{\eta \omega_{mh}}{\omega_b} \end{cases} \quad (5.19)$$

Therefore, when the machine operates on the current limit circle, ζ can be derived as

$$\zeta = \frac{\omega_{cc} (1 - \sigma_I \eta \omega_{mh} / \omega_b)}{2\sqrt{\eta \omega_{mh}}} \quad (5.20)$$

Therefore, by setting $\zeta=1$ on the operation point where $\sigma_I=\sigma_s$, $\eta=\eta_s$, ω_{mh} can be obtained as

$$\omega_{mh}|_{On} = \frac{1}{\eta} \frac{\omega_{cc}}{4} \left/ \left(1 + \frac{\omega_{cc}}{\omega_b} \frac{\sigma_s}{2} \right) \right. \quad (5.21)$$

Since $\omega_{mh}|_{On}$ is obtained on the current limit circle, proper σ_s and η_s in (5.21) can be selected according to the variation of σ_I and η on the current limit circle by referring to (5.8) and (5.18). Fig. 5.4 illustrates the numerical results of the variation of σ_I and η against i_{dn} with

the parameters in Table 5.3 (shown in the experimental verification section). According to Fig. 5.4, σ_s and η_s can be set to a value larger than most of the operation points by reasonably ignoring the condition $i_{dn} = -1$ on the current limit circle. For example, σ_s and η_s are both set at 2 in the experiment.

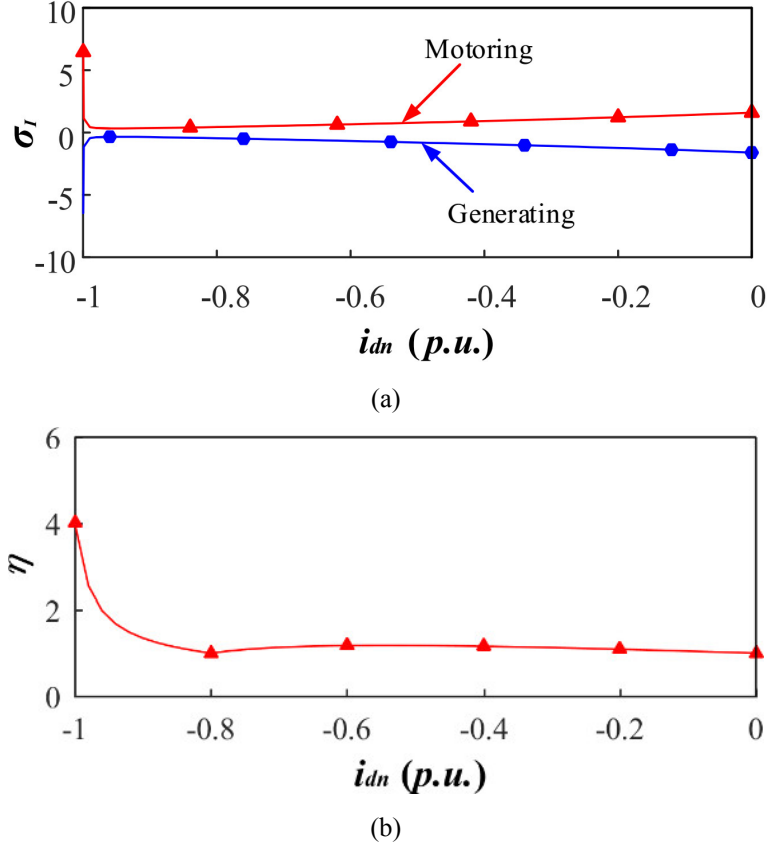


Fig. 5.4. The variation of σ_l and η against i_{dn} on the current limit circle. (a) σ_l . (b) η .

Finally, by considering the regions, i.e. on and in the current limit circle, the control parameters λ_{Ih} and $\lambda_{\theta h}$ can be tuned as

$$\lambda_{Ih} = \frac{\omega_{mh}}{2V_m L_s |\omega_e^0|}, \lambda_{\theta h} = \frac{\omega_{mh}}{2V_m L_s |\omega_e^0| i_c}, \omega_{mh} = \min\{\omega_{mh}|_{On}, \omega_{mh}|_{In}\} \quad (5.22)$$

5.4 Experimental Verification

The experiments are implemented based on the dSPACE platform on a non-salient-pole PMSM with MTPV region ($i_{cn}=0.8$). The power switches of the inverter are IRFH7440 MOSFET. The PWM switching frequency is 10 kHz. The load torque is provided by the test

rig-II (Appendix A), i.e. a would field excited DC machine with rated power at 150 w and rated speed at 4000 rpm. The machine and drive parameters are listed in Table 5.3.

Table 5.3 Machine and Drive Parameters

Parameters	Values
Machine stator resistance (R_s)	0.25 ohm
Synchronous inductance (L_s)	1.7 mH
PM-flux linkage(ψ_m)	10 mWb
Number of pole pairs	10
DC link voltage (V_{dc})	14 V
Current limit (I_m)	7.35A
Current bandwidth (ω_{cc})	1200 rad/s
Control parameter (λ_s)	200 rad/s

Since $w_I = |V_{qn}|$ and $w_\theta = |V_{dn}|$ in the flux-weakening region, for the practical application, in order to smooth the weight factors when the system transfers from the constant torque region to the flux-weakening region, w_I and w_θ can be processed with low pass filters and can be obtained as

$$\begin{cases} w_\theta = \frac{|V_d|}{|V_{th}|} \frac{\omega_w}{s + \omega_w}, w_I = \sqrt{1 - w_\theta^2}, \text{ if } |V_s| < V_{th} \\ w_\theta = \frac{|V_d|}{|V_s|} \frac{\omega_w}{s + \omega_w}, w_I = \sqrt{1 - w_\theta^2}, \text{ if } |V_s| \geq V_{th} \end{cases} \quad (5.23)$$

where ω_w is the bandwidth of the low pass filter, which is set at 1000 rad/s; V_{th} is the threshold value in order to avoid zero divide, which is set at $0.2|V_{sr}^*|$. Since when the resistance is ignored, $V_q=0$ defines the MTPV curve. In the experiments, when $V_q < 0$, w_θ and w_I are limited at 1 and 0, respectively. Therefore, the HVFC will become a CAVFC when the system operates on the left side of the MTPV curve. The whole control diagram is shown in Fig. 5.5.

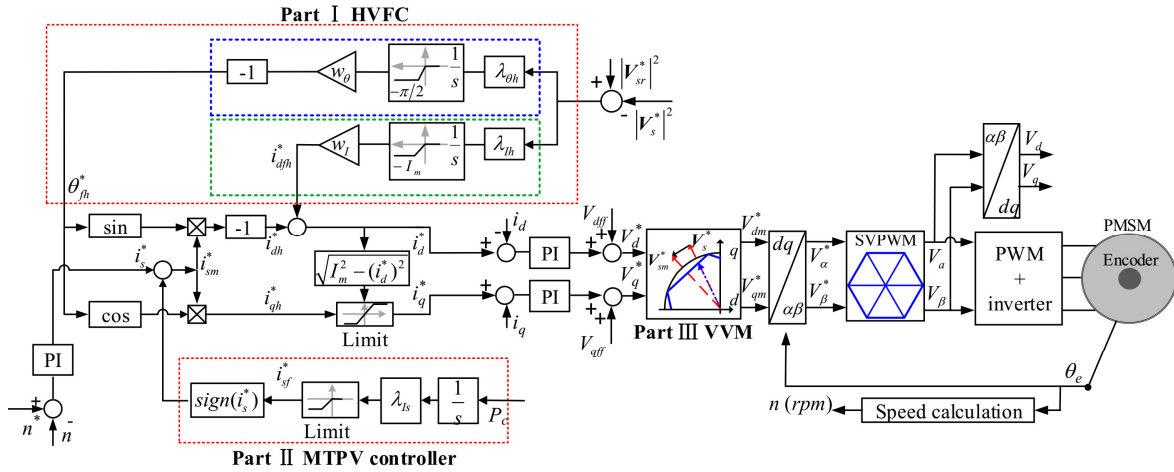
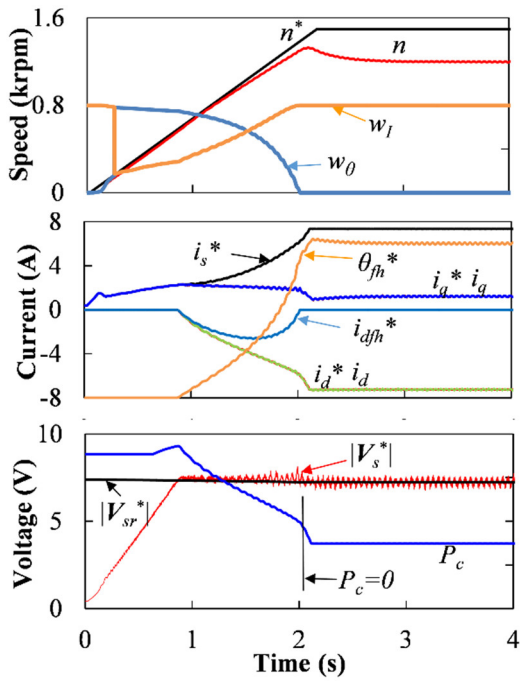


Fig. 5.5. Schematic of HFVC based on CVC system.

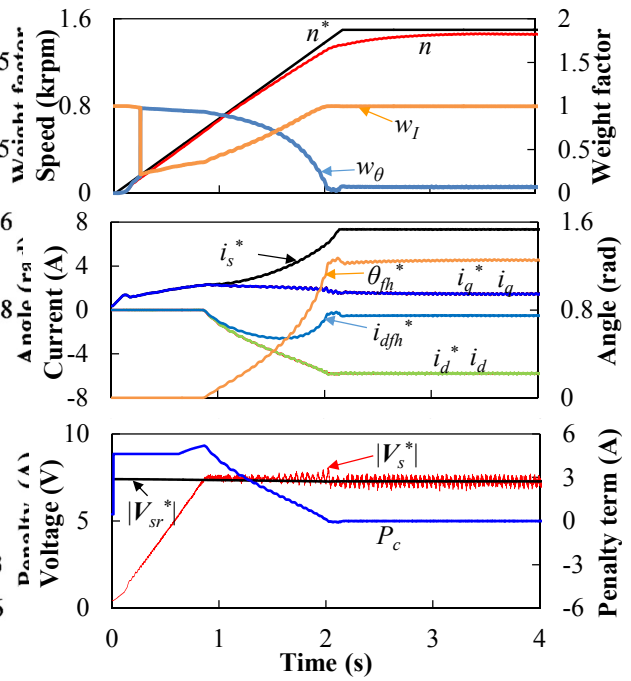
5.4.1 With and Without MTPV Controller in HFVC

When $M=0.9$, for a given speed command $n^*=1500$ rpm with the speed ramp at 750 rpm/s, Fig. 5.6 shows the dynamic performance and the current trajectory when the MTPV controller is disabled in HFVC. In Fig. 5.6(a), it can be seen that the system without MTPV controller cannot stabilize on the MTPV curve ($P_c=0$). However, the voltage magnitude $|V_s^*|$ is tracked well with the reference $|V_{sr}^*|$ during the acceleration process even after the system passes $P_c=0$. The profile of the weight factors, i.e. w_I and w_θ indicate that the HVFC is gradually dominated by the CAVFC part as the system approaches the MPTV curve, which can also be confirmed by the variation of i_{dth}^* and θ_{fh}^* . Since the MTPV controller is disabled, the system is finally stabilized on the current limit circle as shown in Fig. 5.6(b).

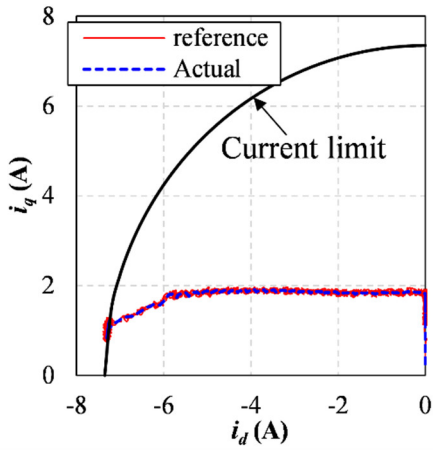
Fig. 5.7 shows the dynamic performance and the current trajectory with the integral MTPV controller in HFVC. It shows that the system can stabilize on the MTPV curve ($P_c=0$) with the applied integral MTPV controller. Therefore, the machine can achieve a higher speed than the system without MTPV controller.



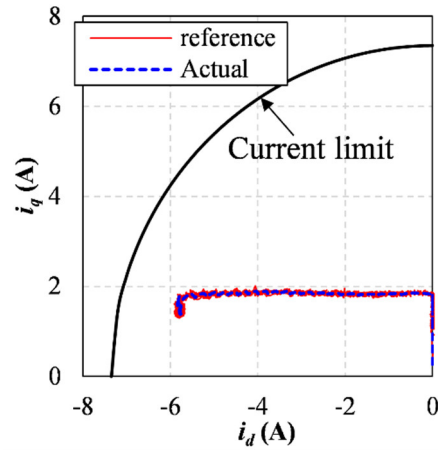
(a) Dynamic performance.



(a) Dynamic performance.



(b) Current trajectory.



(b) Current trajectory.

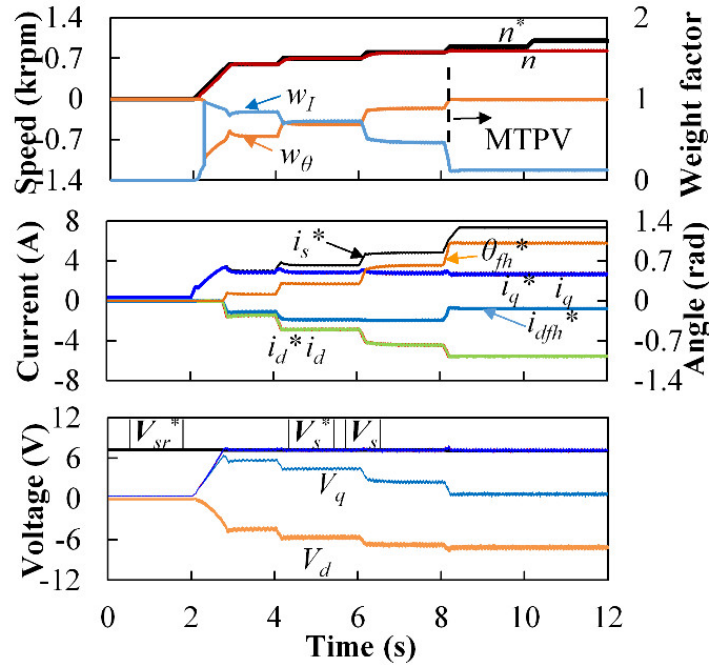
Fig. 5.6. HFFC without MTPV controller.

Fig. 5.7. HFFC with integral MTPV controller.

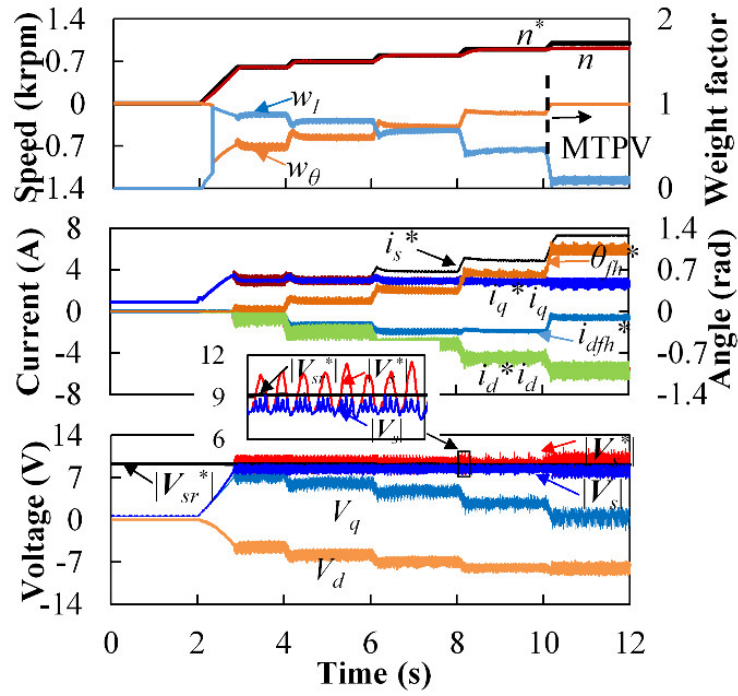
5.4.2 Performance When Approaching MTPV Curve

With the applied MTPV controller, the system performance when approaching MTPV curve is observed by changing the speed command from 0 rpm to 600rpm, 700rpm, 800rpm, 900rpm and 1000 rpm every 2 seconds, as shown in Fig. 5.8. Fig. 5.8(a) shows the system

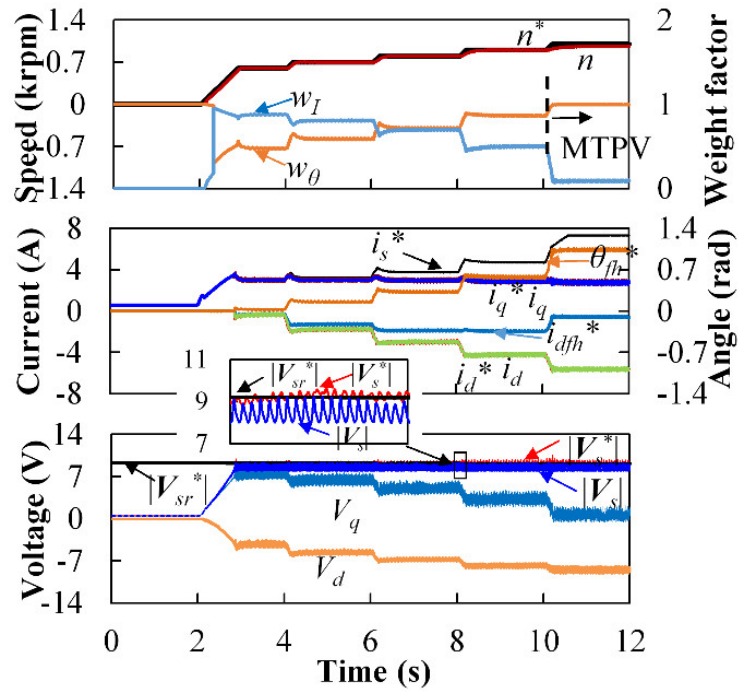
performance of HFFC in the linear modulation region and $M=0.9$. It can be seen that no oscillation appears at each speed stage. The variation of the weight factors also show that the HVFC is gradually dominated by the CAVFC part as the system approaches MTPV curve, which can also be observed in the variation of i_{dfh}^* and θ_{fh}^* . Fig. 5.8(b) shows the system performance of HFFC without VVM in the over modulation region and $M=1.15$. In Fig. 5.8(b), although the machine can achieve a higher speed in the over modulation region, the oscillation occurs in $|V_s^*|$ and much ripples appear in the current. When the VVM is applied in HFFC, as shown in Fig. 5.8(c), the feedback voltage magnitude $|V_s^*|$ is tracked well with the reference $|V_{sr}^*|$ in the flux-weakening region, and the oscillation is disappeared. The ripples in the voltage and current are much less than that without VVM in the over modulation region. The periodical ripple in $|V_s|$ is due to the over modulation block when the system operates in the over modulation region. The frequency of the ripple in $|V_s|$ is six times of the fundamental frequency.



(a) $M=0.9$.



(b) $M=1.15$ and without VVM.



(c) $M=1.15$ and with VVM.

Fig. 5.8. System (with HFFC) performance when approaching MTPV curve under various conditions.

5.4.3 Transition Between Motoring and Generating Conditions

The transition performance between motoring and generating conditions of the HFFC is demonstrated in Fig. 5.9 with the speed command $n^*=1200$ rpm and when $M=0.9$ and 1.15. In the experiments, the load torque is regulated manually by changing the excitation current of the DC machine. In both linear and over modulation regions, Fig. 5.9 shows that the HVFC is dominated by the DCVFC part ($w_l > w_\theta$) at light load condition. Consequently, as expected, the system can achieve a smooth and stable transition between motoring and generating conditions like the DCVFC in DQFFC.

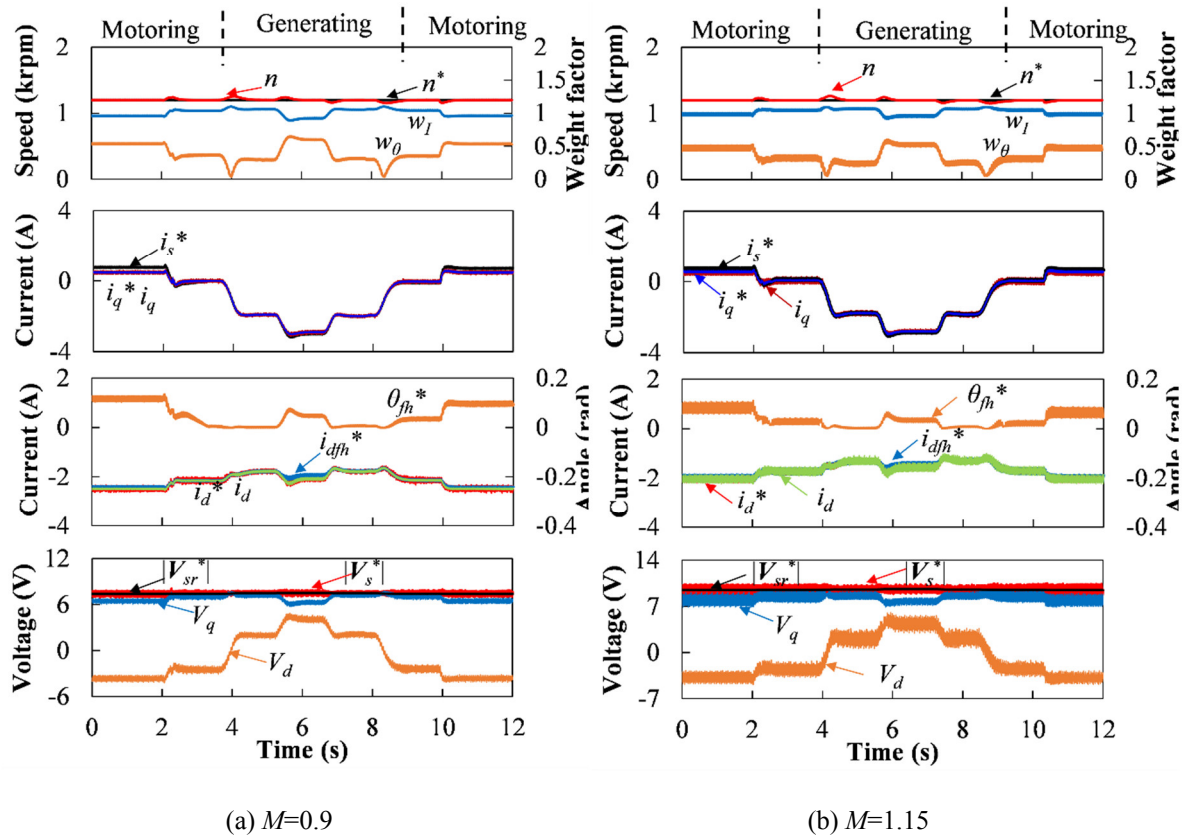


Fig. 5.9. Transition performance between motoring and generating conditions in HFFC.

5.5 Conclusion

In this chapter, by considering MTPV region, an HFFC is proposed based on a novel HVFC, which aims to solve the oscillation or instability problem in DQFFC and CAAFFC. The proposed HVFC in HFFC is achieved by regulating the d-axis current command and

current angle command simultaneously, which can utilize the complementary advantages of the DCVFC and CAVFC at different flux-weakening regions.

The linearized model of the HVFC has been analysed, based on which the key issues of HVFC, i.e. the control parameters and the weight factors (w_I and w_θ), have been designed.

The optimized weight factors show that:

- 1) HVFC is dominated by DCVFC at light load condition;
- 2) HVFC is dominated by CAVFC when approaching the MTPV curve.

Therefore, the design of the MTPV controller in HFFC directly adopts the same method as that in CAAFFC, which has been addressed in chapter 4.

Finally, the experiments are implemented, which have verified that

- 1) The oscillation in over modulation region of DQFFC when approaching MTPV curve is effectively suppressed in HFFC;
- 2) The instability at light load in generating condition of DQFFC is effectively solved in HFFC;
- 3) The proposed HFFC can achieve a smooth transition between motoring and generating conditions.

CHAPTER 6 FUZZY LOGIC SPEED CONTROL OF PMSM AND FEEDBACK VOLTAGE RIPPLE REDUCTION IN FLUX- WEAKENING REGION

Previous chapters have indicated that the stability problem is mainly related to the control parameters of the feedback flux-weakening controller and the operation mode. The nonlinear behaviour of the feedback flux-weakening control renders the system to perform differently at different regions. In addition, the stability problem becomes worse when the system operates in the over modulation region, which is mainly due to less voltage margin. In this chapter, it further investigates the influence of the resultant feedback voltage ripple that originates from the non-ideal drive system based on DCVFC. It indicates that the oscillation could even occur in the linear modulation region if a good speed dynamics is required. Furthermore, an adaptive fuzzy logic speed controller is proposed to reduce the influence of the feedback voltage ripples. It can achieve both good dynamic and steady-state performance in the flux-weakening region.

6.1 Introduction

Although the linearized model can provide a good tool to analyse the small signal behaviour on the equilibrium point, it cannot guarantee the large signal dynamics especially when the voltage is saturated. In the constant torque region, the system is not sensitive to the feedback voltage ripple due to enough voltage margin. However, in the flux-weakening region, as the voltage margin decreases, the system is more sensitive to the feedback voltage ripple than that in the constant torque region. The feedback voltage ripple can be induced by both current command ripple and speed ripple, which can be caused by torque ripple [MAT93] [HOL96] [XIA15] and non-ideal installation of the speed sensors [HWA11] [QIN10] [RAJ17]. In this chapter, it will show that the feedback voltage ripple induced by the current command ripple vary with operation points and could dominate in certain flux-weakening

regions, thus posing difficulty to improve the speed dynamics with a conventional proportional-integral (PI) controller. The feedback voltage ripple in the flux-weakening region can be reduced by using smaller PI gains of the speed PI controller. Therefore, the coupling between the speed PI controller and the voltage feedback controller can be reduced. However, it compromises the speed dynamics [YON12] [HAR13]. In order to solve this conflict, a nonlinear speed PI controller can be employed.

As an alternative to the conventional PI controller, the fuzzy logic speed controller has been widely applied to the variable speed drives [SIL98] [KAD01] [ZHU02] [UDD07] [UDD11]. In [YIN93] [DIN99], the authors prove that the simplest fuzzy logic controller (FLC) is actually a nonlinear PI controller with proportional and integral gains changing with inputs of the controllers. In addition, since the fuzzy logic system (FLS) incorporates expert knowledge to design FLC and does not need an accurate model of the system, it provides an efficient tool to embed human intuitive thinking to achieve the desired performance. Moreover, the robustness of the system in a wide range of changing condition can be further improved with an adaptive FLC by updating the controller parameters online [SIL98] [KAD01]. In [ZHU02], a simple adaptive FLC which aims to reduce steady-state current ripple without compromising the speed dynamics is proposed and the experiments are implemented only in the constant torque region. In this chapter, the adaptive FLC speed controller is designed by applying an adaptive scaling factor at the output of FLC, aiming to reduce the feedback voltage ripple that caused by the current ripple in the flux-weakening region. The systems with the conventional PI controller and adaptive FLC are compared in the constant torque region and different flux-weakening regions. It shows that the adaptive FLC can achieve both good dynamic and steady-state performance in both constant torque and different flux-weakening regions. In addition, the DC-link voltage utilization can be further increased and better flux-weakening capability can be obtained. Finally, the experiments are implemented to verify the analyses and adaptive FLC.

6.2 Flux-weakening Control with Speed PI Controller

6.2.1 Current Vector Control System with Speed PI Controller

Fig. 6.1 shows a conventional current vector control (CVC) system with a d-axis current based voltage magnitude feedback controller (DCVFC). As shown in Fig. 6.1, the control system comprises the current control mode (CCM) and the speed control mode (SCM). The CCM is simply achieved by setting the q-axis current command $i_{q,MTPA}^*$, while $i_{d,MTPA}^*$ is set to zero by considering MTPA. In the SCM, the q-axis current command $i_{q,MTPA}^*$ is obtained through a speed controller which is a PI or a FLC in Fig. 6.1. In this section, the system with a PI controller will be discussed first.

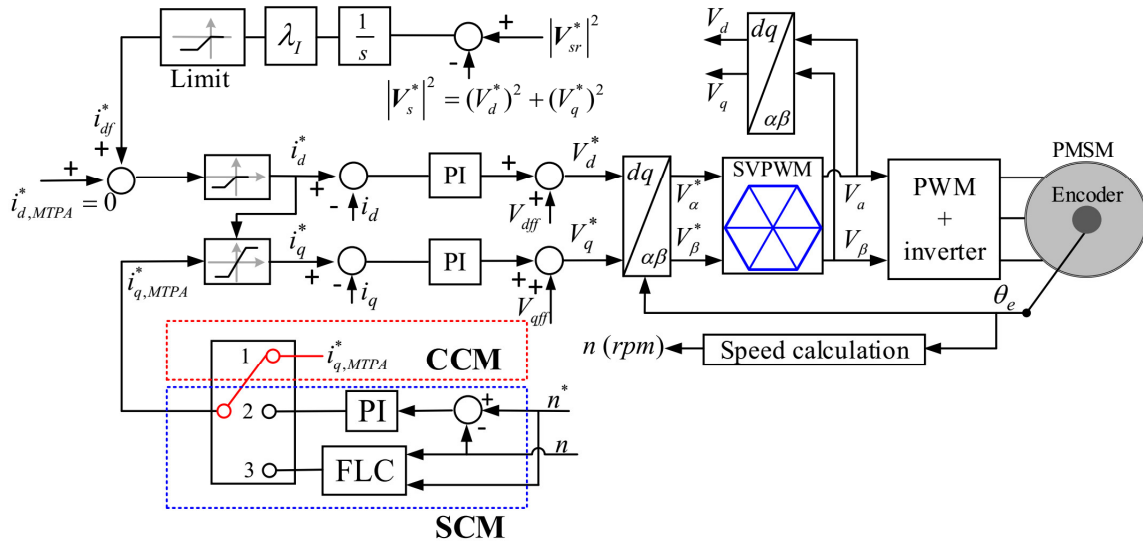


Fig. 6.1. Schematic of current vector control (CVC) system with DCVFC.

The conventional speed PI controller is normally tuned by assuming that:

- 1) The inner current loop is equivalent to a first-order delay element with the time constant $1/\omega_{cc}$;
- 2) The speed controller is not saturated;
- 3) The sampling frequency is much higher than the fundamental frequency.

Therefore, the simplified block diagram of the speed control loop can be depicted in .

6.2.

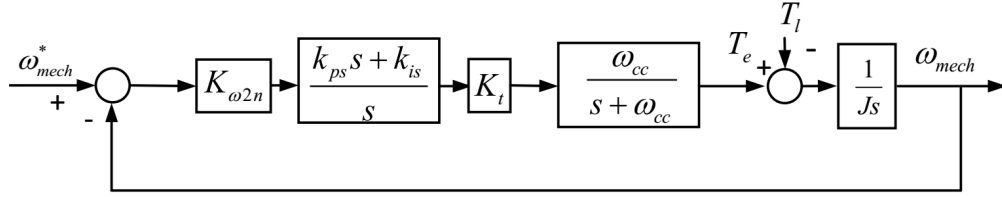


Fig. 6.2. Simplified block diagram of the speed loop.

In . 6.2, ω_{mech}^* and ω_{mech} are the mechanical speed command and the actual mechanical speed, respectively; $K_{\omega 2n}=9.55$, which is the gain needed to convert the speed unit from rad/s to rpm; k_{ps} and k_{is} are the proportional and integral gains of the speed PI controller; K_t is the torque constant. By further assuming that the speed bandwidth is much lower than the current bandwidth, the current loop delay can be reasonably ignored, and the close-loop transfer function of the speed loop can be expressed as

$$\Phi_s(s) = \frac{1}{J} \frac{K_{\omega 2n} K_T (k_{ps} s + k_{is})}{s^2 + \frac{k_{ps} K_{\omega 2n} K_T}{J} s + \frac{k_{is} K_{\omega 2n} K_T}{J}} \quad (6.1)$$

By referring to a typical second-order system, k_{ps} and k_{is} can be tuned as

$$k_{is} = \frac{\omega_{Ns}^2}{K_{\omega 2n} K_T} J, k_{ps} = \frac{2J \omega_{Ns} \zeta}{K_{\omega 2n} K_T} \quad (6.2)$$

where ω_{Ns} is the undamped natural frequency, ζ is the damping factor.

Due to the current limit of the machine, the output of the speed controller is normally imposed by the current limit. Therefore, the anti-windup speed controller is normally adopted to alleviate the saturation problem of the speed controller [PEN96], by which the speed dynamics will be improved, normally with much less overshoot. In this chapter, the anti-windup method of the speed PI controller is achieved by clamping the output of the integrator to the current limit once it is saturated.

When the machine operates in the constant torque region, as there is enough voltage control margin, the system is less sensitive to the voltage ripple in the feedback voltage magnitude $|V_s^*|$, where $|V_s^*| = \sqrt{(V_d^*)^2 + (V_q^*)^2}$. However, due to reduced voltage margin in

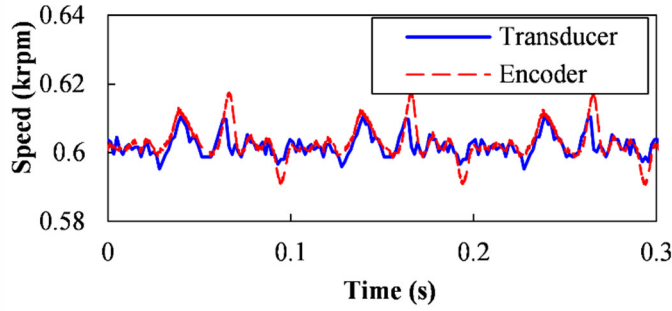
the flux-weakening region, the system performance could be seriously affected by the feedback voltage ripple. Therefore, in this section, the speed and torque ripples in the test rig I (Appendix A) which has a torque transducer will be shown first. Then, the feedback voltage ripple will be analysed.

6.2.2 Voltage Ripples Analysis in Flux-weakening Region

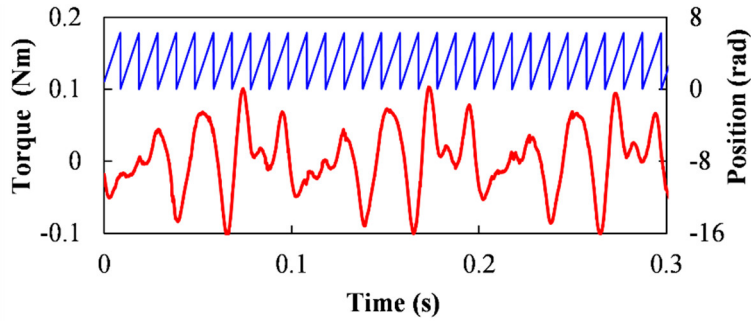
6.2.2.1 Speed and Torque Ripples in Test Rig

In theory, many factors, such as load torque ripple, misalignment of the transmission system, non-ideal installation of the encoder and even the eccentricity of the rotor of PMSM or the load machine can cause disturbances to the control system. These disturbances could result in excessive voltage ripple, which could deteriorate the system performance, especially in the flux-weakening region.

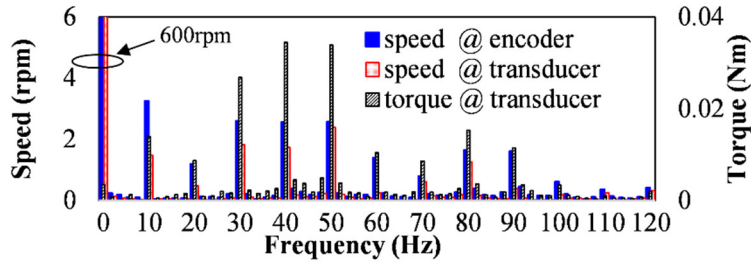
In order to check the speed and torque ripples which may be caused by the test rig, including wound field DC machine, position sensor, and the coupling, etc., Fig. 6.3(a) and Fig. 6.3(b) show the measured speed and torque waveforms when the test rig is driven by the wound field DC machine at 600 rpm while the PMSM is disconnected from the power supply. The speed ripples are double checked by using two different sensors, i.e. encoder and torque transducer. The measured speed in Fig. 6.3(a) shows that almost the same speed ripples appear by using encoder and torque transducer. Fig. 6.3(c) shows the spectra of the measured speed and torque. It indicates that the frequency of the speed ripple is consistent with torque ripple, which is dominant in the low-frequency range and appears at the integer multiples of the mechanical frequency. The measured speeds obtained from two speed sensors still show some discrepancies, which are mainly caused by the different installation methods and locations. According to the measured speeds from the two sensors, it implies that the speed ripple could also be induced by the speed sensors.



(a) Waveforms of the speed.



(b) Waveforms of torque obtained by the torque transducer and position obtained from the encoder.



(c) Spectra for speed and torque. (Frequency resolution: 2 Hz, @transducer: measured by torque transducer box, @encoder: measured and calculated by encoder)

Fig. 6.3. Speed and torque ripples.

6.2.2.2 Feedback Voltage Ripple Analysis

Although many non-ideal factors could cause speed ripples, in the following analysis, the non-ideal factors are regarded as a black box, only the ripple in the measurable speed is considered as the original source of the feedback voltage ripple.

The speed ripple can directly contribute to the feedback voltage ripple through the voltage decoupling terms, and can also indirectly induce feedback voltage ripple through q -

axis current command ripple by the speed PI controller. In this section, the phenomenon that the voltage ripple could differ in different flux-weakening regions will be analyzed, and the phenomenon that the system is more sensitive in certain flux-weakening region will be explained.

In the flux-weakening region, since the actual voltage ripple should also consider the effect of the regulation of voltage loop, the feedback voltage ripple without consideration of the voltage loop can be considered as the voltage disturbance to the voltage loop. Voltage disturbances induced by the q-axis current command ripple and the speed ripple, i.e. the feedback voltage ripples in $|V_s^*|^2$ without consideration of the voltage loop, can be evaluated through the small-signal gain characteristics, i.e. $K_{HI}(s)$ and $K_{H\omega}(s)$, which are defined as

$$\begin{cases} K_{HI}(s) = \frac{\Delta |V_s^*|^2}{\Delta i_q^*} \approx \frac{\Delta |V_s|^2}{\Delta i_q} T_{iq}(s) \\ K_{H\omega}(s) = \frac{\Delta (|V_s^*|^2)}{\Delta \omega_e} \approx \frac{\Delta (|V_s|^2)}{\Delta \omega_e} \end{cases} \quad (6.3)$$

where the variables with the prefix ‘ Δ ’ indicate the corresponding small signals.

Therefore, it can be derived that

$$\begin{cases} K_{HI}(s) = (-2V_d^0 \omega_e^0 L_s + 2V_q^0 L_s s) \frac{\omega_{cc}}{s + \omega_{cc}} \\ K_{H\omega}(s) = 2V_q^0 (L_s i_d^0 + \psi_m) - 2V_d^0 L_s i_q^0 \end{cases} \quad (6.4)$$

Assuming that the voltage ripple is small enough, the voltage disturbances caused by the q-axis current ripple and the speed ripple can be approximated as

$$V_{DI} \approx K_{HI}(s) i_{qH}^*, V_{D\omega} \approx K_{H\omega}(s) \omega_{eH} \quad (6.5)$$

where i_{qH}^* and ω_{eH} are the ripples in i_q^* and ω_e , respectively; V_{DI} and $V_{D\omega}$ are the voltage disturbances that are induced by i_{qH}^* and ω_{eH} , respectively.

For the speed PI control, the relationship between i_{qH}^* and ω_{eH} can be obtained as

$$\frac{i_{qH}^*}{\omega_{eH}} = \frac{\Phi_i(s)}{P} = \frac{J}{PK_T} 2\omega_{Ns} \frac{(s^2 + 0.5\omega_{Ns}s)}{s^2 + 2\omega_{Ns}s + \omega_{Ns}^2} \quad (6.6)$$

where $\Phi_i(s)$ is the transfer function from ω_{mech} to i_q^* . $\Phi_i(s)$ is a second order lower pass filter, the dominant pole of which is $-\omega_{Ns}$. As the harmonics in the ripple mainly appear at integer multiple times of the mechanical frequency ω_{mech} , assuming that ω_{Ns} is much lower than ω_{mech} , (6.6) can be approximated as

$$i_{qH}^* \approx 2\omega_{Ns} \frac{J}{PK_T} \omega_{eH} \quad (6.7)$$

Therefore, V_{DI} can be approximated as

$$V_{DI} \approx 2K_{HI}(s)\omega_{Ns} \frac{J}{PK_T} \omega_{eH} \quad (6.8)$$

Fig. 6.4 shows the equivalent linearized block diagram of the voltage loop with considering voltage disturbance V_{dst} .

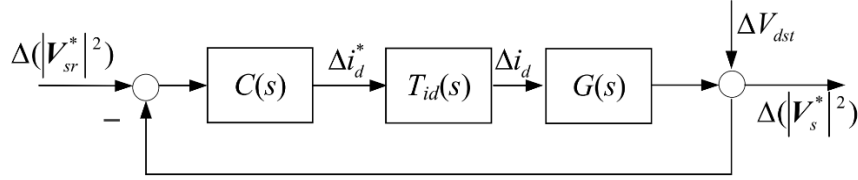


Fig. 6.4. Block diagram of linearized model of voltage loop considering voltage disturbance.

In Fig. 6.4, V_{dst} represents the voltage disturbance that is the combination of V_{DI} and $V_{D\omega}$, i.e.

$$V_{dst} = V_{DI} + V_{D\omega} \quad (6.9)$$

The actual voltage ripple in $|V_s^*|^2$ can be evaluated by the small-signal gain characteristic, i.e. $\Phi_v(s)$, which is the transfer function from ΔV_{dst} to $\Delta|V_s^*|^2$.

$$\Phi_v(s) = \frac{\Delta|V_s^*|^2}{\Delta V_{dst}} = \frac{1}{1 + T_{id}(s)C(s)G(s)} \quad (6.10)$$

Therefore, the actual voltage ripple can be approximated as

$$V_{sH} \approx \Phi_v(s)V_{dst} \quad (6.11)$$

where V_{sH} is the feedback voltage ripple in $|V_s^*|^2$ after the regulation of the voltage loop.

In order to provide more insight of the variation of the voltage ripple, $T_{id}(s)$ in (6.10) can be seen as a unit gain by assuming that the current bandwidth is much higher than the bandwidth of the voltage loop. Therefore, $\Phi_v(s)$ can be further derived as

$$\Phi_v(s) = K_v \frac{s}{s + \omega_v} \quad (6.12)$$

where K_v , ω_v are expressed as

$$K_v = \frac{1}{(1 + \lambda b)}, \quad \omega_v = \frac{\lambda a}{(1 + \lambda b)} \quad (6.13)$$

It can be seen that $\Phi_v(s)$ is a high pass filter multiplied by a gain K_v . The bandwidth of the high pass filter is ω_v . In mode A and mode B, K_v and ω_v can be derived as

$$\begin{cases} K_{vA} = \frac{1}{(1 - \omega_{mA}\sigma / \omega_b)}, & \omega_{vA} = \frac{\omega_{mA}}{(1 - \omega_{mA}\sigma / \omega_b)} \\ K_{vB} = \frac{1}{(1 + V_d^0 \omega_m / (|V_{sr}^*| \cdot |\omega_e^0|))}, & \omega_{vB} = \omega_m |V_q^0| / |V_{sr}^*| \end{cases} \quad (6.14)$$

where K_{vA} and K_{vB} represent K_v in mode A and mode B, respectively; ω_{vA} and ω_{vB} represent the value of ω_v in mode A and mode B, respectively.

Based on the parameters in Table 6.2, the numerical results of the coefficients ω_{vA} and K_{vA} are illustrated in Fig. 6.5, while the numerical results of the coefficients K_{vB} , ω_{vB} are illustrated in Fig. 6.6.

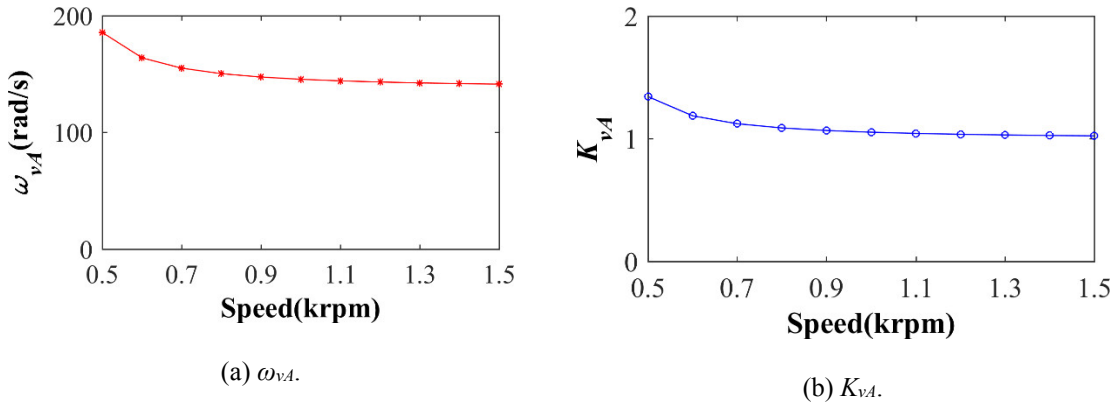


Fig. 6.5. Coefficients of ω_{vA} and K_{vA} in the flux-weakening region.

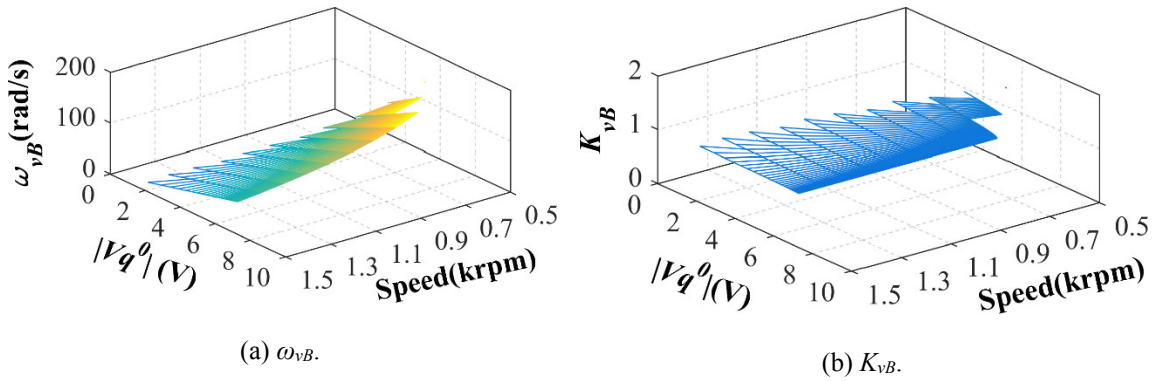


Fig. 6.6. Coefficients of ω_{vB} and K_{vB} in flux-weakening region.

It can be seen from Fig. 6.5 and Fig. 6.6 that the coefficients K_{vA} and K_{vB} are almost equal to 1. The bandwidth in mode A, i.e. ω_{vA} , is almost a constant while the bandwidth in mode B, i.e. ω_{vB} , becomes smaller in the lower $|V_q^0|$ region. The decrease of ω_{vB} implies weaker attenuation of the harmonics.

Furthermore, in mode A, since the machine ideally operates on the current limit circle, i_q^* is constrained by the current limit and determined by i_d^* . Therefore, in mode A, the voltage disturbance mainly originates from the speed ripple. In mode B, the machine operates inside the current limit circle, and i_d^* and i_q^* are controlled independently. The voltage disturbance is the combination of the ripples that are caused by the speed ripple and the q-axis current command ripple.

Consequently, with combination of (6.5), (6.8), (6.9), (6.11) and (6.12), the magnitude of feedback voltage ripple in mode A and mode B can be approximated as

$$\begin{cases} |V_{sHA}| \approx K_{vA} \left| \frac{s}{s + \omega_{vA}} \right| \cdot |K_{H\omega}(s)| \cdot |\omega_{eH}| \\ |V_{sHB}| \approx K_{vB} \left| \frac{s}{s + \omega_{vB}} \right| \cdot \left| 2K_{HI}(s)\omega_{Ns} \frac{J}{PK_T} + K_{H\omega}(s) \right| \cdot |\omega_{eH}| \end{cases} \quad (6.15)$$

where V_{sHA} and V_{sHB} represent the value of V_{sH} in mode A and mode B, respectively.

It can be referred from (6.4) that $|K_{HI}(s)|$ is much higher than $|K_{H\omega}(s)|$, and will become higher when $|V_q^0|$ decreases. Based on the parameters in Table 6.2, the numerical results of $|K_{HI}(s)|$ and $|K_{H\omega}(s)|$, at the lowest frequency of the ripple, i.e. when $s=j\omega_{mech}$, are illustrated in Fig. 6.7. It shows that both $|K_{HI}(s)|$ and $|K_{H\omega}(s)|$ are very small in higher $|V_q^0|$ region. However, $|K_{HI}|$ is much higher than $|K_{H\omega}|$ in lower $|V_q^0|$ region.

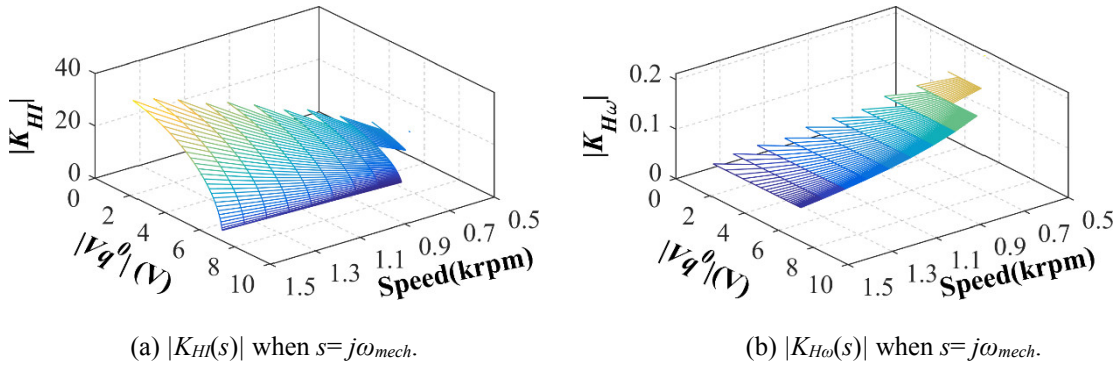


Fig. 6.7. Variation of $|K_{HI}(s)|$ and $|K_{H\omega}(s)|$ at mechanical frequency ω_{mech} in flux-weakening region.

With (6.15), it can be referred that the voltage ripple in mode B in the flux-weakening region tends to be higher than that in mode A, and could be dominated by that caused by the q-axis current command ripple, especially under such conditions, i.e.

- 1) The system with large J and small K_T ;
- 2) In the smaller q-axis voltage region where $|K_{HI}(s)|$ becomes higher and ω_{vB} becomes lower;
- 3) The speed controller tuned with higher ω_{Ns} in the constant torque region.

Due to the limited voltage control margin, the increased feedback voltage ripple could deteriorate the system performance in the flux-weakening region and may even cause oscillation, especially in mode B and lower q-axis voltage region. For the existing drive system, a proper way to reduce the actual voltage ripple that is caused by the q-axis current ripple is to reduce ω_{Ns} . However, the speed dynamic performance and load disturbance rejection capability will be sacrificed. In order to solve this conflict, a nonlinear speed PI controller, such as adaptive fuzzy logic speed controller, can be employed, as will be described in the next section.

6.3 Adaptive Fuzzy Logic Speed controller

6.3.1 PI Controller and FLC

The conventional speed PI controller expressed in the discrete incremental form can be written as

$$\begin{aligned} i_{q,MTPA}^*(n_i) &= i_{q,MTPA}^*(n_i - 1) + Di_{q,MTPA}^*(n_i) \\ Di_{q,MTPA}^*(n_i) &= k_{ps} [e_n(n_i) - e_n(n_i - 1)] + e_n(n_i) k_{is} T_s \end{aligned} \quad (6.16)$$

where n_i denotes the step of the speed control cycle; $Di_{q,MTPA}^*(n_i)$ is the incremental component of current command in each control cycle; e_n is the speed tracking error, i.e. ($n^* - n$).

The incremental component $Di_{q,MTPA}^*(n_i)$ can be further transferred as

$$Di_{q,MTPA}^*(n_i) = T_s [k_{ps} \dot{e}_n(n_i) + e_n(n_i) k_{is}] \quad (6.17)$$

where $\dot{e}_n(n_i)$ is the approximate derivative of machine speed and expressed as

$$\dot{e}_n(n_i) = [e_n(n_i) - e_n(n_i - 1)] / T_s \quad (6.18)$$

Therefore, for a conventional PI controller, the main task is to obtain a proper $Di_{q,MTPA}^*(n_i)$ which is a linear function of the $\dot{e}_n(n_i)$ and $e_n(n_i)$ with the coefficient k_{ps} and k_{is} . However,

for the FLC, it actually maps the crisp inputs to a crisp output through a nonlinear function f_{fuzzy} , i.e.

$$Di_{q,MTPA}^*(k) = f_{fuzzy}(\dot{e}_n(k), e_n(k)) \quad (6.19)$$

Each $Di_{q,MTPA}^*(n_i)$ corresponds to one k_{ps} and k_{is} . In [YIN30] [DIN99], it is proved that the simplest FLC is actually a nonlinear PI controller with the gains changing with process output. Since the FLC actually mimics human thinking, with the aid of the FLS, the human intuitive thinking can be embedded into the FLC. For example, in order to achieve less current ripple at steady state without compromising the dynamic performance, the intuitive thinking is to apply higher gains when the speed tracking error is larger and lower gains when the speed tracking error is smaller. In the FLC, this intuitive thinking can be realized by adjusting the output membership function adaptively, as will be discussed as follows.

6.3.2 Design of Adaptive FLC

A general FLC is mainly composed of four components, i.e. 1) fuzzification; 2) fuzzy rule base; 3) inference; 4) defuzzification [YIN93] [SHE05] [UDD11] [UDD07] [DIN99]. Fig. 6.8 shows a block diagram of a two-input and one-output FLC combined with a scaling factor at the output. In Fig. 6.8, the adaptive changing output membership function is achieved by applying an adaptive scaling factor k_u at the output of the defuzzification block in order to simplify the implementation. According to Fig. 6.8, $Di_{q,MTPA}^*(n_i)$ can be obtained as

$$Di_{q,MTPA}^*(n_i) = T_s k_u u(n_i) \quad (6.20)$$

where k_u is the scaling factor; u is the output of the defuzzification block, which represents the current changing rate when $k_u=1$.

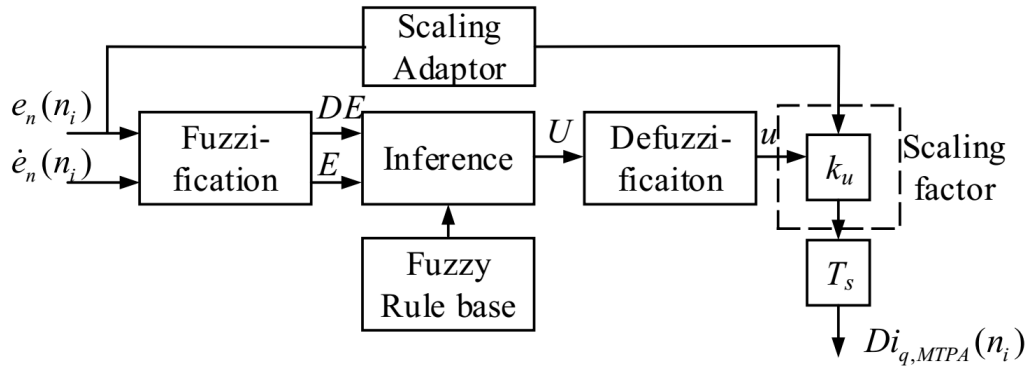
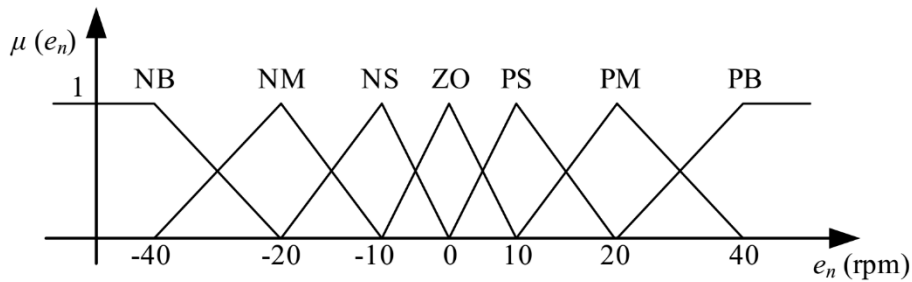


Fig. 6.8. Block diagram of FLC with a scaling adaptor.

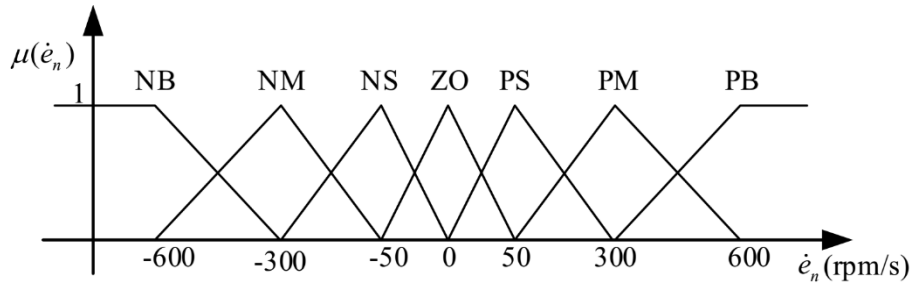
The design procedures of the adaptive FLC are:

1) Fuzzification

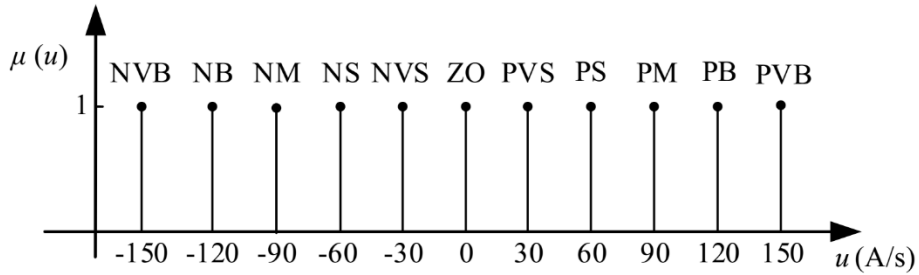
Several linguistic labels are used to describe the fuzzy sets of the two inputs and one output, namely, negative very big (NVB), negative big (NB), negative middle (NM), negative small (NS), zero (ZO), positive small (PS), positive middle (PM), positive big (PB), positive very big (PVB). The universe of the discourse of inputs e_n and \dot{e}_n , i.e. E and DE , are divided into 7 fuzzy sets (NB, NM, NS, ZO, PS, PM, PB). The universe of the discourse of the output u , i.e. U , is divided into 9 fuzzy sets (NVB, NB, NM, NS, ZO, PS, PM, PB, PVB). Fig. 6.9 shows the membership functions of the inputs and output adopted according to the experimental results. The membership functions map the crisp value of the inputs and output to the membership degree μ of the each fuzzy set. As shown in Fig. 6.9(a) and Fig. 6.9(b), the triangular membership functions are used for the inputs e_n and \dot{e}_n due to their high computational efficiency. The singleton membership function is used for output variable u , as shown in Fig. 6.9(c).



(a) Input e_n .



(b) Input \dot{e}_n



(c) Output u .

Fig. 6.9. Membership functions.

2) Fuzzy Rule Base and Inference

Fuzzy rule base is composed of multiple IF-THEN rules with antecedents and consequent parts. The rules have the form as:

$$R_{i,j}: \text{If } e_n \text{ is } E_i \text{ and } \dot{e}_n \text{ is } DE_j, u \text{ is } U_m,$$

where $i, j = 1, 2, \dots, 7$; $m = 1, 2, \dots, 9$.

For example, $R_{1,1}$ and $R_{7,7}$ are

$$R_{1,1}: \text{If } e_n \text{ is NB and } \dot{e}_n \text{ is NB, } u \text{ is NVB};$$

$$R_{7,7}: \text{If } e_n \text{ is PB and } \dot{e}_n \text{ is PB, } u \text{ is PVB};$$

All the control rules can be expressed through a 7×7 matrix, which can be shown in Table 6.1.

Table 6.1 Rule base of FLC

<i>U</i>		<i>DE</i>						
		NB	NM	NS	ZO	PS	PM	PB
<i>E</i>	NB	NVB	NVB	NB	NM	NMS	ZO	PVS
	NM	NVB	NB	NM	NS	NVS	PVS	PS
	NS	NB	NM	NS	NVS	ZO	PS	PM
	ZO	NB	NS	NVS	ZO	PVS	PS	PB
	PS	NM	NS	ZO	PVS	PS	PM	PB
	PM	NS	NVS	PVS	PS	PM	PB	PVB
	PB	NVS	ZO	PVS	PM	PB	PVB	PVB

The inference block aggregates all the IF-THEN rules with their weighting factors according to the input fuzzy sets E and DE . The weighting factor of each rule, i.e. $w_{i,j}$ is obtained by the product operation and can be expressed as

$$w_{i,j} = \mu_{E_i}(e_n) * \mu_{DE_j}(\dot{e}_n) \quad (6.21)$$

3) Defuzzification

The weight average method is applied to get the crisp value of the output variable u , i.e.

$$u = \frac{\sum_{i=1}^7 \sum_{j=1}^7 w_{i,j} u_{i,j}}{\sum_{i=1}^7 \sum_{j=1}^7 w_{i,j}} \quad (6.22)$$

where $u_{i,j}$ is the crisp value of the output fuzzy set of each control rule, which can be directly obtained from the singleton membership function of the output u .

It should be noted that the sum of all membership degrees of e_n is unity, which is also valid for \dot{e}_n , i.e.

$$\sum_{i=1}^7 \mu_{E_i}(e_n) = 1, \sum_{j=1}^7 \mu_{DE_j}(\dot{e}_n) = 1 \quad (6.23)$$

Therefore, u can be rewritten as

$$u = \sum_{i=1}^7 \sum_{j=1}^7 w_{i,j} u_{i,j} \quad (6.24)$$

4) Selecting Adaptive Scaling Factor

The principle of adjusting k_u is defined as that: when the speed tracking error is higher than the threshold value e_{th} , the scaling factor k_u will increase; otherwise, k_u will decrease. Therefore, the adaptive k_u can be realized as

$$k_u(k) = \begin{cases} k_u(k-1) / k_a, & |e_n| \geq e_{th} \\ k_u(k-1) * k_a, & |e_n| < e_{th} \end{cases} \quad (6.25)$$

where k_a is the adjustment coefficient of k_u , which is set as

$$k_a = \frac{0.9995}{k_b}, k_b = \min(2^{\text{floor}(|e_n|/(4e_{th}))}, 10) \quad (6.26)$$

The coefficient k_b is used to amplify the change rate of k_u when the speed error becomes larger. The ‘*floor*’ function in (6.26) is used to reduce computational burden. It should be noted that when the calculated k_u is out of the range [0.1, 1], it is limited at the boundary value. e_{th} is selected slightly higher than the measured speed ripple which can ensure that k_u is a constant at steady state. In addition, e_{th} should not be too high as it could compromise the load disturbances rejection capability. In the experiments, e_{th} is set at 10 rpm according to the experimental results.

6.4 Experimental Verification

The experiments are implemented based on the test rig I. The PM machine is coupled with a wound field type DC machine with the rated speed at 1500 rpm. The combined inertia of the test rig is 0.012 kg·m². The machine and drive parameters are listed in Table 6.2.

Table 6.2 Machine and drive parameters

Parameters	Value
Machine stator resistance (R_s)	0.25 Ω
Synchronous inductance (L_s)	1.7 mH
PM-flux linkage(ψ_m)	10 mWb
Number of pole pairs (N_p)	10
DC link voltage (V_{dc})	14 V
Current limit (I_m)	5.9 A
Current bandwidth (ω_{cc})	1200 rad/s
Characteristic current (i_c)	5.9 A

6.4.1 Voltage Ripples in Current Control Mode and Speed Control Mode

According to the definition of the operation mode, in mode A, the machine ideally operates on the current limit circle, i_q^* is constrained by the current limit and determined by i_d^* . Therefore, in mode A, the feedback voltage ripples origins from the speed ripples. In mode B, the machine operates inside the current limit circle, i_d^* and i_q^* are controlled independently, the feedback voltage ripples are the combination of the ripples that caused by speed and q-axis current command ripples. Therefore, in the speed control mode, the feedback voltage ripples in mode B are much higher than those in mode A, which implies the condition in mode B is worse than the mode A, as will be demonstrated as follows.

6.4.1.1 Current Control Mode (CCM)

In the experiments, in order to exclude the influence of the q-axis current ripples, the system is first controlled in the current control mode. By setting $M=0.9$, Fig. 6.10 shows the voltage, current, torque and speed profile when the q-axis current command $i_{q,MTPA}^*$ changes from 0A to 3 A at 2.5 s. It can be seen that $i_{q,MTPA}^*$ is a constant and well tracked in mode B. As the machine speed increases, the machine enters in mode A due to the current constraint. In mode A, the actual current command i_q^* is limited by $\sqrt{1-i_d^{*2}}$, which is smaller than $i_{q,MTPA}^*$. In CCM, the feedback voltage ripple mainly origins from the speed ripple in both mode A and B, which is relatively small. Consequently, the feedback voltage ripple has no big difference between mode A and mode B.

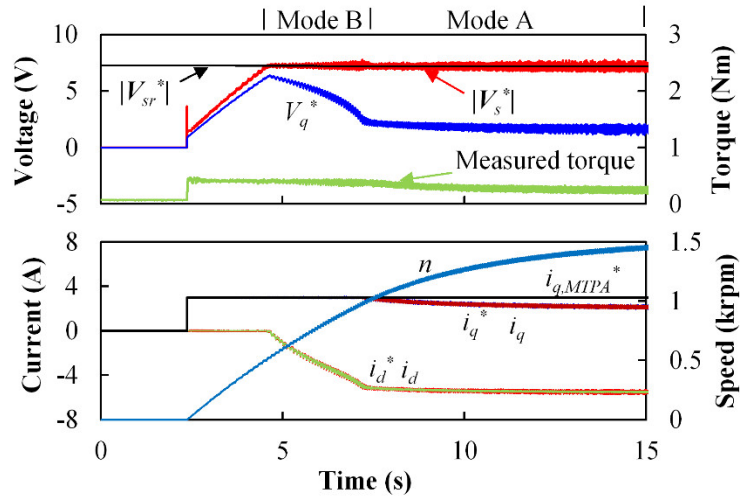
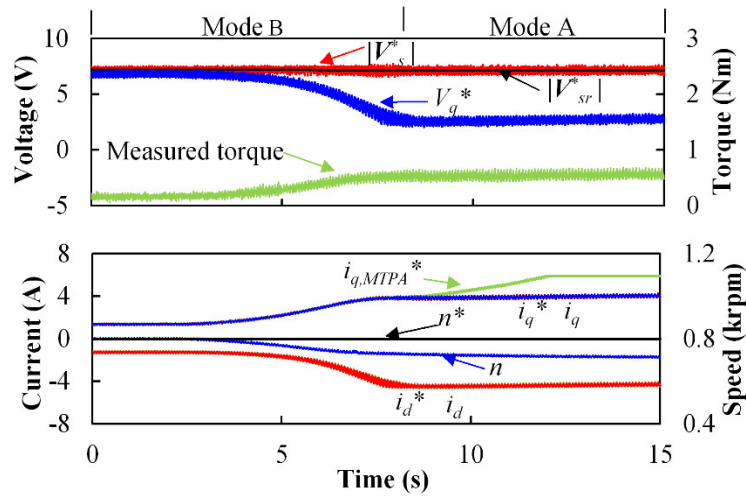


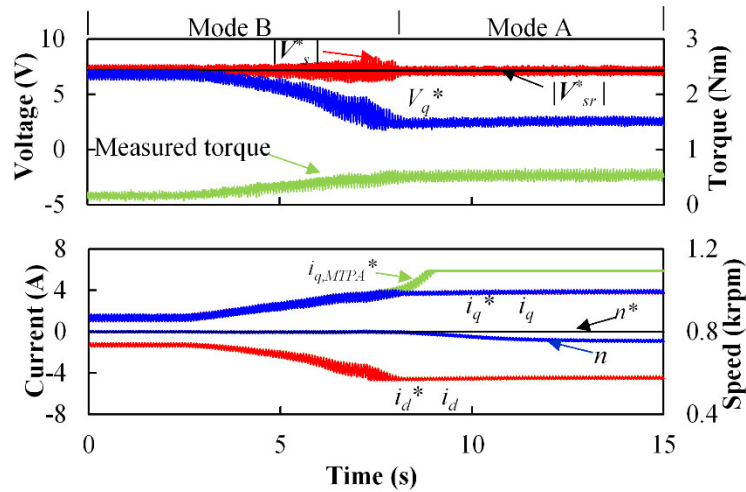
Fig. 6.10. Voltage, current, torque and speed profiles in current control mode.

6.4.1.2 Speed Control Mode

In order to illustrate the feedback voltage ripple that is caused by q -axis current ripple in different operation regions, the speed PI controller is tuned to achieve two different performances with different PI parameters, i.e. case 1 ($\omega_{Ns}=1$) and case 2 ($\omega_{Ns}=4$). Fig. 6.11(a) and Fig. 6.11(b) show the feedback voltage, current, torque and speed profiles in the flux-weakening region when $M=0.9$ under case 1 and case 2, respectively. In Fig. 6.11(a), the machine is firstly controlled at 800 rpm at light condition (0.14Nm) in case 1. Then, by gradually increasing the load torque to 0.55Nm, the machine transfers from mode B to mode A. It can be seen that the ripples of the feedback voltage and currents are quite small in both modes A and B. However, in case 2, the ripples in feedback voltage and currents are more apparent than those in case 1 which are mainly in mode B. In addition, it can be seen that the feedback voltage ripple becomes higher when the load torque increases, which is consistent with the analysis.



(a) Case 1.



(b) Case 2

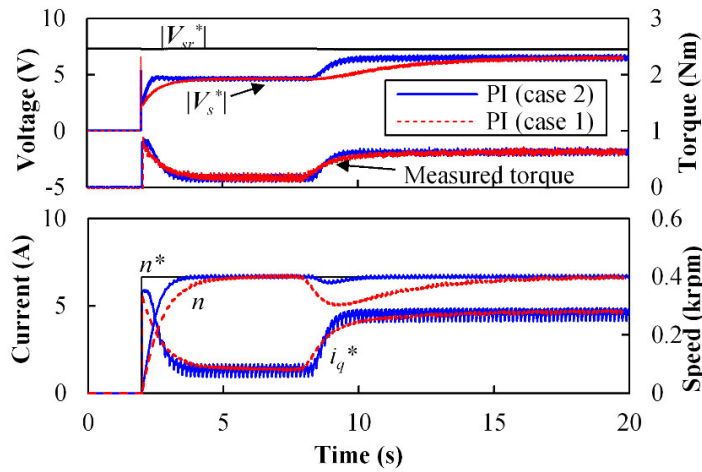
Fig. 6.11. Voltage, current, torque and speed profiles under different PI parameters in the flux-weakening region.

6.4.2 Performance Comparison with PI and FLC

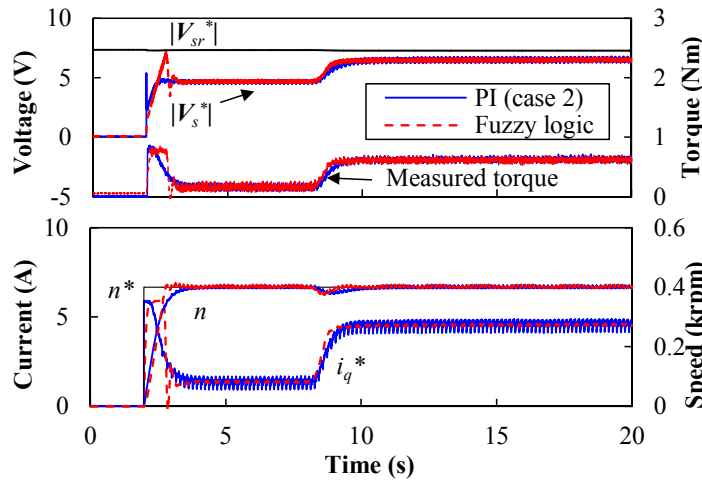
6.4.2.1 Constant Torque Region

Fig. 6.12 shows the measured speed step response and load torque rejection capability in the constant torque region under the condition, i.e. when the speed reference is changed from 0 rpm to 400 rpm at 2 s and the load torque is changed from 0.14 Nm to 0.64 Nm at 8 s. It can be seen from Fig. 6.12(a) that the system in case 1 has slower speed response but

with less current and feedback voltage ripples, while the system in case 2 has faster speed response but with higher current and feedback voltage ripples. Fig. 6.12(b) shows the speed step response ($n^*=400$ rpm) and q -axis current waveforms with the conventional PI controller (case 2) and the adaptive FLC. It can be seen that the machine speed with the adaptive FLC can achieve almost the same response as the conventional PI method with the parameters in case 2. Meanwhile, the q -axis ripples are apparently reduced. Therefore, with the adaptive FLC, the current ripples are reduced without sacrificing the dynamic performances, which is very beneficial to the flux-weakening operation.



(a) With PI controller (Case 1: $\omega_{Ns}=1$, case 2: $\omega_{Ns}=4$).



(b) With PI (case 2) and fuzzy logic controller.

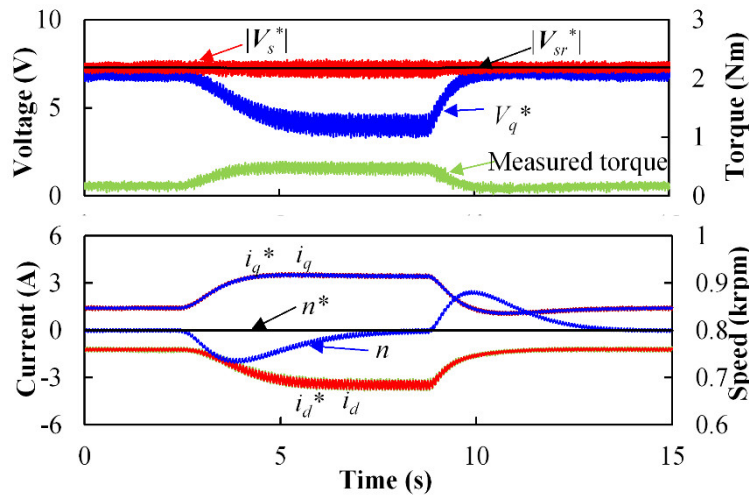
Fig. 6.12. Voltage, current, torque and speed profiles under different speed controllers.

6.4.2.2 Flux-Weakening Region

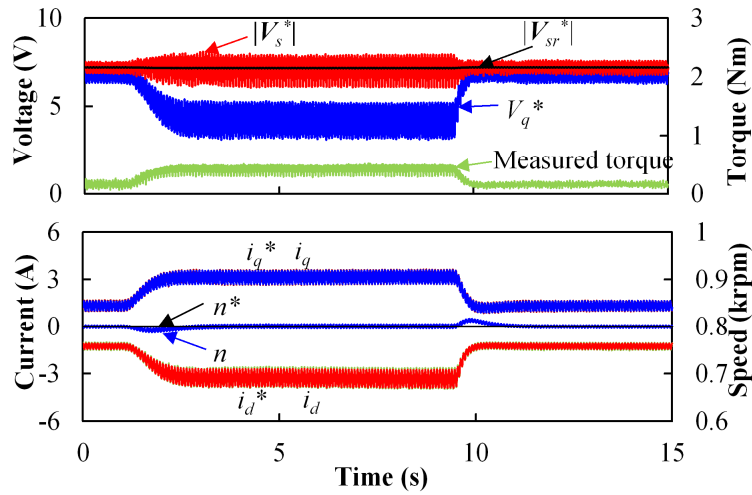
As have been shown in Fig. 6.12, even though the current and voltage ripple in case 2 are higher, the system can still perform well in the constant torque region. However, the system that performs well in the constant torque may not necessarily perform well in the flux-weakening region. In the flux-weakening region, in order to further confirm the advantages of the adaptive FLC, the experiments with different speed controllers are implemented under different coefficient M , i.e. 0.9 and 0.95.

1) $M=0.9$

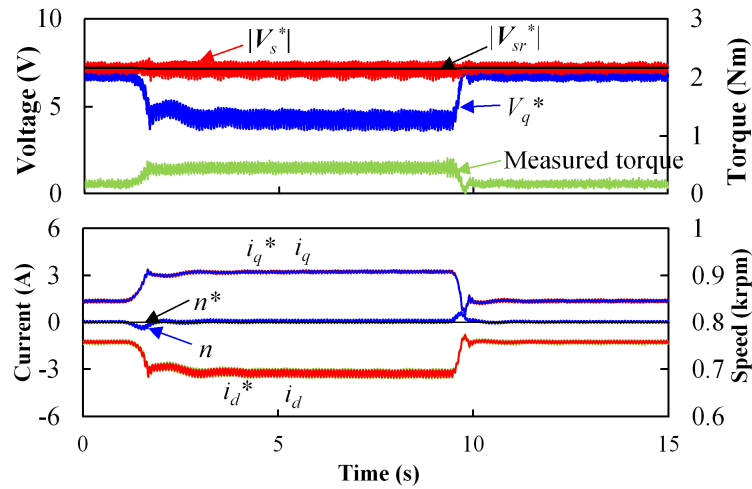
Fig. 6.13 shows the speed dynamic performance under a load disturbance when the machine is controlled at 800 rpm in the flux-weakening region. The higher and lower load torque values equal to 0.42 Nm and 0.14 Nm, respectively, which is achieved by manually switching on and off the excitation current of the DC-load machine. It can be seen in Fig. 6.13(a) and (b) that although the current ripple in case 1 is smaller than that in case 2, the machine has much longer recovery time against the load torque disturbance. However, with adaptive FLC, as shown in Fig. 6.13(c), both low current ripple and high load torque disturbance rejection capability can be obtained.



(a) PI (case 1).



(b) PI (case 2).



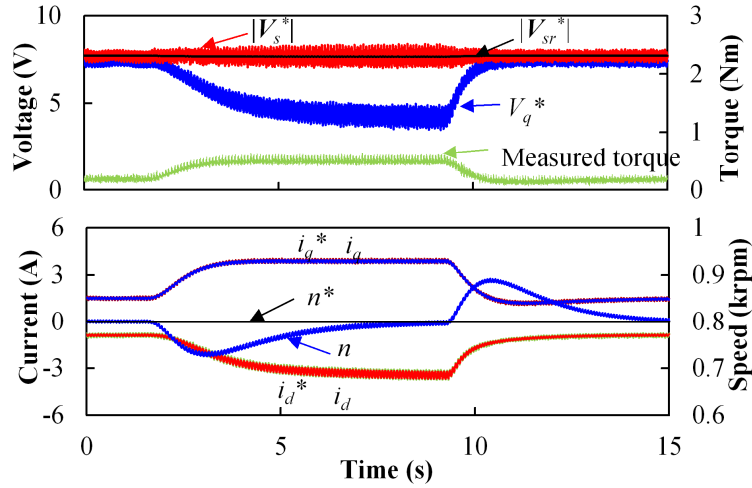
(c) Adaptive FLC.

Fig. 6.13. Voltage, current, torque and speed profiles under load torque disturbance when $M = 0.9$.

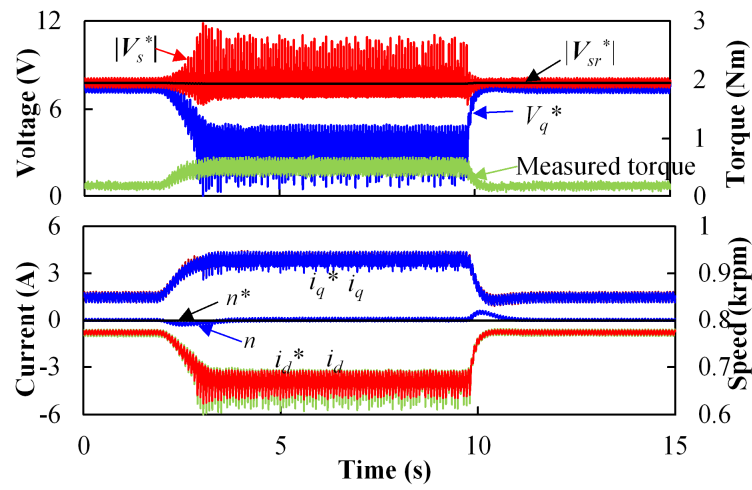
6.4.2.3 $M=0.95$

Fig. 6.14 shows the speed dynamic performance under load torque disturbance when M increases to 0.95. The higher and lower load torque values equal to 0.42 Nm and 0.14 Nm, respectively. It can be seen from Fig. 6.14(b) that in the higher q -axis current area, the current and voltage even oscillate in case 2 while the systems with case 1 and adaptive FLC can still operate well, as shown in Fig. 6.14(a) and (c), respectively. However, the adaptive FLC can achieve much better speed dynamics than that in case 1. Therefore, the DC-link voltage

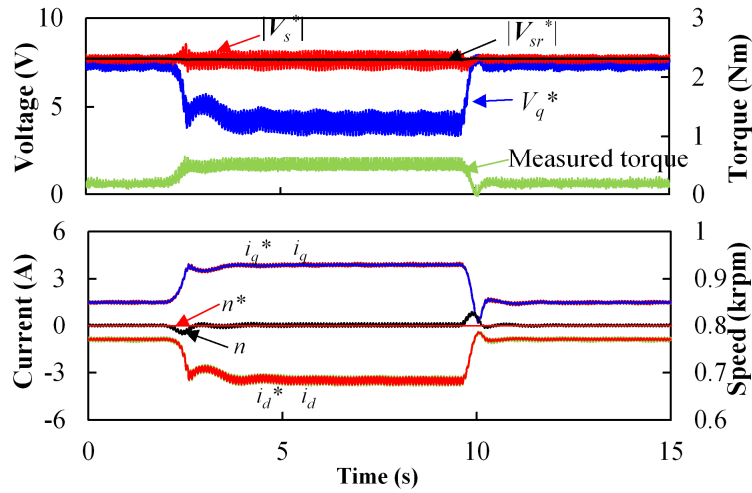
utilization can be further increased while the speed dynamics is still maintained, and the machine can achieve better flux-weakening capability, as can be seen in Fig. 6.15.



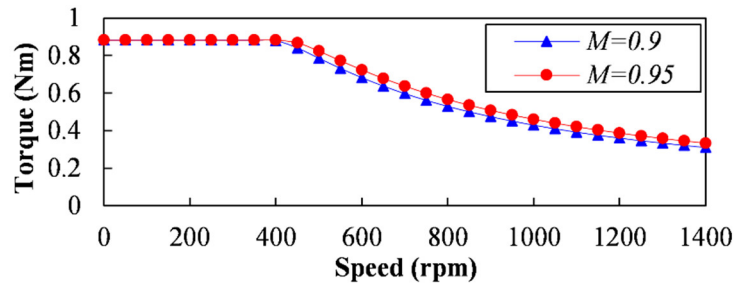
(a) PI (case 1).



(b) PI (case 2).



(c) Adaptive FLC.

Fig. 6.14. Voltage, current, torque and speed profiles under load torque disturbance when $M = 0.95$.Fig. 6.15. Torque-speed curve when $M=0.9$ and $M=0.95$.

6.5 Conclusion

In this chapter, based on DCVFC and the machine without MTPV region, the influence of the feedback voltage ripple is analysed when the system operates in the speed control mode. It has been shown that the system performance in the speed control mode could become worse due to the increased feedback voltage ripples that are dominated by the current command ripples. The current command ripples can be reduced by decreasing the bandwidth of the speed loop, posing difficulty to increase the speed dynamic performance. In order to solve this conflict, an adaptive FLC has been designed and compared with the conventional PI controller in both constant torque and flux-weakening regions. The experimental results have verified that:

1) The increased feedback voltage ripples in small $|V_q|$ area could cause oscillation in the flux-weakening region even in the linear modulation when the system operates in the speed control mode;

2) The system in speed control mode that has been tuned well in the constant region may not necessarily perform well in the flux-weakening region;

3) The speed dynamics in the flux-weakening with a conventional PI controller can be hardly increased, especially for a non-idea drive system, while the adaptive FLC can provide an alternative tool to solve this issue.

CHAPTER 7 GENERAL CONCLUSION AND FUTURE WORK

The flux-weakening control is required for the PMSM to extend the operation speed range and maximize the power capability under the voltage and current constraints. Many control strategies are developed to achieve flux-weakening operation, such as

- Feedforward method
- Feedback method (based on the voltage error, the voltage magnitude, and the switching time)
- Hybrid method
- Single current control
- Single current control and voltage angle control

among which the voltage magnitude feedback method gains popularity due to many advantages, e.g.

- Simple and standard control structure
- Robust against parameter variation
- Both linear and over modulation flux-weakening operation
- Automatic flux-weakening operation

However, in the flux-weakening region, as the drive system operates on the boundary of the voltage limit, more stability problems are prone to occur in this region. In this thesis, based on the voltage magnitude feedback controller on the non-salient-pole PMSM, the stability problems in the flux-weakening region are investigated and the related solutions are proposed.

7.1 Summary of the Research Work

The research work in this thesis can be summarized as the following aspects

- 1) Tuning of voltage feedback controller. The stability in the flux-weakening region is improved with an adaptive control parameter.
- 2) Stability improvement in over modulation region. The stability in over modulation region is improved with CRM and VRM for the machine without MTPV region, and a VVM for the machine with MTPV region.
- 3) Optimization and design of MTPV controller. Firstly, the penalty function is realized in the current command form rather than in the voltage command form, aiming to improve the stability and dynamic performance. Secondly, the MTPV PI controller is designed based on the system with DCVFC. The MTPV integral regulator is designed for the system with CAVFC and HVFC.
- 4) Novel hybrid voltage feedback controller (HVFC). The HVFC contains both DCVFC part and CAVFC part with their optimized weight factors, which can overcome the intrinsic stability problem of the systems with DCVFC and CAVFC.
- 5) Alternative speed controller-FLC. An adaptive FLC is designed aiming to reduce the feedback voltage ripples that origins from the non-idea drive system while maintaining a fast speed dynamics.

The summary of the work in this thesis is illustrated in Fig. 7.1. The switches in Fig. 7.1 represent whether the relevant control strategies are included or excluded. It should be noted that when the state of all the switches are off, the CVC control system is applied with only a voltage magnitude feedback controller, which could be DCVFC, CAVFC or HVFC. The grey dotted line indicates that the relevant control strategy is possible but not discussed in the thesis.

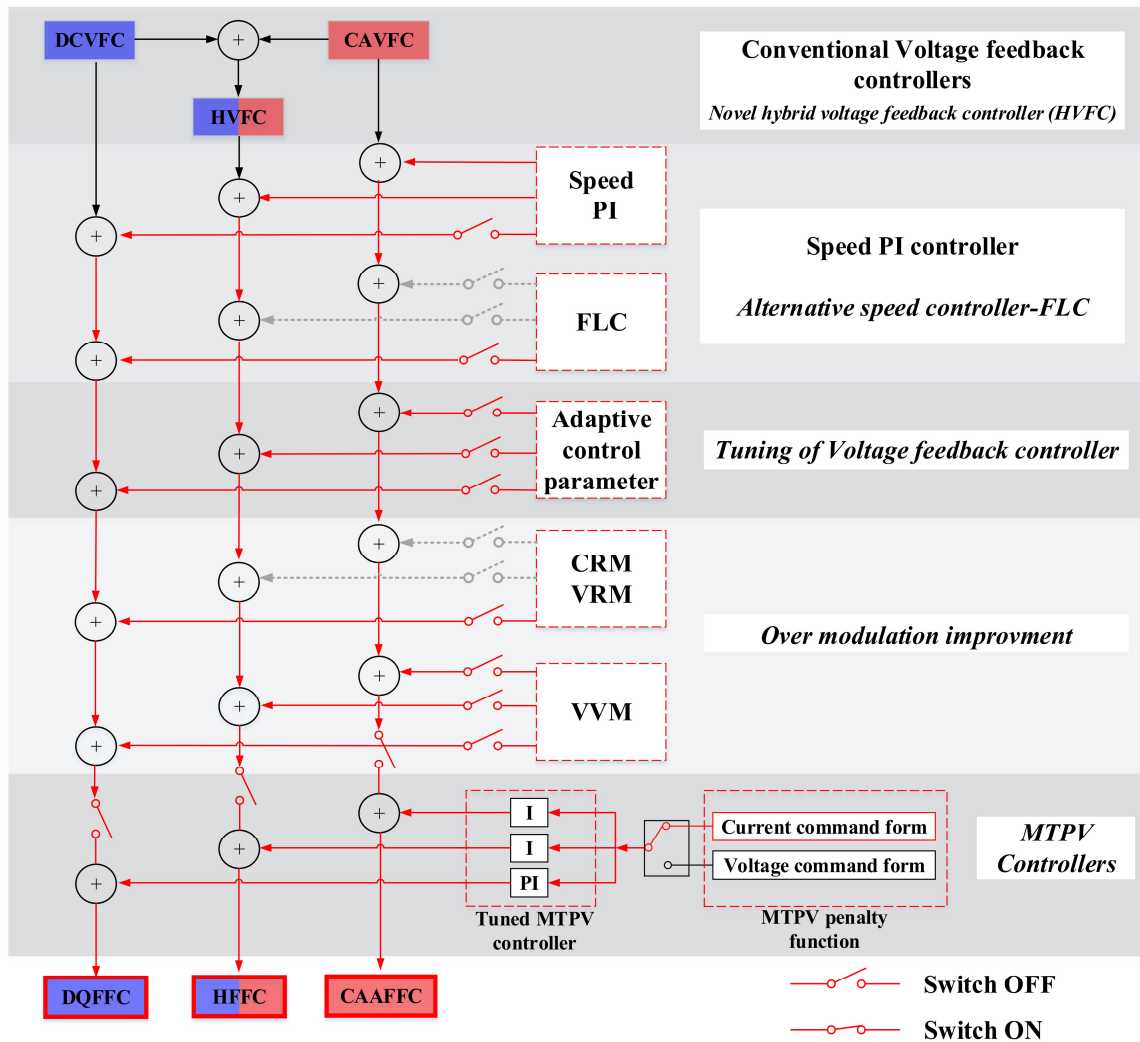


Fig. 7.1 Summary of the work in the thesis.

*Switch ON: the relevant control strategy is included; Switch OFF: the relevant control strategy is excluded.

*Grey dotted line: the relevant control strategy is possible but not discussed in the thesis.

7.2 Conclusion

7.2.1 Tuning of Voltage Feedback Controller

In the thesis, based on the different operation modes that are defined by the different small signal behaviour of the current, the close-loop transfer functions of the voltage loop with DCVFC, CAVFC and HVFC are derived. As the derived close-loop transfer function of the voltage loop varies with operation points, it renders that the constant control parameter tuned well at one operation point could lose its effectiveness on the other operation points.

Thus, the symbolic form of the adaptive control parameters are derived by considering the different operation modes, which can achieve a wider stable operation range and facilitate the practical parameterization. The advantages of the adaptive control parameter are demonstrated on the system with DCVFC by taking a non-adaptive control parameter as a baseline for comparison. Two characteristic current ratios, i.e. $i_{cn}=1$ and $i_{cn}=2$, are considered. The analyses and experimental results have shown that the adaptive control parameter can ensure a much wider stable speed range including both motoring and generating conditions, while the non-adaptive case is only effective in certain speed range.

7.2.2 Stability Improvement in Over Modulation Region

In the over modulation region, the voltage margin decreases, and the voltage is easier to be saturated, which deteriorates the current dynamics. As the current loop is the inner loop of the voltage loop, the current dynamics in the over modulation region is essential. Two methods, i.e. the method with CRM and VRM, and the method with VVM, can be both utilized to improve the current dynamics and ease the voltage saturation problem. The CRM which origins from the voltage error feedback flux-weakening method is utilized in this thesis in the voltage magnitude feedback flux-weakening method, while a VRM is proposed to solve the conflict between the CRM and the voltage magnitude feedback controller in the over modulation region. Therefore, both the current steady-state and dynamic performances are improved. The VVM modifies the voltage vector based on the coupling effect between the d- and q-axes, which can effectively improve the current dynamics in the over modulation region. However, since VVM is based on the voltage vector modification while CRM is based on the q-axis voltage error modification, the CRM could lose its effectiveness in the MTPV region (region III) where the q-axis voltage is close to zero, while VVM can still be used for the stability improvement in region III.

7.2.3 Optimization and Design of MTPV Controller

For the machine with $i_{cn}<1$, the MTPV curve insect with the current limit, the maximum output power current trajectories require that the system should operate on MPTV curve. For the voltage feedback control, the MTPV control strategy can be achieved by introducing an

extra feedback controller with its input as the MTPV penalty function. In this thesis, the MTPV penalty function in the current command form is selected rather than in the voltage command form, aiming to achieve better dynamics and stability. In addition, in order to achieve an optimal current trajectory in the MTPV region, the resistance is considered in the penalty function, which is important for the small power motor. Furthermore, the MTPV controllers in the systems with DCVFC, CAVFC and HVFC, are analysed and designed, which is critical for the stability in the region III. The analysis indicates that a pure integrator MTPV controller is not appropriate for the system with DCVFC while it can be applied to the system with CAVFC and HVFC.

7.2.4 Novel Hybrid Voltage Feedback Controller

Even though the control parameter of the voltage feedback controller is properly tuned, the flux-weakening methods with considering MTPV control based on DCVFC and CAVFC, i.e. DQFFC and CAAFFC, could still have stability problem in region II. Due to the different operation modes of DQFFC and CAAFFC in region II, the voltage regulation capability varies with the operation points. Since the voltage feedback controller is a kind of anti-windup controller, the voltage regulation capability is important to deter the voltage saturation problem, especially in the over modulation region due to the reduced voltage margin. In this thesis, DQFFC and CAAFFC are analysed and compared in terms of the stability problem that are operation mode relevant. The analyses and experimental results have shown that the oscillation could occur when approaching the MTPV curve in DQFFC, while the oscillation could occur in CAAFFC when the system operates at light load in generating condition. In addition, the magnitude and angle control structure in CAAFFC results in a poor transition performance between motoring and generating conditions. This kind of stability problem of DQFFC and CAAFFC is related to the different operation modes, which origin from the different control structures. Therefore, in order to utilize the commentary advantages of DQFFC and CAAFFC, a HFFC is proposed which is based on a novel HVFC, i.e. a hybrid voltage feedback controller containing both DCVFC part and CAVFC part, with their weight factors being optimized. The improved stability of HFFC under various conditions are verified by the experimental results.

7.2.5 Alternative Speed Controller-FLC

As the feedback voltage ripples that origin from the non-ideal drive system can be amplified by a conventional speed PI controller, the speed controller performing well in the constant torque region may oscillate in the flux-weakening region due to the reduced voltage margin, which will cause difficulty to increase the speed dynamics. In order to solve this problem, a nonlinear speed controller, i.e. an adaptive fuzzy logic speed controller, is proposed and implemented successfully to reduce the feedback voltage ripples while maintaining a good speed dynamics.

7.3 Future Work

As shown in Fig. 7.1, other combinations of the control strategies that are not mentioned in this thesis may also work well in the flux-weakening region. For example, the FLC can also be applied to the system with HVFC to reduce the influence of the voltage feedback ripples. The CRM and VRM can also be used on the system with HVFC for the machine without MTPV region. In addition, CRM and VRM can be used simultaneously with VVM. However, since the main objective of this thesis is try to investigate all the possible factors that could lead to stability problem in the flux-weakening region, other combinations of the control strategies will not be discussed further.

Since d- and q-axis currents are controlled separately in DCVFC, an advantage of the system with DCVFC is that the machine can operate in the torque control mode, which can be achieved by simply disabling the speed controller. However, based on the system with HVFC, the toque control cannot be simply achieved by disabling the speed controller since d- and q-axis currents are not controlled separately. Therefore, future work can be carried out to achieve the torque control based on the system with HVFC. By way of example, the speed controller can be replaced by a torque controller, the input of which could be the difference between the demand torque and the actual torque. However, considering the system stability, the bandwidth of the torque control loop cannot be as high as that of the current loop, which could compromise the torque control performance.

Since all the analyses in this thesis are based on the non-salient-pole PMSM, future work can also be carried out on the salient-pole PMSM. For salient-pole PMSM, an extra dimension, i.e. the machine saliency ratio should be introduced. In practice, if the stability problem occurs on a salient-pole PMSM when the voltage magnitude feedback controller is employed, the analyses and the control strategies presented in this thesis can still provide a guidance for troubleshooting the problems, as the underlying principle causing the stability problem on the salient-pole PMSM should be similar to the non-salient-pole PMSM.

REFERENCES

- [AMA08] S. Amarir and K. Al-Haddad, "A modeling technique to analyze the impact of inverter supply voltage and cable length on industrial motor-drives," *IEEE Trans. Power Electron.*, vol. 23, no. 2, pp. 753–762, Mar. 2008.
- [SHI06] Y. F. Shi, Z. Q. Zhu, and D. Howe, "Torque-speed characteristics of interior-magnet machines in brushless AC and DC modes, with particular reference to their flux-weakening performance," in *Proc. Int. Power Electronics and Motion Control*, Shanghai, China, Aug. 13–16, 2006, pp. 1847–1851
- [BAE03] B. H. Bae, N. Patel, S. Schulz, and S. K. Sul, "New field weakening technique for high saliency interior permanent magnet motor," in *Conf.Rec. IEEE IAS Annu. Meeting*, 2003, pp. 898–905.
- [BIA01] N. Bianchi, S. Bolognani, and M. Zigliotto, "High performance PM synchronous motor drive for an electric scooter," *IEEE Trans. Ind. Appl.*, vol. 37, no. 5, pp. 1348–1355, Sep./Oct. 2001
- [BOL08] S. Bolognani, S. Bolognani, L. Peretti and M. Zigliotto, "Combined speed and current model predictive control with inherent field-weakening features for PMSM drives," in *2008 IEEE Electrotechnical conference*, pp. 472-478, 2008.
- [BOL14] S. Bolognani, S. Calligaro, and R. Petrella, "Adaptive flux-weakening controller for interior permanent magnet synchronous motor drives," *IEEE J. Emerg. Sel. Topics Power Electron.*, vol. 2, no. 2, pp. 236–248, Jun. 2014.
- [BOZ14] S. Bozhko, Y. Seang Shen, G. Fei, and C. Hill, "Aircraft starter-generator system based on permanent-magnet machine fed by active front-end rectifier," in *Industrial Electronics Society, IECON 2014*, pp. 2958-2964.
- [BOZ16] S. Bozhko, M. Rashed, S. S. Yeoh, T. Yang, and C. Hill, "Flux weakening control of permanent magnet machine based aircraft electric starter-generator," in *8th IET Int. Conf. on PEMD ,2016*, pp. 1-6.

- [BOZ17] S. Bozhko, M. Rashed, C. I. Hill, S. S. Yeoh, and T. Yang, "Flux-weakening control of electric starter-generator based on permanent-magnet machine," *IEEE Trans. Transport. Electrification*, vol. 3, no. 4, pp. 864-877, 2017.
- [BRI01] F. Briz, A. Diez, M. W. Degner, and R. D. Lorenz, "Current and flux regulation in field-weakening operation of induction motors," *IEEE Trans. Ind. Appl.*, vol. 37, no. 1, pp. 42-50, 2001.
- [BRI99] F. B. d. Blanco, M. W. Degner, and R. D. Lorenz, "Dynamic analysis of current regulators for AC motors using complex vectors," *IEEE Trans. Ind. Appl.*, vol. 35, pp. 1424-1432, 1999.
- [CAO12] W. P. Cao, B. C. Mecrow, G. J. Atkinson, J. W. Bennett and D. J. Atkinson, "Overview of electric motor technologies used for more electric aircraft (MEA)," *IEEE Trans. Ind. Electron.*, vol. 59, no. 9, pp. 3523-3531, Sept. 2012.
- [CAP06] F. G. Capponi, G. D. Donato, L. D. Ferraro, O. Honorati, M. C. Harke, and R. D. Lorenz, "AC brushless drive with low-resolution Hall-effect sensors for surface-mounted PM Machines," *IEEE Trans. Ind. Appl.*, vol. 42, no. 2, pp. 526-535, 2006.
- [CHA08] K. T. Chau, C. C. Chan and C. Liu, "Overview of permanent-magnet brushless drives for electric and hybrid electric vehicles," *IEEE Trans. Ind. Electron.*, vol. 55, no. 6, pp. 2246-2257, June 2008
- [CHE00] J. J. Chen and K. P. Chin, "Automatic flux-weakening control of permanent magnet synchronous motors using a reduced-order controller," *IEEE Trans. Power Electron.*, vol. 15, pp. 881-890, 2000.
- [CHE10] B. Cheng and T. R. Tesch, "Torque Feedforward Control Technique for Permanent-Magnet Synchronous Motors," *IEEE Trans. Ind. Electron.*, vol. 57, no. 3, pp. 969-974, 2010.
- [CHE18] Y. Z. Chen, X. Huang, J. Wang, F. Niu, J. Zhang, Y. Fang, et al., "Improved flux-weakening control of IPMSMs based on torque feedforward technique," *IEEE Trans. Power Electron.*, pp. 1-1, 2018.

- [CHE99] Y. S. Chen, Z. Q. Zhu, and D. Howe, "Influence of inaccuracies in machine parameters on field-weakening performance of PM brushless AC drives," in *Proc. IEEE 1999 Int. Conf. Electr. Mach. Drives*, 1999, pp. 691–693.
- [DEG98] M.W Degner and R.D Lorenz, "Using multiple saliencies for the estimation of flux, position, and velocity in AC machines," *IEEE Trans. Ind. Appl.*, vol. 34, no. 5, pp. 1097–1104, 1998.
- [DEN19] T. Deng, Z. Su, J. Lin, P. Tang, X. Chen, and P. Liu, "Advanced angle field weakening control strategy of permanent magnet synchronous motor," *IEEE Trans. Veh. Technol.*, pp. 1-1, 2019.
- [DHA90] R. Dhaouadi and N. Mohan, "Analysis of current-regulated voltage-source inverters for permanent magnet synchronous motor drives in normal and extended speed ranges," *IEEE Trans. Energy Convers.*, vol. 5, pp. 137-144, 1990.
- [DSP10] dSPACE, *Hardware installation and configuration reference*, Release 6.6, May 2010.
- [FOO10] G. Foo and M. F. Rahman, "Sensorless direct torque and flux-controlled IPM synchronous motor drive at very low speed without signal Injection," *IEEE Trans. Ind. Electron.*, vol. 57, no. 1, pp. 395-403, 2010.
- [FRA94] G. F. Franklin, J. D. Powell, and A. Emami-aeini, "Feedback control of dynamic systems," Reading, MA: Addison-Wesley, 1994.
- [GAB80] R. Gabriel, W. Leonhard, and C. J. Nordby, "Field oriented control of a standard AC motor using microprocessors," *IEEE Trans. Ind. Appl.*, vol. IA-16, pp. 186-192, Mar./Apr. 1980.
- [GON12] Liming. Gong, "Carrier signal injection based sensorless control of permanent magnet brushless AC machines", PhD Thesis, Department of Electronic and Electrical Engineering, University of Sheffield, 2012.
- [GUO09] G.Xinhua, W.Xuhui, Z.Feng, S.Xuele, and Z.Xingming, "PI parameter design of the flux weakening control for PMSM based on small signal and transfer function," in *Electrical Machines and Systems, ICEMS*, 2009 , pp. 1-6.

- [HAR00] L. Harnefors and H.P. Nee, "A general algorithm for speed and position estimation of AC motors," *IEEE Trans. Ind. Electron.*, vol. 47, no. 1, pp. 77-83, 2000.
- [HAR01] L. Harnefors, K. Pietilainen, and L. Gertmar, "Torque-maximizing field-weakening control: design, analysis, and parameter selection," *IEEE Trans. Ind. Electron.*, vol. 48, pp. 161-168, 2001
- [HEN10] Hengstler GmbH, *Incremental Encoder RI 58-D / RI 58TD*, Jul. 2010.
- [HOL92] J. Holtz, "Pulsewidth modulation—A survey," *IEEE Trans. Ind. Electron.*, vol. 38, pp. 410–420, Oct. 1992
- [HOL98] J. Holtz, "Sensorless position control of induction motors – an emerging technology," *IEEE Trans. Ind. Electron.*, Vol. 45, No. 6, pp. 840–852, 1998.
- [HU12] D. Hu, L. Zhu, and L. Xu, "Maximum Torque per Volt operation and stability improvement of PMSM in deep flux-weakening Region," in *2012 IEEE Energy Conversion Congress and Exposition, ECCE, 2012*, pp. 1233-1237.
- [IR12] IRFH7440 *Product Datasheet - Infineon Technologies, 2012*
- [JAH84] T. M. Jahns, "Torque production in permanent magnet synchronous motor drives with rectangular current excitation," *IEEE Trans. Ind. Appl.*, vol. IA-20, no. 4, pp. 803–813, 1984.
- [JAH86] T. M. Jahns, G. B. Kliman and T. W. Neumann, "Interior permanent-magnet synchronous motors for adjustable-speed drives," *IEEE Trans. on Ind. Appl.*, Vols. IA-22, no. 4, pp. 738-747, 1986.
- [JAH87] T. M. Jahns, "Flux-weakening regime operation of an interior permanent magnet synchronous motor drive," *IEEE Trans. Ind. Appl.*, vol. 22, no. 4, pp. 738–747, Jul./Aug. 1987.
- [KHA02] A. M. Khambadkone and J. Holtz, "Compensated synchronous PI current controller in overmodulation range and six-step operation of space-vector-modulation-based vector-controlled drives," *IEEE Trans. Ind. Electron.*, vol. 49, no. 3, pp. 574-580, 2002.

- [KIM97] J. M. Kim and S. K. Sul, "Speed control of interior permanent magnet synchronous motor drive for the flux weakening operation," *IEEE Trans. Ind. Appl.*, vol. 33, no. 1, pp. 43–48, Jan./Feb. 1997.
- [KOC10] H. W. d. Kock, A. J. Rix, and M. J. Kamper, "Optimal Torque Control of Synchronous Machines Based on Finite-Element Analysis," *IEEE Trans. Ind. Electron.*, vol. 57, no. 1, pp. 413-419, 2010.
- [KWO06] T. S. Kwon and S. K. Sul, "Novel antiwindup of a current regulator of a surface-mounted permanent-magnet motor for flux-weakening control," *IEEE Trans. Ind. Appl.*, vol. 42, No. 5, pp. 1293-1300, Sep./Oct. 2006.
- [KWO07] K. Tae-suk and S. Seung-Ki, "A novel flux weakening algorithm for surface mounted permanent magnet synchronous machines with infinite constant power speed ratio," *Int. Conf. on Electr. Mach. Sys.*, 2007, pp. 440-445.
- [KWO08] T.-S. Kwon, G.-Y. Choi, M.-S. Kwak, and S.-K. Sul, "Novel fluxweakening control of an IPMSM for quasi-six-step operation," *IEEE Trans. Ind. Appl.*, vol. 44, no. 6, pp. 1722–1731, Nov./Dec. 2008.
- [LEI11] Z. Lei, W. Xuhui, Z. Feng, K. Liang, and Z. Baocang, "Deep fieldweakening control of PMSMs for both motion and generation operation," in *Proc. Int. Conf. Elect. Mach. Syst.*, 2011, pp. 1–5
- [LEM12] LEM, *Voltage Transducer LV 25-P*, Nov. 2012
- [LEM14] LEM, *Current Transducer LA 25-P*, Nov. 2014.
- [LER08] S. Lerdudomsak, S. Doki, and S. Okuma, "Analysis for unstable problem of PMSM current control system in overmodulation range," in *Industry Applications Society Annual Meeting, IEEE*, 2008, pp. 1-8.
- [LIN12] L. Ping-Yi and L. Yen-Shin, "Voltage control technique for the extension of DC-link voltage utilization of finite-speed SPMSM drives," *IEEE Trans. Ind. Electron.*, vol. 59, no. 9, pp. 3392–3402, Sep. 2012.
- [LIU12] H. Liu, Z. Q. Zhu, E. Mohamed, Y. Fu, and X. Qi, "Flux-weakening control of nonsalient pole pmsm having large winding inductance accounting for resistive voltage drop and inverter nonlinearities," *IEEE Trans. Power Electron.*, vol. 27, no. 2, pp. 942-952, 2012.

- [LOR87] R. D. Lorenz and D. B. Lawson, "Performance of feedforward current regulators for field oriented induction machine controllers," *IEEE Trans. Industry Appl.*, vol. IA-23, no. 4, pp. 597-602, July/Aug. 1987.
- [MAG14] Magtrol, *In-Line Torque Transducers TM 301 – TM 308*, Feb. 2014.
- [MAR99] D. S. Maric, S. Hiti, C. C. Stancu, J. M. Nagashima, and D. B. Rutledge, "Two flux weakening schemes for surface-mounted permanent-magnet synchronous drives. Design and transient response considerations," in *Proc. IEEE Int. Symp. Ind. Electron.*, 1999, vol. 2, pp. 673–678.
- [MIY13] T. Miyajima, H. Fujimoto, and M. Fujitsuna, "A Precise Model-Based Design of Voltage Phase Controller for IPMSM," *IEEE Trans. Power Electron.*, vol. 28, pp. 5655-5664, 2013.
- [MOR03] S. Morimoto, M. Sanada, and Y. Takeda, "High performance current sensorless drive for PMSM and SynRM with only low resolution position sensor," *IEEE Trans. Ind. Appl.*, vol. 39, no. 3, pp. 792–801, May/June. 2003.
- [MOR90] S. Morimoto, Y. Takeda, and T. Hirasu, "Expansion of operating limits for permanent magnet motor by current vector control considering inverter capacity," *IEEE Trans. Ind. Appl.*, vol. 26, no. 5, pp. 866–871, Sep./Oct. 1990.
- [MOR94] S. Morimoto, M. Sanada, and Y. Takeda, "Effects and compensation of magnetic saturation in flux-weakening controlled permanent magnet synchronous motor drives," *IEEE Trans. Ind. Appl.*, vol. 30, pp. 1632-1637, 1994.
- [NAL12] R. Nalepa and T. Orłowska-Kowalska, "Optimum trajectory control of the current vector of a nonsalient-pole PMSM in the field-weakening region," *IEEE Trans. Ind. Electron.*, vol. 59, pp. 2867-2876, 2012.
- [ONE16] Y. Oner, Z. Q. Zhu, L. Wu, X. Ge, H. Zhan, and J. Chen, "Analytical on-load sub-domain field model of permanent magnet Vernier machines," *IEEE Trans. Ind. Electron.*, vol. 63, no. 7, pp. 4105–4117, July 2016.
- [POT14] N. Pothi and Z. Q. Zhu, "A new control strategy for hybrid-excited switched-flux permanent magnet machines without the requirement of machine

- parameters,” in *Proc. 7th IET Int. Conf. Power Electron., Mach.Drives (PEMD)*, Apr. 2014, pp. 1–6.
- [QIA16] L. Qian and K. Hameyer, “A deep field weakening control for the PMSM applying a modified overmodulation strategy,” in *8th IET Int. Conf. on Power Electronics,PEMD 2016*, pp. 1-6.
- [RAH03] M. F. Rahman, D. M. Wilathgamuwa, M. N. Uddin, and K. J. Tseng, “Nonlinear control of interior permanent-magnet synchronous motor,” *IEEE Trans. on Industry Applications*, vol. 39, no. 2, pp. 408-416, 2003.
- [REF05] A. M. El-Refaie, and T. M. Jahns, “Optimal flux weakening in surface PM machines using fractional-slot concentrated windings,” *IEEE Trans. Ind. Appl.*, vol. 41, no. 3, pp. 790-800, May/June 2005.
- [REF06] A. M. El-Refaie, T. M. Jahns, P. J. McCleer, J. W. McKeever, “Experimental verification of optimal flux weakening in surface PM machines using Concentrated Windings,” *IEEE Trans. Ind. Appl.*, vol. 42, no. 2, pp. 443-452, March/April 2006.
- [SCH90] R. F. Schiferl and T. A. Lipo, “Power capability of salient pole permanent magnet synchronous motor in variable speed drive applications,” *IEEE Trans. Ind. Appl.*, vol. 26, no. 1, pp. 115–123, Jan./Feb. 1990.
- [SEO98] S. Jul-Ki, K. Joohn-Sheok, and S. Seung-Ki, “Overmodulation strategy for high-performance torque control,” *IEEE Trans. Power Electron.*, vol. 13, no. 4, pp. 786-792, 1998.
- [SHI02] Y. F. Shi, Z. Q. Zhu, Y. S. Chen, and D. Howe, “Influence of winding resistance on flux-weakening performance of a permanent magnet brushless AC Drive,” in *Proc. IEE Int. Conf. Power Electr., Mach. Drives*, 2002, pp. 392–397
- [SHI04] Y. F. Shi, Z. Q. Zhu, Y. S. Chen, and D. Howe, “Investigation of flux-weakening performance and current oscillation of permanent magnet brushless AC drives,” in *The 4th Int. Conf. Power Electr. Motion Control*, 2004, pp. 1257-1262.

- [SHI07] J. L. Shi, T. H. Liu and S. H. Yang, “Nonlinear-controller design for and interior-permanent-magnet synchronous motor including field-weakening operation,” *IET Electric Power Appl.* vol, 1, no. 1 pp.119-126, 2007.
- [SNE85] B. Sneyers, D. W. Novotny and T. A. Lipo, “Field weakening in buried permanent magnet AC motor drives,” *IEEE Trans. Ind. Appl.*, Vols. IA-21, no. 2, pp. 398-407, 1985.
- [SON96] H. Song, J. M. Kim, and S. K. Sul, “A new robust SPMSM control to parameter variations in flux weakening region,” in *Proc. IEEE Ind. Electron.Soc. Annu. Conf.*, 1996, pp. 1193–1198
- [SOO94] W. L. Soong and T. J. E. Miller, “Field-weakening performance of brushless synchronous AC motor drives,” *IEE Proc. Electr. Power Appl.*, vol. 141, no. 6, pp. 331–340, Nov. 1994
- [STO12] D. Stojan, D. Drevensek, Z. Plantic, B. Grcar, and G. Stumberger, “Novel field-weakening control scheme for permanent-magnet synchronous machines based on voltage angle control,” *IEEE Trans. Ind. Appl.*, vol. 48, no. 6, pp. 2390–2401, Nov./Dec. 2012
- [SUD95] S. D. Sudhoff, K. A. Corzine, and H. J. Hegner, “A flux-weakening strategy for current-regulated surface-mounted permanent-magnet machine drives,” *IEEE Trans. Energy Convers.*, vol. 10, no. 3, pp. 431–437, Sep. 1995
- [SUK07] K. Tae-suk and S. Seung-Ki, “A novel flux weakening algorithm for surface mounted permanent magnet synchronous machines with infinite constant power speed ratio,” *Int. Conf. on Electr. Mach. Sys.*, 2007, pp. 440-445.
- [SUL11] S. K. Sul, “Control of electric machine and drive systems,” John Wiley & Sons, 2011.
- [TAK86] I. Takahashi and T. Noguchi, “A new quick-response and high-efficiency control strategy of an induction motor,” *IEEE Trans. Ind. Appl.*, vol. IA-22, no. 5, pp. 820–827, Sep. 1986.
- [TRA18] E. Trancho, E. Ibarra, A. Arias, I. Kortabarria, J. Jurgens, L. Marengo, et al., “PM-assisted synchronous reluctance machine flux weakening control for

- EV and HEV applications,” *IEEE Trans. Ind. Electron.*, vol. 65, no. 4, pp. 2986-2995, 2018.
- [TUR10] M. Tursini, E. Chiricozzi, and R. Petrella, “Feedforward flux-weakening control of surface-mounted permanent-magnet synchronous motors accounting for resistive voltage drop,” *IEEE Trans. Ind. Electron.*, vol. 57, no. 1, pp. 440–448, Jan. 2010.
- [VAC08] P. Vaclavek and P. Blaha, “Interior permanent magnet synchronous machine field weakening control strategy – the analytical solution,” *The University Electro-communications*, pp. 753-757, 2008.
- [WAI01] J. Wai and T. M. Jahns, “A new control technique for achieving wide constant power speed operation with an interior PM alternator machine,” in *Proc. IEEE 36th IAS Annu. Meeting, Conf. Rec. Ind. Appl. Conf.*, vol. 2, Oct. 2001, pp. 807–814.
- [WAL04] O. Wallmark, “On control of permanent-magnet synchronous motors in hybrid-electric vehicle applications,” Lic thesis, Dept. Elect. Power Eng., Chalmers Univ. Technol., Göteborg, Sweden, 2004.
- [WAN18] C. Wang, Z. Q. Zhu, and H. Zhan, “Adaptive Voltage Feedback Controllers on the Non-Salient Permanent Magnet Synchronous Machine,” in *Int. Conf. on Electr. Mach. ICEM*, 2018, pp. 1374-1380.
- [YON12] Y. Kwon, S. Kim, and S. Sul, “Voltage Feedback Current Control Scheme for Improved Transient Performance of Permanent Magnet Synchronous Machine Drives,” *IEEE Trans. Ind. Electron.*, vol. 59, no. 9, pp. 3373-3382, 2012.
- [YON14] Y. C. Kwon, S. Kim, and S. K. Sul, “Six-step operation of PMSM with instantaneous current control,” *IEEE Trans. Ind. Appl.*, vol. 50, no. 4, pp. 2614-2625, 2014.
- [YOU15] M. Z. Youssef, “Design and performance of a cost-effective BLDC drive for water pump application,” *IEEE Trans. Ind. Electron.*, vol. 62, no. 5, pp. 3277-3284, 2015.

- [ZHA11] Y. Zhang, L. Xu, M. K. Güven, S. Chi, and M. Illindala, "Experimental verification of deep field weakening operation of a 50-kW IPM machine by using single current regulator," *IEEE Trans. Ind. Appl.*, vol. 47, no. 1, pp. 128–133, Jan./Feb. 2011.
- [ZHA18] Z. Zhang, C. Wang, M. Zhou, and X. You, "Flux-weakening in PMSM drives: analysis of voltage angle control and the single current controller design," *IEEE J. of Sel. Topics Power Electron.*, pp. 1-1, 2018.
- [ZHA19] Z. Zhang, C. Wang, M. Zhou, and X. You, "Flux-weakening in PMSM drives: analysis of voltage angle control and the single current controller design," *IEEE J. of Sel. Topics Power Electron.*, vol. 7, no. 1, pp. 437-445, 2019.
- [ZHE18] Z. Dong, Y. Yu, W. Li, B. Wang, and D. Xu, "Flux-Weakening Control for Induction Motor in Voltage Extension Region: Torque Analysis and Dynamic Performance Improvement," *IEEE Trans. Ind. Electron.*, vol. 65, no. 5, pp. 3740-3751, 2018.
- [ZHU00] Z. Q. Zhu, Y. S. Chen, and D. Howe, "Online optimal flux-weakening control of permanent-magnet brushless AC drives," *IEEE Trans. Ind. Appl.*, vol. 36, no. 6, pp. 1661–1668, Nov./Dec. 2000.
- [ZHU02] Z.Q.Zhu, S.Bentouati, and D.Howe, "Control of single-phase permanent magnet brushless DC drives for high-speed applications," in *Proc. 8th IEE Int. Conf. Power Electron. Variable Speed Drives*, London, U.K., Sep. 18–19, 2000, pp. 327–332.
- [ZHU06] Z. Q. Zhu, J. X. Shen, and D. Howe, "Flux-weakening characteristics of trapezoidal back-EMF machines in brushless DC and AC modes," in *Proc. Int. Power Electronics and Motion Control*, Shanghai, China, Aug. 13–16, 2006, pp. 908–912.
- [ZHU07] Z. Q. Zhu and D. Howe, "Electrical machines and drives for electric, hybrid, and fuel cell Vehicles," in *Proceedings of the IEEE*, vol. 95, no. 4, pp. 746-765, 2007.

APPENDIX A EXPERIMENTAL SETUP

The experiments are carried out based on the dSPACE platform, in which the control algorithm can be easily implemented in the Simulink/MATLAB environment with minor modification. Fig. A.1 shows a block diagram of the drive system based on dSPACE platform.

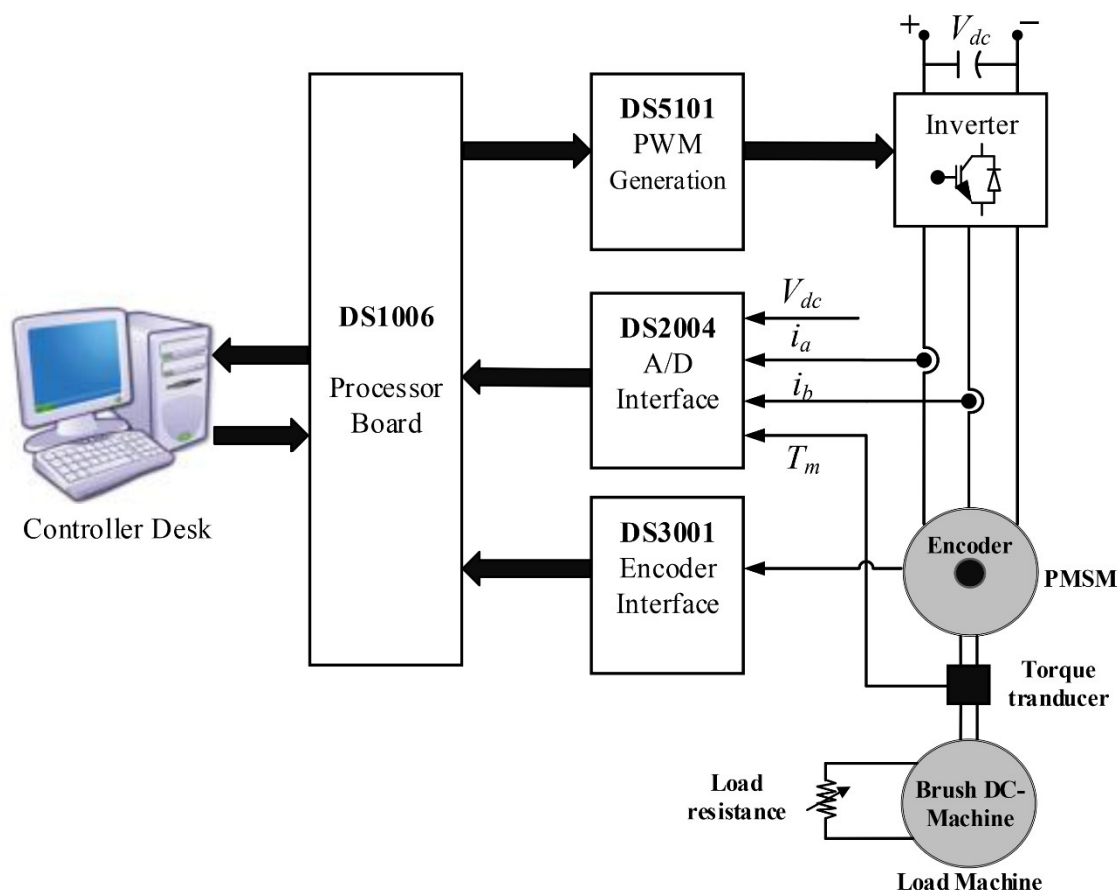


Fig. A.1. Block diagram of the drive system based on dSPACE.

In Fig. A.1, the heart of the control system is the DS1006 processor board, which is based on a 2.4GHz multi-core AMD Opteron CPU. The main processing unit can access modular I/O boards via its PHS-bus, and multiprocessing capable via the DS911 Giga-link Module [DSP10]. The high performance CPU can allow much more complex computation than a normal DSP control system.

The DS5101 board is used to generate switching pulse signals for the inverter according to the algorithm that is computed in DS1006. In this thesis, since the mode PWM6 is selected,

the timing I/O unit of the DS5101 provides 3-phase/6-channel PWM signals with 3 inverted outputs and 3 non-inverted outputs. The three phase inverter board is shown in Fig. A.2. The 6 power switches used in inverter are IRFH7440 MOSFET [IR12], with the continuous current up to 85A and Drain-to-Source breakdown voltage up to 40V. The Static Drain-to-Source On-Resistance is less than $2.4\text{m}\Omega$, which is extremely small when compared with machine resistance.

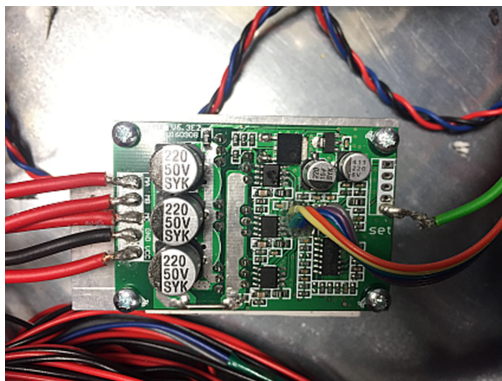
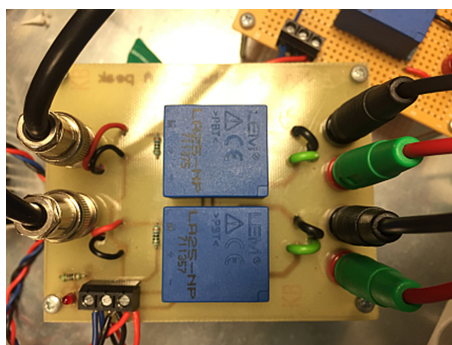
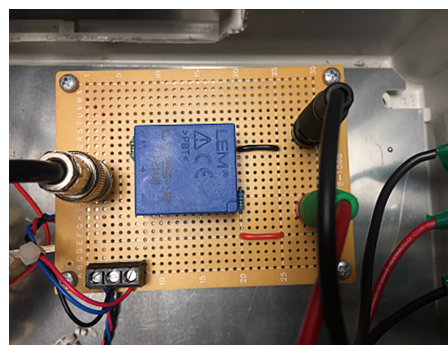


Fig. A.2. Three-phase inverter board.

The DS2004 High-Speed A/D Board is used for digitizing analogue input signals. It contains 16 A/D conversion channels, each of which applies the successive approximation conversion time of 800ns. In this thesis, three analogue signals, i.e. the currents in phases A and B, the DC-link voltage, are measured for the real-time control. The currents in phases A and B are measured by two Hall-effect current transducers (LA 25-P) [LEM14], as shown in Fig. A.3(a). The DC-link voltage is measured by a Hall-effect voltage transducer (LV 25-P) [LEM12], as shown in Fig. A.3(b). A Megtrol torque transducer (TM307) [MAG14] is used for measuring the instantaneous torque. The torque-speed box connected to the torque transducer can be used to acquire the torque and speed. Since the original speed output from the torque transducer is TTL signal with frequency the same as the machine speed, it suffers a big delay. Therefore, the Megtrol torque transducer is only used to measure the instantaneous torque.



(a) Two current Hall-effect transducers.



(b) Voltage Hall-effect transducer.

Fig. A.3. Hall-effect Current and voltage transducers.

The rotor speed and position used for the real-time control are obtained by an incremental rotary encoder with 5000 pulses/revolution (Hengstler RI58-D) [HEN10] through a DS3001 incremental encoder board. As the input encoder lines are from -2^{21} to $+2^{21}$, and the output to the corresponding Simulink block of DS3001 is scaled to -1 to +1, the rotor position (in radian unit) from the scaled output of the DS3001 Simulink block can be calculated as

$$\theta_m = 2^{21} \left(\frac{2\pi}{\text{incremental lines}} \right) \text{scaled output} * N_p \quad (\text{A.1})$$

where N_p is number of pole pairs. For the Hengstler RI58-D, the incremental lines are 5000.

The real drive system based on the dSPACE platform is shown in Fig. A.4. In the experiments, two test rigs are utilized, as shown in Fig. A.5. The test rig-I is shown in Fig. A.5(a), in which the load machine is a wound field excited DC machine with the rated power and rated speed at 1.5 kW and 1500 rpm, respectively. The test rig-I has a big inertia ($0.012\text{kg}\cdot\text{m}^2$) and is coupled with the torque transducer, which can be used to measure the steady-state performance. The test rig-II is shown in Fig. A.5(b), in which the load machine is a wound field excited DC machine with the rated power and rated speed at 150W and 4000 rpm, respectively. In the test rig-I, the influence of the non-ideal drive system, e.g. load torque ripple, misalignment of the transmission system, is more obvious, which is mainly due to its bigger inertial and longer transmission shaft. The test rig-II has a smaller inertial ($0.001\text{kg}\cdot\text{m}^2$) and shorter transmission shaft, the influence of the non-ideal drive system is minor, which is

preferable to verify the speed dynamics. When the load machine is only used to provide the passive torque, the excitation winding of the load machine is powered by a DC-power supply while armature winding is connected to a load resistance. The load torque can be adjusted by regulating the voltage value of DC-power supply or the value of the load resistance. When the load machine is used as an active load, both the armature and excitation windings of the load machine should be powered by two separate power supplies. In the experiments, as the drive machine (PMSM) should also operate under generation condition, a power resistance (4Ω , 14A) is connected to DC-bus of the inverter in order to absorb the feedback energy.

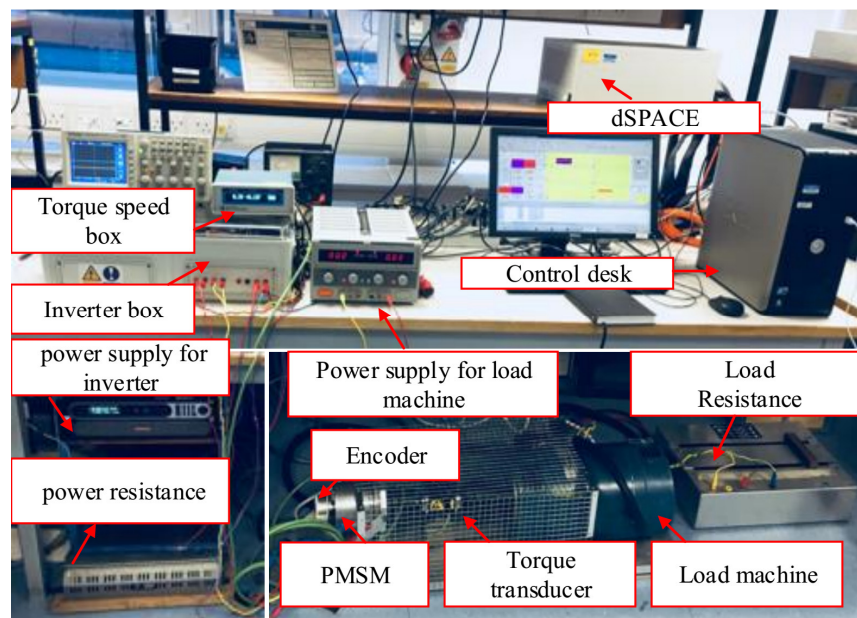
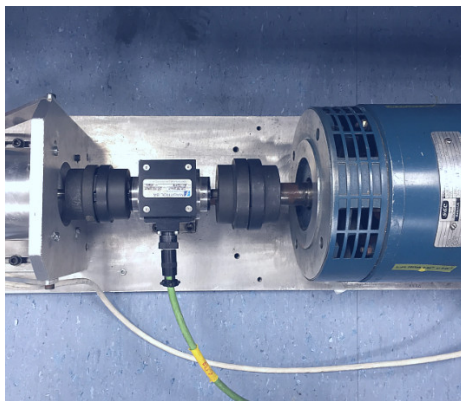


Fig. A.4. Real drive system based on dSPACE platform.



(a) Test rig-I

(a) Test rig-II

Fig. A.5. Two test rigs.

Fig. A.6 shows the stator and rotor of the drive machine, which is a 6-slot/12-flux-modulation-pole/20-pole Vernier machine with concentrated windings. The machine is a non-salient-pole PMSM electromagnetically since it has equal d-axis and q-axis inductances, which is designed by a graduated colleague in EMD group [ONE16]. As only the control performances are investigated in this thesis, the different characteristic current ratios are achieved by setting the different current limit value rather than using the different machines. The major parameters of the machine are shown in Table A.1. The measured back-EMF and the rotor position of the machine at 600rpm are shown in Fig. A.7.



(a) Stator.



(b) Rotor.

Fig. A.6. Stator and rotor of drive machine.

Table A.1 Parameters of the test machine

Parameters	Value
Phase resistance (R_s)	0.25 Ω
Synchronous inductance (L_s)	1.7 mH
PM-flux linkage(ψ_m)	10 mWb
Number of pole pairs (N_p)	10
Characteristic current (i_c)	5.9A

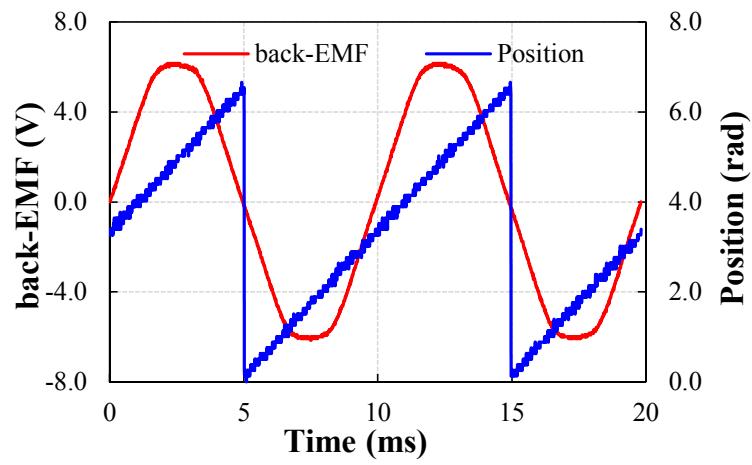


Fig. A.7. Back-EMF waveform (600rpm) and rotor position.

APPENDIX B TUNING OF DCVFC AND CAVFC CONSIDERING MTPV

In chapter 2, the control parameters of the DCVFC for the machine without MTPV region have been designed. For the machine with MTPV region, a similar approach can be employed for both DCVFC and CAVFC. According to (4.11), the characteristic equation of the close-loop transfer function with DCVFC and CAVFC, $q_I(s)$ and $q_\theta(s)$ can be expressed as

$$\begin{cases} q_I(s) = s^2 + \omega_{cc}(1 + b_{\lambda I})s + \omega_{cc}a_{\lambda I}, & DCVFC \\ q_\theta(s) = s^2 + \omega_{cc}(1 + b_{\lambda\theta})s + \omega_{cc}a_{\lambda\theta}, & CAVFC \end{cases} \quad (B.1)$$

where $b_{\lambda I} = b_I \lambda_I$; $a_{\lambda I} = a_I \lambda_I$; $b_{\lambda\theta} = b_\theta \lambda_\theta$; $a_{\lambda\theta} = a_\theta \lambda_\theta$.

For the controller design in the flux-weakening region, the voltage drop on resistance can be ignored. According to the different operation modes, and the coefficients $b_{\lambda I}$, $a_{\lambda I}$, $b_{\lambda\theta}$ and $a_{\lambda\theta}$ can be further derived as

$$\begin{aligned} b_{\lambda I} \Big|_{ModeA} &= -\omega_{mI} \sigma_I / \omega_b \\ a_{\lambda I} \Big|_{ModeA} &= \omega_{mI} \\ b_{\lambda I} \Big|_{ModeB} &= \lambda_I 2V_d^0 L_s \\ a_{\lambda I} \Big|_{ModeB} &= \lambda_I 2\omega_e^0 V_q^0 L_s \end{aligned} \quad (B.2)$$

$$\begin{aligned} b_{\lambda\theta} \Big|_{ModeA} &= -\omega_{m\theta} \sigma_\theta / \omega_b \\ a_{\lambda\theta} \Big|_{ModeA} &= \omega_{m\theta} |V_{dn}| \end{aligned} \quad (B.3)$$

where $\omega_b = V_m / (L_s I_m)$; V_{dn} is V_d^0 normalized by V_m ; ω_{mI} , $\omega_{m\theta}$, σ_I and σ_θ can be expressed as

$$\begin{cases} \omega_{mI} = \lambda_I 2\omega_e^0 L_s i_c \omega_e^0 L_s \\ \sigma_I = (1/i_{cn} + i_{dn}) / (\omega_{en} i_{qn}) \\ \omega_{m\theta} = \lambda_\theta 2|\omega_e^0| L_s i_c V_m \\ \sigma_\theta = (1/i_{cn} + i_{dn}) / \text{sign}(\omega_{en} i_{qn}) \end{cases} \quad (B.4)$$

where i_{dn} and i_{qn} are i_d^0 and i_q^0 normalized by I_m , respectively; i_{cn} is i_c normalized by I_m ; ω_{en} is ω_e^0 normalized by ω_b ; σ_I and σ_θ can be seen as the non-dimensional coefficients which vary with the operation points.

Therefore, the proper λ_I and λ_θ can be obtained with the proper ω_{mI} and $\omega_{m\theta}$. In mode A, according to (B.1)-(B.3), the damping factors for the voltage loop with DCVFC and CAVFC satisfy the following relationships

$$\xi = \begin{cases} \frac{1}{2} \sqrt{\frac{\omega_{cc}}{\omega_{mI}}} \left(1 - \frac{\omega_{mI}}{\omega_b} \sigma_I\right) \geq \frac{1}{2} \sqrt{\frac{\omega_{cc}}{\omega_{mI}}} \left(1 - \frac{\omega_{mI}}{\omega_b} \sigma_{I_{max}}\right), DCVFC \\ \frac{1}{2} \sqrt{\frac{\omega_{cc}}{\omega_{m\theta}}} \frac{\left(1 - \frac{\omega_{m\theta}}{\omega_b} \sigma_\theta\right)}{\sqrt{|V_{dn}|}} \geq \frac{1}{2} \sqrt{\frac{\omega_{cc}}{\omega_{m\theta}}} \left(1 - \frac{\omega_{m\theta}}{\omega_b} \sigma_{\theta_{max}}\right), CAVFC \end{cases} \quad (B.5)$$

where $\sigma_{I_{max}}$ and $\sigma_{\theta_{max}}$ denote the maximum value of σ_I and σ_θ in the flux-weakening region. If the system is designed when $\sigma_I = \sigma_{I_{max}}$ and $\sigma_\theta = \sigma_{\theta_{max}}$, ω_{mI} and $\omega_{m\theta}$ can be solved as

$$\begin{cases} \omega_{mI} = \frac{\omega_{cc}}{\sigma_{I_{max}} \frac{\omega_{cc}}{\omega_b} + 2\xi^2 + \sqrt{\left(\sigma_{I_{max}} \frac{\omega_{cc}}{\omega_b} + 2\xi^2\right)^2 - \left(\frac{\omega_{cc}}{\omega_b}\right)^2 \sigma_{I_{max}}^2}} \\ \omega_{m\theta} = \frac{\omega_{cc}}{\sigma_{\theta_{max}} \frac{\omega_{cc}}{\omega_b} + 2\xi^2 + \sqrt{\left(\sigma_{\theta_{max}} \frac{\omega_{cc}}{\omega_b} + 2\xi^2\right)^2 - \left(\frac{\omega_{cc}}{\omega_b}\right)^2 \sigma_{\theta_{max}}^2}} \end{cases} \quad (B.6)$$

As a conservative design, ω_{mI} and $\omega_{m\theta}$ can be simplified to their lower boundary. For the critical damping condition, i.e. $\xi=1$, the simplified ω_{mI} and $\omega_{m\theta}$ can be obtained as

$$\begin{cases} \omega_{mI} = \frac{\omega_{cc}}{4 + 2\sigma_{I_{max}} \frac{\omega_{cc}}{\omega_b}} \\ \omega_{m\theta} = \frac{\omega_{cc}}{4 + 2\sigma_{\theta_{max}} \frac{\omega_{cc}}{\omega_b}} \end{cases} \quad (B.7)$$

According to (B.4), $\sigma_{\theta_{max}}$ can be obtained as

$$\sigma_{\theta max} = \max\{1/i_{cn}, 1-1/i_{cn}\} \quad (B.8)$$

Therefore, the control parameter of CAVFC can be easily obtained as

$$\lambda_{\theta} = \frac{\omega_{m\theta}}{2|\omega_e^0|L_sV_m i_c} \quad (B.9)$$

For the DCVFC, since $\sigma_{I max}$ could be positive infinity when $i_{dn}=-1$ and $i_{qn}=0$, the control parameter λ_I should be theoretically zero, which is not practical. However, for the machine with MTPV region, the extreme condition, i.e. when $i_{dn}=-1$, can be reasonably ignored as the system will transfer to the mode C when $i_{dn} \approx -i_{cn}$. Therefore, $\sigma_{I max}$ is not necessary to set the as positive infinity, but can set at a value, which is higher than most of the operation points except the region where i_{dn} approaches -1. For a given i_{cn} , a proper $\sigma_{I max}$ can be selected according to the variation of σ_I in mode A. Fig. B.1 shows the variation of σ_I when $i_{cn}=0.8$ (for the given parameter) in the mode A. As can be seen from Fig. B.1, $\sigma_{I max}$ can be reasonably set at 2, which is higher than the most of operation points from $i_{dn}=0$ to $i_{dn}=-1$. When $\zeta=1$, the control parameter of DCVFC in the mode A can be tuned as

$$\begin{aligned} \lambda_I|_{ModeA} &= \frac{\omega_{mI}}{2\omega_e^0 L_s \omega_e^0 L_s i_c} \\ &= \frac{\omega_m}{2|\omega_e^0|L_s V_m}, \omega_m = \omega_{mIA} \end{aligned} \quad (B.10)$$

where $\omega_{mIA} = \omega_{mI}/(|\omega_{en}|i_{cn})$.

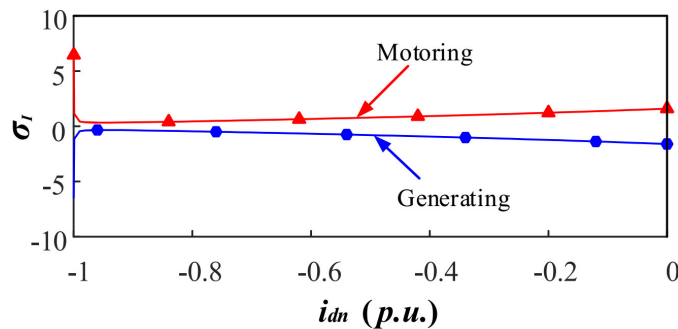


Fig. B.1. Variation of σ_I against i_{dn} when $i_{cn}=0.8$ in mode A.

In mode B, since the Routh stable criterion requires that $1+b_{\lambda I}|_{modeB}>0$ and $a_{\lambda I}|_{modeB}>0$, the worst condition happens when V_d^0 is minimum, i.e. $V_d^0 = -V_m$, which defines the minimum stable range for the control parameter λ_I . Assuming that λ_I is tuned so that $1+b_{\lambda I}|_{modeB}>0.5$ at the worst condition, the control parameter λ_I in the mode B can be set as

$$\lambda_I|_{ModeB} = \frac{\omega_m}{2|\omega_e^0|L_sV_m}, \omega_m \leq \omega_{mB} = \frac{|\omega_e^0|}{2} \quad (B.11)$$

In addition, it should be noted that ω_{mIA} is obtained in mode A and is inversely proportional to the machine speed. When the system transfers to the mode C, ω_{mIA} will be too small if the machine speed is too high. Therefore, the minimum of ω_{mIA} can be limited at the value obtained at the point when the system transfers to mode C. The minimum of ω_{mIA} can be approximately obtained when $i_{dn}=-i_{cn}$, at which condition ω_{mIA} can be approximated as $\omega_{ml}/1.3$ when $i_{cn}=0.8$. Therefore, by considering mode C, ω_{mIA} can be further revised as

$$\omega_{mIA} = \max\left\{\frac{\omega_{ml}}{i_{cn}|\omega_{en}|}, \frac{\omega_{ml}}{1.3}\right\} \quad (B.12)$$

Finally, the control parameter λ_I can be set as

$$\lambda_I = \frac{\omega_m}{2|\omega_e^0|L_sV_m}, \omega_m = \min\{\omega_{mIA}, \omega_{mB}\} \quad (B.13)$$

When the system operates under mode C, ω_{mIA} is much smaller than ω_{mB} . Therefore, $b_{\lambda I}|_{ModeB} \lambda_I$ can be approximated as zero for the MTPV controller design.

APPENDIX C PUBLICATIONS

Conference Papers

- [1] C. Wang, Z. Q. Zhu, and H. Zhan, "Adaptive voltage feedback controllers on the non-salient permanent magnet synchronous machine," in *Int. Conf. on Electr. Mach. ICEM*, 2018, pp. 1374-1380.
- [2] C. Wang, Z. Q. Zhu, "Fuzzy logic speed controller with adaptive voltage feedback controller of permanent magnet synchronous machine," in *Int. Conf. on Electr. Mach. ICEM*, 2018, pp. 1374-1380

Journal Papers Submitted

- [1] C. Wang, Z. Q. Zhu, and H. Zhan, "Adaptive voltage feedback controllers for non-salient permanent magnet synchronous machine," submitted to *IEEE Trans. Ind. Appl.* Under review.
- [2] C. Wang, Z. Q. Zhu, "Fuzzy logic speed control of permanent magnet synchronous machine and feedback voltage ripple reduction in flux-weakening operation region," submitted to *IEEE Trans. Ind. Appl.* Under review.

Papers to be Submitted

- [1] C. Wang, Z. Q. Zhu, "Feedback type flux weakening control on non-salient-pole permanent magnet synchronous machine with maximum torque per voltage region," to be submitted.
- [2] C. Wang, Z. Q. Zhu, "Comparative study of two feedback flux-weakening control methods of permanent magnet synchronous machine," to be submitted.
- [3] C. Wang, Z. Q. Zhu, "A hybrid feedback flux-weakening control of permanent magnet synchronous machine," to be submitted.